A Polarized Strong-Field QED Kinetic Framework for Simulating Relativistic Laser-Plasma Interactions

by

Qian Qian

A dissertation submitted in partial fulfillment
of the requirements for the degree of
Doctor of Philosophy
(Electrical Engineering)
in the University of Michigan
2025

Doctoral Committee:

Professor Alexander Thomas, Chair
Professor Christine Aidala
Professor Almantas Galvanauskas
Professor Christopher Ridgers, University of York
Dr. Daniel Seipt, Helmholtz Institute Jena
Research Scientist Igor Sokolov

Qian Qian
qqbruce@umich.edu
ORCID iD: 0000-0001-6955-769X

© Qian Qian 2025

DEDICATION

Dedicated to my parents, Zhenghua Qian and Lizhen Yu, and my grandma Zhuyin Lai. This degree belongs to all of you.

ACKNOWLEDGEMENTS

I still vaguely remember that in my childhood, I said quite naively that I wanted to become a scientist in the future. It is probably a popular answer for kids at my time to answer the question, What do you want to be in the future? As time grows, our minds change, and our future dreams diversify. Fortunately, I gained a very keen interest in physics during my teenage years. I was fascinated by all the fantastic things happening around us in nature that can be simply described and even predicted by several mathematical formulas, and I am curious to study more. And it is from this original enthusiasm and curiosity that drives me to pursue a Ph.D degree. However, the path is not easy, sometimes frustrating, and it can be hard to see the end in sight. I can firmly say that my Ph.D journey would not have been possible without all the smart, friendly, and warmhearted people I met along this journey. They teach me, support me not just in research, but also in my personal life. They work together with me, and are the people that I can share the bitterness and sweetness with. This acknowledgment section is totally for you.

First and foremost, I want to give thanks to my advisor, Alexander Thomas. I still remember the day we first met, about 7 years ago, during winter break, which was indeed a remarkable meeting. I was a Master student at that time, eager to search for a Ph.D. advisor. I had just seen Alec's photo on the webpage and was wondering how I could contact him. As I went for a walk that afternoon and passed through the EECS building, I saw Alec, who was different from the photo, with gray hair instead of black, but I was pretty sure that person was him. I approached him directly and asked if he could assign me a project to work on and if I could be considered for a Ph.D. student position if that project were successful. My research journey started from this accidental meeting. Throughout my six-year-long

Ph.D. journey, Alec has always been so thoughtful, pleasant, patient, and supportive. There were several times when I actually wanted to give up working on this spin-polarized QED research, as many of our ideas had already been done by our competitor groups. Alec gave me confidence that I can make it through. Not to mention the time he spent on discussing and thinking together with me on the problem I was not able to solve, and gave very valuable advice, or even directly provided an analytical explanation for the result I didn't know how to explain. He also cares a great deal about my future development, as he generously offers many opportunities to attend different conferences and encourages me to present my results. He brought me into many collaborations, which connect me with other scientists in this field. He is a genuinely great advisor, and it is really my fortune to have met him on this journey.

I want to give special thanks to Dr Daniel Seipt and Dr Yong Ma. Throughout my Ph.D. journey, they stood out as two towering figures—one guiding me through the realms of theory, the other through experiment. Their expertise, mentorship, and unwavering support have been both inspiring and invaluable to my growth as a researcher. It will be my pleasure to work together with them in the future. I would also like to extend special thanks to Dr. Brandon Russell, who collaborated with me on various works related to strong-field QED. His enthusiasm, curiosity, and thoughtful insights indeed inspired and encouraged me. I would like to give thanks to to my friends and colleagues in the office and the lab: Dr Jason Cardarelli, Dr Stephen DiIorio, Dr Mario Balcazar, Dr Hongmei Tang, Dr Nicholas Ernst, Dr Nicholas Peskosky, Andre Antione, Rebecca Herbst, Brendan Stassel, Joshua Latham, Veronica Contreras, Tanner Nutting, Jeremy Rebenstock, and all those whose names I may have inadvertently omitted. Sharing our daily research life—whether through collaboration, "coffee breaks," Journal Jams, or Old Chips meetings—has made this journey all the more meaningful and enjoyable. Thank you all for your company and support.

I would like to extend my sincere gratitude to my collaborators on the New Spin Chat meeting. In particular, I wish to thank Prof. Christopher Ridgers, Dr. Tom Blackburn, and Dr. Christopher Arran for their invaluable contributions during our meetings. Your

expertise and thoughtful perspectives have been truly appreciated. On the Osiris QED collaboration side, I am grateful to Prof. Marija Vranic, Dr. Thomas Grismayer, Prof. John Palastro, and Bernardo Barbosa. I greatly admire your deep expertise and your willingness to generously share insights when I faced research challenges. Our discussions have been extremely beneficial and have significantly advanced my work.

I would also like to thank my committee members—Prof. Almantas Galvanauskas, Prof. Christine Aidala, Prof. Christopher Ridgers, Dr. Daniel Seipt, and Dr. Igor Sokolov. Your expertise, constructive feedback, and guidance have been instrumental to the successful completion of my thesis.

Finally, I would like to thank the friends I have met here at Michigan. In particular, I am deeply grateful to the Ann Arbor Chinese Christian Church and all the friends I have come to know there. The church truly became my second home—a place where we worshipped together, shared many cherished memories in the dining hall and fellowship gatherings, and enjoyed time on the badminton and tennis courts. Your prayers have been a great source of strength and encouragement to me. I would also like to express my deepest gratitude to my parents, as well as my grandmother, who sadly passed away during my Ph.D. journey. Their unconditional love and unwavering support have made all of my accomplishments possible.

TABLE OF CONTENTS

DEDICATION ii

ACKNOWLEDGEMENTS iii

LIST OF FIGURES ix

LIST OF TABLES xviii

LIST OF APPENDICES xix

ABSTRACT xx

CHAPTER

1 Introduction **1**

1.1 Thesis Outline 7

2 Background Theory **9**

2.1 Strong Field QED Parameters 9

2.2 Particle Dynamics in Strong Fields 11

2.2.1 Single Charged Particle Motion in a Laser Field 11

2.2.2 The Larmor Power 14

2.2.3 Classical Radiation Reaction 17

2.2.4 Inclusion of Spin and Polarization 19

2.2.5 Justification of Semiclassical Spin Model 20

2.2.6 Classical Spin Motion 22

2.2.7 Polarization and Spin 23

2.2.8 Polarization for Photon 25

2.3 Volkov State and Furry Picture 27

2.4 Nonlinear Compton Scattering and Nonlinear Breit-Wheeler Process 28

2.5 Important Approximations in SFQED 31

2.5.1 Formation Length 31

2.5.2 LCFA Approximation 33

2.6 Quantum Radiation Reaction 34

2.7 Extending SFQED to Include Spin and Polarization 35

2.8 Kinetic Theory for Spin-Polarized Relativistic Plasmas with Radiation and Electron Self-Loop Correction . . . 38
2.9 Spin and Polarization-Dependent QED in PIC Code . . . 43
2.10 Lepton Spin and Photon Polarization Basis in PIC . . . 44
2.10.1 Lepton Spin Basis . . . 46
2.10.2 Photon Polarization Basis . . . 48

3 Method . . . 53

3.1 QED-PIC Code in General . . . 53
3.1.1 Decision Making in QED-PIC . . . 54
3.1.2 Sampling the Spectrum . . . 55
3.1.3 Wrap up the Calculation . . . 56
3.2 Spin and Polarization-Resolved QED-PIC Code . . . 57
3.2.1 Spin and Polarization Dependent NLCS Implementation . . . 59
3.2.2 Spin and Polarization Dependent NBW Implementation . . . 63
3.3 Quantum Non-Transition Event . . . 68
3.4 Code Verification . . . 71
3.4.1 NLCS Photon Spectrum for Different Spin-Polarized Lepton . . . 71
3.4.2 NBW Pair Production Spectrum for Different Polarized Photon . . . 73
3.5 Code Validation . . . 74
3.5.1 Sokolov Ternov Effect . . . 74
3.5.2 Comparing with Classical Polarization Spectrum . . . 75
3.5.3 Spin Evolution for Arbitrary Initial Conditions and Field Configurations . . . 78
3.5.4 Benchmark against Ptarmigan . . . 79
3.5.5 Benchmark against Previously Published Results . . . 81
3.5.6 Spin Polarization from Colliding with an Elliptically Polarized Laser 84

4 Parametric Study of the Polarization Dependence of the Nonlinear Breit-Wheeler Pair Creation Process Using Two Laser Pulses . . . 97

4.1 Introduction . . . 97
4.2 Scheme Demonstration using Polarization-Dependent QED PIC Simulations 98
4.3 Analytic Model for Polarization Dependent Pair Production Yield . . . 101
4.4 Designing Optimal Parameters . . . 103
4.5 Conclusion . . . 108

5 Gamma Flash Measurement by Polarization . . . 110

5.1 Introduction . . . 110
5.2 Model for Hard Photon Polarization . . . 112
5.3 Comparison of Hard Photon Polarization Model to PIC Simulations . . . 114
5.4 Conclusions . . . 118

6 Spin and Polarization-Resolved QED Cascades . . . 119

6.1 Introduction . . . 119
6.2 Spin Polarized Avalanche Cascade by Two CP Lasers . . . 121

6.3 Spin Polarized Shower-Type Cascade by Collision Between a CP Laser and an Unpolarized Beam . . . 127
6.4 Study the Origin of Longitudinal Spin Polarization . . . 133
6.5 Conclusion . . . 142

7 Other SFQED Laser-Plasma Studies . . . 144

7.1 On Strong Magnetic Field Measurement . . . 144
7.2 SFQED in a Plasma Wakefield . . . 151
7.2.1 QED Effect for Beam Transportation Inside Wakefield . . . 152
7.2.2 Radiation Induced Energy Spread . . . 155
7.2.3 Radation-induced emittance cooling . . . 160
7.2.4 Asymptotic Limit for Beam Transverse Distribution Inside Wakefield 160
7.2.5 QED Effect on Spin Transportation . . . 165
7.2.6 Beam Inside an Ion Channel . . . 165
7.2.7 Boltzmann Radiation Reaction . . . 168
7.3 Conclusion . . . 171

8 Conclusion . . . 173

8.1 Parametric Study of the Polarization Dependence of NBW Process Using Two Laser Pulses . . . 174
8.2 Gamma Flash Measurement by Polarisation . . . 175
8.3 Spin Polarized QED Cascades . . . 176
8.4 Ultrafast Relativistic Electron Probing of Extreme Magnetic Fields . . . 177
8.5 Radiation Effect for Future Tev-Classed Plasma-Based Accelerators . . . 178
8.6 Perspective . . . 179

APPENDICES . . . 183

BIBLIOGRAPHY . . . 215

LIST OF FIGURES

FIGURE

1.1 Schematic representation of the modulation of electromagnetic radiation in the magnetosphere of a neutron star. Electric currents (yellow), composed mainly of electrons and positrons, flow along the magnetic field lines (magenta). The X-ray emission from the star's surface (black) is scattered resonantly by these charge carriers. The resulting high-energy gamma rays can create further electron-positron pairs. Image Credit: Max-Planck-Gesellschaft, München, "Asteroseismology of magnetars", by Michael Gabler. [1] 6

2.1 (a) The electric field lines at time t, for a charge that accelerates to velocity Δv in a interval Δt. (b) The tangential and radial components of the electric fields E_θ and E_r at a distance ct from the charge. (Adapted from [2]) 15
2.2 (a) Emission of a photon by a dressed lepton. (b) Production of an electron and positron pair by a gamma ray photon. 28
2.3 (a) photon absorption by a dressed lepton (b) One-photon electron-positron pair annihilation. p and p' are the electron momenta. s and s' are spin states and j is the polarization state. 28
2.4 Geometric definition of formation length L_f, which is related to the instantaneous radius of curvature of the electron trajectory r_c and the radiation angle θ_γ . . . 32
2.5 Spin and polarization involved-NLC spectra for lepton with initial spin state s. ξ_k is the Stokes parameter of the radiated photon. 44
2.6 Spin and polarization involved-NBW spectrums for the photon with Stokes parameter ξ_k. The generated positron spin state is s_p. 45
2.7 Schemetic of spin measurement under the basis ($\hat{\boldsymbol{\varepsilon}}$, $\hat{\boldsymbol{\beta}}$, $\hat{\boldsymbol{k}}$) 47
2.8 Photon polarization basis. A high-energy lepton with momentum in direction $\hat{\boldsymbol{u}}$ emits a photon whose momentum direction $\hat{\boldsymbol{k}} = \hat{\boldsymbol{u}}$. The polarization basis vector for the photon is $\hat{\boldsymbol{\varepsilon}}$, $\hat{\boldsymbol{\beta}}$. When $\hat{\boldsymbol{\kappa}} = -\hat{\boldsymbol{k}}$, $\boldsymbol{\sigma}$ and $\boldsymbol{\pi}$ are in the same direction as $\hat{\boldsymbol{\varepsilon}}$ and $\hat{\boldsymbol{\beta}}$. 49

3.1 Flow chart for spin-polarized QED algorithm 58
3.2 Flow chart for spin-polarized NLCS algorithm 60
3.3 Flow chart for spin-polarized NBW algorithm 64
3.4 The influence of no-quantum radiation correction to the lepton spin evolution . 69

3.5 (a) The evolution of linear polarization state, calculated without non-pair creation polarization state change. (b) The evolution of the linear polarization state, calculated with non-pair creation polarization state change. The unpolarized beams in the simulation were constructed here from two identical parts with opposite polarization states. The black curve is for opposite linear polarization states, the red curve is for opposite circular polarization states, and the blue curve is for opposite diagonal polarization states initially. 70
3.6 Benchmark of linearly polarized (ξ_3) photon spectrum from the NLC process for an unpolarized lepton beam inside a constant magnetic field. The classical particle dynamics, radiation back reaction, and radiation-induced spin change are all switched off for simplicity. We scan the spectrum through $\chi = 0.1$, $\chi = 1$, $\chi = 10$ and $\chi = 99$. 72
3.7 Benchmark of positron spectrum for spin component S_β from the NBW process for an unpolarized photon beam inside a constant magnetic field. The classical particle dynamics, radiation back reaction, and radiation-induced spin change are all switched off for simplicity. We scan the spectrum through $\chi = 0.5$, $\chi = 1$, $\chi = 10$ and $\chi = 99$. 73
3.8 The spin evolution along magnetic field direction for a 1 GeV beam inside a 2.26 MT constant magnetic field. Radiation back-reaction is switched off for simplicity. The simulation result is compared with the well-known Sokolov-Ternov effect prediction. 75
3.9 π and σ polarized photon spectrum from the simulation (blue and yellow solid line) compared with the classical radiation equations (red and purple dashed line) when $\chi = 0.01$. 76
3.10 The evolution spin component along the x, y, z direction for a fully polarized electron beam inside a constant B field. The beam is initially polarized along the x direction, while the magnetic field is along the z direction. The radiation back-reactions are switched off for simplicity. The red curve shows the simulation result using rest frame B field $\hat{\boldsymbol{\beta}}$ as the spin basis. The black curve shows the simulation result using the spin quantization axis $\boldsymbol{S}_{SQA}$ defined in Eq. 2.99 as the spin basis. The dashed cyan curve is the analytic prediction using the B-K-S equation. 77
3.11 The evolution spin component along the x, y, z direction for an unpolarized electron beam inside a changing B field. The magnetic field is initially along the z direction and stays in z for a while. It then quickly rotates to the y direction at a rotation speed close to the electron gyro frequency. The amplitude of the magnetic field remains the same. The radiation back-reactions are switched off for simplicity. The red curve shows the simulation result using rest frame B field direction $\hat{\boldsymbol{\beta}}$ as the spin basis. The black curve shows the simulation result using the spin quantization axis $\boldsymbol{S}_{SQA}$ defined in Eq. 2.99 as the spin basis. The dashed cyan curve is the analytic prediction using the B-K-S equation. 80

3.12 Photon polarization spectrum from Osiris compared with Ptarmigan. (a), (c), (e), Simulation result from ptarmigan. (a), (b) The total photon density distribution in py-pz space, (c),(d) The density distribution for photons with polarization state $\xi_3 > 0$. (e)(f) The density distribution for photons with polarization state $\xi_3 < 0$. (a),(c),(e) are the results from Ptarmigan. Our code results are shown in (b), (d), (f). 81
3.13 Electron and positron beam spin polarization evolution in a bichromatic laser. (a) From the paper [3] (b) from the OSIRIS spin and polarization-resolved QED simulation. Subplot (a) reproduced from Yue-Yue Chen et al. Phys. Rev. Lett. **123**, 174801 (2019).© American Physical Society. 83
3.14 Spin polarization in a bichromatic laser, with the full spin and polarization model in our code 83
3.15 Spin polarization from colliding with an elliptically polarized laser. (a), (b) The spin distribution in the $\theta_y - \theta_z$ base space after the interaction. (c), (d) The spin and density distribution with respect to the deflection angle θ_y. (a),(c) is from the paper [4]. (b), (d) from the OSIRIS spin and polarization-resolved QED simulation. Subplots (a) (c) reproduced from Yan-Fei Li et al. Phys. Rev. Lett. **122**, 154801 (2019).© American Physical Society. 85
3.16 Linear polarization gamma-ray in laser-solid target interaction, from paper [5]. (a) Photon density distribution in the photon energy ε_γ -deflection angle θ phase space. (b) Photon linear polarization distribution in the $\varepsilon_\gamma - \theta$ phase space. (c) Photon density distribution with respect to the photon energy ε_γ for laser $a_0 = 50,\ 100,\ 150$. (d) Photon linear polarization distribution with respect to the deflection angle θ for lasers $a_0 = 50,\ 100,\ 150$. This figure is from "Generation of highly-polarized high-energy brilliant γ-rays via laser-plasma interaction" Matter Radiat. Extremes **5**, 054402 (2020) by Kun Xue et al., which is licensed under CC BY 4.0. 86
3.17 Linear polarization gamma-ray in laser-solid target interaction, from the OSIRIS spin and polarization-resolved QED simulation. (a) Photon density distribution in the photon energy ε_γ -deflection angle θ phase space. (b) Photon linear polarization distribution in the $\varepsilon_\gamma - \theta$ phase space. (c) Photon density distribution with respect to the photon energy ε_γ for laser $a_0 = 50,\ 100,\ 150$. (d) Photon linear polarization distribution with respect to the deflection angle θ for lasers $a_0 = 50,\ 100,\ 150$. 87
3.18 Helicity transfer in a laser field due to the electron anomalous Magnetic Moment, from the paper [6]. (a) Polar plot of electron density distribution (b) Polar plot of electron longitudinal spin distribution. Figure reproduced from Yan-Fei Li et al. Phys. Rev. Lett. **128**, 174801 (2022) © American Physical Society. 88
3.19 Helicity transfer in laser field due to the electron Anomalous Magnetic Moment, from OSIRIS spin and polarization-resolved QED simulation. (a) Polar plot of electron density distribution (b) Polar plot of electron longitudinal spin distribution. 89
3.20 Helicity transfer in laser field due to the electron anomalous magnetic moment, (a) from paper [6](b) from OSIRIS spin and polarization-resolved QED simulation. Subplot (a) is reproduced from Yan-Fei Li et al. Phys. Rev. Lett. **128**, 174801 (2022) © American Physical Society. 90

3.21 Circular-polarized high-energy gamma-ray pulse via Laser-Electron Interaction (a) from paper [7], (b) from OSIRIS spin and polarization-resolved QED simulation. Subplot (a) is reproduced from Yan-Fei Li et al. Phys. Rev. Lett. **125**, 044802 (2020) © American Physical Society. 91
3.22 Production of Highly Polarized Positron Beams via Helicity Transfer from Polarized Electrons (a) from paper [8], (b) from OSIRIS spin and polarization-resolved QED simulation. Subplot (a) is reproduced from Yan-Fei Li et al.Phys. Rev. Lett. **124**, 014801 (2020) © American Physical Society. 92
3.23 Snapshot of the electron (a), (c) and positron (b), (d) distribution functions in an up (a), (b) or down (c), (d) spin state for $a_0 = 10^3$ and $\omega t = 10$ in a rotating radial frame. Green curves are χ isocontours. Black dashed curves represent the separatrix of the classical advection $p = -2a_0 q \sin\varphi$, and black crosses are the corresponding fixed points at $\varphi = -q\pi/2.0$, $p = a_0$. This figure is from "Polarized QED cascades" New J. Phys. **23** 053025 (2022) by D. Seipt, C. P. Ridgers, D. Del Sorbo, and A. G. R. Thomas, which is licensed under CC BY 4.0. 94
3.24 Snapshot of the electron (a), (c) and positron (b), (d) distribution functions in an up (a), (b) or down (c), (d) spin state for the same conditions as the paper calculated using Osiris spin and polarization-dependent QED module. 95
3.25 Time evolution of electron (a), a positron (b), and photon (c) yields during a cascade seeded by unpolarized electrons calculated by the Osiris spin and polarization QED module. 95
3.26 Time evolution of the electron yield of photon-seeded cascade calculated using Osiris spin and polarization QED module. 96

4.1 (a) Two-pulse pair production setup. (b) Energy spectrum and averaged linear polarization stokes parameter of the gamma-ray beam from the first collision. (c) Temporal evolutions of the electron mean energy, positron yield, and high energy photon ($E > 300$ MeV) yield. (d) Angular spectrum of the gamma-ray after the first collision. (e) The energy spectrum of the generated positron when the polarization direction of the two colliding beams is parallel or perpendicular. 100
4.2 The phase space plot for the ratio of the positron yield when changing the polarization directions of two colliding laser pulses from parallel to perpendicular for different χ_1 and χ_2. 105
4.3 The minimum requirement for pulse duration of the first laser pulse for different input beam energies and laser intensities in the first collision. The regions on the upper right and lower left are where $\chi_e < 0.05$ and $\chi_e > 0.5$. 106
4.4 The maximum duration of the second laser pulse for different input gamma-ray beam energies and laser intensities in the second collision. The regions on the lower left are where $\chi_e < 0.5$. The upper right corner is the region with laser duration is $t_2 < 5$ fs. 107

5.1 Top row: Photon density distribution in x-y simulation plane for the population with energy above (a) 10 keV, (b) 100 keV, (c) 1MeV after the laser fully reflected from the target. Bottom row: Photon linear polarization distribution in the x-y simulation plane for the population with energy above (d) 10 keV, (e) 100 keV, (f) 1MeV after the laser fully reflected from the target. $\langle\xi_3\rangle$ measures the photon averaged linear polarization degree, which, when the photon is fully polarized along the laser polarization direction, is $\langle\xi_3\rangle = 1$. The gray scale plot shows the target electron density distribution. 114
5.2 Angle-resolved (a) Photon density distribution $\frac{d^2N}{d\theta dE}$, (b) Photon linear polarization $\langle\xi_3\rangle$ distribution. This angular density/polarization map corresponds to the same simulation shown in Fig. 5.1. 115
5.3 NLCS x-ray photon number above energy ε_{th} in a laser solid target interaction with different laser intensity a_0 116
5.4 NLCS x-ray photon polarization in a laser solid target interaction as a function of a_0 and the energy of the emitted photon 117
5.5 NLCS x-ray photon polarization for photon above energy ε_{th} in a laser solid target interaction with different laser intensity a_0 118

6.1 Spin polarized QED cascades 122
6.2 QED cascade simulation result of (a) spatial distribution of longitudinal spin for electrons and (b) positrons; (c) spatial distribution of density for electrons and (d) positrons. 123
6.3 QED cascade simulation result of (a) spatial distribution of longitudinal spin for electrons and (b) positrons; (c) spatial distribution of density for electrons and (d) positrons when changing the helicity of both CP lasers 124
6.4 The positron longitudinal spin distribution in angular and energy phase space (a) both CP lasers polarization right-handed (b) both CP lasers polarization left-handed 124
6.5 Parameter scan to demonstrate the relationship between longitudinal spin and yield, with respect to target density n_0, laser intensity a_0, and laser duration τ . 125
6.6 The spatial distribution of longitudinal spin S_{lon}, without radiation-induced spin change, for pair production with a particle born unpolarized, and with the anomalous magnetic moment equal to zero 126
6.7 Evolution of the longitudinal spin compared with the result calculated using equation 6.1 126
6.8 Spin polarized QED cascade 128
6.9 QED cascade simulation result of (a) spatial distribution of longitudinal spin for electrons and (b) positrons; (c) spatial distribution of density for electrons and (d) positrons. 129
6.10 QED cascade simulation result of (a) spatial distribution of longitudinal spin for electrons and (b) positrons; (c) spatial distribution of density for electrons and (d) positrons. 130
6.11 Parameter scan to demonstrate the relationship between longitudinal spin and yield, with respect to laser intensity a_0, initial beam energy γ, and laser duration τ130

6.12 The spin and positron density with respect to energy for a beam with an initial energy of 511 MeV ($\gamma = 1000$) collides with a CP laser with $a_0 = 1500$. The averaged longitudinal spin is 45% and the spin for the high-energy part of the beam is 70%, with a population of 8.7% of the initial electron beam. 131
6.13 The spatial distribution of longitudinal spin S_{lon}, without radiation-induced spin change, for pair production with a particle born unpolarized, and with the anomalous magnetic moment equal to zero 132
6.14 Evolution of the longitudinal spin compared with the result calculated using equation 6.1 133
6.15 The initial spin direction with respect to the rest frame E and B field direction for (a) shower-type cascade, (b) avalanche-type cascade. 134
6.16 The evolution of longitudinal polarization for 500 particles in the simulation and the average longitudinal polarization for (a) shower-type cascade, (b) avalanche-type cascade. The blue curve shows the change in the spin length. 135
6.17 The evolution of χ_e for 500 particles tracked in the simulation and the averaged $\langle\chi\rangle$ (a) shower-type cascade, (b) avalanche-type cascade. 136
6.18 The correlation between the length of the spin and the time when the particles are born in the simulation, for (a) shower-type cascade, (b) avalanche-type cascade. The earlier the particles are born, the longer they interact with the field. 136
6.19 The spin trajectory from the particle tracking code for an electron born initially inside an infinite plane wave laser field with intensity $a_0 = 700$ and counterpropagating with the laser with spin pointing in the magnetic field direction. It then deflected and travels together with the laser. (a), (b), (c): the red curve shows the spin trajectory in $(\hat{\boldsymbol{v}}, \hat{\boldsymbol{B}}, \hat{\boldsymbol{E}})$ coordinate, which for highly relativistic particle are nearly mutually orthogonal with each other, the black dashed arrow shows the time averaged spin direction when spin trajectory forms a stable circle under the $(\hat{\boldsymbol{v}}, \hat{\boldsymbol{B}}, \hat{\boldsymbol{E}})$ bases. (d), (e), (f): The evolution of the length of the spin $|\boldsymbol{S}|$ (black) and spin component in $\hat{\boldsymbol{B}}$ (blue), $\hat{\boldsymbol{E}}$ (cyan), and $\hat{\boldsymbol{v}}$ (red), direction. (a), (d), (b), (e) are calculated with real anomalous magnetic moment value $\alpha(\chi)$, which depends on χ_e, while (c), (f) are calculated with anomalous magnetic moment $a_e = 0$. (a), (d) and (b), (e) are calculated with different laser helicities. 137
6.20 The spin rotation axis along B field direction for (a) when anamalous magnetic moment $\alpha = 0$, (b) with real anamalous magnetic moment value $\alpha(\chi_e)$, which depends on χ_e. 138

6.21 (a), (b), (c): Prediction of nonprecession spin direction, calculated using Eq. (6.13) compared with the averaged spin direction under $(\hat{\boldsymbol{v}}, \hat{\boldsymbol{B}}, \hat{\boldsymbol{E}})$ basis. The averaged spin direction are calculated by taking the time average of the spin direction when the spin trajectory forms a stable circle under the $(\hat{\boldsymbol{v}}, \hat{\boldsymbol{B}}, \hat{\boldsymbol{E}})$ basis. (d), (e), (f): The predicted averaged longitudinal spin (purple dashed), calculated using Eq. (6.15) compared with the time-averaged longitudinal spin result (red dashed) from the particle tracking code. The averaged spin direction and the time-averaged longitudinal spin value are calculated by taking the time-average of the spin direction when the spin trajectory forms a stable circle under the $(\hat{\boldsymbol{v}}, \hat{\boldsymbol{B}}, \hat{\boldsymbol{E}})$ basis. We show the comparison for a variety of laser intensity a_0: (a), (d) are calculated with $a_0 = 400$; (b), (e) $a_0 = 700$;(c), (f) $a_0 = 1000$. 141

7.1 Relative difference of the mean energy prediction between the PIC simulations and the simplified analytic model. The orange region marks the parameter space where the LCFA breaks down. The dark blue region shows where the simplified analytic model breaks down. 147

7.2 Illustration of how we can use the mean energy and energy spread measurement of the electron beam before and after it passes through a constant magnetic field region to obtain the strength and the length of the field. The cyan curve and the blue curve represent all the potential magnetic field strength and length combinations for a particular mean energy and the energy spread. The crossing point of the two curves coincides with the ground truth from the PIC simulation, represented by a white star. The black star is the prediction using the analytic Eqns. (7.6) and (7.7). 148

7.3 Demonstration of the non-linear dependence of the aspect ratio of the overlapping region with the position of the region. Here, we assume a 10% measurement error in mean energy loss and spread. For an energy loss of 51 MeV, the plot shows what the possible values of B-field strength and length are if the energy spread is 10%, 8%, or 6%, corresponding to the (a) red, (b) blue, and (c) purple areas in plot (d). 150

7.4 (left) Quantum parameter χ_e heat map for a matched gaussian beam as a function of beam emittance, accelerated to 1 TeV using plasma accelerator stages with different plasma densities. (right) Including radiation friction restricts acceleration. 154

7.5 Simulation results of the beam energy spread evolution for initial beam energy (a) 50 GeV, (b) 100 GeV, (c) 200 GeV using classical radiation and quantum radiation model. The results are compared with the model that estimates only classical orbit effect-induced energy spread (blue dashed curve), only quantum stochastic effect-induced energy spread (green dashed curve), and the summation of the two contributions together (red curve). 158

7.6 (a) Energy spread σ_γ/γ heat map for a Gaussian beam with different emittance accelerated to 1 TeV using LWFA stages with different plasma densities. (b) Heat map for purely quantum radiation effect induced energy spread. 159

7.7 Radiation-induced emittance cooling for a beam propagating inside a channel field with constant acceleration. The field is the same as the wakefield in the bubble region for plasma density n_p equal 10^{18} cm^{-3}, 10^{20} cm^{-3} and 10^{22} cm^{-3}. The beam normalized starts at $1\mu m$. The emittance cooling becomes substantial for a high-density wakefield. 161
7.8 The phase space distribution at the end of the simulation for plasma density n_p equal 10^{18} cm^{-3}, 10^{20} cm^{-3} and 10^{22} cm^{-3}. The beam starts with a 2D Gaussian distribution in transverse phase space, and in a high-density scenario where radiation reaction is significant, the transverse phase space distribution evolves into a ring-shaped distribution. This ring-shaped distribution can suppress the radiation-induced energy spread from the orbit effect. 161
7.9 Asymptotic limit of transverse phase space distribution for a beam inside the channel field with constant acceleration in radiation dominanted region. 164
7.10 Transverse phase space result compared with the asymptotic orbits predicted by our model 164
7.11 QED effect for spin transportation inside wakefield 166

B.1 Flow chart for spin-polarized NLCS algorithm with under reduced spin and polarization basis 199
B.2 Flow chart for spin-polarized NBW algorithm under reduced spin and polarization basis 200

C.1 Benchmark of linearly polarized (ξ_3) photon spectrum from the NLC process for a fully polarized lepton beam inside a constant magnetic field. The particle spin is either fully parallel or antiparallel to the rest frame electric field direction $\hat{\boldsymbol{\beta}}$. The classical particle dynamics, radiation back reaction, and radiation-induced spin change are all switched off for simplicity. We scan the spectrum through $\chi = 0.01$, $\chi = 1$, and $\chi = 99$. 203
C.2 Benchmark of linearly polarized (ξ_3) photon spectrum from the NLC process for a fully polarized lepton beam inside a constant magnetic field. The particle spin is either fully parallel or antiparallel to the rest frame electric field direction $\hat{\boldsymbol{\varepsilon}}$. The classical particle dynamics, radiation back reaction, and radiation induced spin change are all switched off for simplicity. We scan the spectrum through $\chi = 0.01$, $\chi = 1$, and $\chi = 99$. 204
C.3 Benchmark of diagonal polarized (ξ_1) photon spectrum from the NLC process for a fully polarized lepton beam inside a constant magnetic field. The particle spin is either fully parallel or antiparallel to the rest frame electric field direction $\hat{\boldsymbol{\varepsilon}}$. The classical particle dynamics, radiation back reaction, and radiation induced spin change are all switched off for simplicity. We scan the spectrum through $\chi = 0.01$, $\chi = 1$, and $\chi = 99$. 205

C.4 Benchmark of linearly polarized (ξ_3) photon spectrum from the NLC process for a fully polarized lepton beam inside a constant magnetic field. The particle spin is either fully parallel or anti-parallel to the particle momentum direction $\hat{\boldsymbol{k}}$. The classical particle dynamics, radiation back reaction, and radiation-induced spin change are all switched off for simplicity. We scan the spectrum through $\chi = 0.01$, $\chi = 1$, and $\chi = 99$. 207
C.5 Benchmark of circularly polarized (ξ_2) photon spectrum from the NLC process for a fully polarized lepton beam inside a constant magnetic field. The particle spin is either fully parallel or anti-parallel to the particle momentum direction $\hat{\boldsymbol{k}}$. The classical particle dynamics, radiation back reaction, and radiation-induced spin change are all switched off for simplicity. We scan the spectrum through $\chi = 0.01$, $\chi = 1$, and $\chi = 99$. 208
C.6 Benchmark of positron spectrum for spin component S_β from the NBW process for a polarized photon beam inside a constant magnetic field. The photon polarization is either $\xi_3 = -1$ or $\xi_3 = 1$. The classical particle dynamics, radiation back reaction, and radiation-induced spin change are all switched off for simplicity. We scan the spectrum through $\chi = 1$, $\chi = 10$, and $\chi = 99$. 209
C.7 Benchmark of positron spectrum for spin component S_β from the NBW process for a polarized photon beam inside a constant magnetic field. The photon polarization is either $\xi_3 = -1$ or $\xi_3 = 1$. The classical particle dynamics, radiation back reaction, and radiation-induced spin change are all switched off for simplicity. We scan the spectrum through $\chi = 1$, $\chi = 10$, and $\chi = 99$. 210
C.8 Benchmark of positron spectrum for spin component S_ε from the NBW process for a polarized photon beam inside a constant magnetic field. The photon polarization is either $\xi_1 = -1$ or $\xi_1 = 1$. The classical particle dynamics, radiation back reaction, and radiation-induced spin change are all switched off for simplicity. We scan the spectrum through $\chi = 1$, $\chi = 10$, and $\chi = 99$. 211
C.9 Benchmark of positron spectrum for spin component S_β from the NBW process for a polarized photon beam inside a constant magnetic field. The photon polarization is either $\xi_3 = -1$ or $\xi_3 = 1$. The classical particle dynamics, radiation back reaction, and radiation induced spin change are all switched off for simplicity. We scan the spectrum through $\chi = 1$, $\chi = 10$, and $\chi = 99$. 212
C.10 Benchmark of positron spectrum for spin component S_k from the NBW process for a polarized photon beam inside a constant magnetic field. The photon polarization is either $\xi_2 = -1$ or $\xi_2 = 1$. The classical particle dynamics, radiation back reaction, and radiation induced spin change are all switched off for simplicity. We scan the spectrum through $\chi = 1$, $\chi = 10$, and $\chi = 99$. 213

LIST OF TABLES

TABLE

4.1 Simulation parameters used to investigate the optimized parameters to maximize the measurable difference in positron yield when we change the laser polarization direction and their results. Here, the pulse duration is defined in scaled time $\tau = t/\gamma_0$. We compare the positron yields, characterized by the ratio between the number of generated positrons and initial beam charge, and the polarization effect induced difference in positron yields $\Delta_p = (N_p^{\perp} - N_p^{\parallel})/N_p^{\parallel}$ in the simulations with the predictions from our model. 104

5.1 Simulation results shown in Fig. 5.3 to compare with the analytic prediction of NLCS x-ray photon number above energy ε_{th} in a laser solid target interaction with different laser intensity a_0. 116

5.2 Simulation results shown in Fig. 5.4 to compare with the analytic prediction of NLCS x-ray photon polarization in a laser solid target interaction as a function of a_0 and the energy of the emitted photon 117

5.3 Simulation results shown in Fig. 5.5 to compare with the analytic prediction of NLCS x-ray photon polarization for photons above energy ε_{th} in a laser solid target interaction with different laser intensity a_0 117

LIST OF APPENDICES

A Spin and Polarization Resolved-QED Cross Section 183

NLCS Process 183
NBW Pair Production Process 190

B Simplified Algorithm under the Reduced Basis 198

C Code Verification for Initially Polarized Beam 202

NLCS Photon Spectrum for Different Spin-Polarized Lepton 202
NBW Pair Production Spectrum for Different Polarized Photon 206

ABSTRACT

Modern ultra-intense laser facilities can generate electromagnetic fields strong enough to accelerate particles to near-light speeds over micron-scale distances and also approach the QED critical field, resulting in highly nonlinear and relativistic quantum phenomena. For such conditions, ab-initio modeling techniques are required that capture the electromagnetic, relativistic particle, and quantum emission processes in the plasma. One such technique is particle-in-cell (PIC) simulation. In the first part of this thesis, we describe the underlying theory for and development, validation, and verification of an extension to standard QED-PIC in the OSIRIS framework to include spin- and polarization-resolved QED processes central to next-generation laser-plasma experiments. In the second part, the new code framework is used for physics studies across a range of scenarios, including laser-beam collisions, laser-solid interactions, QED cascades, and plasma-based acceleration. A polarization-resolved experiment using a two-laser-beam configuration is designed. Measurements of polarized x-ray flashes are shown to provide clear signatures of QED plasma formation in high-intensity laser interactions with solid targets. Spin and polarization dynamics are explored in both avalanche- and shower-type QED cascades, which introduces a novel approach for generating polarized electron-positron pair plasmas in the laboratory. The use of quantum radiation effects is demonstrated to be a powerful diagnostic tool for probing extremely strong-field environments. Finally, quantum radiation effects are shown to have critical implications for the development of future TeV-class laser wakefield accelerators (LWFA), influencing energy spread, emittance, and beam polarization. These results reveal the importance of the inclusion of spin/polarization effects in modeling, introduce efficient, all-optical pathways to producing polarized beams in laboratory settings, and advance the

current understanding of spin- and polarization-dependent QED phenomena in ultra-intense laser-plasma interactions.

CHAPTER 1

Introduction

The frontier of human knowledge is usually pushed forward by technology that reaches unprecedented limits in terms of condition/measurement precision. The high-intensity, short-pulse laser is one of them. The invention of the chirped pulse amplification (CPA) [9] technique carved out a way to deliver and compress energy to just a few um^3 spaces, thus creating ultra-strong electromagnetic (EM) fields in the lab. This high-intensity laser interacts with plasma to generate strong electromagnetic fields, which are highly desirable for accelerating particles to high energies. Recent advances have led to the development of novel particle acceleration schemes, such as laser wakefield acceleration (LWFA), which can accelerate electrons to several GeV over just a few centimeters of plasma [10, 11]. The focusing structure of laser-driven plasma fields also enables the generation of short, intense X-ray bursts [12, 13]. Additionally, when laser pulses strike solid targets, they can produce strong sheath fields capable of efficiently accelerating protons to tens of MeV [14, 15]. These accelerated ions can then be directed at converter materials to induce nuclear reactions that release neutrons. High-harmonic generation (HHG) during laser-solid interactions provides a source of extreme ultraviolet (XUV) light [16, 17], while laser-driven ion radiators, energized via inverse Bremsstrahlung absorption, can facilitate the production of soft X-ray lasers [18, 19].

Research employing petawatt lasers has produced prolific results with transformative potential across a wide range of fields, including medicine, materials science, and environmental

science. These advancements encompass the generation of secondary radiation sources for phase-contrast X-ray imaging [20], the development of pulsed neutron imaging techniques [21], and innovations in therapies utilizing very high-energy radiation [22, 23]. However, the commercialization and industrial adoption of these technologies are currently limited by the lack of high-average-power laser systems capable of operating continuously at the high repetition rates necessary for many practical applications. Furthermore, high-repetition-rate lasers are essential for making precise measurements of theoretical predictions in high-field science research. However, building a high-power laser with a high repetition rate and high efficiency is still a big challenge for current laser technology. Beam-combined fibers, which use optical fibers as the gain medium to manage heat generation and allow a higher repetition rate, have been developed quickly recently [24, 25, 26, 27, 28, 29]. It could be a possible solution for eventually building a highly efficient kHz repetition rate PW laser, opening the full potential of high-energy lasers for various applications.

The interaction of these ultra-strong EM fields with matter naturally opens up a new regime of relativistic plasma physics. That boundary can be quantified in terms of the laser strength parameter a_0, which in a monochromatic laser is equivalent to the work done on an electron over a (reduced) laser wavelength in units of the electron rest energy $m_e c^2$:

$$a_0 = \frac{eE_0}{m_e c \omega_L} = 0.85 \left(\frac{I}{10^{18} \mathrm{Wcm}^{-2}} \right)^{1/2} \left(\frac{\lambda}{\mu m} \right) \tag{1.1}$$

where e is the electron charge, E the laser peak electric field, ω_L its angular frequency and I its average intensity. When $a_0 > 1$, for example, electrons can be accelerated to relativistic velocities over a single laser wavelength. At relativistic velocity, the magnitude of the magnetic component of the Lorentz force becomes comparable to that of the electric component, and electron motion becomes highly non-linear. This is the regime of relativistic plasma physics.

Current petawatt and even ten petawatt class lasers constructed worldwide are approach-

ing the regime having peak intensity $I > 10^{23}$ Wcm^{-2}, corresponding to normalized laser intensity $a_0 > 100$, where strong field quantum electrodynamics (SFQED) effects can appear. The SFQED processes occur when electromagnetic fields exceed the quantum critical field strength E_{cr} [30]. Even though the most intense laser pulse nowadays cannot reach E_{cr} in the laboratory by many orders of magnitude, SFQED effects necessarily depend on Lorentz-invariant parameters, including $\chi_e \sim E_{RF}/E_{cr}$ which is equivalent to the magnitude of the electric field in the rest frame of an electron, where p^ν is the four-momentum of the electron and $F^{\mu\nu}$ is the electromagnetic tensor. E_{cr} is the QED critical field, or the Schwinger field, which, for a static electric field, would lead to the breakdown of the vacuum. Due to the coupling of relativistic dynamics and strong electromagnetic fields, the SFQED regime may become accessible at lower intensities when relativistic plasma flows interact with the laser fields. In this region, the electrons will be accelerated so strongly that their loss of energy to radiation must be taken into account in the equations of motion. Furthermore, the photons of that radiation will be sufficiently energetic that they can produce electron-positron pairs by colliding with photons of the laser pulse. Even if pair production is not dynamically significant, it is necessary to include quantum corrections to the radiation damping, as classical electromagnetism predicts the emission of photons with energy greater than that of the electron and so overestimates the emissivity.

SFQED effects can play a crucial role in the dynamics of relativistic plasmas. Two fundamental quantum processes—photon emission and electron-positron pair production—significantly impact plasma behavior. When a charged particle emits an energetic photon, the radiation back-reaction alters its trajectory and energy. Conversely, the absorption of high-energy photons via pair production increases the plasma density by generating electron-positron pairs. In environments where electromagnetic fields are sufficiently strong and the plasma is highly energetic, these quantum effects can continuously modify basic plasma parameters, ultimately influencing the collective behavior of the system. As a result, the plasma dynamics may diverge sharply from classical expectations. Such systems are

often referred to in the literature as "QED plasmas" [31, 32, 33, 34, 35].

QED plasmas naturally arise in some of the most extreme astrophysical environments, such as neutron star atmospheres [36, 37], pulsar magnetospheres [38], and the vicinity of black holes [39]. Creating such QED plasmas in the laboratory is a major goal of next-generation high-intensity laser facilities, offering the prospect of exploring a rich array of phenomena that remain poorly understood.

Research in SFQED has reached an advanced stage: theoretical frameworks and simulation tools for studying particle dynamics in strong fields are now well developed [40, 41, 42, 43], and experimental investigations in this regime are emerging [44, 45, 46, 47, 48]. This progress motivates a critical reassessment of the standard SFQED models, which typically rely on specific approximations. In particular, traditional SFQED calculations often assume unpolarized particles by averaging (summing) over initial (final) spin states [49]. In this thesis, we relax this approximation to examine how the spin and polarization of particles evolve within intense fields.

Spin is an intrinsic form of angular momentum present in elementary particles, composite particles (such as hadrons), and atomic nuclei [50]. Unlike classical angular momentum—which arises from actual spinning or rotation—quantum spin is a fundamental property of particles. It does not correspond to any physical spinning, but is instead a purely quantum mechanical phenomenon with no classical equivalent. A pivotal moment came with the 1922 Stern-Gerlach experiment [51], which demonstrated that electrons and other particles exhibit a quantized form of angular momentum that cannot be explained by orbital motion alone. This experiment exposed the inherently quantum nature of spin. Dirac's relativistic equation [52] for the electron later provided a theoretical foundation for spin, naturally incorporating it into the quantum description and, importantly, predicting both electron spin and the existence of antimatter.

The QED theory, developed by Dirac and others [52], also formalizes the quantum description of photons and their polarization—a key intrinsic property. An individual photon

exhibits polarization, which can be described in terms of right- or left-handed circular polarization, or as a superposition of both. Alternatively, photon polarization can be expressed as horizontal or vertical linear polarization, or any superposition of both.

The fundamental processes of photon emission and pair creation are intrinsically dependent on the spin and polarization states of the participating particles. Consequently, these processes can shape the distribution of spin and polarization in the plasma, leading to the generation of polarized particle beams. Such polarized beams are not only scientifically interesting in their own right, but may also serve as powerful experimental probes—offering new diagnostics for the structure and properties of strong-field environments. The polarization state of the particles will also influence the SFQED processes, thereby modifying the rates of photon emission and pair creation.

Spin and polarization-resolved SFQED has recently received increased interest. Novel methods for generating highly polarized lepton and gamma ray beams on a femtosecond timescale and under a compact full-optics setup are proposed [53, 4, 54]. Spin-polarized lepton beams are crucial tools in contemporary physics. They are used extensively to probe the properties of matter, reveal atomic and molecular structures [55, 56], and, in the relativistic domain, study nuclear structure [57, 58], generate polarized photons [59, 60] and positrons [59, 61], investigate parity violation [62], and explore phenomena beyond the Standard Model [63]. In conventional synchrotron facilities, this polarization process is slow due to the relatively weak magnetic fields (around 1 Tesla). In the context of high-intensity laser-plasma interaction, as the laser field strength can be many orders of magnitude higher than that in synchrotrons, enabling polarization timescales on the order of a few femtoseconds, comparable to the duration of high-intensity, ultrashort laser pulses.

Walking out of the laser lab and looking up to the sky, the light from the star is like a messenger coming to us with a story waiting to be interpreted. The scientific potential of polarized high-energy X-ray signals has long been recognized by the astrophysics community [64]. It has been used to understand the magnetic configuration near the black holes [65],

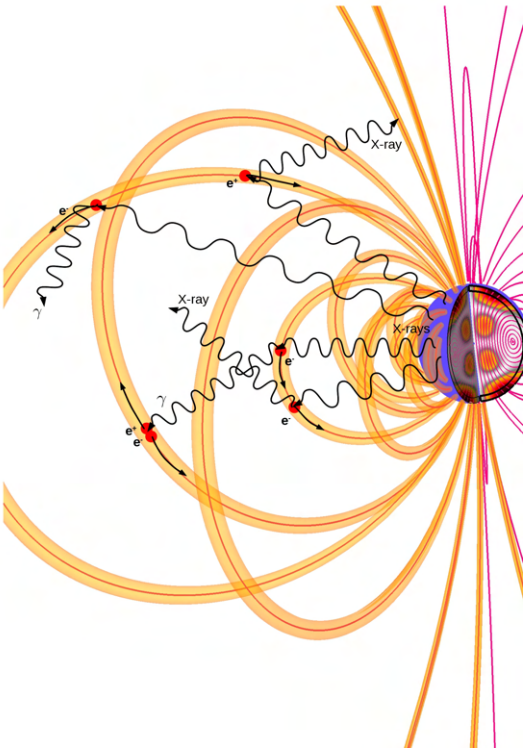

Figure 1.1: Schematic representation of the modulation of electromagnetic radiation in the magnetosphere of a neutron star. Electric currents (yellow), composed mainly of electrons and positrons, flow along the magnetic field lines (magenta). The X-ray emission from the star's surface (black) is scattered resonantly by these charge carriers. The resulting high-energy gamma rays can create further electron-positron pairs. Image Credit: Max-Planck-Gesellschaft, München, "Asteroseismology of magnetars", by Michael Gabler. [1]

crab nebulae [66], and to analyze the particle acceleration in blazars' jets [67]. Measuring the polarization of high-energy photons is much more challenging, but significant progress has been made recently [68, 69, 70]. The emission mechanism of this high-energy gamma-ray could be relevant to the SF QED process; polarization-resolved QED simulation tools could help explore the origin of the polarization signal in this new energy regime [71]. As a relevant example, Fig. 1.1 illustrates the possible strong-field process occurring at the magnetosphere of a neutron star, which can carry a field strength greater than 10^{14} Gauss.

The inclusion of spin and polarization effects is also important in the context of QED plasma. The studies have shown that the spin/polarization-distinguished QED code can more accurately simulate multi-staged processes, such as avalanche and shower-type electron-

positron pair production cascades [72, 73, 74]. The spin and polarization signal can also serve as an indicator of some extreme plasma processes like ultrarelativistic plasma current filamentation instabilities [75], as well as radiation reaction-dominated magnetic reconnection, which may be realized in extreme power laser facilities and intrinsically exist in extreme astrophysical reconnection scenarios [76].

1.1 Thesis Outline

This thesis is organized as follows:

Chapter 2: Introduction of the theoretical foundations necessary for this work. Topics covered include particle dynamics in strong fields, the theoretical framework for SFQED, key estimations employed in SFQED calculations, and the kinetic theory for spin-polarized relativistic plasmas.

Chapter 3: The detailed discussion of the implementation of spin- and polarization-resolved SFQED processes within a Monte Carlo algorithm, which is integrated into the OSIRIS particle-in-cell (PIC) code platform. The algorithm is rigorously verified under various conditions and thoroughly validated by reproducing notable benchmark results.

Chapter 4: The application of spin- and polarization-resolved SFQED simulations to future high-intensity laser-plasma interaction experiments. This includes the study of polarization-dependent pair production by colliding high-energy electron beams with two linearly polarized laser pulses, as well as the use of polarized light signals as diagnostics for detecting bright x-ray flashes via nonlinear Compton scattering — a hallmark of QED plasma formation.

Chapter 5: The investigation of spin and polarization phenomena in QED cascades, examining both avalanche and shower-type cascade setups. Simulation results reveal the robust generation of longitudinally polarized electron–positron pair plasmas, largely insensitive to initial conditions. Particle tracking is used to elucidate the underlying polarization mechanisms, and a simplified theoretical model is proposed to further interpret these findings.

Chapter 6: The exploration of quantum radiation effects in various laser-plasma interaction scenarios. The roles of radiation back-reaction and stochastic broadening as diagnostic tools for the strong-field conditions are discussed. Additionally, the potential impact of quantum radiation reaction effects on beam energy spread, emittance evolution, and spin polarization is examined in the context of future multi-stage TeV-class laser wakefield accelerator (LWFA) systems.

CHAPTER 2

Background Theory

2.1 Strong Field QED Parameters

Before diving into the detailed theory of strong field QED, one question that we might want to answer is, how strong does the field need to be for quantum effects to be important? The simple answer for this is that the quantum effects arise when electric fields are as strong as the QED critical field $|\boldsymbol{E}| \to E_{cr}$. This is the characteristic field strength that does $m_e c^2$ work over a (reduced) Compton wavelength, so that the virtual electron-positron pairs can be separated. However, due to the Lorentz transform, even a very weak field in a frame of reference moving at nearly speed of light can reach the critical field strength $\boldsymbol{E}'_\perp = \gamma(\boldsymbol{E}_\perp + \boldsymbol{v} \times \boldsymbol{B})$, $\boldsymbol{B}'_\perp = \gamma(\boldsymbol{B}_\perp - \frac{1}{c^2}\boldsymbol{v} \times \boldsymbol{E})$. Here, if γ is sufficiently large, the E and B fields can be arbitrarily and equally large, depending on γ. That is, when v is close to c, $\boldsymbol{E}'_\perp \approx \boldsymbol{B}'_\perp c$, $\boldsymbol{E}'_\perp \cdot \boldsymbol{B}_\perp \approx 0$. As a result, the process needs to be quantified by the Lorentz invariant quantities. For quantum effects inside the vacuum, this can be captured by two purely field-dependent Lorentz invariant parameters [77]:

$$\mathcal{F} = -\frac{F^{\mu\nu}F_{\mu\nu}}{2E_{cr}^2} = \frac{|\boldsymbol{E}|^2 - |\boldsymbol{B}|^2 c^2}{E_{cr}^2}, \quad \mathcal{G} = -\frac{F^{\mu\nu}\tilde{F}_{\mu\nu}}{2E_{cr}^2} = \frac{\boldsymbol{E}\cdot\boldsymbol{B}c}{E_{cr}^2}. \tag{2.1}$$

Here, $F_{\mu\nu}$ is the electromagnetic field tensor, and $\tilde{F}_{\mu\nu}$ is its dual. The Sauter-Schwinger pair production mechanism is significant only as $\mathcal{F} \to +1$ and $\mathcal{G} = 0$ [77], i.e., only fields that (in some frame) are purely electric. And when $\mathcal{F} \to -1$ and $\mathcal{G} = 0$, the fields are purely

magnetic, which are stable against the creation of vacuum pairs, but will, for example, induce birefringence effects [78].

The other dimension we think about for this problem is during an interaction, how many background (coherent) photons get involved inside the interaction. Quantum electrodynamics becomes non-linear when the background photon field is dense, so that electrons are more likely to interact with more than one photon. The nonlinearity of interaction can be captured by the Lorentz-invariant parameter [79]:

$$a_0 = \frac{e}{m_e c}\sqrt{||A^2||} = \frac{eE_0}{m_e c\omega_0} \tag{2.2}$$

This is the same a_0 presented in Eq. (1.1) in the Introduction section, but we provide its meaning in the context of relativistic laser-plasma interaction. However, we can also rewrite this expression as follows:

$$a_0 = \frac{eE_0}{m_e c\omega_0} = \frac{eE_0\lambda\!\!\!^{-}_c}{\hbar\omega_0}. \tag{2.3}$$

which compares the work done by the electromagnetic wave over a Compton length to the energy of a photon of that wave. As a result, a_0 can also serve as a measurement of the multiphoton, or nonlinear, nature of the electromagnetic interaction. If $a_0 \gg 1$, the interaction is unavoidably nonlinear in the number of participating photons.

Finally, we discuss the regime which is most relevant to this work, where quantum corrections to electron-light interactions are important. This can be captured by the Lorentz invariants that mix particle and field properties:

$$\chi_e = \frac{||F_{\mu\nu}p^\nu||}{mcE_{cr}} = \gamma\frac{\sqrt{(\boldsymbol{E}+\boldsymbol{v}\times\boldsymbol{B})^2 - (\boldsymbol{E}\cdot\boldsymbol{v}/c)^2}}{E_{cr}}, \tag{2.4}$$

$$\chi_\gamma = \frac{\hbar||F_{\mu\nu}k^\nu||}{mcE_{cr}} = \frac{\hbar\omega}{m_e c}\frac{\sqrt{(\boldsymbol{E}+(c^2\boldsymbol{k}/\omega)\times\boldsymbol{B})^2 - (\boldsymbol{E}\cdot(\boldsymbol{k}/\omega))^2}}{E_{cr}} \tag{2.5}$$

χ_e and χ_γ are called the quantum nonlinearity parameters [30]. For the electrons and positrons, χ_e compares the field strength observed in its instantaneous rest frame with E_{cr}, or the typical energy of the radiation spectrum with its energy $\gamma m_e c^2$. It therefore parametrizes the importance of quantum corrections to the particle dynamics and radiation emission [80]. For photons, because it does not have a rest frame, so a physical interpretation of χ_γ is obtained by considering the following argument [81]. For a photon with momentum $\hbar\boldsymbol{k}$, embedded in an electromagnetic field, to create an electron-positron pair there must be a transfer of energy from the field of $\Delta E_{energy} = m_e^2 c^4/\hbar\omega$. This energy transfer must take place over $\Delta t \approx m_e c/eE_{eff}$, the time taken for the electron and positron to gain a transverse momentum of $m_e c$ if the field has an effective magnitude $E_{\text{eff}} = \gamma|\boldsymbol{E}_\perp + (c^2\boldsymbol{k}/\omega)\times\boldsymbol{B}|$ (we have assumed that $\hbar\omega \gg m_e c^2$ and $\gamma \gg 1$). The uncertainty principle requires that $\Delta E_{energy}\Delta t \geq \hbar/2$ or, equivalently, that $\chi_\gamma > 1$. This condition then defines the regime where electron-positron pair creation becomes probable.

In conclusion, we discuss the Lorentz-invariant parameters that can describe the QED processes. $\mathcal{F}$ and $\mathcal{G}$ describe electromagnetic interactions with the quantum vacuum. $\mathcal{F}$ or $\mathcal{G}$ close to unity requires the laboratory field strength to be critical. a_0 describes the nonlinearity of QED/relativistic motion of electrons in a crossed field. χ_e (χ_γ) describes the importance of quantum corrections to interactions involving an electron or positron (photon).

2.2 Particle Dynamics in Strong Fields

2.2.1 Single Charged Particle Motion in a Laser Field

We begin with the fundamental process of the classical dynamics of a point particle with charge q, mass m and four momentum $p^\mu = \gamma m(c, \boldsymbol{v}) = mu^\mu$ inside an electromagnetic field described by the electromagnetic field tensor $F^{\mu\nu}$. $\gamma = (1 - |\boldsymbol{v}|^2/c^2)$ is the Lorentz factor, $|\boldsymbol{v}|$ is the three-velocity and u^μ is the four-velocity:

$$m\frac{du^\mu}{d\tau} = \frac{q}{c}F^{\mu\nu}u_\nu \tag{2.6}$$

Here, τ is the proper time. The electromagnetic field tensor $F_{\mu\nu}$ is defined as the anti-symmetrised derivative of the four-potential $A^\mu \equiv (\Phi, c\boldsymbol{A})$:

$$F_{\mu\nu} = \partial_\mu A_\nu - \partial_\nu A_\mu \tag{2.7}$$

Where $\partial_\mu = \frac{\partial}{\partial x^\mu}$. In Cartesian coordinates, its components are:

$$F^{\mu\nu} = \begin{bmatrix} 0 & -E_1 & -E_2 & -E_3 \\ E_1 & 0 & -B_3 & B_2 \\ E_2 & B_3 & 0 & -B_1 \\ E_3 & -B_2 & B_1 & 0 \end{bmatrix} \tag{2.8}$$

where E_i, B_i are components of the electric and magnetic fields, respectively. The dual tensor is given by:

$$\tilde{F}_{\mu\nu} = \frac{1}{2}\epsilon_{\mu\nu\alpha\beta}F^{\alpha\beta} \tag{2.9}$$

which $\epsilon_{\mu\nu\alpha\beta}$ is the antisymmetric Levi-Civita symbol.

Now we consider the case of a plane wave, which can be characterised by a four-potential

$$A^\mu = A_1^\mu \cos(\phi) + A_2^\mu \sin(\phi) \tag{2.10}$$

that is a function of laser phase $\phi = k \cdot x$, which is a Lorentz-invariant parameter. Here, k is the wave's four-wave vector $k^\mu = (\omega/c)(1, \hat{\boldsymbol{k}})$, ω its angular frequency and $\hat{\boldsymbol{k}}$ is directed along its axis of propagation. $A_{1,2}^\mu$ are constant four vectors that satisfy $A_1 \cdot A_2 = 0$; in the Lorenz gauge, the four-potential must be divergence-free, i.e., $\partial \cdot A = 0$, so

$$k \cdot A_1 = k \cdot A_2 = 0 \tag{2.11}$$

The components of the electromagnetic field arising from the potential Eq. 2.10 are then:

$$F^{\mu\nu} = (k^\mu A_2^\nu - k^\nu A_2^\mu)\cos\phi - (k^\mu A_1^\nu - k^\nu A_1^\mu)\sin\phi. \tag{2.12}$$

Using Eq. (2.11), and also the light-like nature of k^μ, i.e. $k \cdot k = 0$, we can see that the field is perpendicular to $\hat{\boldsymbol{k}}$. Contracting Eq. (2.6) with k^μ, we can show that $k \cdot u$ is a constant of motion:

$$\frac{d}{d\tau}(k \cdot u) = 0 \tag{2.13}$$

As the EM field is a function only of the laser phase ϕ, we can also rewrite the electron motion as a function of ϕ. Using the relationship between ϕ and τ:

$$\frac{d\phi}{d\tau} = k \cdot u = \text{constant} \neq 0 \tag{2.14}$$

We can then rewrite Eq. (2.6) as

$$m\frac{du^\mu}{d\phi} = \frac{q}{c}\frac{F^{\mu\nu}u_\nu}{k \cdot u} \tag{2.15}$$

By substituting $F_{\mu\nu}$ with Eq. (2.12), the equation of motion becomes

$$m\frac{du^\mu}{d\phi} = \frac{q}{c}\left[\left(A_1^\mu - \frac{A_1 \cdot u}{k \cdot u}k^\mu\right)\sin\phi - \left(A_2^\mu - \frac{A_2 \cdot u}{k \cdot u}k^\mu\right)\cos\phi\right] \tag{2.16}$$

And

$$\frac{dx^\mu}{d\phi} = \frac{u^\mu}{k \cdot u} \tag{2.17}$$

Taking only the components perpendicular to k^μ, we have

$$u^\mu_\perp = u^\mu_{0\perp} - \frac{q}{mc} A^\mu \tag{2.18}$$

Where u_0 is the electron four-velocity in the absence of the wave. Eq. (2.16) can then be integrated by recognizing that $A_{1,2} \cdot u = A_{1,2} \cdot u_\perp$ as A is always transverse. The result is

$$u^\mu = u^\mu_0 - \frac{q}{mc} A^\mu + \frac{q}{mc} \frac{A \cdot u_0}{k \cdot u_0} k^\mu - \frac{q^2}{2m^2c^2} \frac{A^2}{k \cdot u_0} k^\mu. \tag{2.19}$$

Here, we derive the exact analytical solutions for plane waves. However, as a plane wave does not exist in reality, it does not completely describe the electron motion caused by a real laser pulse. We can generalize these results to some extent by imposing a temporal envelope on the wave vector for the form:

$$A^\mu(\phi) = \varepsilon^\mu a(\phi) = \varepsilon^\mu (f_1(\phi) \sin\phi + f_2(\phi) \cos\phi) \tag{2.20}$$

where $f_{1,2}(\phi)$ is considered to be slowly varying relative to the laser cycle. In this adiabatic approximation, we can directly substitute $A^\mu(\phi)$ for A^μ in the Eq. 2.16 and integrated directly.

2.2.2 The Larmor Power

The power radiated by an accelerating charge is given by the Larmor formula. We will derive this result using a classical treatment originated by J.J. Thomson [82] and revived by Malcolm Longair. The result is the same as the derivation using the Liénard-Wiechert potentials [83].

We start by taking a stationary charge q at rest at $t = 0$. The field lines of the charge

point radially outward and are uniformly distributed in space. The charge then accelerates to a velocity $\Delta v \ll c$ over a short time interval Δt. The field line configuration after a time t is plotted in Fig. 2.1 (a). The information about that acceleration has propagated outward to a radial distance of $r = ct$.

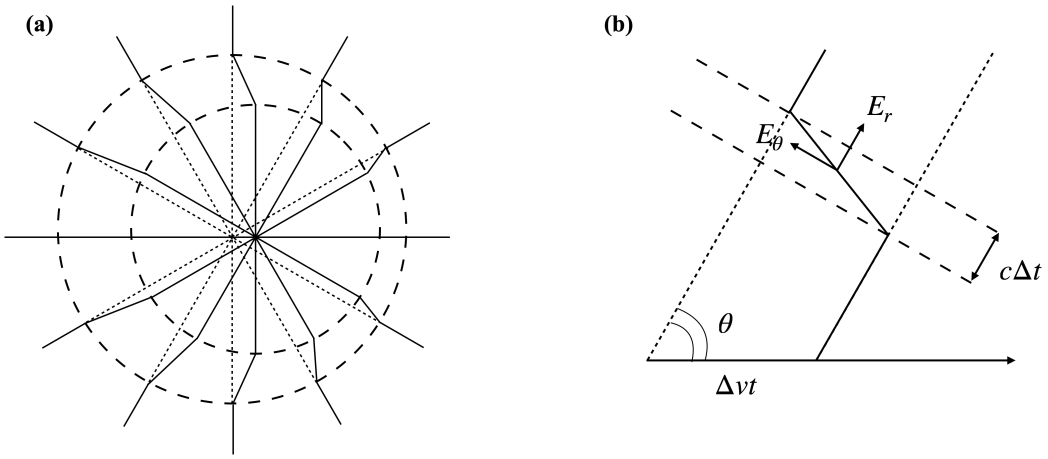

Figure 2.1: (a) The electric field lines at time t, for a charge that accelerates to velocity Δv in a interval Δt. (b) The tangential and radial components of the electric fields E_θ and E_r at a distance ct from the charge. (Adapted from [2])

Outside that sphere with radius $r = ct$, the electric field still points radially outward from the original position of the charge at $t = 0$. This is because the information about the acceleration has not yet moved farther out than distance r. Inside the sphere, the field lines are directed radially outward from the location of the charge after the acceleration and drift at a new velocity Δv. Because the electric field lines have to be connected, there is a small region of width $c\Delta t$ in which the electric field has a nonradial component. The observer in this region will see a temporal change in the tangential component of the E-field or a pulse of electromagnetic radiation. which is illustrated in Fig. 2.1 (b). From simple geometry, the ratio of the tangential and radial electric fields is given by:

$$\frac{E_\theta}{E_r} = \frac{t\Delta v \sin\theta}{c\Delta t} \tag{2.21}$$

Identifying $t = r/c$, $E_r = q/(4\pi\epsilon_0 r^2)$ and $\Delta v/\Delta t$ with the acceleration $|\boldsymbol{a}|$, we find that

$$E_\theta = \frac{q|\boldsymbol{a}|\sin\theta}{4\pi\epsilon_0 c^2 r} \tag{2.22}$$

During the pulse, the $\boldsymbol{E}$ field in the θ direction changes from 0 to E_θ and back to 0. By Ampere's law, there must be an azimuthal magnetic field $B_\phi = E_\theta/c$. The Poynting flux $\boldsymbol{S} = \boldsymbol{E} \times \boldsymbol{B}/\mu_0$ is therefore directed radially outwards with magnitude

$$S = \frac{q^2|\boldsymbol{a}|^2\sin^2\theta}{16\pi^2\epsilon_0 c^3 r^2} \tag{2.23}$$

By integrating S over the surface of the spherical shell, we obtain the radiated power:

$$P = \frac{q^2|\boldsymbol{a}|^2}{6\pi\epsilon_0 c^3} \tag{2.24}$$

This is the non-relativistic form of the Larmor formula [84]. The total radiated power is a Lorentz invariant, so Eq. 2.24 can be written in the covariant form as [83]:

$$P = -\frac{q^2}{6\pi\epsilon_0 c^3}\left(\frac{du}{d\tau}\cdot\frac{du}{d\tau}\right) \tag{2.25}$$

Expanding the scalar product, the radiated power in a reference frame where the charge moves with velocity $\boldsymbol{v}$ and acceleration $\boldsymbol{a}$ is

$$P = \frac{q^2\gamma^4}{6\pi\epsilon_0 c^3}\left[|\boldsymbol{a}|^2 + \left(\frac{\gamma\boldsymbol{a}\cdot\boldsymbol{v}}{c}\right)^2\right]. \tag{2.26}$$

The γ^4 factor indicates that for non-relativistic particles, radiative losses are negligible, but they become significant for accelerating charges as their velocity approaches the speed of light, $|\boldsymbol{v}| \to c$. In the particle's instantaneous rest frame, the radiation is dipolar and does not carry any net momentum. However, this will change in a general reference frame due to the effects of relativistic beaming. In such a frame, radiation is concentrated into a narrow cone with an opening angle of approximately $1/\gamma$, aligned with the charge's velocity vector. Since this radiation carries momentum, it results in a back-reaction on the particle. This

back-reaction is referred to as radiation reaction and will be further explored in the following section.

2.2.3 Classical Radiation Reaction

When the electron interacts with a high-intensity laser pulse, the back-reaction of the emission of radiation on the electron motion, the so-called radiation reaction (RR), can become significant. The radiation power is given by the Larmor formula Eq. (2.25), which for an electron in a plane EM waves can be written as:

$$P = -\frac{e^4}{6\pi\epsilon_0 m_e^2 c^5} \left(k \cdot u\right)^2 \left(A_1^2 \cos\phi^2 + A_2^2 \sin\phi^2\right) \tag{2.27}$$

For a circularly polarized wave, $A_1^2 = A_2^2 = -A_0^2$. The vector potential can be written in terms of the Lorentz-invariant dimensionless vector potential a_0, the power radiated by a counter-propagating, ultra-relativistic electron with $\gamma \gg 1$ is then:

$$P = \frac{e^2(2\gamma a_0 \omega)^2}{6\pi\epsilon_0 c} \tag{2.28}$$

Although this expression is a classical result, it can be recast to make the relationship with the quantum-mechanical result explicit,

$$P = \frac{2}{3}\frac{e^2}{4\pi\epsilon hc}\frac{(m_e c^2)^2}{h}\left(\frac{2\gamma a_0 h\omega}{mc^2}\right)^2 = \frac{2\alpha_f}{3}\frac{m_e c^2}{\tau_c}\chi_e^2\,, \tag{2.29}$$

where $\alpha_f \approx 1/137$ is the fine-structure constant, $\tau_c = h/(m_e c^2) = 1.288 \times 10^{-21}$ is the Compton time; it will suffice for now to comment that the classical radiated power scales with a_0^2 and the square of the electron energy.

When the radiation energy becomes comparable to the electron's initial energy $\gamma m_e c^2$,

the equations of motion take into account the radiation force F_R^μ

$$m\frac{du^\mu}{d\tau} = \frac{q}{c}F^{\mu\nu}u_\nu + F_R^\mu \tag{2.30}$$

where u^μ denotes the four-velocity and F_R^μ represents the radiation reaction (RR) term. Since the pioneering studies by Lorenz and Abraham over a century ago [85, 86, 87, 88], numerous formulations of the RR force F_R^μ have been proposed. One famous form proposed by Dirac, referred to as the Lorentz-Abraham-Dirac (LAD) equation [86], is given by:

$$m\frac{du^\mu}{d\tau} = \frac{q}{c}F^{\mu\nu}u_\nu + F_{R,LAD}^\mu \tag{2.31}$$

$$F_{R,LAD}^\mu = \frac{q^2}{6\pi\epsilon_0 m^3}\left[\frac{d^2p^\mu}{d\tau^2} + \frac{p^\mu}{(mc)^2}\left(\frac{dp}{d\tau}\cdot\frac{dp}{d\tau}\right)\right] \tag{2.32}$$

However, this LAD model is not completely self-consistent. The main problem arises from the second-order derivative of the momentum term, which allows for a self-accelerating solution. This pathological behavior can be resolved by reducing the order of the equation, as has been proposed by Landau and Lifshitz [89, 90]. This so-called Landau-Lifshitz force is frequently employed in numerical simulations of high-intensity laser-matter interactions [91, 92, 93]). It reads

$$F_{R,LL}^\mu = \frac{q^3}{6\pi\epsilon_0 m^3 c^4}\left[(\partial_\sigma F^{\mu\nu})p_\nu p^\sigma + \frac{q}{c}F^{\mu\nu}F_{\nu\sigma}p^\sigma + \frac{q}{m_e^2c^3}(F^{\mu\nu}p_\sigma)^2 p^\mu\right] \tag{2.33}$$

We note that the classical radiation reaction is a continuous process, in contrast to quantum RR, which is stochastic. Quantum radiation effects are important whenever the emission of a single photon can already alter the electron trajectory significantly due to the momentum recoil. The transition from the classical to the quantum RR regime is characterized by $\chi_e \geq 1$.

2.2.4 Inclusion of Spin and Polarization

To initiate the discussion on spin and polarization in the charged particle dynamics, it is essential to first elaborate on how both quantities are represented in our calculation. The evolution of a quantum spin state for spin 1/2 particles is characterized by precession, a continuous process in time. Under these conditions, a classical spin model, which treats the spin using a three-component unit vector in space, will be sufficient. However, if the spin state changes discontinuously from an 'up' to a 'down' state, as it can when emitting a photon, then quantum mechanics must necessarily be employed. Fortunately, under most circumstances for laser plasma interaction, the formation length (which will be discussed in detail in following chapter 2.5.1) of the quantum process is much shorter than the characteristic length of the field (such as the laser wavelength). We can treat this spin flip change as an instantaneous event. The spin dynamics between two quantum processes follows the classical spin precession.

Now, we examine the spin dynamics for an ensemble of particles. We define the average spin state of an ensemble of particles as polarization [94]. Here, we consider a situation in which we have two groups of particles with identical momentum and spatial distributions. One set of particles has classical spins that are all vertically aligned, with 75% up and 25% down. For the second set of particles, their classical spin vectors are uniformly distributed in an upright cone with an opening angle of 60°. From a quantum dynamics point of view, the degree of polarization is 50% in both cases:

$$P_a = \frac{0.75 - 0.25}{0.75 + 0.25} = 0.5, \quad P_b = \cos 60^\circ = 0.5. \tag{2.34}$$

As a result, we need to treat these two groups of particles as equivalent.

This simple example also illustrates the point that the direction of the polarization vector for an ensemble of particles is not the same as the direction of the spin vector for each individual particle. This is because the polarization vector collectively belongs to an ensemble

of particles and is not associated with a specific point in phase space. The direction of the polarization cannot, in general, coincide with the spin direction of every individual particle. In the following section, we will provide a more rigorous definition of these two quantities in detail.

2.2.5 Justification of Semiclassical Spin Model

As the particle spin is an intrinsic quantity which can only be defined in quantum mechanics, for a rigorous definition of the classical spin model, we need to first look at its quantum mechanical description and link to the classical model using a semi-classical approach. To begin, we will first introduce Ehrenfest's theorem [95]. The generalized form of Ehrenfest's theorem states that

$$\frac{d\langle \hat{A} \rangle}{dt} = \left\langle \frac{\partial \hat{A}}{\partial t} \right\rangle + \frac{1}{i\hbar}\langle [\hat{A}, \hat{H}] \rangle. \tag{2.35}$$

Here $\hat{H}$ is the Hamiltonian operator. This theorem gives the equation of motion for the expectation value of a quantum operator $\hat{A}$, for a system in a state $|\psi\rangle$. In the case of the spin operator $\hat{\boldsymbol{s}}$, we have the magnetic dipole Hamiltonian:

$$\hat{H} = -\hat{\boldsymbol{\mu}} \cdot \hat{\boldsymbol{B}} = \hat{\boldsymbol{\Omega}} \cdot \hat{\boldsymbol{s}} \tag{2.36}$$

Here, $\hat{\boldsymbol{\mu}} = g_e \mu_B \hat{\boldsymbol{s}}$, which g_e is the electron g-factor, μ_B is the Bohr magneton, $\hat{\boldsymbol{s}}$ is the spin operator. $\hat{\boldsymbol{B}}$ is the magnetic field (in principle, also an operator), $\hat{\boldsymbol{\Omega}}$ is the spin precession vector operator. Using the spin operator commutation relations $[\hat{\boldsymbol{s}}_j, \hat{\boldsymbol{s}}_k] = i\hbar\varepsilon_{jkl}\hat{\boldsymbol{s}}_l$, the commutator between the Hamiltonian and the spin operator is:

$$[\hat{\boldsymbol{s}}, \hat{H}] = [\hat{\boldsymbol{s}}, \hat{\boldsymbol{\Omega}} \cdot \hat{\boldsymbol{s}}] = i\hbar\hat{\boldsymbol{\Omega}} \times \hat{\boldsymbol{s}} \tag{2.37}$$

We substitute $\hat{A}$ in Eq. 2.35 with spin operator $\hat{\boldsymbol{s}}$, and also since there is no $\partial\hat{\boldsymbol{s}}/\partial t$ term, we have:

$$\frac{d\langle\hat{\boldsymbol{s}}\rangle}{dt} = \langle\hat{\boldsymbol{\Omega}} \times \hat{\boldsymbol{s}}\rangle. \tag{2.38}$$

In general, the spin precession operator $\hat{\boldsymbol{\Omega}}$ depends on the orbital dynamical operators $\hat{\boldsymbol{x}}$ and $\hat{\boldsymbol{p}}$, then the equation of motion Eq. 2.38 reads:

$$\frac{d\langle\hat{\boldsymbol{s}}\rangle}{dt} = \langle\hat{\boldsymbol{\Omega}}(\hat{\boldsymbol{x}}, \hat{\boldsymbol{p}}) \times \hat{\boldsymbol{s}}\rangle. \tag{2.39}$$

As the spin precession operator $\hat{\boldsymbol{\Omega}}$ does not depend on $\hat{\boldsymbol{s}}$, we can write

$$\frac{d\langle\hat{\boldsymbol{s}}\rangle}{dt} = \langle\hat{\boldsymbol{\Omega}}\rangle \times \langle\hat{\boldsymbol{s}}\rangle. \tag{2.40}$$

where on the right-hand side we can calculate the expectation value over orbital and spin states separately. In general, the expectation value for the $\hat{\boldsymbol{\Omega}}$ is not easy to calculate. We have to apply the semi-classical approximation to this equation:

$$\langle\hat{\boldsymbol{\Omega}}(\hat{\boldsymbol{x}}, \hat{\boldsymbol{p}})\rangle \approx \hat{\boldsymbol{\Omega}}(\langle\hat{\boldsymbol{x}}\rangle, \langle\hat{\boldsymbol{p}}\rangle) \tag{2.41}$$

Here, $\langle\hat{\boldsymbol{x}}\rangle$ and $\langle\hat{\boldsymbol{p}}\rangle$ are the expectation values of the position and momentum operators, which are just the classical orbital trajectory. We can substitute these expectation values with the classical variables,

$$\boldsymbol{x} \equiv \langle\hat{\boldsymbol{x}}\rangle, \quad \boldsymbol{p} \equiv \langle\hat{\boldsymbol{p}}\rangle, \quad \boldsymbol{s} \equiv \langle\hat{\boldsymbol{s}}\rangle. \tag{2.42}$$

The equation of motion Eq. 2.38 under the semiclassical approximation now becomes:

$$\frac{d\boldsymbol{s}}{dt} \approx \boldsymbol{\Omega}_{sc} \times \boldsymbol{s}. \tag{2.43}$$

Here, $\boldsymbol{\Omega}_{sc} \equiv \boldsymbol{\Omega}(\boldsymbol{x}, \boldsymbol{p})$. Now we have demonstrated that under the semiclassical approximation, the evolution of the spin motion of a quantum system can be described instead by

the precession of a classical spin vector $\boldsymbol{s}$, under the action of a semiclassical spin precession vector $\boldsymbol{\Omega}_{sc}$. The important question is then when this semiclassical description of the orbital trajectory is valid. We define the spread in the coordinates and momenta $\sigma_x^2 = \langle \hat{x}^2 \rangle - \langle \hat{x} \rangle^2$ and $\sigma_p^2 = \langle \hat{p}^2 \rangle - \langle \hat{p} \rangle^2$. The semiclassical description requires the quantum uncertainty in the orbital trajectory to be small, that is, $\sigma_x \ll |\langle \hat{x} \rangle|$, and also $\sigma_p \ll |\langle \hat{p} \rangle|$. These conditions are given in the laser-plasma interactions, as the displacement and momenta are far larger than the quantum uncertainty.

Notice that this classical spin model cannot capture the abrupt spin-flip transition along the spin quantization axis during the quantum radiation process. Usually, in the laser-plasma interaction, we consider this spin-flip process as an instantaneous change. We can represent this change by a collisional operator, as will be demonstrated in the following chapter 2.8. The spin dynamics between two quantum processes still follows the classical spin precession.

2.2.6 Classical Spin Motion

The derivation of classical spin precession can be found in various textbooks on classical electromagnetism. Here, we just present the covariant form of the classical spin-precession equation. The metric we use here is $g_{\mu\nu} = \mathrm{diag}(1, -1, -1, -1)$. The spin four-vector $S = (S^0, \boldsymbol{S})$ in the lab frame reduces to $(0, \boldsymbol{s})$ in the instantaneous rest frame. As a result, the time component of the spin four-vector in the lab frame is related to the space components via $u \cdot S = cS^0 - \boldsymbol{v} \cdot \boldsymbol{S}$, or $S^0 = \boldsymbol{\beta} \cdot S$, where $u = \gamma(c, \boldsymbol{v})$ is the velocity four-vector. The covariant form of the classical spin precession equation, usually named the Thomas-Bargmann-Michel-Telegdi(T-BMT) equation, is written as:

$$\frac{dS}{d\tau} = \frac{e}{m_e c} \left[\frac{g}{2} F \cdot S + \left(\frac{g}{2} - 1 \right) (S \cdot F \cdot U) U \right]. \tag{2.44}$$

The relativistic spin precession equation for $\boldsymbol{s}$, written in the three-vector form is:

$$\frac{d\boldsymbol{s}}{dt} = -\frac{e}{m_e c}\left[\left(a+\frac{1}{\gamma}\right)\boldsymbol{B} - \frac{a\gamma}{\gamma+1}\boldsymbol{\beta}\cdot\boldsymbol{B}\boldsymbol{\beta} - \left(a+\frac{1}{\gamma+1}\right)\boldsymbol{\beta}\times\boldsymbol{E}\right]\times\boldsymbol{s} = \boldsymbol{\Omega}\times\boldsymbol{s} \tag{2.45}$$

Notice that the spin vector here is in the rest frame, whereas the spin precession axis $\boldsymbol{\Omega}$ is represented by the EM field in the lab frame, with

$$\boldsymbol{\Omega} = -\frac{e}{m_e c}\left[\left(a+\frac{1}{\gamma}\right)\boldsymbol{B} - \frac{a\gamma}{\gamma+1}(\boldsymbol{\beta}\cdot\boldsymbol{B})\boldsymbol{\beta} - \left(a+\frac{1}{\gamma+1}\right)\boldsymbol{\beta}\times\boldsymbol{E}\right] \tag{2.46}$$

2.2.7 Polarization and Spin

As mentioned previously, the polarization vector is defined as the statistical average of the classical spin vector for an ensemble of particles.

$$\boldsymbol{P} = \langle\boldsymbol{s}\rangle \tag{2.47}$$

We can also define polarization for a single particle by taking a time-averaged measurement. The polarization can be written as follows.

$$\boldsymbol{P} = \bar{\boldsymbol{s}} \tag{2.48}$$

If the ergodic hypothesis is applicable, then the two definitions yield the same answer. If the classical spin vectors are normalized to unity, the length of the polarization vector can be smaller than 1: $|\boldsymbol{P}| \leq 1$.

To prove that this definition of the polarization state indeed physically makes sense, we should revisit quantum mechanics. One important thing to note is that the classical spin vector is actually also an averaged value, as all three components cannot be specified simultaneously in a single measurement of a quantum spin. However, we usually consider the average of several measurements of the spin operator as a polarization, not a single spin

measurement. To clarify these definitions, we need to examine pure states and statistical mixtures. We introduce the density matrix ρ, which describes the information about a quantum statistical ensemble. It can be written as:

$$\rho = \sum_i w_i |\psi_i\rangle\langle\psi_i| \tag{2.49}$$

Here, $|\psi_i\rangle$ are a complete orthonormal set of states. The weights w_i are non-negative real numbers that sum to unity. By convention, the trace of the density matrix is normalized to unity, and the weights take the value between 0 and 1, $0 \leq w_i \leq 1$. A pure state is defined as a statistical system that can be specified by a single wavefunction. The density matrix of a pure state has the form:

$$\rho = |\psi\rangle\langle\psi|, \tag{2.50}$$

in which there is only one state in the system, and the weight for this state is unity. The expectation of any operator $\hat{A}$ is given by taking the trace of the product of $\hat{A}$ with the density matrix:

$$\langle A\rangle = \mathrm{Tr}[\rho\hat{A}] = \sum_i w_i \langle\psi_i|\hat{A}|\psi_i\rangle \tag{2.51}$$

As a result, for the spin operator, the average is given by

$$\langle \boldsymbol{s}\rangle = \mathrm{Tr}[\rho\hat{\boldsymbol{s}}] = \sum_i w_i \langle\psi_i|\hat{\boldsymbol{s}}|\psi_i\rangle = \sum_i w_i \boldsymbol{s}_i \tag{2.52}$$

The polarization vector $\boldsymbol{P}$ is therefore a weighted sum of classical spin vectors:

$$\boldsymbol{P} = \langle \boldsymbol{s}\rangle = \sum_i w_i \boldsymbol{s}_i \tag{2.53}$$

We can also find that the classical spin vector $\boldsymbol{s}$ is, by construction, the expectation of the spin operator for a system in a pure state.

We have demonstrated the definition of polarization and spin from the density matrix. Notice that for spin 1/2 particles, there is an important relationship between the density

matrix ρ and polarization vector $\boldsymbol{P}$:

$$\rho = \frac{1}{2}(1 + \boldsymbol{P} \cdot \boldsymbol{\sigma}) \ , \tag{2.54}$$

where $\boldsymbol{\sigma}$ is the set of Pauli matrices. It is important to note that the dynamics of polarization vectors do not follow the same form as the classical spin precession, as

$$\frac{d\boldsymbol{P}}{dt} = \sum_i w_i \boldsymbol{\Omega_i} \times \boldsymbol{s}_i \ \stackrel{?}{=} \ \boldsymbol{\Omega} \times \sum_i w_i \boldsymbol{s}_i = \boldsymbol{\Omega} \times \boldsymbol{P} \tag{2.55}$$

The left and right parts of the equations are not always equal. There are two main reasons: 1. The spin precession vector $\boldsymbol{\Omega}$ is not always the same for all particles: there is a distinction between $\boldsymbol{\Omega}$ and $\boldsymbol{\Omega}_i$; 2. the weights w_i need not be constant: $dw_i/dt \neq 0$. One important consequence is that, unlike the classical spin vectors that maintain a constant length, there is no guarantee that the magnitude of the polarization vector can be preserved with time.

2.2.8 Polarization for Photon

As the photon is a massless spin-1 particle, it may only have *helicities* +1 and -1 rather than the three spin states of a massive particle [96]. We may therefore use two complex orthogonal vectors to describe the polarization state of the photon.

$$\hat{\boldsymbol{\psi}} = \sum_i a_i \boldsymbol{\psi_i} = a_1 \hat{\boldsymbol{\psi}}_1 + a_2 \hat{\boldsymbol{\psi}}_2 \tag{2.56}$$

Here, $\boldsymbol{\psi}_1$ and $\boldsymbol{\psi}_2$ can represent either the two helicity states or any two orthonormal states of polarization obeying $\boldsymbol{\psi}_i \cdot \boldsymbol{k} = 0$ and $\boldsymbol{\psi}_i \cdot \boldsymbol{\psi}_j^* = \delta_{ij}$. The parameter a_i is generally complex. $|a_1^2|$ and $|a_2^2|$ give the probabilities of detection of a photon in the ψ_1 and ψ_2 states. For a photon in a pure state, we have $|a_1|^2 + |a_2|^2 = 1$.

We select the components of our basis to be $\hat{\boldsymbol{\psi}}_1 = [\boldsymbol{E} - \hat{\boldsymbol{k}} \cdot (\hat{\boldsymbol{k}} \cdot \boldsymbol{E}) + (\hat{\boldsymbol{k}} \times \boldsymbol{B})]/|\boldsymbol{E} - \hat{\boldsymbol{k}} \cdot (\hat{\boldsymbol{k}} \cdot \boldsymbol{E}) + (\hat{\boldsymbol{k}} \times \boldsymbol{B})|$, and $\hat{\boldsymbol{\psi}}_2 = [\boldsymbol{B} - \hat{\boldsymbol{n}} \cdot (\hat{\boldsymbol{n}} \cdot \boldsymbol{B}) - (\hat{\boldsymbol{n}} \times \boldsymbol{E})]/|\boldsymbol{B} - \hat{\boldsymbol{n}} \cdot (\hat{\boldsymbol{k}} \cdot \boldsymbol{B}) + (\hat{\boldsymbol{k}} \times \boldsymbol{E})|$. Here, $\hat{\boldsymbol{k}}$ represents

the direction of propagation of the photon, and $\boldsymbol{E}$ and $\boldsymbol{B}$ are the electric and magnetic fields experienced by the photon. It is convenient to describe the photon polarization using the Stokes vector $\boldsymbol{\xi} = (\xi_1, \xi_2, \xi_3)$. Note that these Stokes parameters vary with the choice of basis. For linear polarization ξ_3 that measured with respect to basis $\boldsymbol{\psi}_1$ and $\boldsymbol{\psi}_2$. The degree of polarization is given by the difference of the intensity measurements in the $\boldsymbol{\psi}_1$ and $\boldsymbol{\psi}_2$ directions:

$$\xi_3 = |a_1|^2 - |a_2|^2 \tag{2.57}$$

.

The diagonal polarization ξ_1 is measured with respect to the basis $\hat{\boldsymbol{\psi}}_1' = \frac{1}{\sqrt{2}}(\hat{\boldsymbol{\psi}}_1 - \hat{\boldsymbol{\psi}}_2)$ and $\hat{\boldsymbol{\psi}}_2' = \frac{1}{\sqrt{2}}(\hat{\boldsymbol{\psi}}_1 + \hat{\boldsymbol{\psi}}_2)$. Because we are measuring the same beam:

$$\hat{\boldsymbol{\psi}} = a_1\hat{\boldsymbol{\psi}}_1 + a_2\hat{\boldsymbol{\psi}}_2 = a_1'\hat{\boldsymbol{\psi}}_1' + a_2'\hat{\boldsymbol{\psi}}_2' \tag{2.58}$$

Thus, $a_1' = \frac{1}{\sqrt{2}}(a_1 + a_2)$, $a_2' = \frac{1}{\sqrt{2}}(a_2 - a_1)$. The degree of diagnostic polarization is then:

$$\xi_1 = |a_1'^2| - |a_2'^2| = a_1 a_2^* + a_2 a_1^* \tag{2.59}$$

.

Finally, the circular polarization ξ_2 is measured based on $\hat{\boldsymbol{\psi}}_L = \frac{1}{\sqrt{2}}(\hat{\boldsymbol{\psi}}_1 + i\hat{\boldsymbol{\psi}}_2)$ and $\hat{\boldsymbol{\psi}}_R = \frac{1}{\sqrt{2}}(\hat{\boldsymbol{\psi}}_1 - i\hat{\boldsymbol{\psi}}_2)$, which correspond to the left and right circular polarized states. The parameter $a_L = \frac{1}{\sqrt{2}}(a_1 - ia_2)$, $a_R = \frac{1}{\sqrt{2}}(a_2 - ia_1)$. The degree of polarization is then:

$$\xi_2 = |a_L'^2| - |a_R'^2| = i(a_1 a_2^* - a_1^* a_2) \tag{2.60}$$

.

2.3 Volkov State and Furry Picture

Now we start to look at the theory for describing the SFQED process. In high-intensity electromagnetic fields, the background photon density becomes very large. The electron is likely to interact with a huge number of background photons. As a result, the interaction has to be treated in all orders. This can be achieved by going to the Furry interaction picture [97] in which the background field is treated as part of the unperturbed system [98]. In this framework, the photon field A^μ is divided into a large, classical part $A^\mu_{classical}$ and a smaller, fluctuating part A^μ_{QED} [99]:

$$A^\mu = A^\mu_{classical} + A^\mu_{QED} \tag{2.61}$$

The equations of motion that arise from the QED Lagrangian [100] may be trivially reorganized as [101]

$$L = \bar{\psi}(i\not{D} - e\not{A}_{QED} - m)\psi - \frac{1}{4}F_{\mu\nu}F^{\mu\nu} \tag{2.62}$$

where ψ is the Dirac (electron) field, $\bar{\psi}$ its adjoint, 'slashed' quantities are shorthand for $\not{Q} = \gamma \cdot Q$ where γ^μ are the four Dirac matrices and $D^\mu = \partial^\mu + ieA^\mu_{classical}$. This Lagrangian describes the electron's exact interaction with the classical background EM field and its interactions with the quantised radiation field A^μ_{QED}; the former is handled by solving the Dirac equation for the dressed electron basis states; the latter with perturbation theory. The Dirac equation for the laser dressed states in the absence of the interaction term, can be written as:

$$(i\not{\partial} - e\not{A}_{classical} - m)\psi_{ps} = 0 \tag{2.63}$$

Here, $A^\mu_{classical}$ is the four-potential of an unquantized classical EM field. The solutions Eq. (2.63) in a plane wave $A^\mu = A^\mu(\phi)$ (dropping the $_{classical}$ subscript for clarity are called

Volkov wave functions [30]:

$$\psi_{ps} = \left(1 + \frac{e\not{k}\not{A}}{2k \cdot p}\right) u_s(p) \exp\left[-ip \cdot x - i \int_0^{\phi} \left(\frac{eA \cdot p}{k \cdot p} - \frac{e^2 A^2}{2k \cdot p}\right) d\phi\right] \tag{2.64}$$

where p is the electron four-momentum and $u_s(p)$ are the Dirac bispinors that satisfies $(\not{p} - m)u_s(p) = 0$

2.4 Nonlinear Compton Scattering and Nonlinear Breit-Wheeler Process

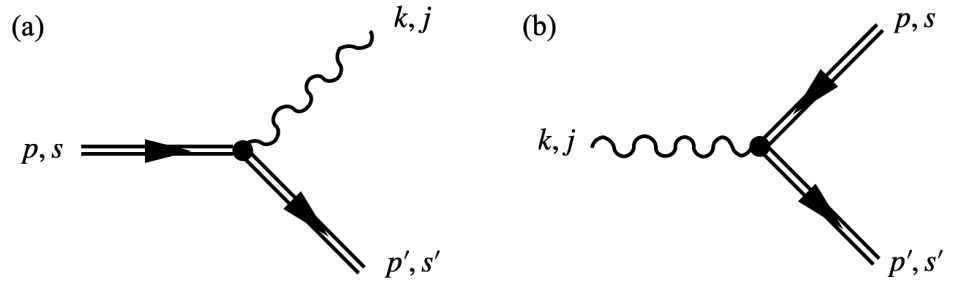

Figure 2.2: (a) Emission of a photon by a dressed lepton. (b) Production of an electron and positron pair by a gamma ray photon.

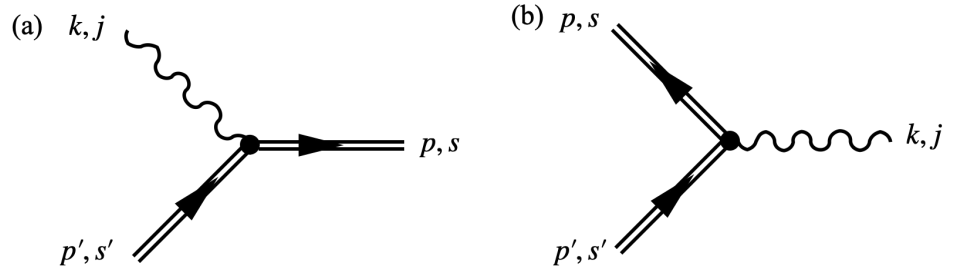

Figure 2.3: (a) photon absorption by a dressed lepton (b) One-photon electron-positron pair annihilation. p and p' are the electron momenta. s and s' are spin states and j is the polarization state.

This thesis mainly focuses on the two lowest-order processes at tree level in strong field QED: Nonlinear Compton scattering (NLCS)[102, 103, 104, 105], and Nonlinear Breit-Wheeler process (NBW)[104, 106, 107]. Fig. 2.2(a) illustrates the NLC process, in which a dressed lepton emits a photon. Fig. 2.2(b) shows the NBW process, in which a photon decays into a dressed electron-positron pair. Here, a dressed lepton means its particle state is in a background electromagnetic field. Compared with high-order quantum processes, the probabilities of these lowest-order processes are dominated by a factor of order $\alpha = 1/137$. In most cases, we can ignore the influence of higher-order processes. Two additional first-order processes in the fine-structure constant are photon absorption by an electron and electron-positron pair annihilation into a single photon. These processes are depicted in Fig.2.3, and correspond to the time-reversed versions of Nonlinear Compton scattering and Breit-Wheeler pair creation shown in Fig.2.2. However, their probabilities are extremely low because the final state comprises only a single particle, whose four-momentum is fixed. As a result, the available final-state phase space collapses to a single point, leading to a strong suppression of their cross-sections. Voroshilo et al. [108] have shown that for single-photon annihilation to occur, the electron and positron must be ultrarelativistic and aligned within 0.01 mrad. A similar argument holds for photon absorption, justifying the omission of both processes from consideration.

To calculate the S matrix elements and the probability of high-intensity QED processes, one may employ the Feynman diagram technique in coordinate space. Here we list the Feynman rules for high-intensity QED in the Furry picture, summarized by [109]:

- External incoming or outgoing electrons with momentum p are represented by the dressed Volkov wave function $\psi_p(x)$ or $\bar{\psi}_p(x)$, respectively. For incoming and outgoing positrons one uses the corresponding negative energy Volkov wave function $\bar{\psi}_p(-x)$ or $\psi_p(-x)$.

- Internal and external photon lines are translated into the free photon propagator and the free photon wave functions, respectively, see e.g., Ref [100].

- Each interaction vertex corresponds to a factor $-ie\gamma^{\mu}$and an integral over d^4x.

- Symmetry factors for identical particles, etc., are the same as in usual QED.

In what follows we discuss the Nonlinear Compton scattering process, but since the analytical structure of the matrix element for the Nonlinear Breit-Wheeler process is similar, these results can be translated to the NBW too. The S matrix for NLCS, i.e., the emission of a high-energy photon by an electron moving in an intense laser field, is given in Fig. 2.2 (a). This diagram translates into the formula:

$$S_{NLCS} = \int d^4x \bar{\psi}_{p's'}(x)[-ie\gamma^{\mu}\varepsilon'^{*}_{\mu}e^{ik'\cdot x}]\psi_{ps}(x) \tag{2.65}$$

Here p and k are momenta of the initial electron and photon, respectively, s are the initial spin state of the electron, and primed momenta refer to the same particle but in the final state. The wave function of the emitted photon with momentum k' and polarization vector ε' is given by $\varepsilon'^{*}_{\mu}e^{ik'\cdot x}$. Having integrated Eq. 2.65 over light-front variables $x^{\perp}$ and x^{-} (which defined as: $x^{\perp} = (x^1, x^2)$, $x^{\pm} = x_0 \pm x^3$), we obtain [72]:

$$S_{NLCS} = -ie(2\pi)^4 \int \frac{ds}{2\pi}\delta^{(4)}(p' + k' - p - nk)M_{NLC}(s) \tag{2.66}$$

The variable n enters from the four-momentum conservation $p + nk = p' + k'$ and can be defined as the amount of four-momentum absorbed from the background field ($n = pk'/p'k$). Note that this is sometimes referred to as the total number of background-field photons absorbed. The amplitude M_{NLCS} contains an integral over the laser phase $\phi = \omega x^{+}$:

$$M_{NLCS}(n) = \varepsilon'^{*}_{\mu}\int d\phi u_{s'}(p')J^{\mu}u_s(p)(\phi)e^{i\int_0^{\phi}d\phi'\frac{k'\cdot\pi(\phi')}{k\cdot p'}} \tag{2.67}$$

With the Dirac current

$$J^{\mu}(\phi) = \gamma^{\mu} + \frac{\not{A}\not{k}\gamma^{\mu}}{2k\cdot p'} + \frac{\gamma^{\mu}\not{k}\not{A}}{2k\cdot p} + \frac{\not{A}\not{k}\gamma^{\mu}\not{k}\not{A}}{4(k\cdot p)(k\cdot p')} \tag{2.68}$$

and with the classical kinematic four-momentum of the electron

$$\pi^{\mu}(\phi) = p^{\mu} - A^{\mu}(\phi) + k^{\mu}\frac{A \cdot p}{k \cdot p} - k^{\mu}\frac{A \cdot A}{2k \cdot p} \tag{2.69}$$

The differential probability of the Compton process is

$$dP_{NLCS} = \frac{\alpha\omega' |M_{NLCS}(n(\omega')|^2)}{16\pi^2 (p \cdot k)(p' \cdot k)} d\omega' d\Omega \tag{2.70}$$

where $d\Omega$ is the solid angle element related to the energy of the emitted photon ω'.

2.5 Important Approximations in SFQED

2.5.1 Formation Length

The radiation formation length denotes the spacetime region over which the probability amplitudes for processes in strong fields are established [30]. This parameter plays a critical role in the calculation and analysis of processes such as Compton scattering and Breit-Wheeler pair production. Interactions occurring within the formation length can suppress or enhance the total emission intensity and modify the spectral shape. Several approaches exist for defining the formation length within classical theory [110, 111]. One common method is to consider it as the distance L_f over which an electron, traveling at velocity β, and its emitted photon become separated by one photon wavelength λ. In the ultrarelativistic limit ($\gamma \gg 1$), this leads to

$$L_f = \frac{2\gamma^2 c}{\omega} \tag{2.71}$$

Blackburn, Seipt et al. [112] adopted a more general, geometric perspective on the formation length (see Fig. 2.4). In their approach, the photon formation length L_f is expressed in terms of the emission angle θ_γ and the instantaneous radius of curvature r_c of the electron's trajectory, according to $L_f = 2r_c\theta_\gamma$. For the special case of a constant, homogeneous field,

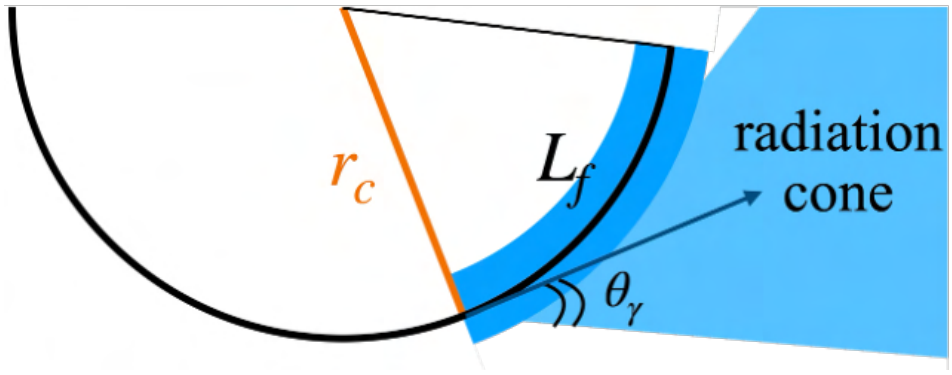

Figure 2.4: Geometric definition of formation length L_f, which is related to the instantaneous radius of curvature of the electron trajectory r_c and the radiation angle θ_γ

the radius of curvature can be written as:

$$r_c = \frac{\lambda(\gamma^2 - 1)}{\sqrt{\chi_e^2 - (\boldsymbol{E} + \boldsymbol{v} \times \boldsymbol{B})^2 / E_{cr}^2}} \tag{2.72}$$

In the ultrarelativistic regime ($\gamma \gg 1$), the radius of curvature is given by $r_c = \lambda\gamma^2/\chi$ ($\lambda = \lambda/2\pi$). For a head-on collision between an electron and a plane electromagnetic wave, the quantum parameter is $\chi = 2a_0\gamma(\hbar\omega/mc^2)$. By taking the characteristic emission angle $\theta = 1/\gamma$, one recovers the well-known result for the formation length: $L_f = c/(a_0\omega_0)$ [30]. If one further accounts for the angular dependence of photon emission—where the emission cone is characterized by the energy transfer ratio $f_c = \hbar\omega/(\gamma mc^2)$ between the electron (or positron) and the photon—it can be shown that the formation length also depends on the photon energy:

$$L_f \approx \frac{c\chi^{1/3}}{a_0\omega_0}\left(\frac{1 - f_c}{f_c}\right)^{1/3} \tag{2.73}$$

As a consequence, photons emitted with sufficiently low energy can have a formation length comparable to the wavelength of the background field. This finding is in agreement with the results of a comprehensive theoretical analysis based on SFQED presented in [113]. In summary, during laser-plasma interactions, the formation length is determined by both the laser intensity a_0 and the energy transfer ratio between the electron (or positron) and

the photon, f_c.

2.5.2 LCFA Approximation

In most of our works, we use the local constant field approximation (LCFA) [114] rates, which requires a weak field approximation, i.e., that the laboratory fields are weak compared to E_{cr}. This condition means, first, that the fields in the rest frame (for a massive particle, for a photon corresponding to the center of momentum frame for the electron-positron pair that would be generated) approximate crossed fields, and so the rates need only to be calculated for a crossed field configuration. Second, because the fields are weak and therefore, for quantum processes of interest, the initial and final particles need to be energetic. The "formation length" of such processes [115] is short compared to the scales of spatiotemporal fluctuations in the fields in practice, so they can be considered to be constant, and the emitted particles can be considered to be collinear with the initial particle momentum. Hence, the rates only need to be calculated for constant and crossed electromagnetic field configurations. For the interaction with a laser field, this approximation is effectively valid (at least for the high energy photons) if the normalized field strength $a_0 = eE_0/m_e c\omega \gg 1$, where E_0 is the peak electric field of the laser, while the field is much smaller than the critical field strength, $E/E_{cr} \ll 1$. This implies that two normalized Lorentz invariants during the interaction: $\mathcal{S} = \left(E^2 - c^2B^2\right)/E_{cr}^2$ and $\mathcal{P} = |\boldsymbol{E} \cdot c\boldsymbol{B}|/E_{cr}^2$ are much smaller than 1 [116, 117]. These approximations can break down [118, 119], so it is important to consider when this numerical LCFA framework is applicable. For example, at the transition region where $a_0 \sim 1$, the LCFA approximation will not be valid. In this case, we need to use other approximations such as the locally monochromatic approximation (LMA)[120, 121, 122, 123, 124], which also recently was used for studies into the polarization-dependent QED effect[125].

The LCFA forms the foundation for numerical tools used to simulate quantum regime interactions between lasers and plasma. When effective, LCFA enables a hybrid approach to calculating the interaction of charged particles with electromagnetic fields, combining

step-by-step solutions of the classical motion of point-like particles and their background with Monte Carlo sampling of the LCFA rate for SF-QED processes [49]. In simulations, it is typically assumed that sequences of first-order processes, during which intermediate particles travel along classical paths, provide a satisfactory approximation to higher-order interactions. This assumption rests on sufficiently long pulse durations that allow the neglect of coherent process contributions. The main distinctions from purely classical propagation are: (i) photon emission from a charge (or photon decay into an electron-positron pair) occurs stochastically, which can lead to effects such as deeper pulse penetration than purely classical predictions ('straggling') or reduced radiation emission rates in very short pulses ('quenching'); (ii) the classical trajectory of charges is 'adjusted' to account for the recoil from every Compton emission. Consequently, the LCFA serves as a flexible approach for incorporating strong-field QED processes, particularly in settings where the background field is unknown beforehand, such as in scenarios with numerous charges like intense laser-plasma collisions. As a result, it is extensively utilized in laser-plasma particle-in-cell (PIC) codes.

2.6 Quantum Radiation Reaction

A complete calculation of the interaction between an electron and a prescribed strong electromagnetic field in QED means solving for the scattering amplitude and the final state for an initial state containing only a single electron. In the perturbative approach to this problem, the quantum radiation reaction manifests itself as high-order contributions to the S matrix. However, as will be discussed in the following section, if $a_0 \gg 1$, the small size of the formation length [30] means that high-order terms are dominated by incoherent contributions, where each elementary QED process occurs in a distinct region of space [98]. Thus, we may identify quantum radiation reaction as the recoil arising from the sequential, incoherent emission of many photons [126]. As a result, as we will see later in this section 2.8, the quantum radiation reaction can be represented by a collisional operator in the kinetic equation

or calculated using the Monte Carlo method in the PIC code. As both methods are usually computationally expensive, it is sometimes useful to use the semiclassical form of quantum radiation reaction, which is modified from e.g. the Landau-Lifshitz formula, if we only care about the evolution of the averaged energy of the plasma during SF-QED processes. In the region of interest, the radiation is strongly beamed forward along the electron's direction of propagation, and the recoil must be antiparallel to its momentum. Thus we have:

$$P = \frac{2\alpha_f}{3}\frac{m_e c^2}{\tau_c}\chi^2 g(\chi) \tag{2.74}$$

Here, $g(\chi)$ is the Gaunt factor, which is defined as the ratio between the power of classical and quantum radiation.

$$g(\chi) = \frac{P_{quantum}}{P_{classical}} = \frac{\int_0^\infty F(\chi,\omega)d\omega}{\int_0^\infty F_{\chi\to 0}(\chi,\omega)d\omega} \tag{2.75}$$

.

Here, $F(\chi,\omega)$ is the quantum radiation spectrum, whose form can be found in appendix A.1. $F_{\chi\to 0}(\chi,\omega)$ is its classical limit. The Gaunt factor $g(\eta) = P_{quantum}/P_{classical}$, where P is the power spectrum, is used to correct the overestimation of the classical radiation reaction. A useful fit for the Gaunt factor is:

$$g(\chi) = [1 + 4.8(1+\chi)\ln(1+1.7\chi) + 2.44\chi^2] \tag{2.76}$$

2.7 Extending SFQED to Include Spin and Polarization

Although typically neglected or averaged over, the SFQED emission rates depend on the spin of the electrons and positrons, as well as on the polarization of the photons, as discussed by Ilderton, King, and Tang (2020) [127] and Seipt and King (2020) [72]. This can result in

the generation of polarized electron, positron, and photon beams [see Chen et al. (2019) [3], Seipt et al. (2019)[54], King and Tang (2020) [128], and Tang, King, and Hu (2020)[129], which can be important for high-energy physics applications. We begin with the definition of basis for spin and polarization proposed by G. Torgrimsson [124], as well as Seipt and King [72]. Under the high-intensity laser plasma interaction scenario, a convenient basis for transverse photon polarization vectors is given as:

$$\epsilon_1^\mu = e_1^\mu - \frac{\kappa \cdot e_1}{\kappa \cdot k} k, \qquad \epsilon_2^\mu = e_2^\mu - \frac{\kappa \cdot e_2}{\kappa \cdot k} k \tag{2.77}$$

Which e_1 and e_2 are two space-like unit vectors in the transverse plane, κ is the laser four-wave vector. $e_1 \cdot k = 0$, $e_2 \cdot k = 0$. The vectors ϵ_j for j = 1, 2 are not only mutually orthogonal, but also fulfill $k \cdot \epsilon_j = \kappa \cdot \epsilon_j = 0$. If the photon is linearly polarized, one calls $j = 1(j = 2)$ the E (B) polarization. For a circularly polarized laser, one conveniently also defines the complex left/right-handed basis vectors $\epsilon_\pm = (\epsilon_1 \pm i\epsilon_2)/\sqrt{2}$

The spin 4-vector α^μ of an electron in a pure state is related to the spinors

$$u\bar{u} = \frac{1}{2}(\not{p} + m)(1 + \gamma^5 \not{\alpha}) \tag{2.78}$$

Where α_μ refers to the asymptotic spin state of the particle (with $\alpha^2 = -1$, $p \cdot \alpha = 0$). A convenient spin basis was given by [130, 131, 132, 124]:

$$\alpha_{(1)}^\mu = e_1^\mu - \frac{p \cdot \varepsilon}{p \cdot k} k^\mu, \qquad \alpha_{(2)}^\mu = e_2^\mu - \frac{p \cdot \beta}{p \cdot k} k^\mu, \qquad \alpha_{(3)}^\mu = p^\mu - \frac{1}{p \cdot k} k^\mu, \tag{2.79}$$

$\alpha_{(i)} \cdot \alpha_{(j)} = \delta_{ij}$. The third vector $\alpha_{(3)}$ is called the lightfront helicity vector. The vectors e_1, e_2 are mutually orthogonal and perpendicular to k_μ. The polarisation vector α^μ of a partially polarised electron in a mixed state, $-1 < \alpha^2 \leq 0$ can be expanded in the basis as

$$\alpha^\mu = \sum_i n_i \alpha_{(i)}^\mu \tag{2.80}$$

which defines the Stokes vector for electrons $\boldsymbol{n} = (n_1, n_2, n_3)$. For an electron at rest, $\boldsymbol{n}$ points in the spin direction [130, 132, 124],

$$\boldsymbol{n} = \frac{1}{2} u^\dagger \Sigma u \quad (\text{when } \boldsymbol{p} = 0) \tag{2.81}$$

where $\Sigma = \mathbf{I}\{\gamma^2\gamma^3,\ \gamma^3\gamma^1,\ \gamma^1\gamma^2\}$, which $\mathbf{I}$ is the identity marix. A fully polarised electron has $\boldsymbol{n}^2 = 1$, an unpolarised has $\boldsymbol{n} = \mathbf{0}$, and $0 < \boldsymbol{n}^2 < 1$ represents a partially polarised state.

The probability of spin and polarization dependent nonlinear Compton scattering and nonlinear Breit–Wheeler pair production can be expressed as [124]:

$$\begin{aligned} \mathbb{P} =& \langle \mathbb{P} \rangle + \mathbf{n}_\gamma \cdot \mathbf{P}_\gamma + \mathbf{n}_1 \cdot \mathbf{P}_1 + \mathbf{n}_0 \cdot \mathbf{P}_0 + \mathbf{n}_\gamma \cdot \mathbf{P}_{\gamma 1} \cdot \mathbf{n}_1 + \mathbf{n}_\gamma \cdot \mathbf{P}_{\gamma 0} \cdot \mathbf{n}_0 \\ &+ \mathbf{n}_1 \cdot \mathbf{P}_{10} \cdot \mathbf{n}_0 + \mathbf{P}_{\gamma 10, ijk} \mathbf{n}_{\gamma i} \mathbf{n}_{1j} \mathbf{n}_{0k}, \end{aligned} \tag{2.82}$$

where $\boldsymbol{n}_\gamma$ is the Stokes vector for the photon, and $n_{1,0}$ are the Stokes vectors for the fermions. $\langle \mathbb{P} \rangle$ gives the spin and polarization averaged probability, $\mathbf{P}_i$ gives the dependence on the spin or polarization of one particle when averaging over the spin or polarization of the other two particles, $\mathbf{P}_{ij}$ describes the correlation between the spin or polarization of two particles, and $\mathbf{P}_{ijk}$ describes the correlation between the spin and polarization of all three particles.

In [132, 124], the authors present a gluing approach, where higher-order processes are approximated by linking together the spin- and polarization-dependent probabilities of nonlinear Compton scattering and Breit-Wheeler pair production. They demonstrate that this approach works under the regime where the formation length is small, so the field can be treated as approximately constant during particle production. This is the basis of particle-in-cell (PIC) codes. They presented general results for the Mueller matrices of nonlinear Compton scattering and Breit–Wheeler pair production, in this method, the first-order prob-

abilities can be expressed as:

$$\mathbb{P} = \mathbf{M}_{ijk}\mathbf{N}_{1i}\mathbf{N}_{0j}\mathbf{N}_{jk} \tag{2.83}$$

where M is a $4 \times 4 \times 4$ matrix and $i, j, k = 1, \cdots, 4$. $N = \{1, \boldsymbol{n}\}$ is the 4D Stokes vector. The Stokes vectors are used in conjunction with strong-field QED Mueller matrices for treating spin sums in higher-order processes. The 'N-step' can be obtained by matrix multiplication. For example, if a photon is emitted at step m and decays at step n, then the sum over its polarization is included via $\mathbf{M}^{(m)}_{i_m j_m k}\mathbf{M}^{(n)}_{i_n j_n k}$. The detailed discussion of this method can be found in [132, 124].

2.8 Kinetic Theory for Spin-Polarized Relativistic Plasmas with Radiation and Electron Self-Loop Correction

Recently, Seipt and Thomas [133] developed a kinetic description for leptons in strong fields starting from transport equations resulting from a Wigner operator formalism in the mean field approximation and including coupling of the fermion field to the high-energy photons, through a Boltzmann-like collision operator representing the point-like quantum emission/decay events. By taking moments of a delta distribution in phase-space, they derived effective quasi-classical equations of motion for leptons, including the effects of spin and radiation reaction. This development also confirms the validity of the Monte-Carlo-based QED-PIC code, which tries to recover the kinetic equation result by sampling a large ensemble of particles. For completeness, we summarize their main results here.

Their full transport equations for a polarized plasma has the following form:

$$\mathcal{T}f = \left(\frac{\partial f}{\partial \tau}\right)_{rad} + \left(\frac{\partial f}{\partial \tau}\right)_{loop} \tag{2.84}$$

$$\mathcal{T}\boldsymbol{a} - q\boldsymbol{a} \times \boldsymbol{\Omega}_0 = \left(\frac{\partial \boldsymbol{a}}{\partial \tau}\right)_{rad} + \left(\frac{\partial \boldsymbol{a}}{\partial \tau}\right)_{loop}, \tag{2.85}$$

which describes the evolution of the particle density f and the rest-frame spin density $\boldsymbol{a}$ distribution. This formulation incorporates both the effects of radiation emission and electron self-energy loop corrections, evaluated to the same order in α_f. The vector $\boldsymbol{\Omega}_0$ represents the spin precession axis in Eq. 2.46 for the case of zero anomalous magnetic moment ($a = 0$). The left-hand side of the equation features Vlasov-type transport operators acting on on-shell distribution functions. The transport operator is given by where the partial derivative with respect to position is $(\partial_x)_\mu = (\partial_t, \nabla_{\boldsymbol{x}})$, and the on-shell momentum derivative is $\partial_p = (0, \nabla_{\boldsymbol{p}})$. Here, $\boldsymbol{L} = \epsilon_p \boldsymbol{E} + \boldsymbol{p} \times \boldsymbol{B}$, with ϵ_p denoting the particle energy, and $\boldsymbol{E}$ and $\boldsymbol{B}$ the electric and magnetic fields, respectively.

The photon formation length is much shorter than the characteristic scale of the strong background field. As a result, the photon emission rate can be evaluated using the locally constant crossed field approximation (LCFA). In this regime, photon emission can be treated as a local process—effectively a short-range interaction—which allows it to be modeled using local collision operators: $C_f = (\partial f/\partial \tau)\,\mathrm{rad}$ and $C_a = (\partial \boldsymbol{a}/\partial \tau)\,\mathrm{rad}$. The explicit forms of C_f and C_a are provided below; for a detailed derivation, see Ref. [133]:

$$\begin{aligned} C_f(\boldsymbol{p}) = \int \frac{d^3\boldsymbol{k}}{\omega_k} \frac{\epsilon_p}{\epsilon_{p+k}} [f(\boldsymbol{p}+\boldsymbol{k}) w_0(\boldsymbol{p}+\boldsymbol{k}, \boldsymbol{k}) + \boldsymbol{a}(\boldsymbol{p}+\boldsymbol{k}) \cdot \boldsymbol{w}_i(\boldsymbol{p}+\boldsymbol{k}, \boldsymbol{k})] \\ - f(\boldsymbol{p}) W_0(\boldsymbol{p}) - \boldsymbol{a}(\boldsymbol{p}) \cdot \boldsymbol{W}_i(\boldsymbol{p}) \end{aligned} \tag{2.86}$$

$$\begin{aligned} C_a(\boldsymbol{p}) = \int \frac{d^3\boldsymbol{k}}{\omega_k} \frac{\epsilon_p}{\epsilon_{p+k}} [f(\boldsymbol{p}+\boldsymbol{k}) \boldsymbol{w}_f(\boldsymbol{p}+\boldsymbol{k}, \boldsymbol{k}) + \boldsymbol{a}(\boldsymbol{p}+\boldsymbol{k}) \cdot \underline{w}_{if}(\boldsymbol{p}+\boldsymbol{k}, \boldsymbol{k})] \\ - f(\boldsymbol{p}) \boldsymbol{W}_i(\boldsymbol{p}) - \boldsymbol{a}(\boldsymbol{p}) \cdot W_0(\boldsymbol{p}) \end{aligned} \tag{2.87}$$

with

$$w_A(\boldsymbol{p}, \boldsymbol{k}) = \int_0^1 d\lambda \omega_k \delta^{(3)}(\boldsymbol{k} - \lambda \boldsymbol{p}) \frac{dR_A}{d\lambda} \tag{2.88}$$

where λ denotes the fraction of the electron's momentum transferred to the photon, and the label A represents the various polarization-dependent contributions. The explicit expression for $dR_A/d\lambda$ can be found in Appendix A.1. The corresponding total rates are given by:

$$W_A(\boldsymbol{p}) = \int \frac{d^3\boldsymbol{k}}{\omega_k} w_A(\boldsymbol{p}, \boldsymbol{k}) = \int_0^1 d\lambda \frac{dR_A}{d\lambda} = R_A \tag{2.89}$$

To preserve unitarity, it is essential to include loop corrections at the same order as emission processes [124, 88, 134]. For high-energy photon emission at order α_f, the relevant loop contribution arises from the interference between the electron self-energy loop and the $O(\alpha_f^0)$ component of electron propagation. The general procedure for incorporating loop contributions into the kinetic equations is as follows: calculate the loop term, such as $(\partial f/\partial\tau)_{\text{loop}}$, using the same LCFA building blocks as for the emission operator, but substitute the corresponding expressions with their loop counterparts, $R_A \to R_A^L$. Since the loop insertion does not change the particle momentum, the quantities R_A^L—already integrated over all photon momenta circulating in the loop—are used directly. For the scalar density f, this loop correction vanishes:

$$\left(\frac{\partial f}{\partial \tau}\right)_{loop} = f R_0^L + \boldsymbol{a}\cdot\boldsymbol{R}_i^L - f R_0^L - \boldsymbol{a}\cdot\boldsymbol{R}_i^L = 0 \tag{2.90}$$

For the axial-vector density

$$\begin{aligned}\left(\frac{\partial \boldsymbol{a}}{\partial \tau}\right)_{loop} =& f\boldsymbol{R}_f^L + \boldsymbol{a}\cdot\boldsymbol{R}_{if}^L - f\boldsymbol{R}_i^L - \boldsymbol{a}R_0^L \\ =& \alpha\int_0^1 d\lambda\lambda \frac{Gi(z)}{\sqrt{z}}\boldsymbol{a}\cdot(\hat{\boldsymbol{K}}\hat{\boldsymbol{E}} - \hat{\boldsymbol{E}}\hat{\boldsymbol{K}})\end{aligned} \tag{2.91}$$

where $\hat{\boldsymbol{E}}$, $\hat{\boldsymbol{K}}$, and $\hat{\boldsymbol{B}}$ are unit vectors associated with the instantaneous rest-frame field components, forming an approximately orthogonal basis. This expression describes the anomalous spin precession. To make this explicit, note that integrating over the Scorer function

Gi yields the one-loop, field-dependent value of the anomalous magnetic moment:

$$a_e(\chi_e) = \frac{\alpha}{\chi_e}\int_0^1 d\lambda\lambda\frac{Gi(z)}{\sqrt{z}} \tag{2.92}$$

which was first derived by Ritus [135]. In the weak-field limit ($\chi_e \to 0$), this expression reduces to Schwinger's one-loop value, $a_e(\chi_e \to 0) = \alpha_f/2\pi$. As χ increases, $a_e(\chi)$ decreases monotonically toward zero. Consequently, the loop contribution to the collision operator for the axial vector is given by:

$$\begin{aligned}\left(\frac{\partial \boldsymbol{a}}{\partial \tau}\right) =& \chi_e a_e(\chi_e)\boldsymbol{a}\cdot(\hat{\boldsymbol{K}}\hat{\boldsymbol{E}} - \hat{\boldsymbol{E}}\hat{\boldsymbol{K}}) \\ =& -\chi_e a_e(\chi_e)\boldsymbol{a}\times\hat{\boldsymbol{B}} = \boldsymbol{a}\times\boldsymbol{\Omega}_{anomalous}(a_e(\chi_e))\end{aligned} \tag{2.93}$$

Here, we have neglected the term proportional to $(\hat{\boldsymbol{E}}\cdot\hat{\boldsymbol{B}})\hat{\boldsymbol{E}}$, which is expected to be negligible within the LCFA framework. The anomalous component of the spin precession vector is given by $\boldsymbol{\Omega}_{\text{anomalous}} = \boldsymbol{\Omega} - \boldsymbol{\Omega}_0 = a_e(\chi_e)\hat{\boldsymbol{B}}$. Thus, within the kinetic approach, we find that the loop contribution reproduces precisely the anomalous term in the spin precession, with the field-dependent anomalous magnetic moment $a_e(\chi_e)$.

To derive the relativistic moment equations, we integrate the two kinetic equations for f and $\boldsymbol{a}$ against a generic kernel $\Psi = \Psi(p^\alpha, p^\beta)$, using the Lorentz-invariant measure $\int d^3\boldsymbol{p}/\epsilon_p$. Introducing the shorthand notation for momentum-space integrals, $\langle Y\rangle = \int \frac{d^3\boldsymbol{p}}{\epsilon_p} fY$ where f serves as the weight function, we obtain:

$$\frac{\partial}{\partial x^\mu}\langle\Psi p^\mu\rangle = -qF^\nu_\mu\left\langle p^\mu\frac{\partial\Psi}{\partial p^\nu}\right\rangle + \int\frac{d^3\boldsymbol{p}}{\Psi}C_f \tag{2.94}$$

$$\frac{\partial}{\partial x^\mu}\langle\Psi p^\mu\boldsymbol{s}\rangle = -qF^\nu_\mu\left\langle \boldsymbol{s}p^\mu\frac{\partial\Psi}{\partial p^\nu}\right\rangle + q\langle\Psi\boldsymbol{s}\times\boldsymbol{\Omega}\rangle + \int\frac{d^3\boldsymbol{p}}{\Psi}C_{\boldsymbol{a}} \tag{2.95}$$

In the terms involving electromagnetic fields, integration by parts has been performed,

and surface contributions have been neglected. Recall that the polarization degree is defined as $\boldsymbol{s} = \boldsymbol{a}/f$.

By applying the moment hierarchy and modeling the distribution function as a delta function, one can derive effective semiclassical equations of motion for a radiating lepton, encompassing the effects of its spin polarization. It is important to note that the spin polarization here refers to a classical quantity, representing the expectation value of the four components of the particle's spin vector. Consequently, these single-particle equations describe the trajectory of an "average" lepton, rather than that of an individual particle.

$$\frac{du^\mu}{d\tau} = qF^{\mu\nu}(x(\tau))u_\nu(\tau) - u^\mu(\tau)(I_0(\chi_e) + \boldsymbol{s}(\tau)\cdot\boldsymbol{I}_i(\chi_e)) \tag{2.96}$$

Here, $\chi_e = \chi_e(x(\tau), u(\tau))$ denotes the local value of the quantum parameter evaluated at the particle's position. The quantity $I_A = \int d\lambda\lambda\frac{dR_A}{d\lambda}$ represents the first moment of the photon spectrum, corresponding to the normalized radiated power. This quasi-classical equation for particle acceleration includes the conventional Lorentz force, as well as an additional spin-dependent radiation reaction term (the second term on the right-hand side). In the unpolarized limit ($s = 0$), this result is consistent with previous findings in the literature (see, e.g., [136, 116, 137]). The quasi-classical equation governing the evolution of the polarization vector is obtained from Eq. 2.95 as

$$\frac{d\boldsymbol{s}}{d\tau} = q\boldsymbol{s}(\tau)\times\boldsymbol{\Omega}(\tau) + \boldsymbol{W}_f - \boldsymbol{W}_i + \boldsymbol{s}\cdot(\underline{W}_{if} - W_0\mathbf{1}) \tag{2.97}$$

Here, as before, the four-divergence is recast as a proper time derivative. Equation2.97 describes spin precession, now with the anomalous magnetic moment taking its field-dependent form $a_e(\chi_e)$, as given in Eq.2.92. The additional terms account for the radiative polarization of electrons, providing a generalization of the Sokolov–Ternov effect. In the weak-field limit, i.e., to leading order in χ, this equation reduces to the Baier–Katkov–Strakhovenko equation. Both of these effects have recently been implemented in simulations of spin dynamics in

laser–electron interactions (see, e.g. [138, 8, 139]). In summary, the newly developed kinetic framework for leptons in strong fields, which incorporates spin evolution, offers a robust physical foundation for advancing spin- and polarization-resolved QED-PIC algorithms.

2.9 Spin and Polarization-Dependent QED in PIC Code

Most of the studies for QED plasma use a PIC code with spin-averaged QED rates [114, 140, 141], in which the QED processes only depend on the momentum of the particles and the EM field they experience. Fundamentally, the quantum emission and pair production processes are all spin-dependent. The particles' spin evolves through precession in the fields and due to radiative spin transitions. To apply the theory presented in the previous section to the framework of the PIC code, it will be convenient to represent the particle spin state with the classical spin vector $\boldsymbol{s}$ in the rest frame of the particle. This vector represents the expectation over many measurements and evolves via the T-BMT equations. The radiative spin transitions are represented by a Monte-Carlo sampling algorithm, where point-like photon emissions result in the spin vector collapsing onto a chosen spin basis. The choice of the spin basis will be discussed in detail in the next section.

To demonstrate how spin and polarization state will influence the SFQED process, the spectrum of the NLCS and NBW processes is plotted for particles at different spin and polarization states interacting with a constant magnetic field. Fig. 2.5 shows the radiation spectrum of the NLC process for an initial lepton spin state $s = \uparrow$ or $\downarrow$ and the radiated photon Stokes parameter is $\xi_3 = \pm 1$ when the quantum parameter is $\chi_q = 1.0$. The up or down arrow indicates that the spin is either parallel or antiparallel to the rest frame magnetic field direction. The Stokes parameter here will be explained in detail in Section 2.10. Fig. 2.6 shows the generated positron energy spectrum from the NBW process for a photon with Stokes parameter $\xi_3 = \pm 1$ and the generated positron spin state $s_p = \uparrow$ or $\downarrow$.

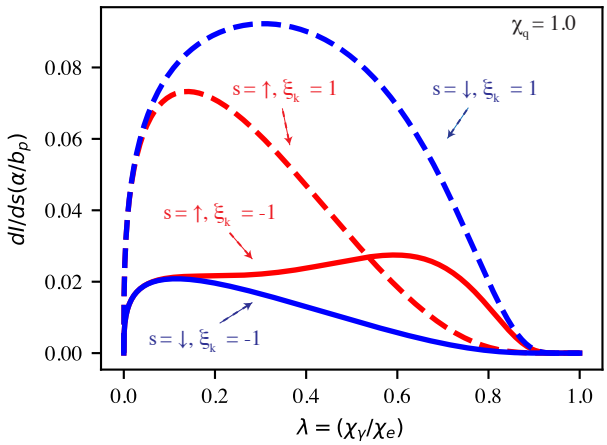

Figure 2.5: Spin and polarization involved-NLC spectra for lepton with initial spin state s. ξ_k is the Stokes parameter of the radiated photon.

We can see that in the NLC process, the lepton's initial spin state will modify the radiation spectrum and the radiated photon's polarization state. In the NBW process, the photon's polarization state will influence the generated lepton's energy spectrum and spin state. Note that the spectra are asymmetrical for photon polarization $\xi_3 = +1$ or -1 and lepton spin states $s_p = \uparrow$ or $\downarrow$ [72, 73]. This asymmetry in the spectra allows us to explore possible regimes for generating polarized gamma-ray and lepton bunches using the SF QED process [142, 143, 4].

2.10 Lepton Spin and Photon Polarization Basis in PIC

In the quantum calculation of our QED algorithm, the particle spin or polarization state will be projected onto a spin basis. In other words, the code measures the particle spin or polarization state after every quantum event. The choice of spin and polarization basis is crucial to retaining important information about particle polarization after the projection. There are various ways to construct the spin and polarization basis. For example, in some literature [144, 145, 8], the particle acceleration direction $\hat{\boldsymbol{a}}$, velocity direction $\hat{\boldsymbol{v}}$, and their

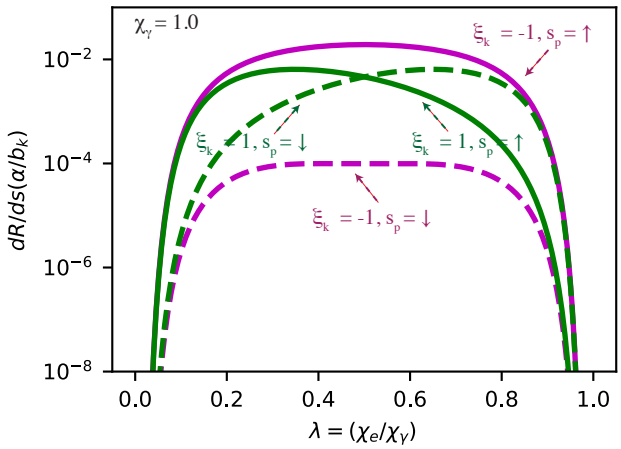

Figure 2.6: Spin and polarization involved-NBW spectrums for the photon with Stokes parameter ξ_k. The generated positron spin state is s_p.

cross-project $\hat{\boldsymbol{v}} \times \hat{\boldsymbol{a}}$ is used to construct the basis. In the SF QED model under the local constant field approximation (LCFA),the direction of the electric and magnetic fields in the particle's rest frame and the momentum vector should be close to mutually perpendicular. Here, for consistency with the SF QED framework, this inherently orthogonal system is used to construct a spin and polarization basis (as the spin is also evaluated in the rest frame of the particle, this provides another reason to use the rest frame EM field direction to construct the basis). Because the PIC code uses three-vector objects, we express the bases in three-vector form instead of four-vector form. Note that in Eq. 2.79, if we set $e_1^\mu = (0, \hat{\boldsymbol{\varepsilon}}_0)$, $e_2^\mu = (0, \hat{\boldsymbol{\beta}}_0)$, where $\hat{\boldsymbol{\varepsilon}}_0$ and $\hat{\boldsymbol{\beta}}_0$ are electric field the magnetic field direction in the lab frame, when we transform the basis to the rest frame of an electron $\alpha_{(i)} \xrightarrow{\Lambda(-p)} \alpha_{(i)}^{RF}$, the time-like component will be zero, and we get three mutually orthogonal three-vectors ($\hat{\boldsymbol{\varepsilon}}$, $\hat{\boldsymbol{\beta}}$, $\hat{\boldsymbol{k}}$). They are exactly the direction of the electric, magnetic, and wave vectors of the background field in the rest frame of the particle [131].

$$\alpha_{(1)}^{RF} = (0, \hat{\boldsymbol{\varepsilon}}), \quad \alpha_{(2)}^{RF} = (0, \hat{\boldsymbol{\beta}}), \quad \alpha_{(3)}^{RF} = (0, \hat{\boldsymbol{k}}) \,, \tag{2.98}$$

where $\hat{\boldsymbol{\varepsilon}} = \boldsymbol{E}_{RF}/|\boldsymbol{E}_{RF}|$, $\hat{\boldsymbol{\beta}} = \boldsymbol{B}_{RF}/|\boldsymbol{B}_{RF}|$, $\hat{\boldsymbol{k}}$ is the lepton momentum direction, which under the collinear emission approximation, is also the direction of the radiated photon momentum. As a result, we choose the three vectors ($\hat{\varepsilon}$, $\hat{\boldsymbol{\beta}}$, $\hat{\boldsymbol{k}}$) to construct the spin basis for our algorithm.

2.10.1 Lepton Spin Basis

For leptons, the logical choice for the spin quantization axis is along the rest frame B-field direction $\hat{\boldsymbol{\beta}}$ and only considers the spin component along $\hat{\boldsymbol{\beta}}$ [72]. This is because this is the non-precessing component for the rest frame spin vector $\boldsymbol{s}$. Furthermore, radiative processes only increase the spin component in the $\hat{\boldsymbol{\beta}}$ direction and only cause the $\hat{\boldsymbol{\varepsilon}}$ and $\hat{\boldsymbol{\kappa}}$ components to decay away. This basis is suitable for calculating an unpolarized lepton beam interacting with a constant magnetic field or a linearly polarized plane wave. We need to resolve all three spin components during a quantum process for more complicated field configurations or a polarized lepton beam. Seipt et al. [131] calculated radiation-induced spin changes for all three spin components along ($\hat{\varepsilon}$, $\hat{\boldsymbol{\beta}}$, $\hat{\boldsymbol{k}}$). Yuhui Tang [139] introduces the variation of radiative spin polarization due to instantaneous no-photon emission and proposes a recipe to implement this radiation-induced spin change into the Monte-Carlo quantum radiation algorithm. Cain's manual [121] also offers a recipe for constructing a spin basis. They use transverse acceleration direction $\hat{\boldsymbol{e}}_{\boldsymbol{1}} = \boldsymbol{a} - (\boldsymbol{a}\cdot\boldsymbol{v})\boldsymbol{v}$ particle velocity direction $\hat{\boldsymbol{e}}_{\boldsymbol{v}} = \hat{\boldsymbol{v}}$ and their cross product $\hat{\boldsymbol{e}}_{\boldsymbol{2}} = \hat{\boldsymbol{v}} \times \hat{\boldsymbol{e}}_{\boldsymbol{1}}$. It is easy to prove that under ultra-relativistic approximation, the basis used in Cain's manual is essentially the same as the basis ($\hat{\varepsilon}$, $\hat{\boldsymbol{\beta}}$, $\hat{\boldsymbol{k}}$).

From the spin- and polarization-resolved spectrum, we can calculate the probability of spin state in the $\hat{\varepsilon}$, $\hat{\boldsymbol{\beta}}$, or $\hat{\boldsymbol{k}}$ direction after every quantum process. The QED-PIC code requires the use of a vector quantity to represent the spin state for the classical spin precession calculation. The expected spin vector $\langle \boldsymbol{s}_f \rangle$ becomes the best candidate to keep most of the spin information. In some literature, the unit vector along this direction is called the spin quantization axis [145, 8]. It is constructed from the expected radiation-induced spin change for all three spin components ($\hat{\varepsilon}$, $\hat{\boldsymbol{\beta}}$, $\hat{\boldsymbol{k}}$): $\langle \boldsymbol{s}_f \rangle = \langle S_E \rangle \hat{\boldsymbol{\varepsilon}} + \langle S_B \rangle \hat{\boldsymbol{\beta}} + \langle S_K \rangle \hat{\boldsymbol{k}}$ (Fig. 2.7).

The detailed derivation of the expected spin direction for both NLC and NBW processes is shown in Appendix A. The expression for the expected spin direction of an electron in the NLC processes is:

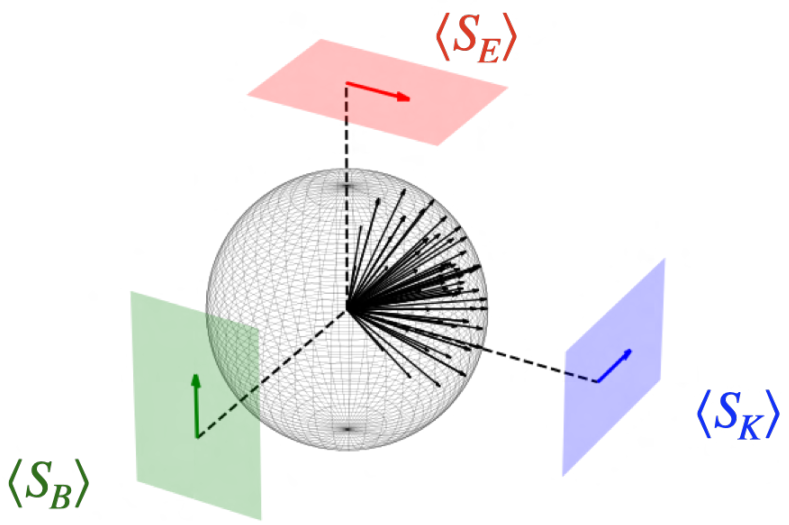

Figure 2.7: Schemetic of spin measurement under the basis ($\hat{\varepsilon}$, $\hat{\boldsymbol{\beta}}$, $\hat{\boldsymbol{k}}$)

$$\langle \boldsymbol{s}_f \rangle_{NLC} = \frac{\boldsymbol{g}}{w_0} \tag{2.99}$$

which

$$w = -\mathrm{Int}\mathrm{K}_{1/3}(u') + \kappa \mathrm{K}_{2/3}(u') + \lambda(\mathbf{s}_i \cdot \hat{\boldsymbol{\beta}})\mathrm{K}_{1/3}(u'), \tag{2.100}$$

$$\begin{aligned} \mathbf{g} =& u\mathrm{K}_{1/3}(u')\hat{\boldsymbol{\beta}} + \left(-\mathrm{Int}\mathrm{K}_{1/3}(u') + 2\mathrm{K}_{2/3}(u')\right)\mathbf{s}_i \\ &+ \lambda u \left(-\mathrm{Int}\mathrm{K}_{1/3}(u') + \mathrm{K}_{2/3}(u')\right)(\mathbf{s}_i \cdot \hat{\mathbf{k}})\hat{\mathbf{k}} \end{aligned} \tag{2.101}$$

Here, λ is the momentum ratio between the radiated photon and the initial energy of the electron, $u = \lambda/(1-\lambda)$ is the momentum ratio between the radiated photon and the final energy of the electron. $\kappa = 1/(1-\lambda) + (1-\lambda)$, $\tilde{\kappa} = 1/(1-\lambda) - (1-\lambda)$, $u' = \frac{2u}{3\chi_e}$.

The expected spin direction for positron in the NBW process is:

$$\langle \boldsymbol{s}_p \rangle_{NBW} = \frac{\boldsymbol{j}_p}{w_0} \tag{2.102}$$

which:

$$w_0 = \mathrm{Int}\mathrm{K}_{1/3}(\tilde{u}') + \rho \mathrm{K}_{2/3}(\tilde{u}') - \xi_3 \mathrm{K}_{2/3}(\tilde{u}') \tag{2.103}$$

$$\begin{aligned} \boldsymbol{j}_p = &\left(-\frac{1}{\tilde{\lambda}} + \xi_3 \frac{1}{1-\tilde{\lambda}} \right) \mathrm{K}_{1/3}(\tilde{u}') \hat{\boldsymbol{\beta}} - \xi_1 \frac{1}{1-\tilde{\lambda}} \mathrm{K}_{1/3}(\tilde{u}') \hat{\boldsymbol{\varepsilon}} \\ &+ \xi_2 \left(\frac{1}{\tilde{\lambda}} \mathrm{Int}\mathrm{K}_{1/3}(\tilde{u}') - \tilde{\rho} \mathrm{K}_{2/3}(\tilde{u}') \right) \hat{\boldsymbol{k}} \end{aligned} \tag{2.104}$$

Here, $\tilde{\lambda}$ are the momentum ratios between the positron and the initial photon. $\rho = (1-\tilde{\lambda})/\tilde{\lambda} + \tilde{\lambda}/(1-\tilde{\lambda})$, $\tilde{\rho} = (1-\tilde{\lambda})/\tilde{\lambda} - \tilde{\lambda}/(1-\tilde{\lambda})$, $\tilde{u} = 1/\tilde{\lambda} + 1/(1-\tilde{\lambda})$ and $\tilde{u}' = \frac{2}{3\chi_\gamma}\tilde{u}$.

2.10.2 Photon Polarization Basis

Describing the polarization of the emitted photons requires choosing a basis for this polarization. The photon polarization state can be represented as in section 2.2.8 with $\hat{\boldsymbol{\psi}} = a_1 \hat{\boldsymbol{\psi}}_1 + a_2 \hat{\boldsymbol{\psi}}_2$.

When the photon is born, $\hat{\boldsymbol{\psi}}_1 = \hat{\boldsymbol{\varepsilon}}$ and $\hat{\boldsymbol{\psi}}_2 = \hat{\boldsymbol{\beta}}$ are the same as the directions of the rest frame electric and magnetic field experienced by the incoming lepton, respectively. The components of the Stokes vector $\boldsymbol{\xi} = (\xi_1, \xi_2, \xi_3)$ corresponding to this basis are $\xi_1 = a_1 a_2^* + a_1^* a_2$, $\xi_2 = i(a_1 a_2^* - a_1^* a_2)$, $\xi_3 = |a_1|^2 - |a_2|^2$. Fig. 2.8 demonstrates the polarization basis under the simple synchrotron radiation geometry. An electron gyrating inside a constant magnetic field will undergo synchrotron radiation. The two polarization directions $\boldsymbol{\sigma}$ and

$\boldsymbol{\pi}$ generally used in synchrotron radiation are the same as the directions $\hat{\boldsymbol{\varepsilon}}$ and $\hat{\boldsymbol{\beta}}$. Similar to how the lepton spin basis is constructed, the photon-polarization Stokes vector is set to the expected photon Stokes vector: $\boldsymbol{\xi}_{ave} = (\langle\xi_1\rangle, \langle\xi_2\rangle, \langle\xi_3\rangle)$. The detailed expression for the expected photon Stokes vector is given in the appendix A, in equation A.21, A.23, and A.25.

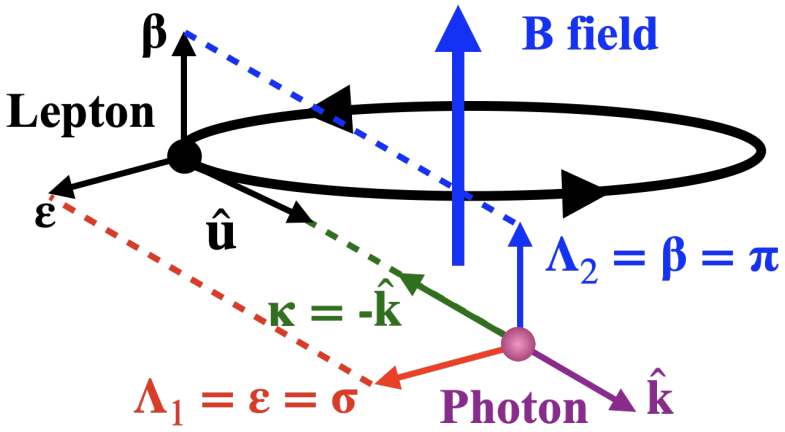

Figure 2.8: Photon polarization basis. A high-energy lepton with momentum in direction $\hat{\boldsymbol{u}}$ emits a photon whose momentum direction $\hat{\boldsymbol{k}} = \hat{\boldsymbol{u}}$. The polarization basis vector for the photon is $\hat{\boldsymbol{\varepsilon}}$, $\hat{\boldsymbol{\beta}}$. When $\hat{\boldsymbol{\kappa}} = -\hat{\boldsymbol{k}}$, $\boldsymbol{\sigma}$ and $\boldsymbol{\pi}$ are in the same direction as $\hat{\boldsymbol{\varepsilon}}$ and $\hat{\boldsymbol{\beta}}$.

For observation, however, the basis will be different because of the different field configurations with which the photon interacts. The observation basis, in general, can be expressed as:

$$\hat{\boldsymbol{o}}_1 = \hat{\boldsymbol{\psi}}_1 \cos(\phi) + \hat{\boldsymbol{\psi}}_2 \sin(\phi),\ \hat{\boldsymbol{o}}_2 = -\hat{\boldsymbol{\psi}}_1 \sin(\phi) + \hat{\boldsymbol{\psi}}_2 \cos(\phi) \tag{2.105}$$

The Stokes parameter under the new observation basis $\boldsymbol{\xi}^{(o)}$ is then:

$$\xi_1^{(o)} = \xi_1 \cos(2\phi) - \xi_3 \sin(2\phi),\ \xi_2^{(o)} = \xi_2,\ \xi_3^{(o)} = \xi_1 \sin(2\phi) + \xi_3 \cos(2\phi) \tag{2.106}$$

In the actual code implementation, we can obtain the Stokes parameter when the photon is born from our polarisation-resolved NLCS rate calculation. However, we must translate the Stokes parameter from the frame when it is born to the observation frame when the photon interacts with other EM fields. This means that besides information about the Stoke

parameters, we also need to record information about the basis when a photon is born. We want to reduce the number of parameters required to record the full information of the photon polarisation state to reduce the computational memory cost. Here, we find that it is possible to use one vector quantity to represent the polarisation state and record all information about the photon polarisation state.: $\boldsymbol{P} = (P_{\psi_1},\ P_{\psi_2},\ P_k)$, where $P_{\psi_1},\ P_{\psi_2},\ P_k$ is the component in the $(\hat{\boldsymbol{\psi}}_1, \hat{\boldsymbol{\psi}}_2, \hat{\boldsymbol{k}})$ coordinate. We begin by transforming the coordinate to the circular polarization basis:

$$\hat{\boldsymbol{e}}_{\boldsymbol{+}} = \frac{1}{\sqrt{2}}(\hat{\boldsymbol{e}}_{\boldsymbol{1}} + i\hat{\boldsymbol{e}}_{\boldsymbol{2}}),\ \hat{\boldsymbol{e}}_{\boldsymbol{-}} = \frac{1}{\sqrt{2}}(\hat{\boldsymbol{e}}_{\boldsymbol{1}} - i\hat{\boldsymbol{e}}_{\boldsymbol{2}}) \tag{2.107}$$

The photon polarization state can be rewritten under the new coordinate

$$\psi = A_+\hat{\boldsymbol{e}}_{\boldsymbol{+}} + A_-\hat{\boldsymbol{e}}_{\boldsymbol{-}} \tag{2.108}$$

Which, $A_+ = (a_1 - ia_2)/\sqrt{2}$, $A_- = (a_1 + ia_2)/\sqrt{2}$.The Stokes parameter can be represented, under the circular polarization basis, as:

$$\xi_1 = (A_+^* A_- - A_+ A_-^*)/i,\ \xi_2 = |A_+|^2 - |A_-|^2,\ \xi_3 = (A_+^* A_- + A_+ A_-^*) \tag{2.109}$$

We can simplify the expression by rewriting the complex parameter A_+ and A_- as: $A_+ = |A_+|e^{i\theta_+}$, $A_- = |A_-|e^{i\theta_-}$, so that:

$$\xi_1 = 2|A_+||A_-|\frac{e^{i(\theta_- - \theta_+)} - e^{i(\theta_- - \theta_+)}}{2i} = 2|A_+||A_-|\sin 2\Delta\theta \tag{2.110}$$

Which $\Delta\theta = (\theta_- - \theta_+)/2$. Also, we can have

$$\xi_3 = 2|A_+||A_-|\frac{e^{i(\theta_- - \theta_+)} + e^{i(\theta_- - \theta_+)}}{2} = 2|A_+||A_-|\cos 2\Delta\theta \tag{2.111}$$

Since the intensity is normalized to unity: $|A_+|^2 + |A_-|^2 = 1$, and from Eq. 2.109, $|A_+|^2 -$

$|A_-|^2 = \xi_2$, we can obtain the magnitude of A_+ and A_-:

$$|A_+| = \sqrt{\frac{1+\xi_2}{2}},\ |A_-| = \sqrt{\frac{1-\xi_2}{2}}. \tag{2.112}$$

The linear Stokes parameter can be written in terms of the circular Stokes parameter ξ_2 and a phase term $\Delta\theta$:

$$\xi_1 = \sqrt{1-\xi_2^2}\sin 2\Delta\theta,\ \xi_3 = \sqrt{1-\xi_2^2}\cos 2\Delta\theta \tag{2.113}$$

We can then reconstruct a unit vector to represent the polarization state: $\boldsymbol{P} = (P_{\psi_1}, P_{\psi_2}, P_k)$. The component along the momentum direction is set to be the circularly polarized Stokes parameter $P_k = \xi_2$. We provide a geometric meaning for angle $\Delta\theta$, which is the angle between $\boldsymbol{P}$ component in $\hat{\boldsymbol{\psi}}_1 - \hat{\boldsymbol{\psi}}_2$ plane: $\boldsymbol{P}_{\psi_1-\psi_2} = (P_{\psi_1}, P_{\psi_2}, 0)$ and $\hat{\boldsymbol{\psi}}_1$. The component P_{ψ_1} and P_{ψ_2} can be written as:

$$P_{\psi_1} = \sqrt{1-P_k^2}\cos(\Delta\theta) = \sqrt{1-\xi_2^2}\cos(\Delta\theta),\ P_{\psi_2} = \sqrt{1-\xi_2^2}\sin(\Delta\theta) \tag{2.114}$$

The relationship between P_{ψ_1}, P_{ψ_2}, P_k and the Stokes parameter can be written as:

$$\xi_1 = \frac{2P_{\psi_1}P_{\psi_2}}{\sqrt{1-P_k^2}},\quad \xi_2 = P_k,\quad \xi_3 = \frac{P_{\psi_1}^2 - P_{\psi_2}^2}{\sqrt{1-P_k^2}} \tag{2.115}$$

Under the observation frame, we can obtain the observed Stokes parameters by projecting the vector $\boldsymbol{P}$ to the observation basis $(\hat{\boldsymbol{o}}_1, \hat{\boldsymbol{o}}_2, \hat{\boldsymbol{k}})$.

$$P_{o_1} = \boldsymbol{P}\cdot\hat{\boldsymbol{o}}_1 = P_{\psi_1}\cos(\phi) + P_{\psi_2}\sin(\phi) \tag{2.116}$$

$$P_{o_2} = \boldsymbol{P}\cdot\hat{\boldsymbol{o}}_2 = -P_{\psi_1}\sin(\phi) + P_{\psi_2}\cos(\phi) \tag{2.117}$$

Because the direction of the photon momentum does not change during propagation, $\xi_2^{(o)} = P_k = \xi_2$ remains unchanged. The Stokes parameter under the observation basis,

calculated using Eq. 2.115 can be written as:

$$\xi_1^{(o)} = -\sin(2\phi)\xi_3 + \cos(2\phi)\xi_1, \quad \xi_3^{(o)} = \cos(2\phi)\xi_3 + \sin(2\phi)\xi_1 \tag{2.118}$$

Which is the same as Eq. 2.106. As a result, we can just use the reconstructed vector $\boldsymbol{P}$ with the proper transformation rule to represent the full photon polarization states. In most of this thesis, the photon polarization is measured on the basis of $(\hat{\boldsymbol{o}}_2, \hat{\boldsymbol{o}}_2, \hat{\boldsymbol{k}})$, which $\hat{\boldsymbol{o}}_1$ is the polarization direction of the linearly polarized laser, $\hat{\boldsymbol{k}}$ is the photon momentum direction, $\hat{\boldsymbol{o}}_2$ is the obtained by taking the cross product of $\hat{\boldsymbol{o}}_1$ and $\hat{\boldsymbol{k}}$.

CHAPTER 3

Method

3.1 QED-PIC Code in General

We start with a general overview of QED-PIC codes before introducing our spin and polarization-resolved QED-PIC module. This well-developed method provides a solid foundation for our work. When estimating the scale length of quantum processes in high-intensity laser-plasma interactions, it is found that the formation length of QED processes can be significantly smaller than the typical inhomogeneities of the EM field. Thus, the calculation of quantum processes can be greatly simplified by treating them as occurring instantaneously, and the EM field strength can be viewed as a constant during these processes. The simulation of SFQED phenomena in this thesis is generally based on the local constant field approximation (LCFA), which is discussed in detail in the previous section. The LCFA approximation enables the calculation of quantum processes as discrete events that occur with a certain probability, which allows the Monte Carlo method to be used to calculate the SFQED processes. This method accounts for the probabilistic nature of quantum processes. Integrating this Monte Carlo Quantum calculation together with the PIC code is commonly referred to as QED-PIC. The QED-PIC code splits the electromagnetic field into two parts: a coherent classical field sampled on the grid of the simulation domain and a population of high-frequency photons that originate from the incoherently summed synchrotron emission of the particles. In much the same way that charged particles are treated in ordinary PIC

codes, the distribution of high-frequency photons is sampled with an ensemble of so-called macro photons. These macro photon particles are created through the NLC process and propagate ballistically at the speed of light. The only interaction experienced by these photons in the QED-PIC algorithm is the NBW process, which, when photons travel through an intense EM field, has a certain probability of decaying into electron-positron pairs. In the following subsection, we will discuss the general framework of how this QED-PIC works.

3.1.1 Decision Making in QED-PIC

The QED-PIC method extends the traditional PIC loop in that, at every step, each energetic particle inside the strong field is evaluated to determine whether quantum events happen. Based on the information provided by the PIC code, such as particle momentum and the instantaneous electromagnetic field experienced by the particle, we can calculate the probability of the quantum events for each particle at every step. In the most common case, this probability is based on spin- and polarization-averaged rates $R_f(\chi) = \int_0^1 R'_f(\chi, f')df'$, which depend only on the instantaneous quantum parameter χ calculated through the particle moment and the local field strength experienced by the particle. Here, $R'_f = \partial R/\partial f$ is the differential rate of the relevant process. One has to choose a sufficiently short time step, such that the probability of multiple events occurring within a single time step is negligible, i.e., $N_f = \Delta t R_f \ll 1$. For the two quantum processes considered in this work, the NLCS process typically has a much higher rate than the NBW. This maximum time step Δt_{QED} that satisfies the NLC rate sets this condition. It may be compared to the maximum time step permitted by the Courant-Friedrichs-Lewy condition for finite-difference-time-domain methods Δt_{CFL} and the need to resolve the Debye length Δt_D as follows [41]:

$$\frac{\Delta t_{QED}}{\Delta t_{CFL}} \approx \frac{10N}{a_0}, \ \frac{\Delta t_{QED}}{\Delta t_D} \approx \frac{100}{a_0}\sqrt{\frac{n_e mc^2}{n_{cr}k_B T}} \tag{3.1}$$

where N is the number of grid cells used to resolve the laser wavelength, n_e is the electron

number density, n_{cr} is the critical density, and T is the plasma temperature.

Whether or not the event happens can be decided by simply generating a uniformly distributed pseudo-random value $r_1 \in [0, 1]$, and the event is accepted if $r_1 < N_f$. The probability N_f must be less than 1 for all possible values of χ, and the smaller the time step, the more accurate the calculation. An alternative way is based on the computation of the cumulative path. The cumulative probability of a quantum event after the particle travels through an EM field of optical depth τ_{em} is $P(t) = 1 - \exp[-\tau_{em}]$. Each electron, positron, and gamma-ray photon is assigned an optical depth $\tau_{em} = \exp[-\int_0^t R_f(t')dt']$. In the actual numerical simulation, this integral is solved by first-order Eulerian integration, i.e., $\tau_{em}(t + \Delta t) = \tau(t) + R_f(t)\Delta t$. A pseudo-random value is first generated from the unit interval $P_1 \in [0, 1)$. Then, it is inverted according to the equation of cumulative probability $\tau_1 = -ln(1 - P_1)$ and compared with the optical depth of the particle τ_{em}. The event is accepted when $\tau_1 \leq \tau_{em}$.

3.1.2 Sampling the Spectrum

Once the algorithm accepts the event, the energy and momentum of the generated photons or electron-positron pairs are sampled through the quantum spectrum. A method based on inverse transform sampling was developed. The momentum fraction f is determined by solving $r_2 = C(f, \chi) = \int_0^t R'_f(\chi, f')df'$; where r_2 is another pseudorandom value from $r_2 \in [0, 1]$ and C is the cumulative distribution function. This equation can be solved by obtaining the inverse cumulative distribution function $C^{-1}(f, \chi)$ and applying r_2 as the input of the function to obtain the momentum fraction f. This inverse function can be precalculated and tabulated for computation efficiency. For nonlinear Compton scattering, the differential rate $R'_f \to \infty$ as $f \to 0$ as $f^{-2/3}$, which is integrable. A low f cutoff is commonly applied to exclude this region: a cutoff equivalent to $2mc^2$ is sufficiently small not to affect subsequent pair production and does not affect the magnitude of radiation emission too much if γ is sufficiently large. The need for a cutoff can be avoided by augmenting the

tabulated values of $C(f, \chi)$ (or its inverse) with the asymptotic analytical expressions.

One may instead use rejection sampling, which bypasses the calculation of the cumulative distribution function and can determine whether the event happens and the momentum of the generated particle simultaneously. One uniformly distributed random value $r_1 \in [0, 1]$ defines the candidate value of the energy ratio f. This procedure requires that $R'_f(\chi, f)\Delta t < 1$ for all values of $f \in [0, 1]$ and all possible values of χ. As a result, a flat function is usually preferred for this method, and we cannot sample a distribution that diverges with f or χ. Due to the shape of the spectrum, we can easily apply this method to the Breit-Wheeler process. However, the infrared divergence for nonlinear Compton scattering means this will be violated for some vicinity of $f = 0$. This problem can be eliminated (following Gonoskov et al. (2015) [42]). The candidate f can be generated as $f = r_1^3$ (i.e., with small values) more often, such that the corresponding acceptance probability $3r_1^2 R'_f(\chi, r_1^3)$ becomes bounded from above.

3.1.3 Wrap up the Calculation

After the NLCS/NBW calculation, radiation reaction is incorporated by subtracting the photon's momentum from that of the emitting electron (or positron). In pair production events, the photon transfers all its momentum to the resulting electron-positron pair and is subsequently removed from the simulation. A common challenge in large-scale QED simulations is the massive number of particles generated during extremely strong-field QED phenomena, such as QED cascades. This proliferation of particles greatly increases both memory usage and computation time, scaling exponentially with laser duration and intensity. Consequently, this severely restricts the range of parameters that can be studied for extreme QED processes.

An effective strategy to address this issue is the particle merging algorithm. This technique reduces memory requirements by combining particles that are close to each other in both position and momentum (phase space) into a single representative particle. This approach

has already been utilized in OSIRIS for unpolarized strong-field QED models, enabling more efficient exploration of high-intensity regimes [146].

3.2 Spin and Polarization-Resolved QED-PIC Code

The spin- and polarization-resolved QED-PIC module builds upon the same framework as the conventional, spin- and polarization-averaged QED-PIC codes. However, explicitly tracking spin and polarization increases the dimensionality of the problem, introducing many additional variables. Consequently, the underlying algorithms become considerably more complex, necessitating certain approximations to maintain computational efficiency—a topic we will explore in detail in this section.

Traditionally, the spin-averaged, unpolarized QED algorithm focuses on calculating the spectrum of generated particles—either photons in nonlinear Compton scattering (NLCS) or electron-positron pairs in nonlinear Breit-Wheeler (NBW) processes—described by $S(\chi, \lambda)$, where λ is the momentum transfer ratio. The quantum parameter χ_e/χ_γ for the initial particle is known from its momentum and the local electromagnetic field. The Monte Carlo method is then used to sample this spectrum over various momentum transfer ratios for given values of χ_e/χ_γ.

Incorporating spin and polarization adds significant complexity to this procedure. For example, the NLCS spectrum in the spin- and polarization-resolved algorithm is written as $S(\chi_e, \boldsymbol{s}_i, \lambda, \boldsymbol{s}_f, \boldsymbol{\xi})$, where the spectrum now depends on the initial quantum parameter χ_e and spin state $\boldsymbol{s}_i$ of the lepton, the momentum transfer ratio λ , the final lepton spin $\boldsymbol{s}_f$, and the polarization state $\boldsymbol{\xi}$ of the emitted photon. In practice, only χ_e and $\boldsymbol{s}_i$ are directly known; the other variables must be sampled. The amplitude of $S(\chi_e, \boldsymbol{s}_i; \lambda, \boldsymbol{s}_f, \boldsymbol{\xi})$ prescribes the probability of outcomes for λ, $\boldsymbol{s}_f$, and $\boldsymbol{\xi}$.

Ideally, direct sampling from this full spectrum would be possible; however, the resulting function is nine-dimensional: χ_e and λ are scalar variables, while $\boldsymbol{s}_f$ and $\boldsymbol{\xi}$ are vector

quantities (accounting for six additional variables), and only the component of the initial spin along the magnetic field in the particle's rest frame (a scalar) is relevant—giving nine variables total. Pre-tabulating such a high-dimensional function would require an impractically large amount of storage and memory. Moreover, accurately sampling this multidimensional distribution via Monte Carlo methods would necessitate an unfeasibly large number of macro-particles, rendering the algorithm computationally intractable.

To address these challenges, our approach employs conditional probabilities to determine unknown quantities sequentially, rather than sampling all variables simultaneously. Specifically, the algorithm first determines the momentum transfer ratio λ, given the initial χ_e and spin $\boldsymbol{s}_i$, using a spectrum averaged over all possible final lepton spins and photon polarizations, $S(\chi_e, \boldsymbol{s}_i, \lambda)$. Next, having fixed λ, we determine the final lepton spin $\boldsymbol{s}_f$ (still averaged over photon polarizations), using $S(\chi_e, \boldsymbol{s}_i, \lambda, \boldsymbol{s}_f)$. Finally, the photon polarization state $\boldsymbol{\xi}$ is selected based on the full spectrum $S(\chi_e, \boldsymbol{s}_i, \lambda, \boldsymbol{s}_f, \boldsymbol{\xi})$, given the previously determined quantities. This hierarchical, conditional sampling process is outlined in Figure 3.1, with detailed implementation discussed in the following section.

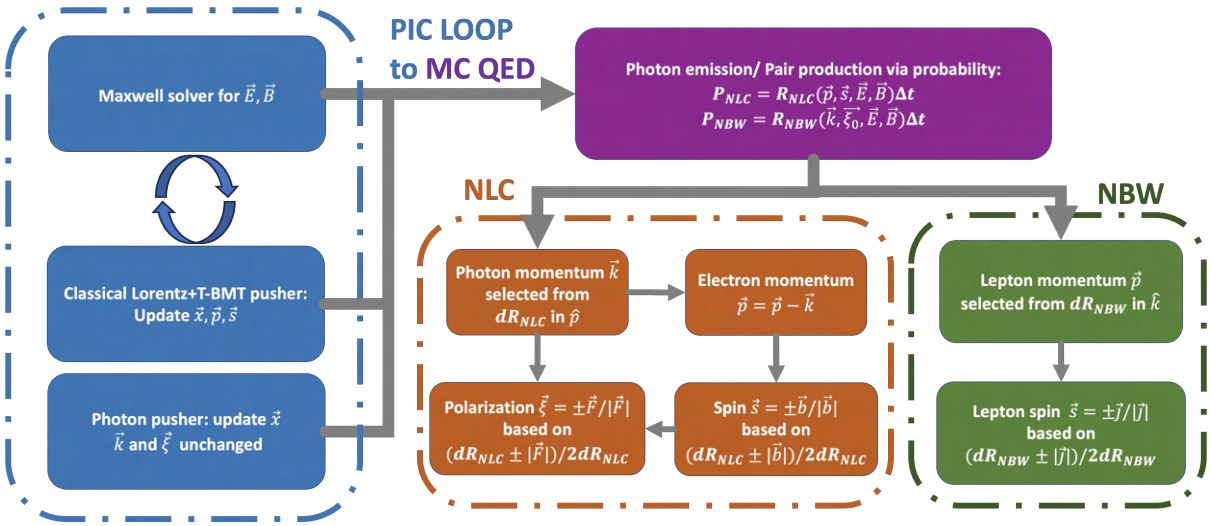

Figure 3.1: Flow chart for spin-polarized QED algorithm

3.2.1 Spin and Polarization Dependent NLCS Implementation

A detailed flow chart of the algorithm for the quantum radiation process with spin and polarization effects is presented in Fig. 3.2. The code integrates a Monte Carlo-based quantum process into the main PIC loop. At each time step, the position, momentum, and spin of each lepton are updated through the classical Lorentz pusher and the T-BMT spin pusher. The quantum parameter χ_e is then calculated for each lepton. Additionally, the direction of the magnetic field in the particle's rest frame, denoted by $\hat{\boldsymbol{\beta}}$, is determined, since the spin-dependent quantum emission rate depends solely on the component of the initial spin along this direction. We only precompute spin-dependent quantum emission rates for cases where the initial spin is fully aligned or anti-parallel ($W_\uparrow/W_\downarrow$) to the rest frame magnetic field. The emission rate for an arbitrary spin projection s_β can then be obtained as a linear combination of these two pre-tabulated rates:

$$W_{s_i} = W_\uparrow \frac{1 + \boldsymbol{s}_i \cdot \hat{\boldsymbol{\beta}}}{2} + W_\downarrow \frac{1 - \boldsymbol{s}_i \cdot \hat{\boldsymbol{\beta}}}{2} \tag{3.2}$$

A random number $r_1 \in [0, 1]$ is generated and compared to the quantum radiation probability to determine whether a quantum radiation event occurs. If the event takes place, the next step is to sequentially determine the momentum transfer ratio λ, the post-radiation spin state, and the polarization state of the emitted photon, as previously described.

The first quantity to be sampled is the momentum transfer ratio, $\lambda = \hbar\omega/E$. The spectrum employed for this step incorporates the dependence on the initial spin projection along the rest-frame magnetic field, s_β, but averages over the final spin and photon polarization states. For efficient sampling, we tabulate the inverse cumulative distribution function (ICDF) of the photon spectrum. A second random number, $r_2 \in [0, 1]$, is generated and used as the input to the ICDF, representing a cumulative probability. The ICDF then returns the value of λ corresponding to the specified r_2.

Ideally, we would tabulate the ICDF for all possible values of s_β, yielding a three-

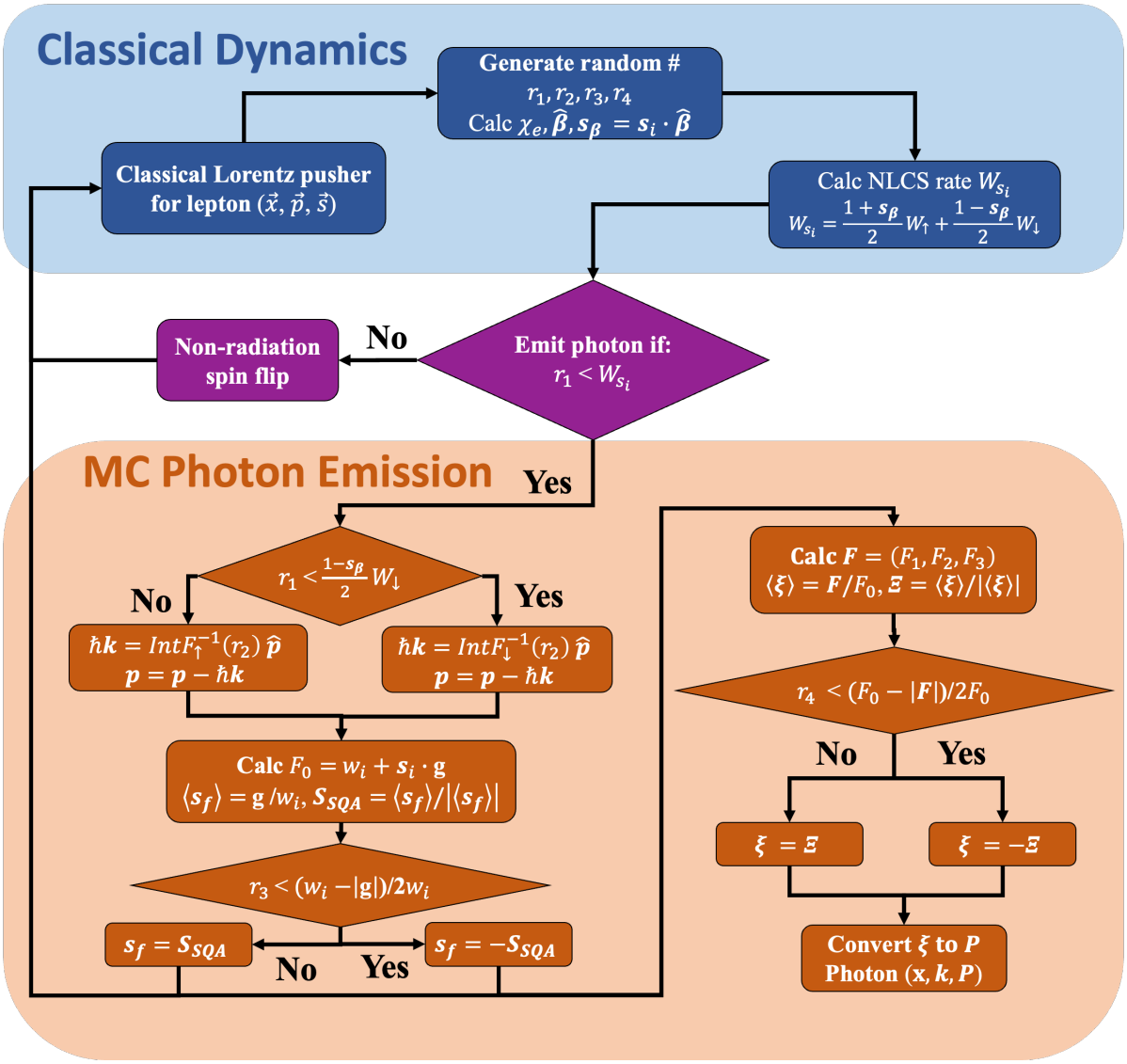

Figure 3.2: Flow chart for spin-polarized NLCS algorithm

dimensional table. However, this approach would substantially increase memory requirements. To optimize storage and computational efficiency, we instead precompute the ICDF only for the cases where the initial spin is fully aligned or anti-parallel to the rest-frame magnetic field ($IntF_\uparrow^{-1}/IntF_\downarrow^{-1}$). Unlike the emission rates, the ICDF for an arbitrary s_β cannot be reconstructed as a linear combination of these two cases. To resolve this, we make use of the previously generated random variable r_1, employing it as a criterion to select between the two precomputed ICDF spectra—aligned or anti-parallel—for the sampling of

λ:

$$\begin{cases} \text{if } \; r_1 < W_{\downarrow}\frac{1-\boldsymbol{s}_i\cdot\hat{\boldsymbol{\beta}}}{2}, \quad \lambda = IntF_{\uparrow}^{-1}(r_2) \\ \text{if } \; W_{\downarrow}\frac{1-\boldsymbol{s}_i\cdot\hat{\boldsymbol{\beta}}}{2} < r_1 < W_{s_i}, \quad \lambda = IntF_{\uparrow}^{-1}(r_2) \end{cases} \tag{3.3}$$

While this selection scheme is not fully rigorous from a statistical standpoint, it produces results that do not significantly deviate from the actual ICDF spectrum for a given $s_{\boldsymbol{\beta}}$.

Once the momentum transfer ratio λ has been determined, the momentum of the emitted photon can be assigned. Under the ultra-relativistic approximation, the direction of the emitted photon is assumed to align with the lepton's initial momentum, which gives $\hbar\boldsymbol{k} = \boldsymbol{p}_i\lambda$. Consequently, the post-emission lepton momentum is simply $\boldsymbol{p}_f = \boldsymbol{p}_i(1-\lambda)$.

The next step is to determine the final spin state of the lepton following emission. Given the quantum parameter χ_e, the direction of the rest-frame magnetic field, the initial spin, and the momentum transfer ratio λ, we obtain the probability distribution for the lepton's final spin state:

$$F_0(\chi, \boldsymbol{s}_i, \lambda; \boldsymbol{s}_f) = w_i + \boldsymbol{s}_f \cdot \boldsymbol{g} \tag{3.4}$$

The explicit forms of w_i and g are provided in Appendix A.1. It is important to note that the function F_0 depends not only on the initial spin component along the rest-frame magnetic field, but also on the components $\boldsymbol{s}_\varepsilon$ and $\boldsymbol{s}_\kappa$. The value of F_0 determines the likelihood of each possible final spin state: a higher F_0 corresponds to a higher probability of realizing that particular spin state. From this distribution, F_0, we can then compute the expectation value (mean) of the final spin state:

$$\langle \boldsymbol{s}_f \rangle = \frac{\int \boldsymbol{s}'_f F_0 d\boldsymbol{s}'_f}{\int F d\boldsymbol{s}'_f} = \boldsymbol{g}/w_i \tag{3.5}$$

Ideally, one would sample the complete distribution of possible final spin states as a function of χ_e, $\boldsymbol{s}_i$, and λ. However, accurately capturing this distribution requires a substantial

number of simulation particles, which can become computationally prohibitive given that sampling the main spectrum is already resource-intensive.

To address this, we simplify the determination of the final spin state by assigning it the expectation value under the distribution F_0; that is, we set $\boldsymbol{s}_f = \langle \boldsymbol{s}_f \rangle$. If it is desirable to maintain the spin length at unity throughout the simulation, we instead use the normalized expectation value as the spin quantization axis, namely $\boldsymbol{S}_{\mathrm{SQA}} = \langle \boldsymbol{s}_f \rangle / |\langle \boldsymbol{s}_f \rangle|$. A random number $r_3 \in [0, 1]$ is then generated, and used to decide whether the spin after emission is aligned or anti-aligned with this quantization axis:

$$\begin{cases} \text{if} \quad r_3 < (w_i - |g|)/2w_i, \quad \boldsymbol{s}_f = -\boldsymbol{S}_{SQA} \\ \text{if} \quad r_3 > (w_i - |g|)/2w_i, \quad \boldsymbol{s}_f = \boldsymbol{S}_{SQA} \end{cases} \tag{3.6}$$

Finally, we decide what the polarization state is, represented by the Stokes parameter $\boldsymbol{\xi}$ of the photon. Given the quantum parameter of lepton χ_e, initial spin $\boldsymbol{s_i}$, final spin $\boldsymbol{s_f}$, and the momentum transfer ratio λ, we can obtain the probability distribution of the photon polarization state:

$$F_{full}(\chi, \boldsymbol{s}_i, \boldsymbol{s}_f, \lambda; \boldsymbol{\xi}) = F_0 + \boldsymbol{\xi} \cdot \boldsymbol{F} \tag{3.7}$$

The detailed expression of $\boldsymbol{F}$ can be seen in the appendix. Similarly to how we decide the final spin state, we first look at the mean of all possible photon polarization states under this distribution F_{full}:

$$\langle \boldsymbol{\xi} \rangle = \frac{\int F_{full} \boldsymbol{\xi}' d\boldsymbol{\xi}'}{\int F_{full} d\boldsymbol{\xi}'} = \boldsymbol{F}/F_0 \tag{3.8}$$

For similar reasons as with the final spin state assignment, we set the photon polarization state to the expectation value under the distribution F, that is, $\boldsymbol{\xi} = \boldsymbol{F}/F_0$. If it is necessary for each macro-photon to be $|\boldsymbol{\xi}| = 1$, we instead define the polarization quantization axis as $\boldsymbol{\Xi}_{\mathrm{PQA}} = \langle \boldsymbol{\xi} \rangle / |\langle \boldsymbol{\xi} \rangle|$, which is a superposition of linear, diagonal, and circular polarization

components, but as a pure state. A random number $r_4 \in [0,1]$ is then generated to determine whether the photon polarization state aligns with $\boldsymbol{\Xi}_{\mathrm{PQA}}$ or $-\boldsymbol{\Xi}_{\mathrm{PQA}}$:

$$\begin{cases} \text{if} \quad r_4 < \frac{F_0 - |\boldsymbol{F}|}{2F_0}, & \boldsymbol{s}_f = -\boldsymbol{\Xi}_{PQA} \\ \text{if} \quad r_4 > \frac{F_0 - |\boldsymbol{F}|}{2F_0}, & \boldsymbol{s}_f = \boldsymbol{\Xi}_{PQA} \end{cases} \tag{3.9}$$

The polarization vector $\boldsymbol{\xi}$ determined above specifies the photon's polarization state in the emission basis $(\hat{\boldsymbol{\varepsilon}}, \hat{\boldsymbol{\beta}}, \hat{\boldsymbol{k}})$ in which the photon is generated. However, to analyze the photon's polarization at the point of observation—particularly when it interacts with external electromagnetic fields—it is necessary to transform the Stokes parameters from the emission frame to the observation (or laboratory) frame. This transformation requires knowledge of both the Stokes parameters at emission and the polarization basis at that instant.

To minimize computational memory usage, we aim to reduce the number of parameters needed to fully specify the photon polarization state. We find that the polarization state can be uniquely represented by a single vector quantity, the photon polarization vector $\boldsymbol{P} = (P_{\psi_1}, P_{\psi_2}, P_k)$, whose components correspond to the $(\hat{\boldsymbol{\psi}}_1, \hat{\boldsymbol{\psi}}_2, \hat{\boldsymbol{k}})$ coordinate axes. The definitions of these coordinates and their connection to the Stokes parameters have already been discussed in Section 2.10.2.

Through the procedure described above, we have developed a fully spin- and polarization-resolved NLCS algorithm compatible with the PIC loop. Finally, in accordance with the conditional probability structure of our Monte Carlo approach [121, 145], the electron's spin is also carefully updated in cases where emission does not occur. In a later section, we will provide a detailed discussion of the treatment of spin for non-radiative events.

3.2.2 Spin and Polarization Dependent NBW Implementation

A detailed flow chart illustrating the spin- and polarization-dependent quantum radiation process for the NBW algorithm is presented in Fig. 3.3. The dynamics of photons in the classical PIC loop are considerably simpler than those for charged particles: each photon

is treated as effectively a point particle (a wavepacket with small extent) that propagates along its momentum direction at the speed of light in vacuum, while both its momentum and polarization vectors remain unchanged.

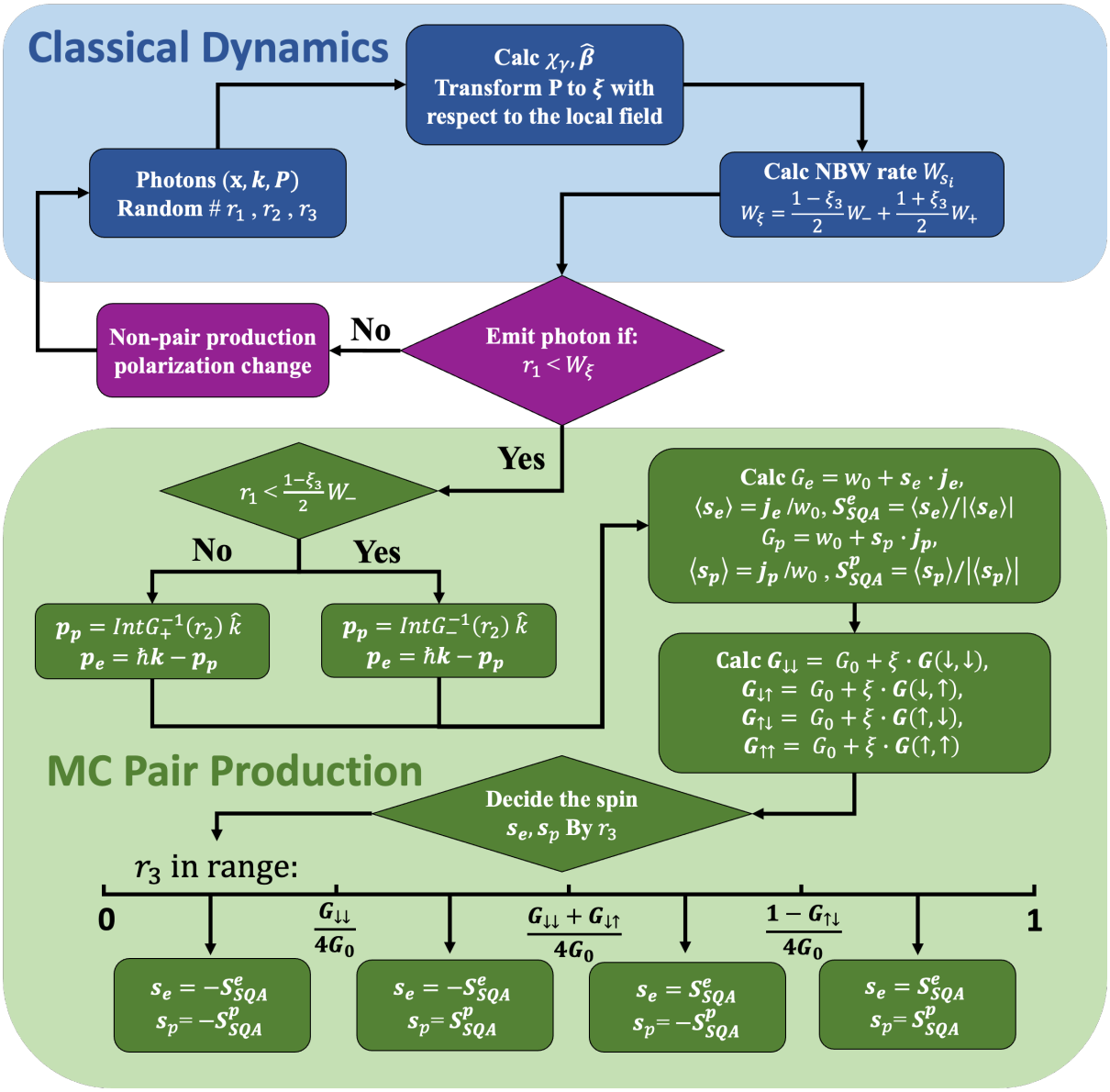

Figure 3.3: Flow chart for spin-polarized NBW algorithm

In the quantum calculations, the electromagnetic field experienced by each photon is monitored at every simulation step, allowing the quantum parameter χ_γ to be computed. For each photon, the polarization basis vectors $\hat{\boldsymbol{\varepsilon}}$, $\hat{\boldsymbol{\beta}}$, and $\hat{\boldsymbol{\kappa}}$ are constructed with respect to

the local field. The photon polarization vector is then projected onto this basis to extract the Stokes parameters corresponding to the photon's polarization state in the given field.

The polarization-resolved NBW pair-production rate depends on both the quantum parameter χ_γ and the linear Stokes parameter ξ_3 of the photon, with ξ_3 taking values between -1 and $+1$. For computational efficiency, we pre-tabulate the NBW rates only for the cases where the linear Stokes parameter is either $+1$ or -1 (W_+ and W_-). The rate for arbitrary ξ_3 is then obtained by a linear combination of these two pre-tabulated rates:

$$W_\xi = \frac{1-\xi_3}{2} W_- + \frac{1+\xi_3}{2} W_+ \tag{3.10}$$

A random number $r_1 \in [0,1]$ is generated and compared with the NBW pair production probability to determine whether a pair creation event occurs. If the event takes place, it is then necessary to determine the momentum transfer ratio λ between the positron and the photon, as well as the spin states of the generated electron and positron.

Analogously to the procedure for NLCS, the first quantity to be sampled is the momentum partition ratio, defined as $\lambda = |\boldsymbol{p}_p|/\hbar k$, where $\boldsymbol{p}_p$ is the positron momentum and $\hbar k$ is the incident photon momentum. The energy spectrum utilized in this step incorporates the dependence on the photon's polarization—specifically, only the linear Stokes parameter ξ_3—and is averaged over all possible spin states of the generated pair.

For efficient sampling, we tabulate the inverse cumulative distribution function (ICDF) for the positron spectrum. A second random number $r_2 \in [0,1]$ is generated and serves as the input for the ICDF, representing the cumulative probability. The ICDF yields the corresponding value of the momentum transfer ratio λ for the chosen r_2.

To minimize the computational memory requirements, we precompute the ICDF only for photons with linear polarization $\xi_3 = +1$ and $\xi_3 = -1$ ($IntG_+^{-1}/IntG_-^{-1}$). Following a procedure analogous to that used in the NLCS algorithm, we use the previously generated random value r_1 to select which ICDF -corresponding to $\xi_3 = +1$ or $\xi_3 = -1$ - will be used to sample the momentum transfer ratio λ.

$$\begin{cases} \text{if } \ r_1 < \frac{1-\xi_3}{2} W_-, \quad \lambda = IntG_-^{-1}(r_2) \\ \text{if } \ \frac{1-\xi_3}{2} W_- < r_1 < W_\xi, \quad \lambda = IntG_+^{-1}(r_2) \end{cases} \tag{3.11}$$

Once the momentum transfer ratio λ has been determined, the momenta of the generated electron and positron can be assigned. Under the ultra-relativistic approximation, the directions of the produced pairs are assumed to align with the incident photon's momentum. Thus, the positron momentum is given by $\boldsymbol{p}_p = \hbar \boldsymbol{k} \lambda$, while the electron momentum is $\boldsymbol{p}_e = \hbar \boldsymbol{k}(1-\lambda)$. In the NBW process, the photon transfers all of its momentum to the electron-positron pair and decays away.

The subsequent step is to determine the spin states of the generated electron and positron. Since their spin states are inherently correlated, the algorithm samples both quantities simultaneously. This is achieved by first evaluating the probability distribution of the electron's spin (averaged over all possible positron spin states) and the probability distribution of the positron's spin (averaged over all possible electron spin states), both conditioned on the previously determined momentum transfer ratio.

$$G_e(\chi, \boldsymbol{\xi}, \lambda; \boldsymbol{s}_e) = w_0 + \boldsymbol{s}_e \cdot \boldsymbol{j}_e \tag{3.12}$$

$$G_p(\chi, \boldsymbol{\xi}, \lambda; \boldsymbol{s}_p) = w_0 + \boldsymbol{s}_p \cdot \boldsymbol{j}_p \tag{3.13}$$

The detailed expression for w_0, $\boldsymbol{j}_e$, $\boldsymbol{j}_p$ can be found in the appendix A.2. One thing worth to mention is that function $\boldsymbol{j}_e$ and $\boldsymbol{j}_p$ depend not only just the linear polarization component $\boldsymbol{\xi}_3$, but other component $\boldsymbol{\xi}_1$ and $\boldsymbol{\xi}_2$ as well. The expectation value of the electron and positron spin is:

$$\langle \boldsymbol{s}_e \rangle = \frac{\int G_e \boldsymbol{s}'_e d\boldsymbol{s}'_e}{\int G_e d\boldsymbol{s}'_e} = \boldsymbol{j}_e / w_0 \tag{3.14}$$

$$\langle \boldsymbol{s}_p \rangle = \frac{\int G_p \boldsymbol{s}'_p d\boldsymbol{s}'_p}{\int G_p d\boldsymbol{s}'_p} = \boldsymbol{j}_p / w_0 \tag{3.15}$$

The spin quantization axes for the electron and positron in the NBW process are defined as $\boldsymbol{S}^e_{\rm SQA} = \langle \boldsymbol{s}_e \rangle / |\langle \boldsymbol{s}_e \rangle|$ and $\boldsymbol{S}^p_{\rm SQA} = \langle \boldsymbol{s}_p \rangle / |\langle \boldsymbol{s}_p \rangle|$, respectively. For computational simplicity, we assign the electron and positron spins to be either fully aligned or anti-aligned with their respective expectation values along these axes. This approach allows us to efficiently sample the correlated spin states according to their associated probabilities:

$$G_{\downarrow\downarrow} = G_0(\downarrow,\downarrow) + \boldsymbol{\xi} \cdot \boldsymbol{G}(\downarrow,\downarrow) \tag{3.16}$$

$$G_{\downarrow\uparrow} = G_0(\downarrow,\uparrow) + \boldsymbol{\xi} \cdot \boldsymbol{G}(\downarrow,\uparrow) \tag{3.17}$$

$$G_{\uparrow\downarrow} = G_0(\uparrow,\downarrow) + \boldsymbol{\xi} \cdot \boldsymbol{G}(\uparrow,\downarrow) \tag{3.18}$$

$$G_{\uparrow\uparrow} = G_0(\uparrow,\uparrow) + \boldsymbol{\xi} \cdot \boldsymbol{G}(\uparrow,\uparrow) \tag{3.19}$$

Here, the first arrow denotes the spin state of the generated positron, while the second arrow corresponds to the spin state of the generated electron. The labels $\uparrow$ and $\downarrow$ indicate whether the spins are aligned or anti-aligned with respect to their respective spin quantization axes. The Monte Carlo method is then employed to determine the spin states of the electron-positron pair. Specifically, a random number $r_3 \in [0,1]$ is generated:

$$\begin{cases} \text{if } \ r_3 < \frac{G_{\downarrow\downarrow}}{4G_0}, \quad \boldsymbol{s}_p = -\boldsymbol{S}^p_{SQA},\ \boldsymbol{s}_e = -\boldsymbol{S}^e_{SQA} \\ \text{if } \ \frac{G_{\downarrow\downarrow}}{4G_0} < r_3 < \frac{G_{\downarrow\downarrow}+G_{\uparrow\downarrow}}{4G_0}, \quad \boldsymbol{s}_p = -\boldsymbol{S}^p_{SQA},\ \boldsymbol{s}_e = \boldsymbol{S}^e_{SQA} \\ \text{if } \ \frac{G_{\downarrow\downarrow}+G_{\uparrow\downarrow}}{4G_0} < r_3 < \frac{1-G_{\uparrow\uparrow}}{4G_0}, \quad \boldsymbol{s}_p = \boldsymbol{S}^p_{SQA},\ \boldsymbol{s}_e = -\boldsymbol{S}^e_{SQA} \\ \text{if } \ r_3 > \frac{1-G_{\uparrow\uparrow}}{4G_0}, \quad \boldsymbol{s}_p = \boldsymbol{S}^p_{SQA},\ \boldsymbol{s}_e = \boldsymbol{S}^e_{SQA} \end{cases} \tag{3.20}$$

At the end of the calculation, the photon involved in the process is removed from the simulation, and the newly generated electron-positron pair is incorporated into the PIC loop. Through the procedure detailed above, we establish a fully spin- and polarization-resolved NBW algorithm that is seamlessly integrated with the PIC framework.

It is also important to note that, analogous to the treatment in the NLCS process, the

photon polarization distribution must be updated in the case of a non-pair creation event. This adjustment is necessary because the NBW process preferentially depletes photons with linear polarization $\xi_3 = 1$. Accordingly, the photon's Stokes parameter is projected along or opposite to the polarization quantization axis whenever pair production does not occur. The detailed treatment of photon polarization in non-pair production events will be discussed in a later section.

It is also worth noting that for certain scenarios where the magnetic field direction does not rotate, for example a uniform magnetic field or linearly polarized laser field, a reduced model may be used. This is given in Appendix B.

3.3 Quantum Non-Transition Event

In the Monte Carlo algorithm, for a given initial spin/polarization state, the spin/polarization resolved rate can be expressed as:

$$\mathbb{P} = \langle \mathbb{P} \rangle + \mathbf{P}_i \cdot \boldsymbol{\zeta}_i \,, \tag{3.21}$$

where $\langle \mathbb{P} \rangle$ is the average spin/polarization rate, $\mathbf{P}_i \cdot \boldsymbol{\zeta}_i$ is the spin/polarization-related transition rate for a given initial state. One crucial point that is somewhat counterintuitive is that the selection effect of the spin/polarization-dependent rate will actually change the polarization state for the macroparticles that do not have the transition. It is easy to assume that the spin state for non-transition particles is just their initial spin state. However, this is not correct. We need to treat carefully the macroparticles that do not undergo quantum transitions:

The probability that the transition does not occur in a time interval dt is $1 - (\langle \mathbb{P} \rangle + \mathbf{P}_i \cdot \boldsymbol{\zeta}_i)$. Consider an ensemble (one macro-particle) of N (real) particles having the polarization vector $\boldsymbol{\zeta}_{i,n}$, which $n = 1, 2, \ldots, N$. Each of this is a unit vector $|\boldsymbol{\zeta}_{i,n}| = 1$. The initial spin/polarization for this macro-particle is then $\boldsymbol{\zeta}_i = \langle \boldsymbol{\zeta}_{i,n} \rangle$.

We can rewrite the transition rate related to the initial polarization state $\boldsymbol{P}_i = P_i \boldsymbol{Q_i}$. $\boldsymbol{Q_i}$ is the quantization axis, which for a lepton is the rest frame B field direction $\hat{\boldsymbol{\beta}}$, and for a photon it is the linear polarization component $\boldsymbol{\xi}_3$. The final polarization state for the Marco particle for the non-quantum transition event along $\boldsymbol{Q_i}$ is then:

$$\begin{aligned}\sum_n \sum_{\pm} \pm \frac{1 \pm \boldsymbol{Q}_i \cdot \boldsymbol{\zeta}_{i,n}}{2} [1 - (\langle \mathbb{P} \rangle \pm \mathbf{P}_i \cdot \boldsymbol{Q_i}) \Delta t] &= \sum_n [\boldsymbol{Q_i} \cdot \boldsymbol{\zeta}_{i,n} (1 - \langle \mathbb{P} \rangle \Delta t) - \mathbf{P}_i \cdot \boldsymbol{Q_i}] \\ &= N \boldsymbol{Q_i} \cdot [\boldsymbol{\zeta}_i (1 - \langle \mathbb{P} \rangle \Delta t) - \boldsymbol{P}_i \Delta t]\end{aligned} \tag{3.22}$$

The total number of real particles inside that macroparticle without transition is $N[1 - (\langle \mathbb{P} \rangle + \mathbf{P}_i \cdot \boldsymbol{\zeta}_i) \Delta t]$. The final polarization vector for the macroparticle is then:

$$\boldsymbol{\zeta}_{f,\ \text{no trans}} = \frac{\boldsymbol{\zeta}_i (1 - \langle \mathbb{P} \rangle \Delta t) - \mathbf{P}_i \Delta t}{1 - (\langle \mathbb{P} \rangle + \mathbf{P}_i \cdot \boldsymbol{\zeta}_i) \Delta t} \tag{3.23}$$

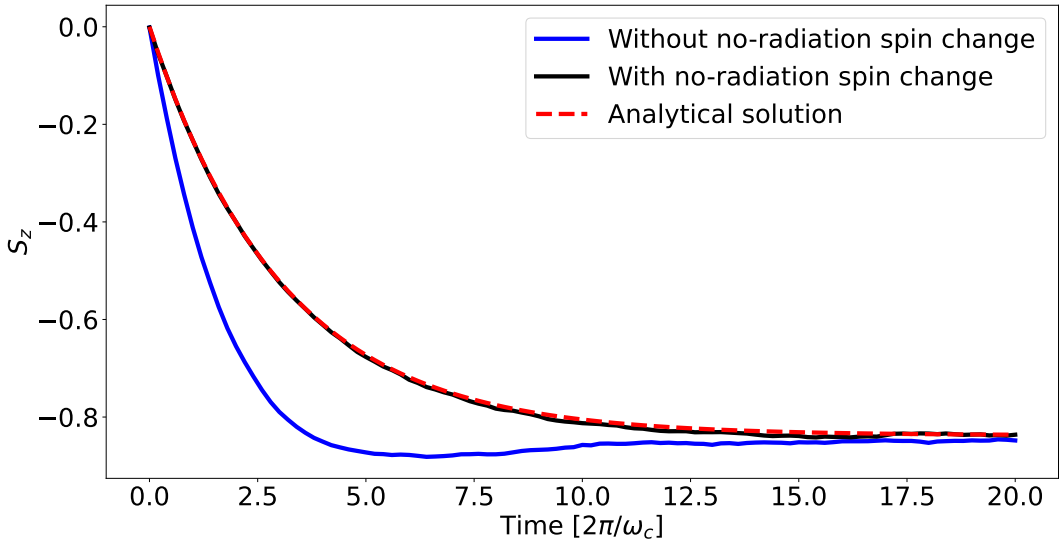

Figure 3.4: The influence of no-quantum radiation correction to the lepton spin evolution

The influence of the non-quantum transition event can be illustrated by two examples here. In the first example, an unpolarized, mono-energetic, 1 GeV lepton beam gyrates inside a constant magnetic field with a field strength equal to 2.26 MT. The field and the

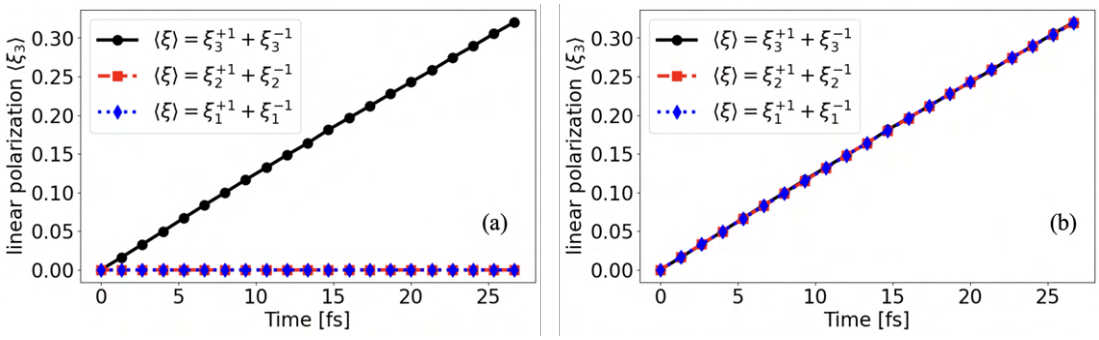

Figure 3.5: (a) The evolution of linear polarization state, calculated without non-pair creation polarization state change. (b) The evolution of the linear polarization state, calculated with non-pair creation polarization state change. The unpolarized beams in the simulation were constructed here from two identical parts with opposite polarization states. The black curve is for opposite linear polarization states, the red curve is for opposite circular polarization states, and the blue curve is for opposite diagonal polarization states initially.

momentum are perpendicular, the electron quantum parameter $\chi_e = 1$. We ignore radiation back-reaction for simplicity. The evolution of spin along the magnetic field direction is shown in Fig. 3.4. The blue curve shows the spin evolution without including the non-emission spin change; the black curve is the result when the non-emission spin change is taken into account. The red dashed curve is from the analytical solution of the Sokolov-Ternov effect, shown in the next section in Eq. 3.24. We can see that the blue curve without the non-emission spin change deviates from the analytical solution, whereas the black curve, including the non-emission spin change, agrees well with the analytical solution.

In the second example, we construct an unpolarized photon beam with two equivalent parts that are at the same location and have the same momentum distribution and beam profiles. These two parts are either fully linearly polarized, diagonally polarized, or circularly polarized, but have opposite polarization states initially. As a result, the average polarization state for these two parts in total will be zero. These constructed beams are mono-energetic with an initial energy equal to 1 GeV and travel inside a constant magnetic field with a field strength equal to 2.26 MT. The field and the momentum are perpendicular, the photon quantum parameter $\chi_\gamma = 1$. For simplicity, the generated electron-positron pair is excluded from the quantum process calculation. The evolution of the degree of linear polarization is

shown in Fig. 3.5 (a) and (b), where the black curve is for when this unpolarized beam is constructed by two parts with opposite linear polarization states, the red curve is when the two parts have opposite circular polarization states, and then the blue curve is when the two parts have opposite diagonal polarization states, initially. Fig. 3.5 (a) is when we don't include the non-pair creation polarization state change, and we can see that the degree of linear polarization for three "unpolarized beams" evolves very differently with time. Fig. 3.5 (b) is when we include the non-pair creation polarization state change, and we can see that the degree of linear polarization for the three "unpolarized beams" evolves exactly the same with time. This result underscores the importance of employing a model in which the time evolution of "unpolarized beams" is consistent, regardless of their initial construction—at least in an average sense. Ensuring such consistency is, in our view, essential for developing a reliable and robust model.

3.4 Code Verification

Ensuring the correct numerical implementation of all quantum processes is essential. To validate this, we first compare the NLC and NBW spectra generated by the code for various quantum parameters χ_e/χ_γ and initial lepton spin or photon polarization states against the corresponding closed-form expressions. In the figures, the orange and blue curves represent simulation results, while the purple and red dashed curves show the analytical, spin- and polarization-resolved NLC and NBW spectra.

3.4.1 NLCS Photon Spectrum for Different Spin-Polarized Lepton

We examine the gamma-ray spectrum produced by a monoenergetic electron beam in a constant magnetic field via the NLCS process. To isolate the quantum effects, we neglect all classical dynamics—including the Lorentz force and spin precession—as well as the effects of radiation reaction and radiation-induced lepton spin changes. Our analysis begins with

unpolarized electron beams.

We tested the spectrum for electron quantum parameters $\chi = 0.1, 1, 10$, and 99, and compared our simulation results to the corresponding closed-form expressions, as shown in Fig. 3.6. The case for $\chi = 0.01$ is discussed in the next section 3.5.2, since this low value allows comparison with the polarization-resolved classical radiation spectrum.

Under these conditions, the emitted photons exhibit only linear polarization. In the figure, the blue curve corresponds to photons with linear polarization component $\xi_3 < 0$, while the orange curve represents $\xi_3 > 0$, both derived from our simulations. Both curves show excellent agreement with the analytical results. The code verification for other spin polarized conditions can be found in appendix C.

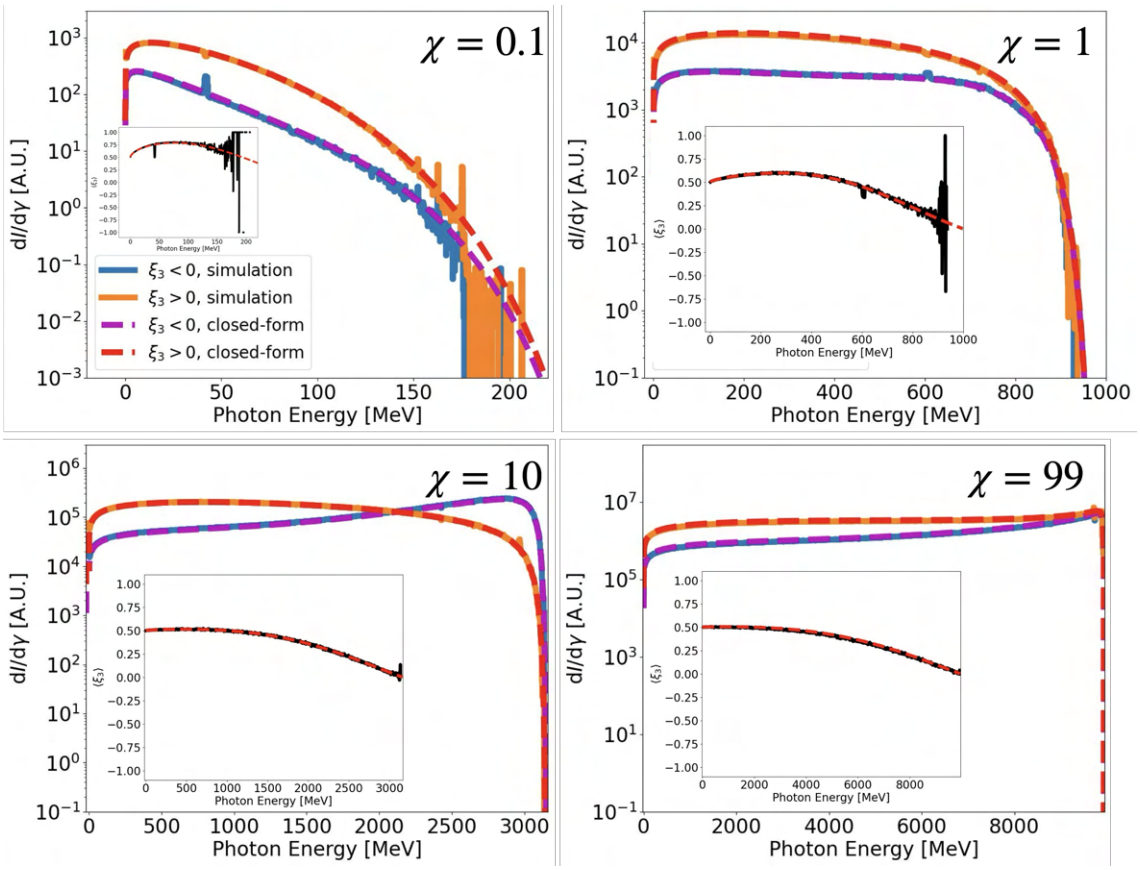

Figure 3.6: Benchmark of linearly polarized (ξ_3) photon spectrum from the NLC process for an unpolarized lepton beam inside a constant magnetic field. The classical particle dynamics, radiation back reaction, and radiation-induced spin change are all switched off for simplicity. We scan the spectrum through $\chi = 0.1$, $\chi = 1$, $\chi = 10$ and $\chi = 99$.

3.4.2 NBW Pair Production Spectrum for Different Polarized Photon

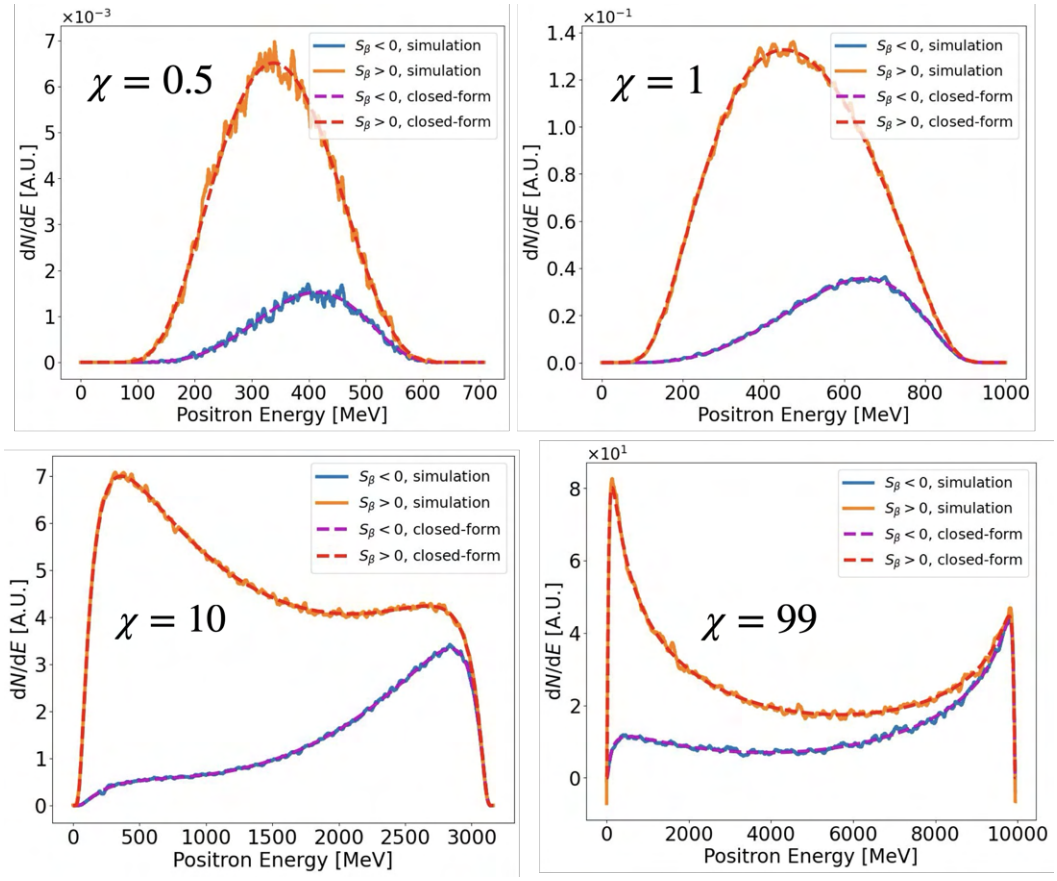

Figure 3.7: Benchmark of positron spectrum for spin component S_β from the NBW process for an unpolarized photon beam inside a constant magnetic field. The classical particle dynamics, radiation back reaction, and radiation-induced spin change are all switched off for simplicity. We scan the spectrum through $\chi = 0.5$, $\chi = 1$, $\chi = 10$ and $\chi = 99$.

For the NBW process, we examine the positron spectrum generated by a monoenergetic photon beam propagating in a constant magnetic field. To facilitate direct comparison, we disregard classical dynamics—such as the Lorentz force and spin precession—as well as the effects of radiation reaction and radiation-induced spin changes in the generated leptons. Our analysis begins with an unpolarized photon beam.

We evaluated the positron spectra for photon quantum parameters $\chi_\gamma = 0.5, 1, 10$, and 99, and compared the simulation results to the corresponding closed-form expressions, as

shown in Fig. 3.7. For an unpolarized photon beam, the generated positron's spin can only be in the direction of the magnetic field in its rest frame, according to Eq. (2.102), so we only plot the spectrum for spin component $S_\beta < 0$ or $S_\beta > 0$. The blue curve depicts the positron spectrum with spin component $S_\beta < 0$ along the magnetic field direction, while the orange curve corresponds to $S_\beta > 0$, as obtained from the simulations. Both spectra show excellent agreement with the analytical results. The code verification for other polarization conditions can be found in appendix C.

3.5 Code Validation

In this section, we present benchmark tests of our spin- and polarization-resolved QED code across a variety of scenarios. The simulation results show excellent agreement with analytical predictions as well as with previously published results. These benchmarks provide further validation of the accuracy and robustness of our algorithm.

3.5.1 Sokolov Ternov Effect

To benchmark our code's performance, we first reproduce the well-known Sokolov-Ternov effect, which describes the self-polarization process of relativistic electrons or positrons traversing a magnetic field at high energies. This effect arises because the transition rates between spin states aligned and anti-aligned with the magnetic field differ, resulting in net polarization of the lepton beam either parallel or antiparallel to the field.

We begin with a two-dimensional PIC simulation: an initially unpolarized, monochromatic 1 GeV electron beam is initialized moving in the x-y plane. A constant magnetic field of 2.26 MT is applied in the z-direction throughout the simulation domain. For this benchmark, radiation reaction and pair production are disabled, so the particle energy remains constant, allowing for direct comparison between the simulation results and the analytical prediction given by Eq. 3.24.

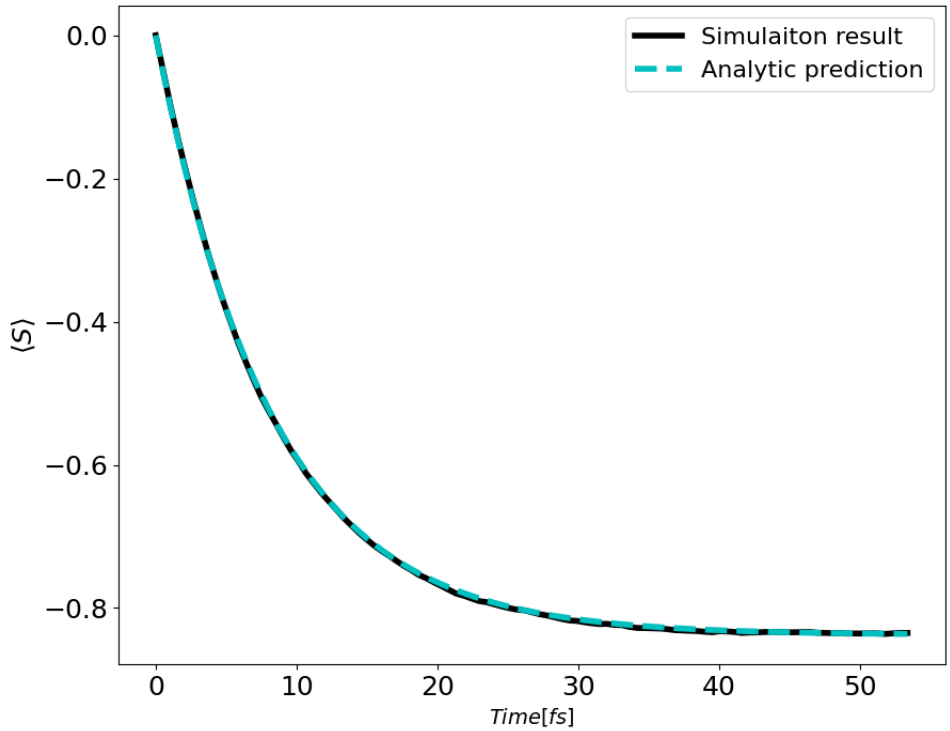

Figure 3.8: The spin evolution along magnetic field direction for a 1 GeV beam inside a 2.26 MT constant magnetic field. Radiation back-reaction is switched off for simplicity. The simulation result is compared with the well-known Sokolov-Ternov effect prediction.

$$\frac{dS_\beta}{dt} = -P(\psi_1(\chi)S_\beta + \psi_3(\chi)) \tag{3.24}$$

Here, $P = \frac{\alpha_f m_e c^2}{\sqrt{3}\gamma\hbar\omega_L}$, $\psi_1(\chi) = \int_0^\infty u''du, K_{2/3}(u')$, $\psi_3(\chi) = \int_0^\infty u''du K_{1/3}(u')$, with $u'' = u^2/(1+u)^3$, $u' = 2u/(3\chi)$, and $u = \hbar\omega/(\gamma - \hbar\omega)$. The Sokolov-Ternov effect specifically describes spin polarization along the magnetic field direction in the particle's rest frame, so our analysis focuses on the time evolution of the S_β component. As shown in Fig. 3.8, the simulation results exhibit excellent agreement with the analytical prediction.

3.5.2 Comparing with Classical Polarization Spectrum

The polarization-resolved spectrum for classical synchrotron radiation is well established. It is therefore natural to ask whether the quantum calculation converges to the classical result

in the limit of a low quantum parameter, χ. Figure 3.9 presents the polarized photon spectrum obtained from our simulation and compares it with the analytical classical synchrotron radiation spectrum for $\chi_e = 0.01$.

The simulation is performed in two dimensions, using a monoenergetic, unpolarized electron beam propagating in a constant magnetic field. We neglect all classical dynamics—including the Lorentz force and spin precession—as well as radiation reaction and radiation-induced lepton spin changes.

The classical radiation spectrum is given by:

$$W_{\sigma,\pi} = \frac{9\sqrt{3}}{16\pi} u' W^{cl} \left[(l_\sigma^2 + l_\pi^2) \int_{u'}^{\infty} K_{5/3}(x)dx + (l_\sigma^2 - l_\pi^2) K_{2/3}(u') \right] \tag{3.25}$$

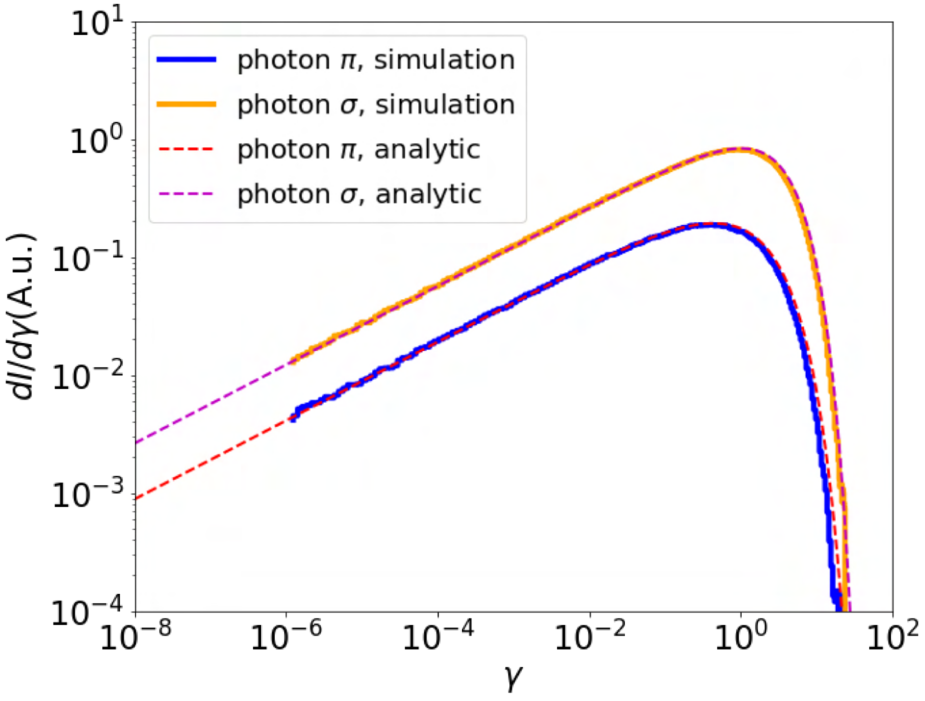

Figure 3.9: π and σ polarized photon spectrum from the simulation (blue and yellow solid line) compared with the classical radiation equations (red and purple dashed line) when $\chi = 0.01$.

Which if photon is polarized in σ direction, $l_\sigma = 1$ and $l_\pi = 0$, otherwise if it is polarized in π direction, $l_\sigma = 0$ and $l_\pi = 1$. $W^{cl} = \frac{2}{3}\frac{e^2 c}{R}\gamma^4$ is the total radiation energy of an ultra-

relativistic electron. R is the gyro-radius. The simulation result shows good agreement with the analytic calculation.

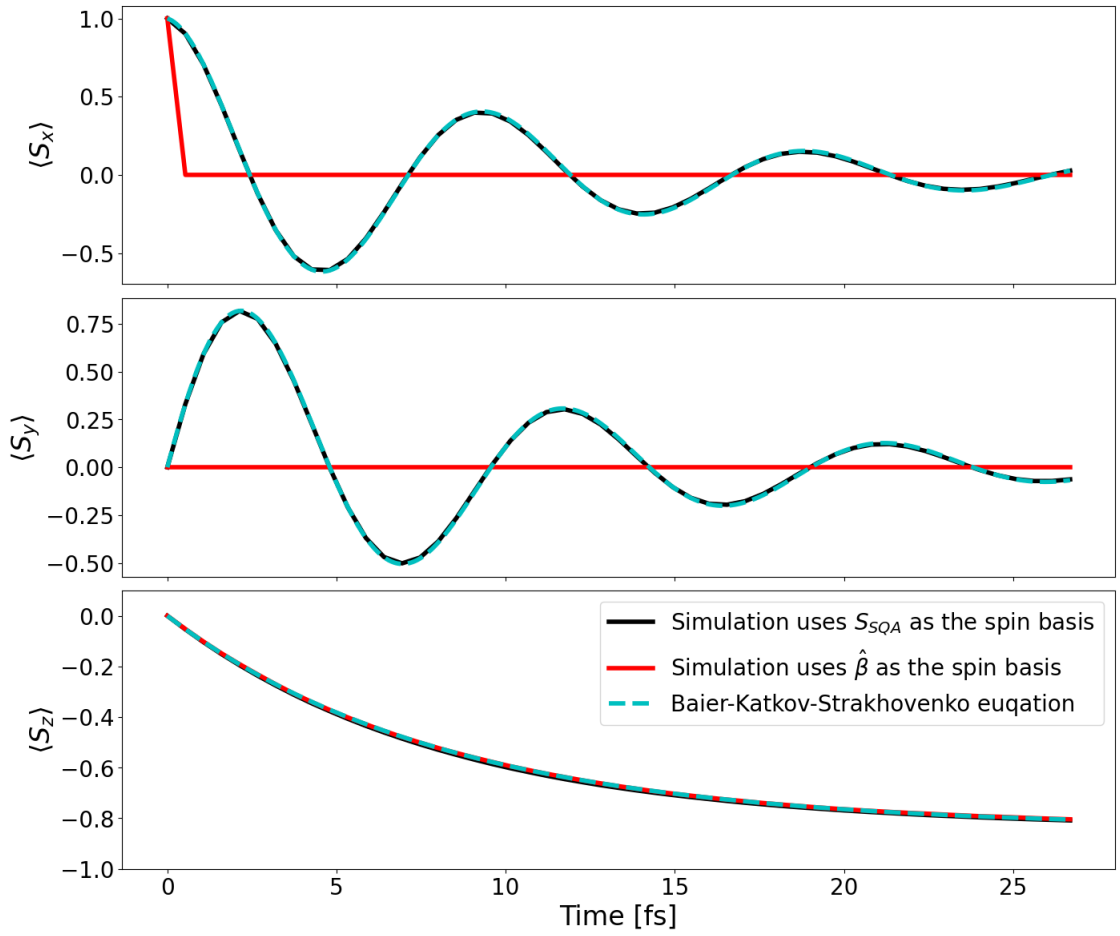

Figure 3.10: The evolution spin component along the x, y, z direction for a fully polarized electron beam inside a constant B field. The beam is initially polarized along the x direction, while the magnetic field is along the z direction. The radiation back-reactions are switched off for simplicity. The red curve shows the simulation result using rest frame B field $\hat{\boldsymbol{\beta}}$ as the spin basis. The black curve shows the simulation result using the spin quantization axis $\boldsymbol{S}_{SQA}$ defined in Eq. 2.99 as the spin basis. The dashed cyan curve is the analytic prediction using the B-K-S equation.

3.5.3 Spin Evolution for Arbitrary Initial Conditions and Field Configurations

In previous tests, we examined the spin evolution of an unpolarized beam in a static field. For more complex scenarios, however, the choice of spin basis becomes increasingly important. Here, we present two benchmark tests: one involving an initially polarized lepton beam in a constant magnetic field, and another featuring an unpolarized electron beam in a time-varying magnetic field. Simulations were conducted using both the spin quantization axis, $\boldsymbol{S}_{SQA}$, as described in Section3.2.1, and the rest-frame magnetic field direction, $\hat{\boldsymbol{\beta}}$, as described in Appendix B.

In the first test, we use a two-dimensional PIC simulation with an initially polarized, monochromatic 1GeV electron beam propagating in the x-y plane. A constant magnetic field of 2.26MT is applied along the z-direction throughout the simulation domain, and the electron beam is initially polarized along the x-direction. Radiation back-reaction and pair production are disabled to facilitate direct comparison with analytical predictions.

Simulation results are benchmarked against the extended Baier-Katkov-Strakhovenko (B-K-S) equation[144], shown in Eq.6.2, which incorporates both radiation-induced spin dynamics and classical spin precession..

$$\frac{d\boldsymbol{S}}{dt} = \left(\frac{d\boldsymbol{S}}{dt}\right)_T - P\left[\psi_1(\chi)\boldsymbol{S} + \psi_2(\chi)(\boldsymbol{S}\cdot\hat{\boldsymbol{v}})\hat{\boldsymbol{v}} + \psi_3(\chi)\hat{\boldsymbol{\beta}}\right] \tag{3.26}$$

Here, $P = \frac{\alpha_f m_e c^2}{\sqrt{3}\gamma\hbar\omega_L}$, $\psi_1(\chi) = \int_0^\infty u'' du K_{2/3}(u')$, $\psi_2(\chi) = \int_0^\infty u'' du \int_{u'}^\infty dx K_{1/3}(x) - \psi_1(\chi)$, $\psi_3(\chi) = \int_0^\infty u'' du K_{1/3}(u)$, and $u'' = u^2/(1+u)^3$. $\left(\frac{d\boldsymbol{S}}{dt}\right)_T$ is the T-BMT equation:

$$\left(\frac{d\boldsymbol{S}}{dt}\right)_T = -\frac{e}{m_e c}\left[\left(a_e + \frac{1}{\gamma}\right)(\boldsymbol{B} - \boldsymbol{v}\times\boldsymbol{E}) - \boldsymbol{v}\frac{a_e\gamma}{\gamma+1}\boldsymbol{v}\cdot\boldsymbol{B}\right]\times\boldsymbol{S} = \boldsymbol{\Omega}\times\boldsymbol{S} \tag{3.27}$$

The evolution of the three spin components along the (x, y, z) axes is shown in Fig. 3.10.

I performed simulations using two different spin bases. The red curves represent results obtained with $\hat{\boldsymbol{\beta}}$ as the spin basis, where the simulated spin evolution matches the analytic results only along the magnetic field direction (z-axis). In contrast, the black curves show results using the spin quantization axis $\boldsymbol{S}_{SQA}$ as the basis. In this case, the evolution of all three spin components agrees well with the analytic calculations.

The second test examines the spin dynamics of an unpolarized electron beam in a time-varying magnetic field. Here, an initially unpolarized 100 MeV lepton beam is placed inside a 2.26 MT magnetic field. The field strength remains constant, but its direction is initially aligned with the z-axis before rotating towards the y-axis at a rate comparable to the gyrofrequency. Simulation results are compared with predictions from the B-K-S equation. The spin components' evolution is shown in Fig. 3.11. Again, simulations were conducted with both spin bases. The red curves, using $\hat{\boldsymbol{\beta}}$ as the basis, align with analytical predictions only prior to the field rotation; deviations appear when the field direction rotates from z to y. However, for the black curves, calculated using $\boldsymbol{S}_{SQA}$ as the basis, the evolution of all spin components maintains excellent agreement with analytical results throughout the simulation.

3.5.4 Benchmark against Ptarmigan

We also benchmark our code against other well-known polarization-resolved QED algorithms. Specifically, we utilize the Monte Carlo particle-tracking code Ptarmigan, developed by Tom Blackburn et al. [147], which recently implemented polarization dependence in both photon emission and pair creation. Since Ptarmigan does not include lepton spin effects, we conduct a simple test case involving an unpolarized, high-energy electron beam colliding with a circularly polarized laser pulse.

In this setup, the laser has a peak intensity of $a_0 = 64$, a wavelength of $\lambda_0 = 0.8\mu$m, a pulse duration of $\tau_0 = 40$fs, and a focal radius of $w_0 = 32\mu$m. The electron beam is mono-energetic with an initial energy of 5 GeV, and its density follows a Gaussian distribution

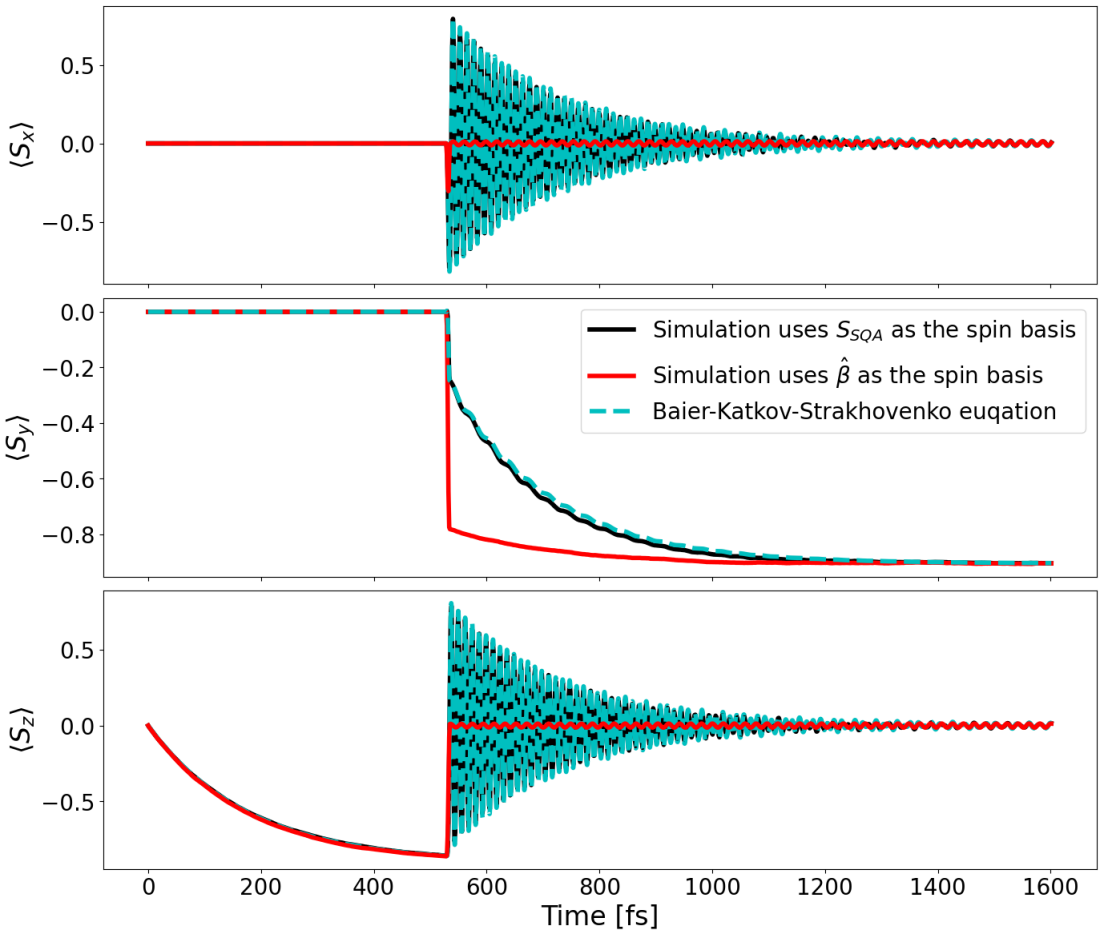

Figure 3.11: The evolution spin component along the x, y, z direction for an unpolarized electron beam inside a changing B field. The magnetic field is initially along the z direction and stays in z for a while. It then quickly rotates to the y direction at a rotation speed close to the electron gyro frequency. The amplitude of the magnetic field remains the same. The radiation back-reactions are switched off for simplicity. The red curve shows the simulation result using rest frame B field direction $\hat{\boldsymbol{\beta}}$ as the spin basis. The black curve shows the simulation result using the spin quantization axis $\boldsymbol{S}_{SQA}$ defined in Eq. 2.99 as the spin basis. The dashed cyan curve is the analytic prediction using the B-K-S equation.

transversely ($\sigma_y = 4.8\mu$m) and longitudinally ($\sigma_x = 0.8\mu$m).

We track the transverse distribution of linearly polarized photons produced during the interaction. The results from Ptarmigan are shown in Fig.3.12(a), (c), and (e): (a) depicts the total photon density distribution in p_y-p_z space, (c) corresponds to photons with polarization state $\xi_3 > 0$, and (e) to photons with $\xi_3 < 0$. Our code's results are shown in Fig.3.12(b), (d), and (f). The polarized photon density distributions produced by both codes are nearly

identical, demonstrating strong agreement between the two approaches.

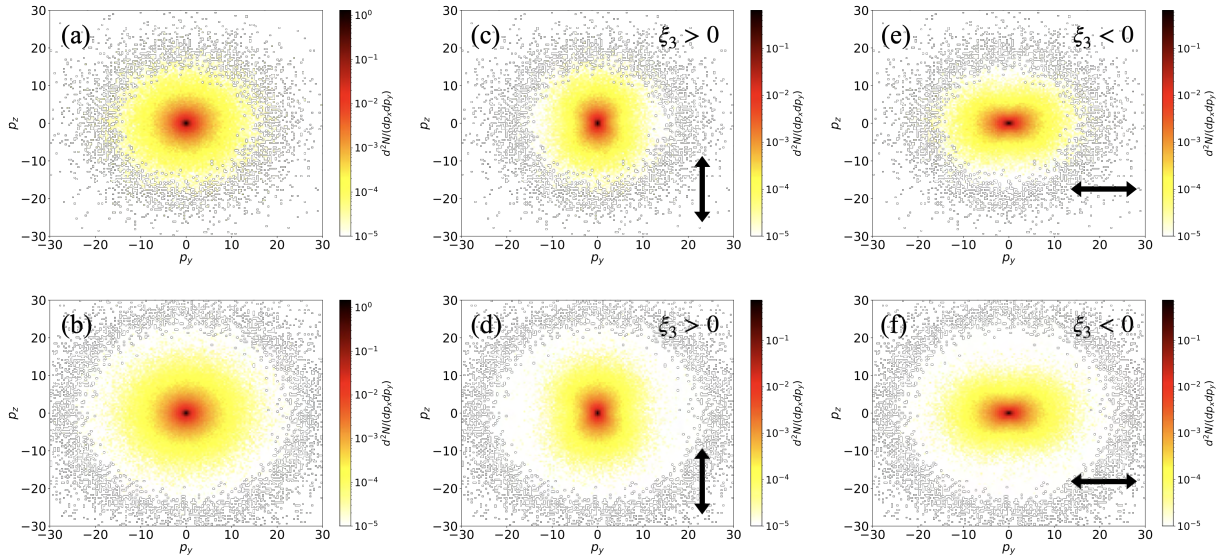

Figure 3.12: Photon polarization spectrum from Osiris compared with Ptarmigan. (a), (c), (e), Simulation result from ptarmigan. (a), (b) The total photon density distribution in py-pz space, (c),(d) The density distribution for photons with polarization state $\xi_3 > 0$. (e)(f) The density distribution for photons with polarization state $\xi_3 < 0$. (a),(c),(e) are the results from Ptarmigan. Our code results are shown in (b), (d), (f).

3.5.5 Benchmark against Previously Published Results

The previous benchmarks clearly demonstrate the accuracy of our code, although they were performed under highly idealized conditions that are challenging to replicate in real-world experiments. To further validate our approach, we now aim to reproduce results recently reported in several publications, which propose experimentally accessible setups involving a lepton beam colliding with a laser pulse. The parameters suggested in these works are realistic and could be realized in the near future.

These studies systematically explore various characteristics of spin- and polarization-resolved NLCS and NBW processes by varying the properties of the lepton beam and laser pulse. We divide the scenarios into three main categories:

Spin Polarization along the Rest Frame Magnetic Field: This examines how the NLCS and NBW processes tend to polarize lepton spins along the rest frame magnetic field. For

example, the collision of an unpolarized electron beam with a linearly polarized laser pulse generates linearly polarized photons.

Interplay Between Quantum Radiation and Classical Spin Precession: Here, the interaction between quantum-induced spin alignment and classical spin precession is explored—demonstrating, for instance, how spin, initially aligned by quantum processes, can be rotated to the longitudinal direction through precession.

Spin Polarization Along the Longitudinal Direction: This case focuses on helicity transfer in spin-polarized NLCS and NBW processes, where longitudinally polarized lepton beams and circularly polarized photons exchange angular momentum, as predicted by polarization-resolved QED.

Most existing works employ Monte Carlo-based particle tracking algorithms. In what follows, we employ our own spin- and polarization-resolved QED code to reproduce and validate the key results reported in these recent studies.

3.5.5.1 Spin Polarization from Colliding with a Bichromatic Laser

As predicted by the Sokolov-Ternov effect, particle spins tend to align either parallel or antiparallel to the magnetic field in the particle's rest frame. However, simply colliding an unpolarized lepton beam with a strong, symmetric laser field does not produce a polarized beam, as the net effect of the field averages to zero over an optical cycle. To achieve polarization, one approach is to break the symmetry of the laser field, for example, by using a bichromatic laser pulse.

In this work, we reproduce the bichromatic laser pulse setup described in recent literature [3]. The pulse consists of two copropagating lasers with wavelengths $\lambda_1 = 1\mu$m and $\lambda_2 = 0.5\mu$m, both with a pulse duration $\tau = 33$fs and a focal radius $w_0 = 5\mu$m. The ratio of peak field strengths is $R = a_{01}/a_{02} = 2$, with a total field strength of $a_0 = a_{01} + a_{02} = 83$. The electron beam is initialized with a transverse Gaussian width of $\sigma_y = 0.4\mu$m, a longitudinal length of $\sigma_x = 10\mu$m, and an initial energy of 2 GeV with a 2% energy spread.

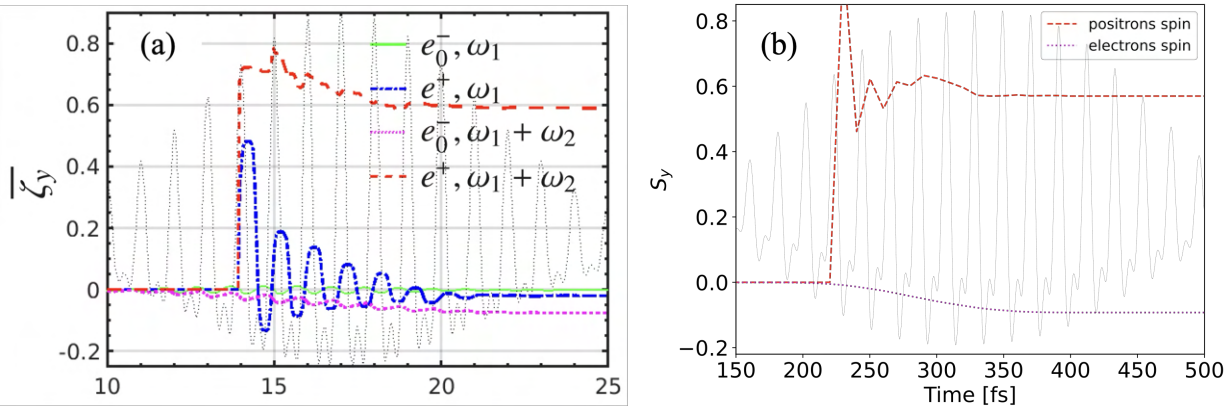

Figure 3.13: Electron and positron beam spin polarization evolution in a bichromatic laser. (a) From the paper [3] (b) from the OSIRIS spin and polarization-resolved QED simulation. Subplot (a) reproduced from Yue-Yue Chen et al. Phys. Rev. Lett. **123**, 174801 (2019).© American Physical Society.

We compare the results of our spin- and polarization-resolved QED simulations to those reported in the reference paper, as shown in Fig. 3.13. The paper reports an average positron polarization of about 58%; our simulation yields a value of 57.9%. The average lepton spin polarization is reported to be 7.7%, while our simulation gives 8.8%, indicating strong agreement. The small discrepancy may arise from comparing our 2D PIC simulation with the paper's 3D particle tracking simulations; however, we believe that two-dimensional simulations are sufficient to capture the essential physics of this process.

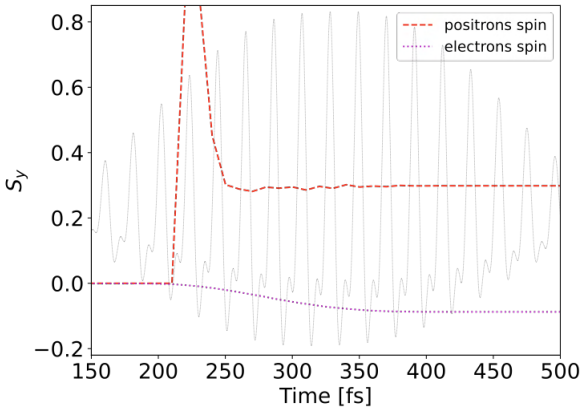

Figure 3.14: Spin polarization in a bichromatic laser, with the full spin and polarization model in our code

It is important to note that the reference paper does not incorporate the full spin- and polarization-resolved QED effects in its calculations; the emitted photons are assumed to be unpolarized. Our algorithm, by contrast, includes a flexible switch that allows specific effects to be toggled on or off. In the earlier comparison, we adopted the same simplified physics model as the paper to ensure consistency, resulting in comparable outcomes.

However, this simplified model does not accurately represent the polarization dynamics. In reality, photons generated during the laser-beam collision are predominantly linearly polarized, and this polarization significantly affects the resulting positron polarization. When we activate the full spin- and polarization-resolved QED effects in our code, as shown in Fig. 3.14, the average positron polarization is reduced to just 31%. This highlights the importance of properly accounting for polarization effects in simulations of these processes.

3.5.6 Spin Polarization from Colliding with an Elliptically Polarized Laser

Yan-fei Li et al. [4] propose a clever and straightforward method for generating a polarized electron beam. Their approach involves colliding a slightly elliptically polarized laser beam with an unpolarized lepton beam. The lepton acquires polarization along the direction of the magnetic field in its rest frame, while the ellipticity of the laser introduces a correlation between the electrons' transverse momentum and their spin. This momentum–spin correlation allows a polarized electron beam to be obtained by selectively collecting electrons emitted at specific angles.

In their setup, the laser beam has a peak intensity of $a_0 = 100$, a wavelength of $\lambda_0 = 1$ μm, a pulse duration of $\tau_0 = 16.7$ fs, and a focal radius of $w_0 = 5$ μm. The electron beam profile follows a Gaussian distribution in both transverse and longitudinal directions, with a width of $\sigma_y = 1$ μm and a length of $\sigma_x = 5$ μm. The initial energy of the electron beam is 4 GeV, with an energy spread of 6%.

Figure 3.15 shows the results of our spin- and polarization-resolved QED simulations

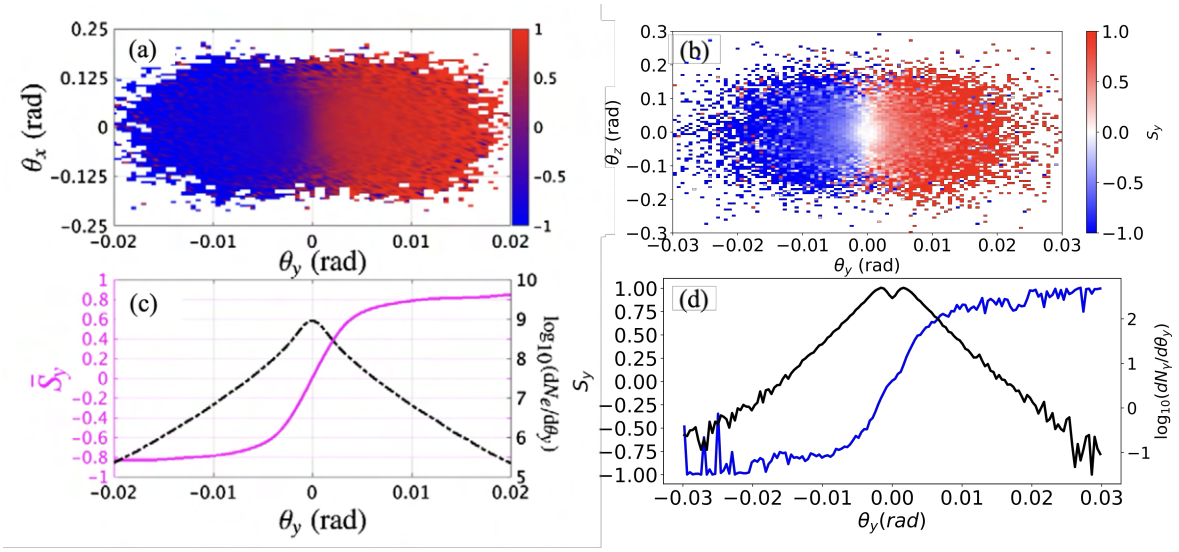

Figure 3.15: Spin polarization from colliding with an elliptically polarized laser. (a), (b) The spin distribution in the $\theta_y - \theta_z$ base space after the interaction. (c), (d) The spin and density distribution with respect to the deflection angle θ_y. (a),(c) is from the paper [4]. (b), (d) from the OSIRIS spin and polarization-resolved QED simulation. Subplots (a) (c) reproduced from Yan-Fei Li et al. Phys. Rev. Lett. **122**, 154801 (2019).© American Physical Society.

compared to those reported in [4]. The simulated spin distribution in the θ_y–θ_z phase space closely matches their findings. The results confirm that the degree of polarization increases with the electron deflection angle along the minor axis of the elliptically polarized laser. Our simulations yield a maximum polarization of about 80% for $|\theta_y| < 0.02$, which agrees well with the predictions in the referenced paper.

3.5.6.1 Linear Polarization Gamma-Ray in Laser-Solid Target Interaction

We next examine the generation of dense, linearly polarized gamma-ray beams in the context of laser–solid interactions. In this study, a strong linearly polarized (LP) laser pulse is directed onto a near-critical-density (NCD) hydrogen plasma, backed by an ultra-thin planar aluminum (Al) target. Electrons in the plasma are accelerated to ultra-relativistic energies and subsequently collide head-on with the reflected laser pulse from the Al target, resulting in copious emission of linearly polarized gamma photons.

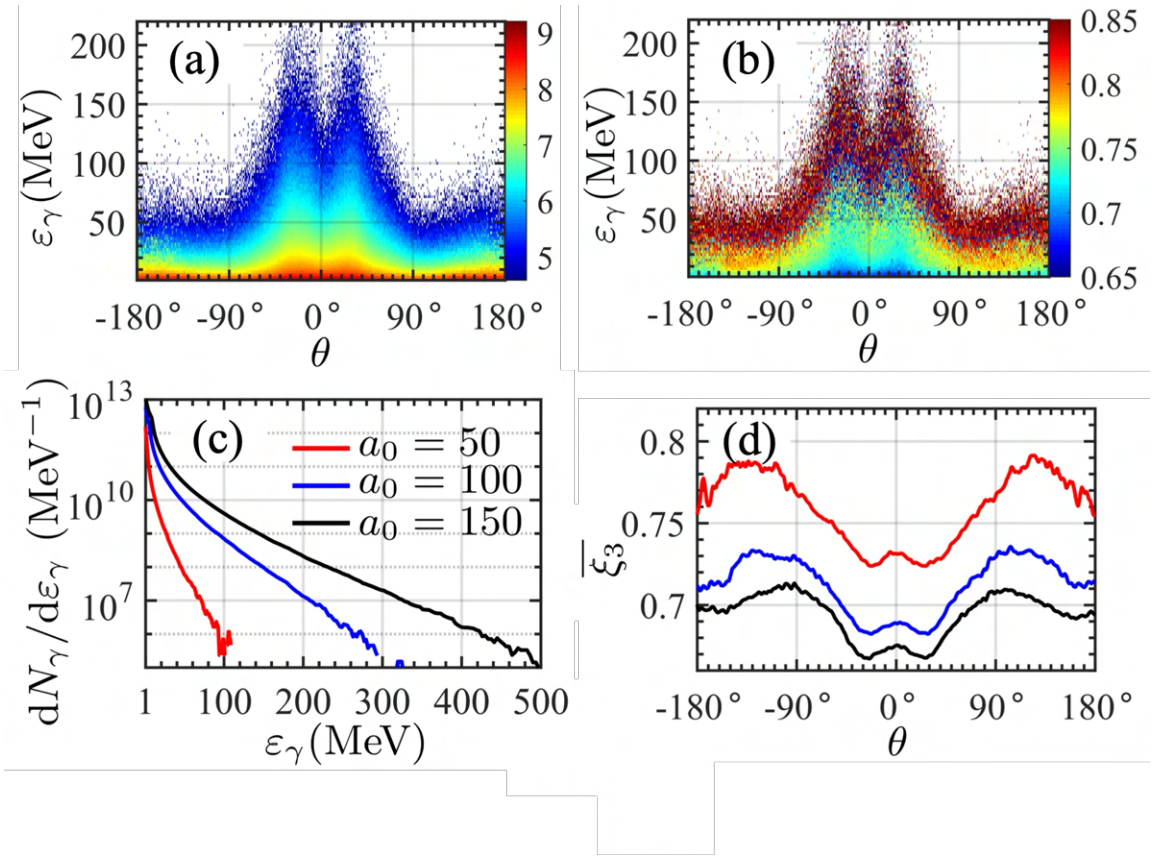

Figure 3.16: Linear polarization gamma-ray in laser-solid target interaction, from paper [5]. (a) Photon density distribution in the photon energy ε_γ -deflection angle θ phase space. (b) Photon linear polarization distribution in the $\varepsilon_\gamma - \theta$ phase space. (c) Photon density distribution with respect to the photon energy ε_γ for laser $a_0 = 50,\ 100,\ 150$. (d) Photon linear polarization distribution with respect to the deflection angle θ for lasers $a_0 = 50,\ 100,\ 150$. This figure is from "Generation of highly-polarized high-energy brilliant γ-rays via laser-plasma interaction" Matter Radiat. Extremes **5**, 054402 (2020) by Kun Xue et al., which is licensed under CC BY 4.0.

The peak intensity of the laser, a_0, is varied between 50, 100, and 150, while the wavelength is fixed at $\lambda_0 = 1, \mu$m, pulse duration at $\tau_0 = 30,$ fs, and focal radius at $w_0 = 5, \mu$m. The planar Al target has an electron density of $n_e^{\rm Al} = 702 n_c$ and thickness $d_{\rm Al} = 1, \mu$m, where the plasma critical density is $n_c = m\omega_0^2/4\pi e^2 \approx 1.1 \times 10^{21}, {\rm cm}^{-3}$. On the laser-incident side of the Al target is the NCD hydrogen plasma with electron density $n_e = 5n_c$ and thickness $d_p = 10, \mu$m.

The main results from the reference paper [5] are illustrated in Fig.3.16: panels (a) and

(b) show the spatial density and degree of linear polarization of the emitted gamma rays for $a_0 = 100$; panel (c) presents the gamma-ray energy spectra for $a_0 = 50$, 100, and 150; and panel (d) displays the angular distribution of linear polarization. Our simulation results, shown in Fig.3.17, closely reproduce these findings, even though fewer particles were used in our model, resulting in reduced computational cost. Nevertheless, we capture the essential conclusion: higher laser intensities generate more gamma-ray photons with higher energies, but at the expense of reduced linear polarization.

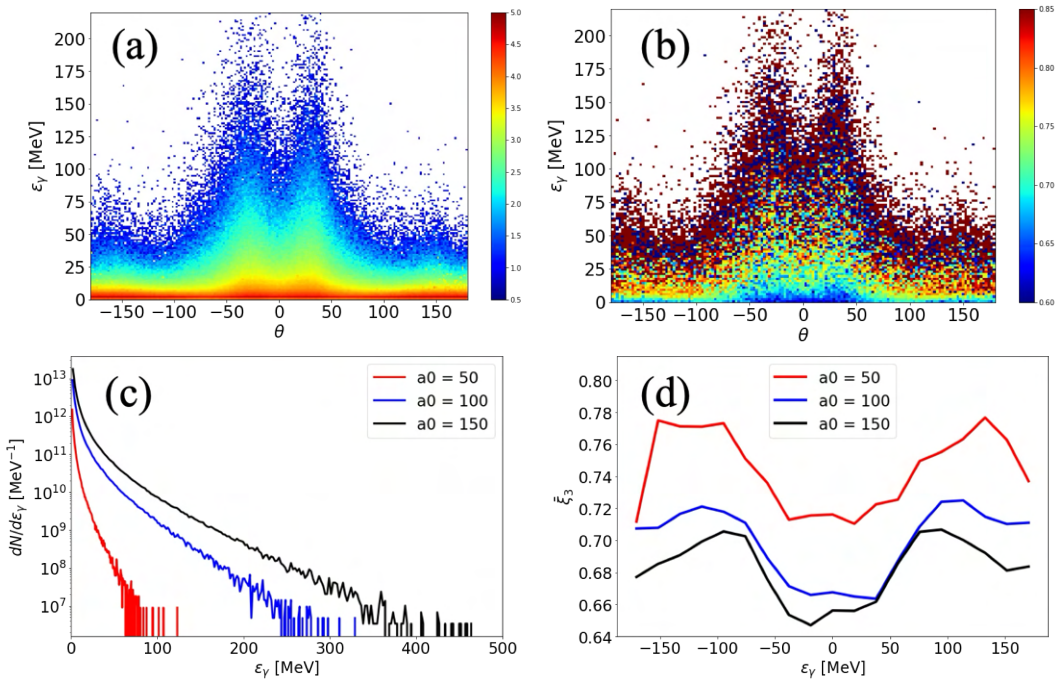

Figure 3.17: Linear polarization gamma-ray in laser-solid target interaction, from the OSIRIS spin and polarization-resolved QED simulation. (a) Photon density distribution in the photon energy ε_γ -deflection angle θ phase space. (b) Photon linear polarization distribution in the $\varepsilon_\gamma - \theta$ phase space. (c) Photon density distribution with respect to the photon energy ε_γ for laser $a_0 = 50,\ 100,\ 150$. (d) Photon linear polarization distribution with respect to the deflection angle θ for lasers $a_0 = 50,\ 100,\ 150$.

3.5.6.2 Helicity Transfer in a Laser Field due to the Electron Anomalous Magnetic Moment

Yan-fei Li et al. [6] discovered a remarkable phenomenon: helicity can be transferred from a circularly polarized (CP) laser pulse to an ultra-relativistic electron beam via the non-linear Compton scattering process within the radiation reaction-dominated regime. Their study identifies the anomalous magnetic moment term in the classical spin precession as a critical factor in enabling this helicity transfer.

In their simulations [6], a right-handed CP, tightly focused Gaussian laser pulse is used with a peak intensity of $a_0 = 100\sqrt{2}$, wavelength $\lambda_0 = 1$ μm, pulse duration $\tau_0 = 16.7$ fs, and focal radius $w_0 = 5$ μm. The counter-propagating electron bunch follows Gaussian distributions both transversely and longitudinally, with a width of $\sigma_y = 1$ μm and a length of $\sigma_x = 5$ μm. The initial electron energy is 1 GeV, with a 10% energy spread.

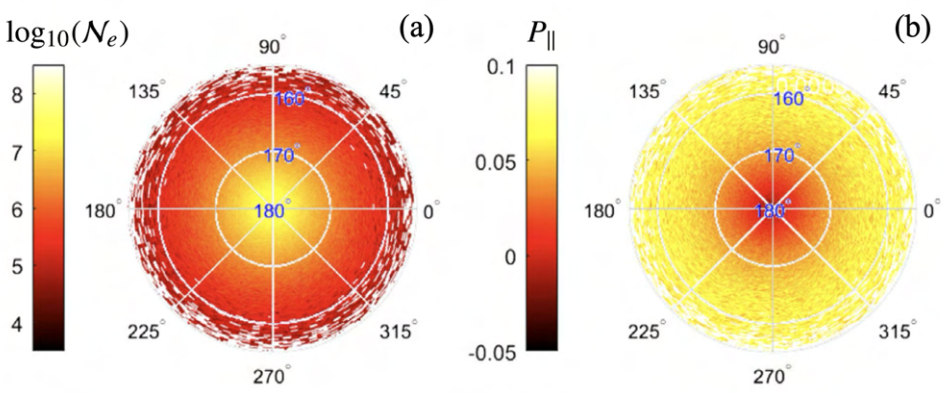

Figure 3.18: Helicity transfer in a laser field due to the electron anomalous Magnetic Moment, from the paper [6]. (a) Polar plot of electron density distribution (b) Polar plot of electron longitudinal spin distribution. Figure reproduced from Yan-Fei Li et al. Phys. Rev. Lett. **128**, 174801 (2022) © American Physical Society.

Figure 3.18 from their paper presents the post-collision electron density and longitudinal polarization distributions. Our simulation results, shown in Fig.3.19, closely match these findings. Specifically, our computed average longitudinal polarization is approximately 2.2%, aligning well with the 2.65% reported in the paper. The data show that longitudinal polar-

ization increases with the electron deflection angle, changing from about -5% at the beam center to around 10% further away from the center.

The role of the anomalous magnetic moment is highlighted in Fig. 3.20, where panel (a) is taken from the reference and panel (b) is from our simulation. The red curve represents results with the true anomalous magnetic moment $g = g(\chi_e)$, while the blue dashed curve corresponds to a fixed $g = 2$. The purple curve shows $g = g(\chi_e)$ but only includes non-emission polarization, omitting radiative polarization. Our results are consistent with those in the paper: when $g = 2$, there is no helicity transfer; only when $g \neq 2$ does the effect appear. Furthermore, transverse spin polarization is also significant in this process—the presence or absence of radiative polarization results in opposite outcomes for longitudinal polarization.

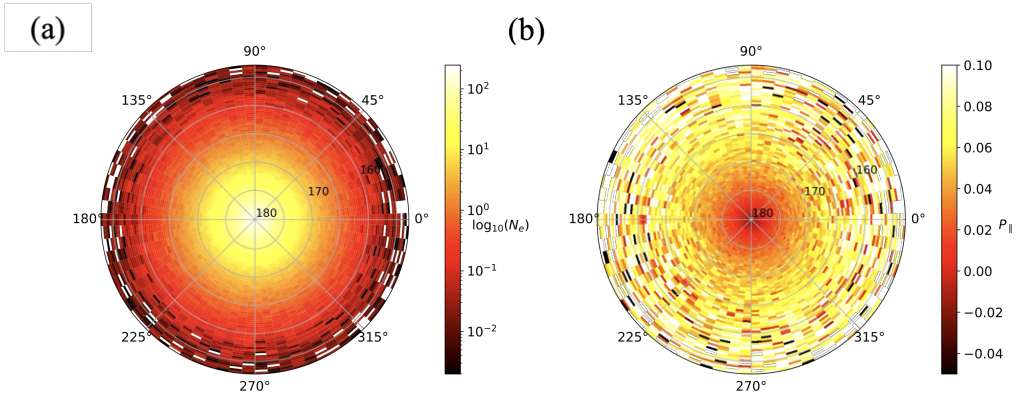

Figure 3.19: Helicity transfer in laser field due to the electron Anomalous Magnetic Moment, from OSIRIS spin and polarization-resolved QED simulation. (a) Polar plot of electron density distribution (b) Polar plot of electron longitudinal spin distribution.

3.5.6.3 Circular-Polarized High-Energy Gamma-Ray Pulse via Laser-Electron Interaction

Next, we examine helicity transfer arising purely from spin- and polarization-resolved non-linear Compton scattering (NLCS) and non-linear Breit–Wheeler (NBW) processes. Yan-fei Li et al. [7] investigate helicity transfer in the polarization-resolved NLCS process by colliding

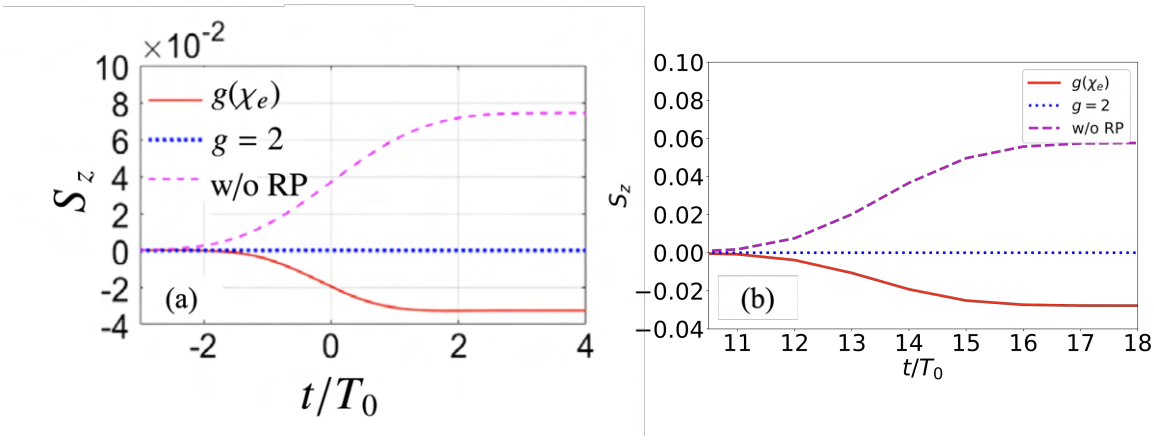

Figure 3.20: Helicity transfer in laser field due to the electron anomalous magnetic moment, (a) from paper [6](b) from OSIRIS spin and polarization-resolved QED simulation. Subplot (a) is reproduced from Yan-Fei Li et al. Phys. Rev. Lett. **128**, 174801 (2022) © American Physical Society.

a linearly polarized laser with a fully longitudinally polarized electron beam, resulting in the generation of a high-energy, circularly polarized gamma-ray beam.

In their setup, a linearly polarized, tightly focused Gaussian laser pulse is used with a peak intensity $a_0 = 50$, wavelength $\lambda_0 = 1$ μm, pulse duration $\tau_0 = 33$ fs, and focal radius $w_0 = 5$ μm. The counter-propagating electron bunch is fully longitudinally polarized with an initial mean energy of 10 GeV and a 6% energy spread, and is modeled using a transverse width of $\sigma_y = 2$ μm and a longitudinal length of $\sigma_x = 3$ μm.

Figure 3.21 (a) shows the generated gamma-ray energy spectrum and its degree of circular polarization, as reported in the paper. Our simulation results, presented in Fig. 3.21(b), closely reproduce these findings. Specifically, we observe that the degree of circular polarization of the emitted gamma-ray photons increases with photon energy, reaching nearly 100% for the highest-energy photons.

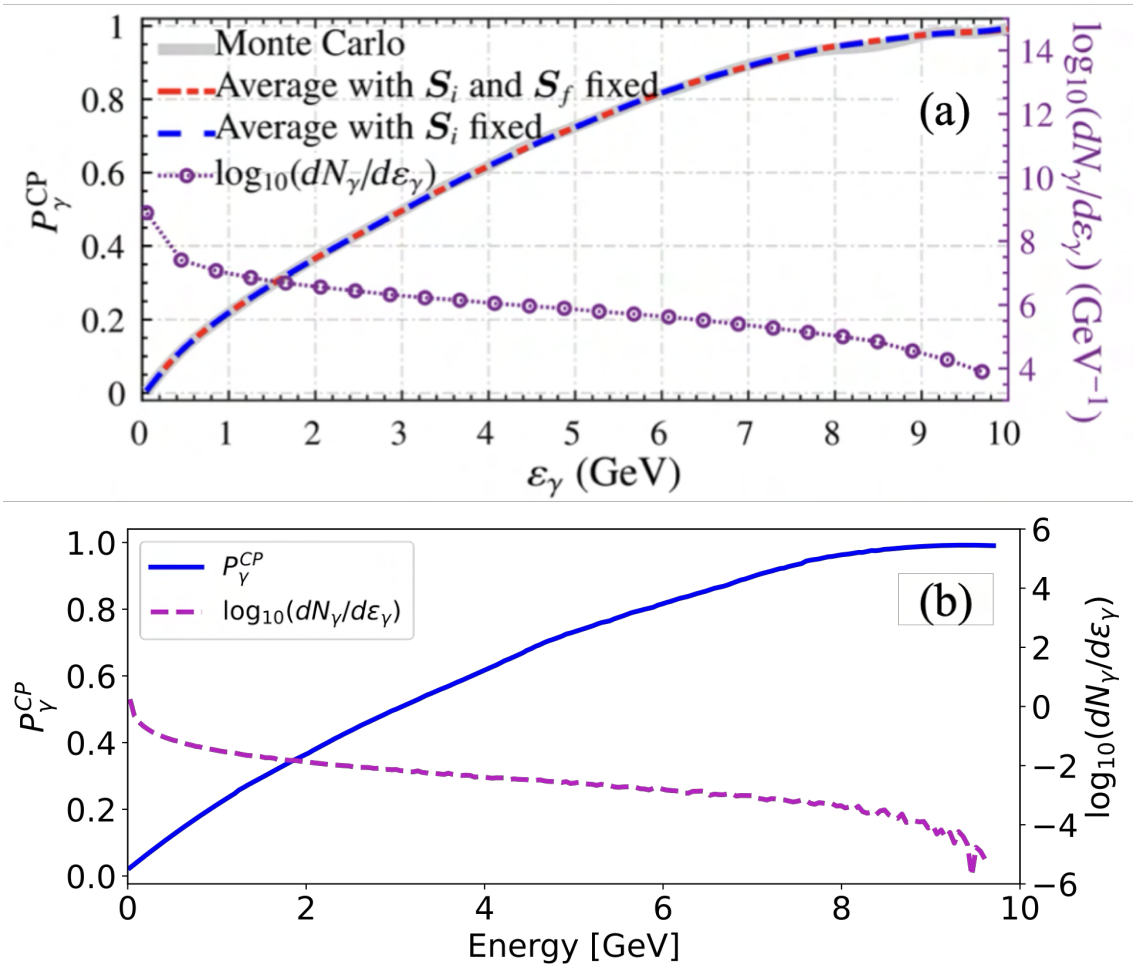

Figure 3.21: Circular-polarized high-energy gamma-ray pulse via Laser-Electron Interaction (a) from paper [7], (b) from OSIRIS spin and polarization-resolved QED simulation. Subplot (a) is reproduced from Yan-Fei Li et al. Phys. Rev. Lett. **125**, 044802 (2020) © American Physical Society.

3.5.6.4 Production of Highly Polarized Positron Beams via Helicity Transfer from Polarized Electrons

Helicity transfer is also observed in the polarization-resolved non-linear Breit–Wheeler (NBW) process, as demonstrated in Yan-Fei Li's second PRL paper on this topic [8]. In their study, a circularly polarized laser is collided with a fully longitudinally polarized electron beam. Here, the laser intensity is increased, enabling the highly circularly polarized gamma-ray photons generated in the NLCS process to be converted into longitudinally polarized positrons via the polarization-resolved NBW process.

The experimental setup uses a circularly polarized, tightly focused Gaussian laser pulse with a peak intensity $a_0 = 100$, wavelength $\lambda_0 = 1$ μm, pulse duration $\tau_0 = 16.7$ fs, and focal radius $w_0 = 5$ μm. The counter-propagating electron bunch is fully longitudinally polarized with an initial mean energy of 10 GeV and a 6% energy spread, described by a Gaussian profile with transverse width $\sigma_y = 0.6$ μm and longitudinal length $\sigma_x = 6$ μm.

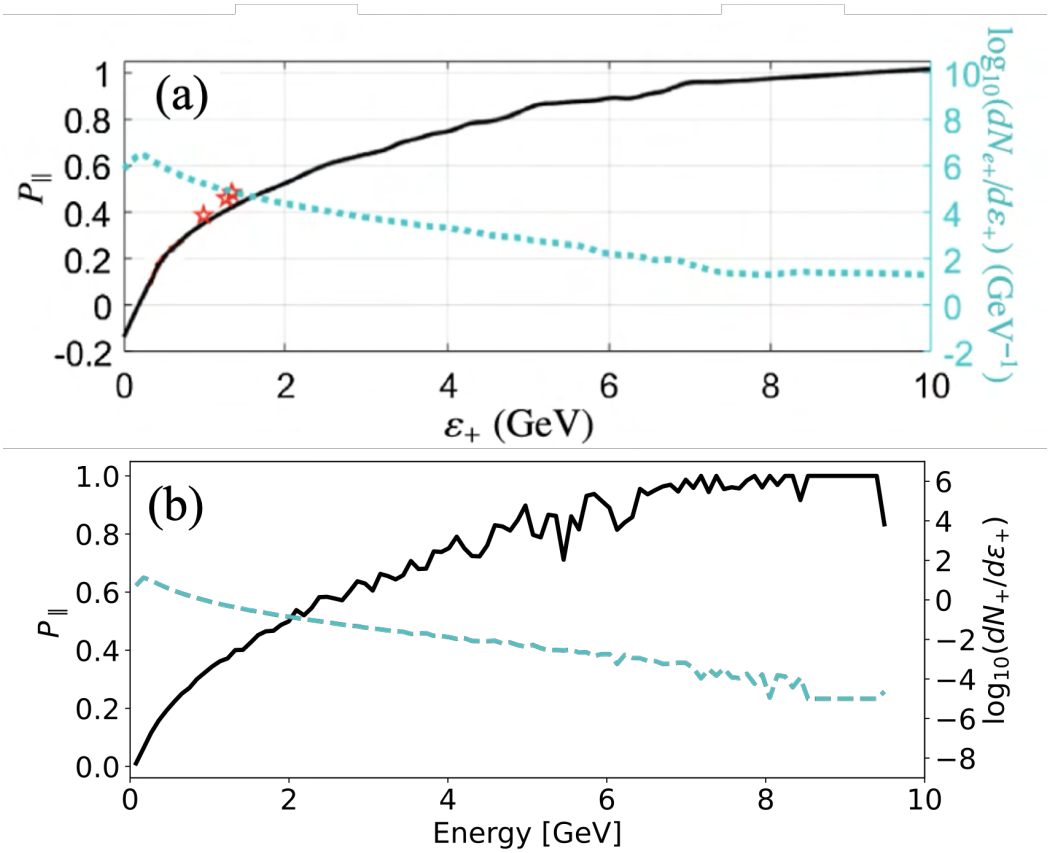

Figure 3.22: Production of Highly Polarized Positron Beams via Helicity Transfer from Polarized Electrons (a) from paper [8], (b) from OSIRIS spin and polarization-resolved QED simulation. Subplot (a) is reproduced from Yan-Fei Li et al.Phys. Rev. Lett. **124**, 014801 (2020) © American Physical Society.

Figure 3.22(a) from the paper [8] presents the generated positron energy spectrum and its degree of longitudinal polarization. Our simulation, shown in Fig. 3.22(b), closely matches these results. We find that the degree of longitudinal polarization of the produced positrons increases with positron energy, reaching nearly 100% for the highest-energy positrons, in agreement with the results reported in the paper.

3.5.6.5 Polarized QED Cascade Implementation

Finally, we use our polarization-resolved QED module to reproduce the results in Ref. [73]. This paper studied the seeded electron-positron pair cascade [148] in a rotating electric field calculated using a polarization-resolved Boltzmann-type solver. The polarized QED cascade is a sensitive process involving the interplay between the quantum emission rates and particle kinetics. Reproducing the main result in this paper can comprehensively test the performance of our spin and polarization-involved QED module. On the other hand, the intensity of the rotating electric field is uniform in space. This reduces the problem to 0-D, which greatly simplifies the simulations. Notice that the paper uses notation $\parallel$ and $\perp$ instead of $\boldsymbol{\sigma}$ and $\boldsymbol{\pi}$ for the photon polarization state, which has a similar meaning.

The first part of the test is to reproduce the electron-seeded cascade result. Following the conditions given in the paper: laser intensity $a_0 = 1000$ and $\omega = 1.55\ eV$, I obtained the electron and positron distributions shown in Fig. 3.24 using our polarization resolved QED module. This is almost identical to Fig. 3.23 from the paper, which shows that my PIC code calculation result agrees with the calculation using the Boltzmann-type kinetic equations. For both Figs. 3.23 and 3.24, the spin-down distributions for the electrons and positrons have the highest peak value inside the black dashed line separatrix. This separatrix is the classical advection for the leptons inside the rotation field without radiation energy loss. Due to the difference in the spin up-to-down and down-to-up transition rate of the quantum radiation process, spin-down leptons have a larger population and accumulate inside the separatrix. The particles outside the separatrix come from the pair production process initiated by photons generated from the oppositely charged particles due to their distribution being in different locations in phase space. The pair production process in this simulation generates a similar number of spin-up and spin-down leptons. The spin-up distribution inside the separatrix has a much lower peak than the spin-down distribution, so the distribution outside the separatrix for spin-up leptons is more significant.

Fig. 3.25 shows the time evolution of electrons, positrons, and photon yields during a

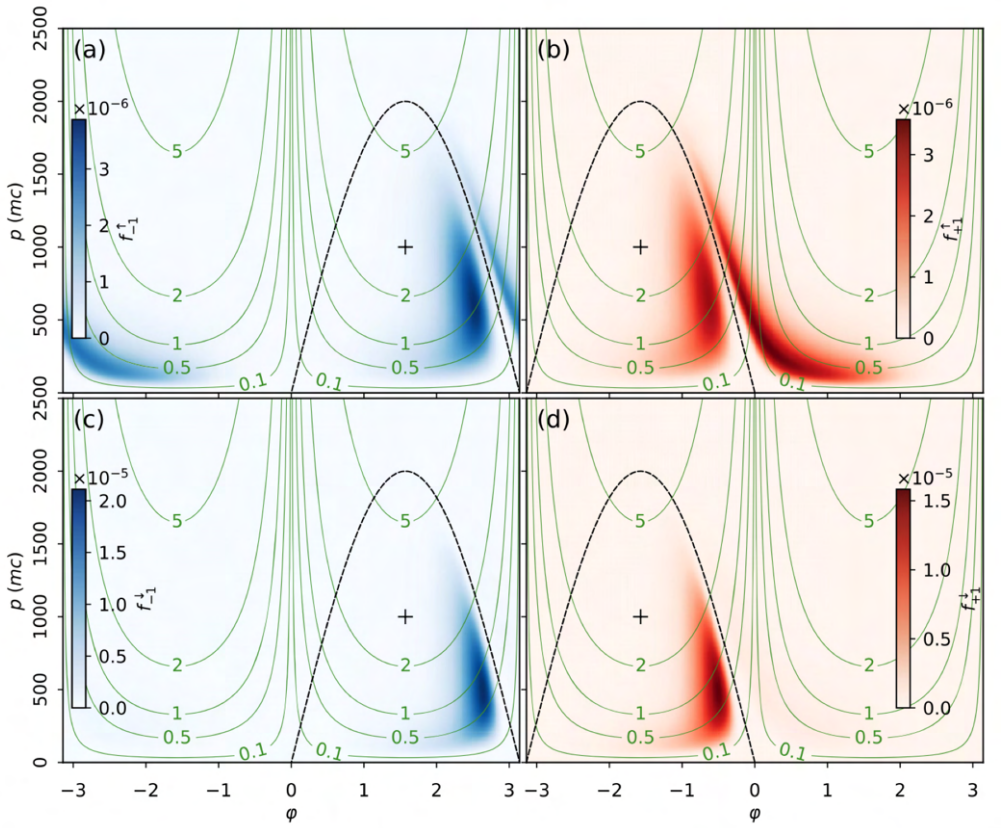

Figure 3.23: Snapshot of the electron (a), (c) and positron (b), (d) distribution functions in an up (a), (b) or down (c), (d) spin state for $a_0 = 10^3$ and $\omega t = 10$ in a rotating radial frame. Green curves are χ isocontours. Black dashed curves represent the separatrix of the classical advection $p = -2a_0 q \sin\varphi$, and black crosses are the corresponding fixed points at $\varphi = -q\pi/2.0$, $p = a_0$. This figure is from "Polarized QED cascades" New J. Phys. **23** 053025 (2022) by D. Seipt, C. P. Ridgers, D. Del Sorbo, and A. G. R. Thomas, which is licensed under CC BY 4.0.

cascade seeded with unpolarized electrons calculated using my QED module. Compared with the result in the paper calculated using the Boltzmann-type solver (see figure 3 in Ref. [73]), the PIC code gives a similar outcome. During the cascade process, the quantum radiation process controls the spin and polarization distribution of the leptons and photons, while the pair production process decides the growth rate of the leptons. Initially, the number of spin-up leptons decreases due to the asymmetry of the spin transition in the quantum radiation process. As the cascade process develops, the growth rate of the lepton becomes constant, and the spin-up-to-down and down-to-up transitions are balanced. There

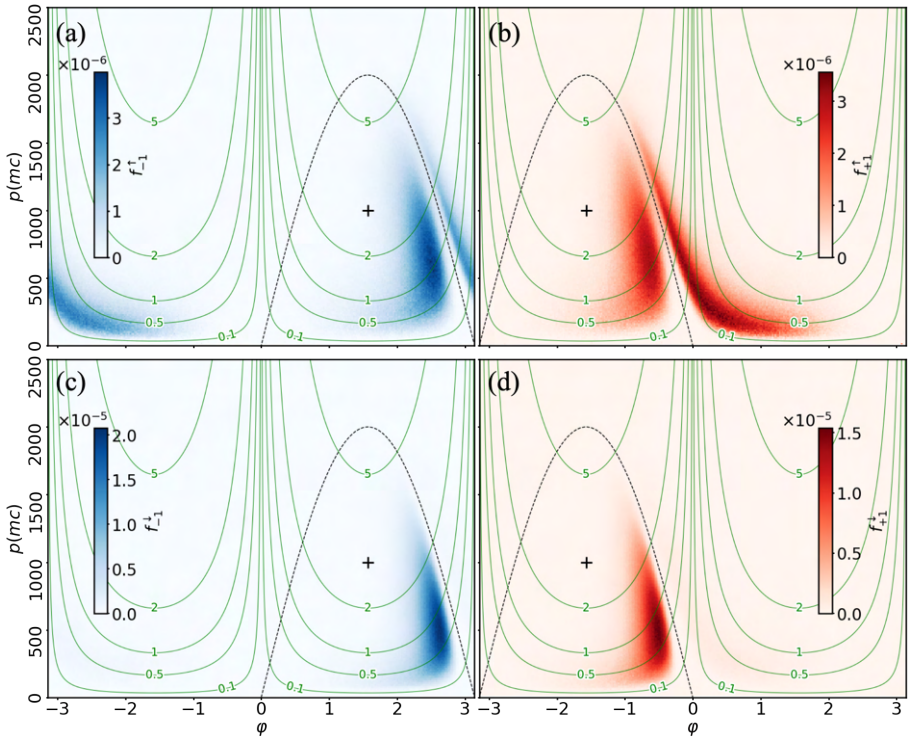

Figure 3.24: Snapshot of the electron (a), (c) and positron (b), (d) distribution functions in an up (a), (b) or down (c), (d) spin state for the same conditions as the paper calculated using Osiris spin and polarization-dependent QED module.

are five times more spin-down leptons than spin-up leptons. The ratio between the photons in different polarization states also becomes a constant in the exponential growth phase. A factor of four more ∥-polarized photons is emitted compared to ⊥-polarized photons. The particles produced in this QED cascade are highly polarized.

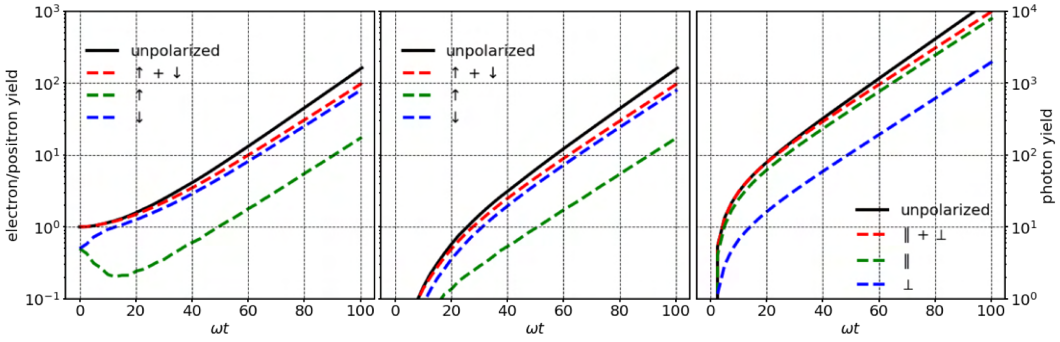

Figure 3.25: Time evolution of electron (a), a positron (b), and photon (c) yields during a cascade seeded by unpolarized electrons calculated by the Osiris spin and polarization QED module.

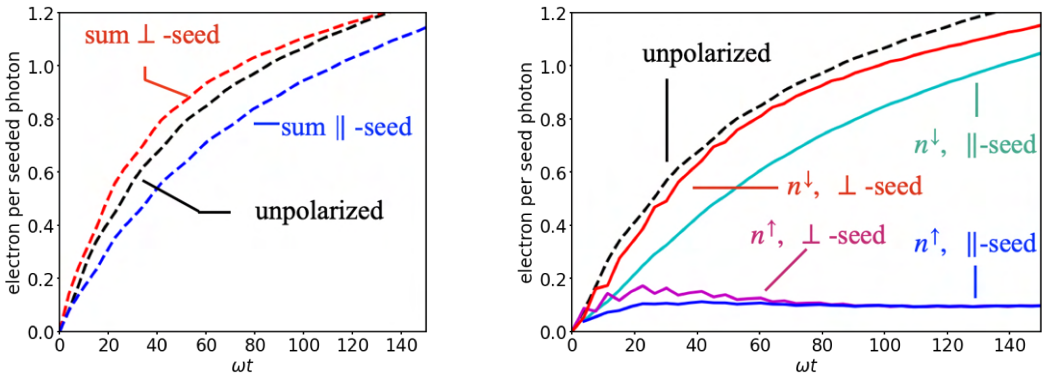

Figure 3.26: Time evolution of the electron yield of photon-seeded cascade calculated using Osiris spin and polarization QED module.

The second test is to reproduce the time evolution of the particle yields for QED-cascade seeded with the polarized photon. Following the same initial conditions in the paper, the simulation results from my polarization QED module are shown in Fig. 3.26. This is similar to the result in the paper (figure 5 in Ref. [73]). The left plot shows that at the early stage, ⊥-polarized photon-seeded cascade has almost two times higher yield than ∥-polarized photon-seeded cascade. As the cascade process develops, the seeding photons are depleted, and the difference in yield becomes smaller. The plot on the right shows the population of spin-down and spin-up electrons. The ⊥-polarized photon-seeded cascade initially generates more spin-down electrons than the ∥-polarized photon-seeded cascade. The seeding photons are depleted as time passes, and the quantum radiation effect on the lepton spin distribution becomes dominant. The number of the spin-down and spin-up leptons for both ⊥-polarized and ∥-polarized photon-seeded cascades would finally become the same.

In conclusion, our polarization-resolved QED module successfully reproduces the result in the "Polarized QED Cascades" paper for both electrons-seeded and polarized photon-seeded cascade simulations. It has also shown good agreement with the analytic prediction of the spin evolution for an initially unpolarized or polarized electron beam inside a constant or changing magnetic field.

CHAPTER 4

Parametric Study of the Polarization Dependence of the Nonlinear Breit-Wheeler Pair Creation Process Using Two Laser Pulses

4.1 Introduction

In this work[1], we present a two-pulse pair production scheme that can be implemented in an all-optical experiment using laser wakefield-accelerated electrons [149]. Our study employs the QED module of the OSIRIS particle-in-cell code [150, 151, 146], which we have extended to include spin- and polarization-dependent rates. In the study here, linear polarization is used and so a reduced model for the spin may be used (as given in Appendix B). This scheme highlights the pronounced sensitivity of the non-linear Breit–Wheeler (NBW) pair production process to laser polarization. By systematically varying the polarization of the second laser pulse, we identify optimal conditions—such as pulse duration and field strength—to maximize the observable difference in pair production yield. Our simulations demonstrate

[1]This chapter summarizes: Q. Qian, D. Seipt, M. Vranic, T. E. Grismayer, T. G. Blackburn, C. P. Ridgers, A. G. R. Thomas, "Parametric study of the polarization dependence of nonlinear Breit-Wheeler pair creation process using two laser pulses." Phys. Plasma 30, 103107, 2023. I conducted all simulations and analyses included in this publication, with theoretical derivations developed in collaboration with A. G. R. Thomas.

that simply changing the relative polarization of two linearly polarized laser pulses can produce more than a 50% change in pair production yield. We also discuss important criteria for selecting laser and electron beam parameters to guide experimental realization. This chapter was published as Qian et al. in [152].

4.2 Scheme Demonstration using Polarization-Dependent QED PIC Simulations

A schematic of our setup is shown in Fig. 4.1, which is analogous to configurations used for probing vacuum birefringence [153, 154]. In our design, a high-energy electron beam generated by laser wakefield acceleration undergoes sequential collisions with two linearly polarized laser pulses [155]. The first pulse features a relatively long duration and moderate intensity, optimized to decelerate the electron beam efficiently while suppressing NBW pair production. This interaction primarily produces energetic, linearly polarized gamma rays. These gamma rays then collide with a second, shorter, and more intense laser pulse, which facilitates efficient electron-positron pair creation via the NBW process. As the electron beam loses most of its energy in the first interaction, its contribution to pair production in the second collision becomes negligible. Consequently, the majority of electron-positron pairs originate from the polarized gamma rays interacting with the intense second pulse. The polarization state of the gamma photons in the second interaction is controlled by the relative orientations of the two laser pulses, allowing straightforward experimental adjustment. The pair production yield is maximized when the laser polarizations are orthogonal and minimized when they are parallel.

We conduct a pair of 2D simulations with our spin and polarization-dependent QED module to demonstrate this idea. In these two simulations, all the parameters remain the same, including the random seed in the QED Monte Carlo algorithm. The only thing we change is the polarization direction of the second laser, from parallel to perpendicular relative

to the first laser. This restriction guarantees that the dynamics of the electron beam and the generated gamma-ray in the first collision are the same for both simulations, and the difference in the generated pairs can only come from the polarization effect in the NBW process. The first laser pulse in the collision has a peak $a_0 = 30$ and a duration of $t_{fwhm} =$ 120 fs. The second laser pulse follows right after the first pulse, with a peak $a_0 = 160$ and a duration of $t_{fwhm} = 19$ fs. Both lasers have the same wavelength $\lambda_0 = 0.8\ \mu m$, and focal spot radius $w_0 = 10\lambda_0$. The electron beam in the simulations starts unpolarized with an average energy of $\langle E \rangle = 1$ GeV, relative energy spread $\sigma_E/\langle E \rangle = 10\%$, beam length $l_e = 2\lambda_0$, beam radius $w_e = 2\lambda_0$, density $n_e \approx 10^{18}$ cm^{-3} with a transversely and longitudinally Gaussian distribution, which is achievable for current laser wakefield acceleration (LWFA) technology. Each macro-particle in the simulations starts with zero spin vector length to represent the initially unpolarized spin state. In the quantum calculation, the probability of these particles being in a spin-up or spin-down state relative to the basis is equal. Fig. 4.1 (b)-(e) shows the results of the simulations. The first collision generates an energetic gamma-ray with a maximum linear polarization degree that reaches over $\xi_k = 70\%$, as shown in Fig. 4.1 (b). Fig. 4.1 (c) shows the temporal evolution of the whole interaction process. The mean energy of the electron beam reduces to below 200 MeV in the first collision; this corresponds to a maximum quantum parameter $\chi_e < 0.27$ when interacting with the second laser. The energy of the electron beam is converted into high-energy photons in the first collision. They will then collide with the second laser and generate positrons in the second collision. The green curve in Fig. 4.1 (c) plots the number of photons above 300 MeV, which increase in the first collision and decrease in the second collision. The red curve plots the positron number, which only increases during the second collision. The generated gamma-ray beam has a divergence of about 5 $mrad$ for energy larger than 300 MeV (Fig. 4.1 (d)). Fig. 4.1 (e) shows the energy spectrum of the positron generated from the second collision. When we change the polarization direction of the second laser pulse from parallel to perpendicular to the first pulse, we find the difference of the positron yields $\Delta_p = \frac{N_p^{\perp} - N_p^{\parallel}}{N_p^{\parallel}} \approx 50\%$. The total charge

of the generated positron beam is about 0.002 of the initial electron beam. For the GeV class electron beam generated by LWFA, the beam charge is $\sim$ 10 pC. There will be over 10^5 positron generated from the collision, which can give good statistics to illustrate this effect in an actual experiment.

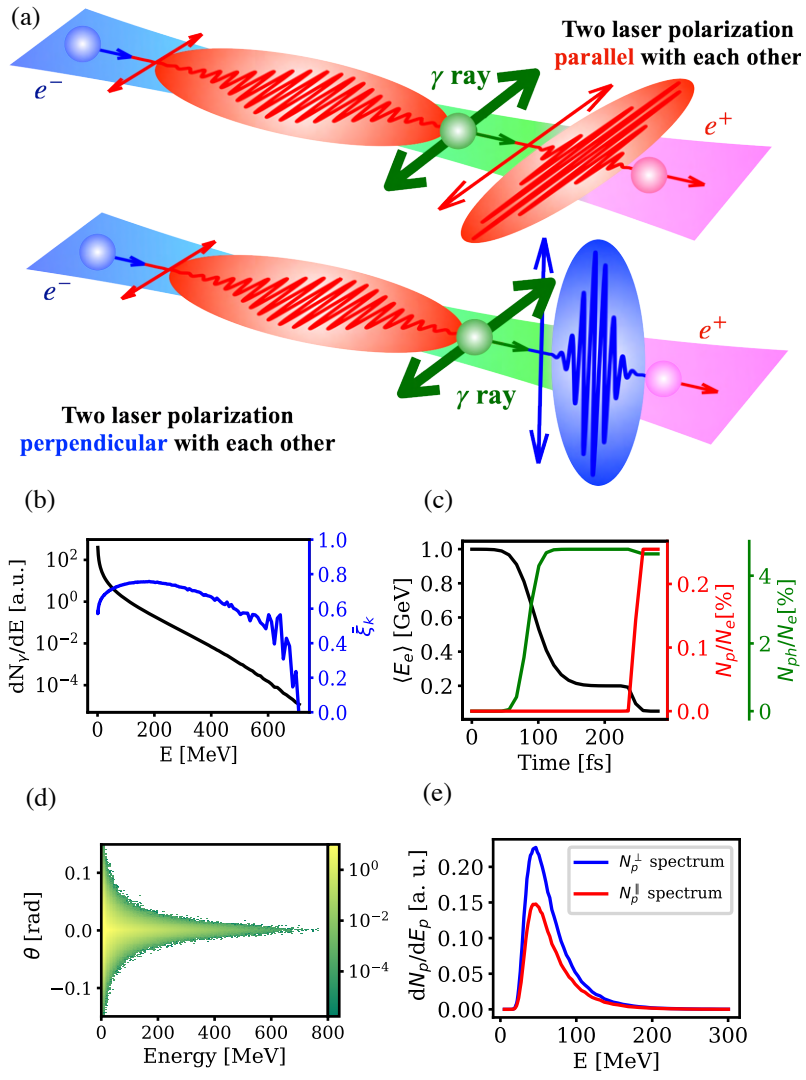

Figure 4.1: (a) Two-pulse pair production setup. (b) Energy spectrum and averaged linear polarization stokes parameter of the gamma-ray beam from the first collision. (c) Temporal evolutions of the electron mean energy, positron yield, and high energy photon ($E > 300$ MeV) yield. (d) Angular spectrum of the gamma-ray after the first collision. (e) The energy spectrum of the generated positron when the polarization direction of the two colliding beams is parallel or perpendicular.

4.3 Analytic Model for Polarization Dependent Pair Production Yield

To help understand the scaling of the electron-positron pair creation, we first formulate scaled equations describing the photon emission, electron beam energy loss, and pair creation in the second laser. For simplicity, we assume the two lasers to be square pulses with infinite spot sizes. This reduces the problem to one dimension. The model does not include 3D effects, such as the overlapping between the laser spot and the electron beam, which could be important for estimating the positron yield. The polarization effect induced positron yield difference Δ_p is less sensitive to the 3D effects and should be well captured by our simplified 1D model. We start from the equation for the radiative energy loss [136]:

$$\frac{d\gamma}{dt} = -\frac{2\alpha_f c}{3\lambda_c}\chi_e^2(t)g(\chi_e) \ , \tag{4.1}$$

where g is the Gaunt factor for quantum radiation correction, $g(\chi_e) \approx [1+4.8(1+\chi_e)\ln(1+1.7\chi_e)+2.44\chi_e^2]^{-2/3}$. We define scaled time τ and scaled energy Γ with respect to the initial energy γ_0:

$$\tau = \gamma_0 t, \ \Gamma(\tau) = \frac{\gamma}{\gamma_0} \ . \tag{4.2}$$

The equation for the radiation force can therefore be rewritten as:

$$\frac{d\Gamma}{d\tau} = -\frac{2\alpha_f c}{3\lambda_c}\chi_1^2\Gamma^2 g(\chi_1\Gamma) \tag{4.3}$$

Here, $\chi_1 = 2\frac{\hbar\omega_0}{m_e c^2}a_{01}\gamma_0$ is the quantum parameter calculated using the *initial* energy of the electron beam γ_0 and normalized intensity a_{01} of the first laser, $\chi_e = \chi_1\Gamma$.

The solution to this equation is

$$\Gamma(\tau) = \frac{1}{1+\frac{2\alpha_f c}{3\lambda_c}\chi_1^2\int_0^\tau d\tau' g(\chi_1\Gamma(\tau'))} \tag{4.4}$$

Note that when $\chi_1\Gamma \ll 1$, the Gaunt factor g tends to 1. In this case, equation 4.4 will recover the exact solution for classical radiation reaction: $\Gamma(\tau) = 1/\left(1 + \frac{2\alpha_f c}{3\lambda_c}\chi_1^2\tau\right)$.

Now assume an electron beam starts with quantum parameter χ_1 and interacts with a square laser pulse whose duration in the rest frame of the electron beam at the beginning is τ_1 ($\gamma_0\tau_1$ in the lab frame). It will generate polarized gamma-rays with spectrum $S(\omega_\gamma, \xi_k)$, where ω_γ is the energy and ξ_k is the polarization state of the gamma-ray beam; in our model $\xi_k \in \{-1, 1\}$. This radiation spectrum can be obtained by integrating the polarization-resolved NLC spectrum generated at every time step over the total interaction time:

$$S(\omega_\gamma, \xi_k) = \int_0^{\gamma_0\tau_1} dt \frac{F_{\mathrm{NLC}}(\chi_e(t), \omega_\gamma, \xi_k)}{\gamma(t)} \tag{4.5}$$

The explicit form of the polarization-resolved NLC spectrum $F_{\mathrm{NLC}}(\chi_e, \omega_\gamma, \xi_k)$ is given in A.26 in the appendix A, where we assume the electron beam to stay unpolarized during the interaction. Replace γ and t with scaled energy and time Γ, τ, and we get:

$$S(\chi_1, \tau_1, \omega_\gamma, \xi_k) = \int_0^{\tau_1} d\tau \frac{F_{\mathrm{NLC}}^{\pi/\sigma}(\chi_1\Gamma(\tau), \omega_\gamma, \xi_k)}{\Gamma(\tau)} \tag{4.6}$$

We then calculate the number of electron-positron pairs after the radiated photon interacts with the second square laser pulse. The second laser pulse's duration in the counter-propagating electron beam's rest frame with energy γ_0 is τ_2. We assume that the electron beam has lost most of its energy after the first collision, so it won't create pairs in the second collision. Hence, the number of pairs generated from the second collision only depends on polarization-resolved NBW rate R_{NBW} and the incoming gamma ray spectrum S, we integrate them over the total interaction time and also the energy of the gamma-ray participants in the pair production process:

$$N_{\rm pair}(\chi_1,\tau_1,\chi_2,\tau_2) = \\ \sum_{\xi_k=\pm 1}\int_0^{\infty} d\chi_\gamma \int_0^{\tau_2} d\tau \frac{R_{\rm NBW}(\chi_\gamma,\xi_k^o)S(\chi_1,\tau_1,\omega_\gamma,\xi_k)}{\chi_\gamma/\chi_2} \tag{4.7}$$

Here, the explicit form of the polarization-resolved NBW rate $R_{\rm NBW}(\chi_\gamma,\xi_k^o)$ is given in Eq. (A.61) in the appendix A. Note that ξ_k^o is the Stokes parameter in the observation frame of the second laser, which for the polarization direction of the second laser to be either parallel or perpendicular to the first laser, $\xi_k^o = \pm\xi_k$. $\chi_2 = 2\frac{\hbar\omega_0}{m_e c^2}a_{02}\gamma_0$ is the quantum parameter calculated using the initial energy of the electron beam γ_0 and normalized intensity a_{02} of the second laser. $\chi_\gamma = \chi_2\frac{\hbar\omega_\gamma}{m_e c^2\gamma_0}$ is the quantum parameter of the photon in the second laser field. Note that this set of equations shows that the scaled radiation reaction and pair creation dynamics does not explicitly depend on the laser parameters $a_{0,i}$ and T_i and initial beam energy γ_0 independently, but only on $\chi_i \propto a_{0,i}\gamma_0$ and $\tau_i = T_i/\gamma_0$, where $i = 1, 2$, in addition to their relative polarization.

4.4 Designing Optimal Parameters

Now we show explicitly that the polarization-resolved electron-positron pair generation $N_{\rm pair}$ effectively only depends on parameters χ_1, χ_2, τ_1, τ_2 and also on the relative polarization of two lasers. Based on equation 4.7, we generate the phase space plot Fig. 4.2 for the ratio of the positron yield when changing the relative polarization directions of the two colliding laser pulses from parallel to perpendicular for different χ_1 (from 0.05 to 1.0) and χ_2 (from 0.5 to 7.0). The first laser pulse duration is set to be long enough to reduce the electron energy so that it won't create many pairs when interacting with the second laser. The second laser pulse scaled time duration $\tau_2 = T_2/\gamma_0 = 0.027$ fs. The contour on the plot shows the number of positrons generated compared with the initial electrons. We verified our numerical calculation results with simulations using the spin and polarization-dependent QED code.

The simulations' parameters and their results are collected in table 4.1 and compared with the predictions given by the model. We find our model well predicts the polarization effect in the positron yield. The absolute positron yield predicted by the model is always smaller than the PIC simulation result, but of the same order of magnitude. The model provides a reasonable estimation of the actual PIC simulation. The discrepancy in positron yield probably comes from the fact that the model does not include the impact of stochasticity in the calculation, which can underestimate the number of high-energy photons generated from quantum radiation. From the phase space plot and the table, we can find that a maximum difference of over 70% is achievable using this setup. However, there is also a trade-off between generating more positrons and increasing the difference in yield when we change the laser polarization direction. We can find that the region in which most positrons are generated is also where the difference in yield is below 30%. The region in which the difference is highest is where the positron charge is less than 10^{-4} of the initial electron beam charge. We can also find that a lower χ_1 can result in a higher difference in positron yield when the laser's polarization direction changes. The reason for this is that the NLC process at lower χ_1 can generate gamma-rays with a higher linear polarization ξ_k. The NBW process's polarization response can explain why the positron yield difference is higher when χ_2 is between 1 and 2.

χ_1	τ_1 [fs]	χ_2	τ_2 [fs]	Mean energy [GeV]	$\left(N_p^{\parallel}/N_e\right)^{sim}$	$\left(N_p^{\parallel}/N_e\right)^{model}$	Δ_p^{sim}	Δ_p^{model}
0.47	0.164	3.55	0.027	1	0.56	0.45	23%	26%
0.236	0.164	2.84	0.027	1	0.15	0.11	38%	40%
0.236	0.164	1.42	0.027	1	0.0053	0.0034	49%	49%
0.236	0.164	1.42	0.027	2	0.0053	0.0034	49%	49%
0.236	0.164	1.42	0.027	4	0.0054	0.0034	50%	49%
0.118	0.327	1.42	0.027	1	8.5×10^{-4}	6×10^{-4}	60%	59%
0.05	0.654	1.42	0.027	1	2.85×10^{-5}	2.3×10^{-5}	71%	72%

Table 4.1: Simulation parameters used to investigate the optimized parameters to maximize the measurable difference in positron yield when we change the laser polarization direction and their results. Here, the pulse duration is defined in scaled time $\tau = t/\gamma_0$. We compare the positron yields, characterized by the ratio between the number of generated positrons and initial beam charge, and the polarization effect induced difference in positron yields $\Delta_p = (N_p^{\perp} - N_p^{\parallel})/N_p^{\parallel}$ in the simulations with the predictions from our model.

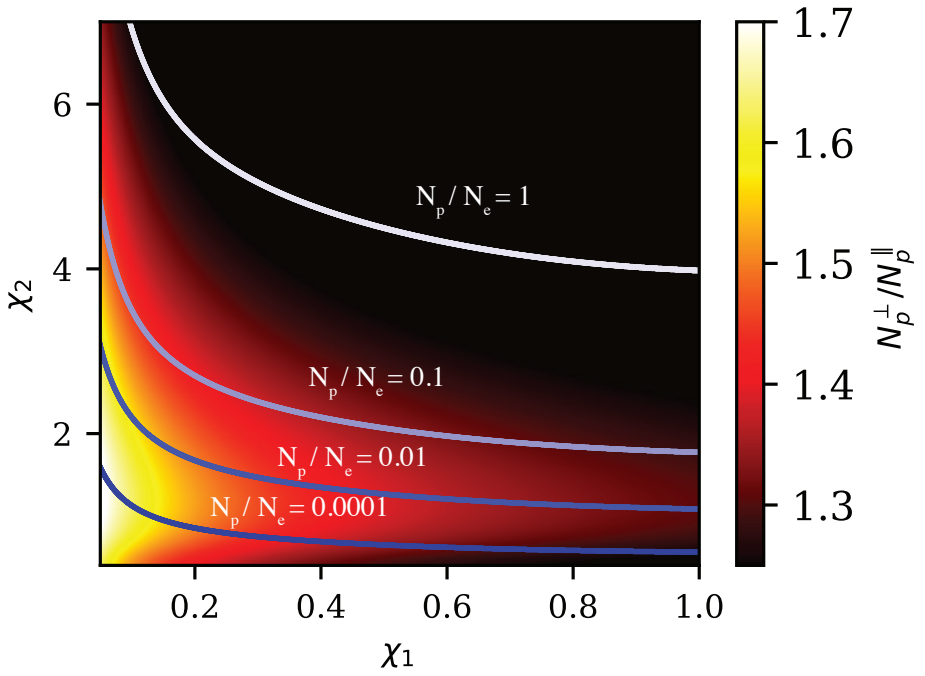

Figure 4.2: The phase space plot for the ratio of the positron yield when changing the polarization directions of two colliding laser pulses from parallel to perpendicular for different χ_1 and χ_2.

We have shown how the difference in positron yield depends on normalized parameters χ_1, χ_2, τ_1, τ_2. To design an actual experiment, giving some criteria for the laser and electron beam parameters in practical units is necessary. We start by considering the criteria for the first laser pulse. We want the pulse duration to be long enough to reduce the energy of the electron beam to the level that its interaction with the second laser pulse in the NBW pair production process becomes unimportant. Using equation 5.2, we predict the minimum requirement of the pulse duration to reduce the electron beam mean energy below 10% of its original value for different laser peak intensities and electron beam initial energy in Fig. 4.3. The reason to choose 10% initial beam energy as the energy reduction criterion is because, as shown in Eq. 4.3, the ability of radiation reaction to slow down the electron beam at this energy level is much weaker than at the beginning. The white and cyan color regions in Fig. 4.3 marks the space unsuitable for the experiment; we want the maximum quantum

parameter $\chi_e(t) = 2\frac{\hbar\omega_0}{m_e c^2} a_0 \langle \gamma_e \rangle_{t=0}$ to be within the range of 0.05 and 0.5. The white region at the bottom left corner of the plot marks the parameter space for $\chi_e < 0.05$, in which insufficient high-energy photons will be generated. The cyan color region at the upper right corner marks the parameter space $\chi_e > 0.5$, in which the NBW pair production process is substantial when the electron beam interacts with the first laser pulse. The generated pairs from the first collision, contributing to the background, will reduce the difference in the positron yield when changing the laser polarization direction in the second collision.

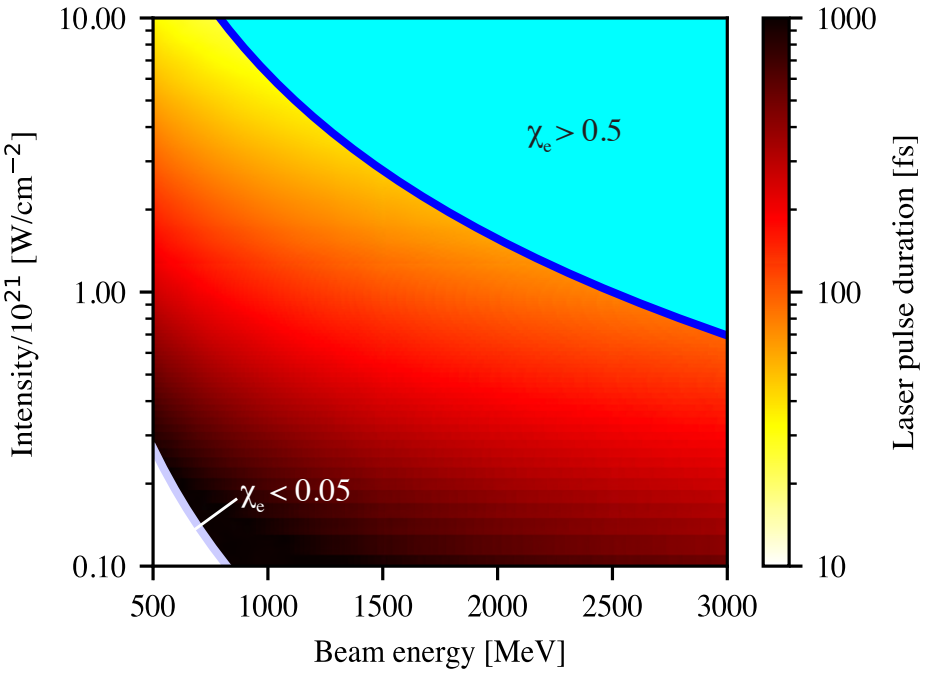

Figure 4.3: The minimum requirement for pulse duration of the first laser pulse for different input beam energies and laser intensities in the first collision. The regions on the upper right and lower left are where $\chi_e < 0.05$ and $\chi_e > 0.5$.

In designing the parameters for the second laser, we also need to consider the depletion of the high-energy photons by the NBW process when the pulse duration is too long. Suppose that all high-energy photons turn into electron-positron pairs after the second collision. In this case, we cannot observe a difference in positron yield when we change the laser polarization direction. Using equation 4.8 and presume the input photon beam to have

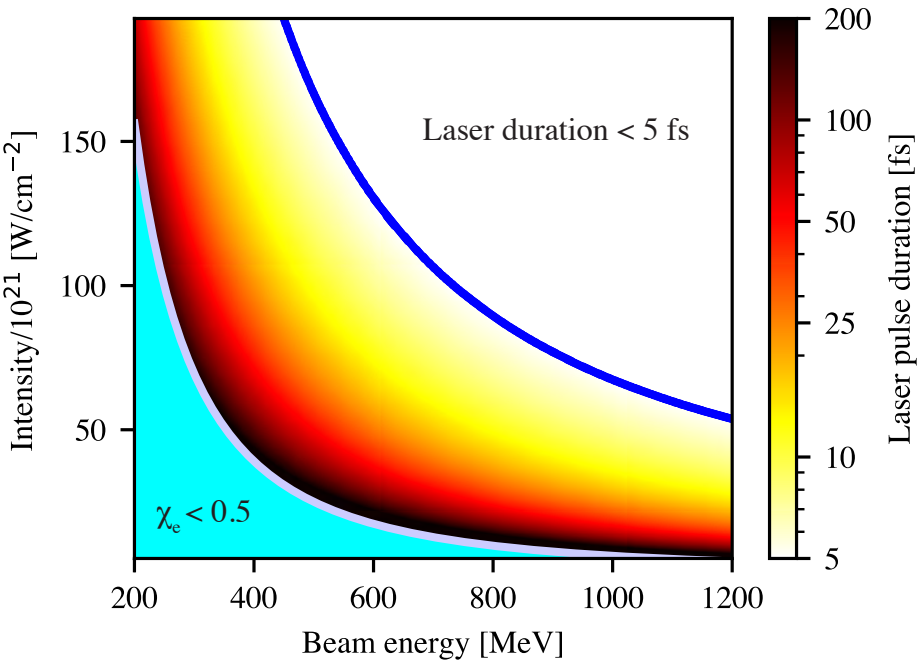

Figure 4.4: The maximum duration of the second laser pulse for different input gamma-ray beam energies and laser intensities in the second collision. The regions on the lower left are where $\chi_e < 0.5$. The upper right corner is the region with laser duration is $t_2 < 5$ fs.

an averaged stokes parameter of the input photon beam $\bar{\xi}_k = 0.6$ ($N_\gamma^{\xi_k=1} = 4N_\gamma^{\xi_k=-1}$), we generate Fig. 4.4 that predicts the maximum laser duration we can have for which greater than 25% difference in positron yield is observable when changing the laser pulse polarization direction for varying laser peak intensity and input beam mean energy:

$$\begin{aligned}\Delta_p &= \frac{N_p^{\perp} - N_p^{\parallel}}{N_p^{\parallel}} \\ &= \frac{\left(N_\gamma^{\xi_k=1} - N_\gamma^{\xi_k=-1}\right)\left(e^{-R_{\mathrm{NBW}}^{\xi_k=1}t} - e^{-R_{\mathrm{NBW}}^{\xi_k=-1}t}\right)}{N_\gamma^{\xi_k=1}\left(1 - e^{-R_{\mathrm{NBW}}^{\xi_k=1}t}\right) + N_\gamma^{\xi_k=-1}\left(1 - e^{-R_{\mathrm{NBW}}^{\xi_k=-1}t}\right)}\end{aligned} \tag{4.8}$$

In Fig. 4.4, we mark two regions that are not ideal for the experiment. The upper right corner of the plot shows a pulse duration smaller than 5 fs, which is too short to generate with current technology. The bottom left corner marks the region in which the maximum quantum parameter $\chi_\gamma = 2\frac{\hbar\omega_0}{m_e c^2} a_0 \langle\gamma\rangle_{t=0}$ is smaller than 0.5. Here, we consider the resolution of

observing the difference in positron yield Δ_p when we change the laser polarization direction, which can be estimated through the statistical uncertainty $1/\Delta_p\sqrt{N_p}$. For a single shot measurement, assuming $\Delta_p = 0.5$; having more than $\sim$ 1000 positrons generated will be desirable. This corresponds to a resolution of about 5%. A laser wakefield beam typically contains charge on the order of several pC, which contains about 10^7 electrons. The positron yield should be at least 10^{-4} of the initial electron beam charge. According to Fig. 4.2, when $\chi_2 < 0.5$, the positron yield will always be below 10^{-4} of the initial electron beam charge. Below this threshold, there won't be many positrons generated during the interaction, which makes the positron charge measurement unlikely.

The parametric study of the polarization dependence NBW process under the two pulse pair production setup provides insight into the ideal parameters to observe a clear signal of polarization effect in pair production yield for an all-optical experiment. Here, we propose a set of optimal experimental parameters. For a 1 GeV electron beam from the laser wakefield accelerator, the laser pulse for the first collision needs to have a moderate intensity of $0.2 - 1.5 \times 10^{21}$ [W/cm^{-2}] and a long duration of 0.1 to 1 ps. The second laser pulse should be with an intensity of $10 - 90 \times 10^{21}$ [W/cm^{-2}] and a duration of $20 - 40$ fs. In the ideal scenario, a $40 - 60\%$ difference in positron yield is expected with the proposed parameter when we change the laser polarization direction.

4.5 Conclusion

With experimental studies of the strong-field QED regime in the laboratory likely to be realized with new facilities coming online, developing a more accurate QED module with the effect of lepton spin and photon polarization taken into account becomes necessary. Recent studies of how including spin and polarization in the calculation will result in a considerable difference in QED cascade simulation [73, 72, 156], as well as polarized gamma-ray and lepton beams generation through strong field QED process [54, 4, 7, 8], add to the value of

developing a full spin and polarization-resolved QED module in PIC code. This work presents our spin and polarization-resolved quantum radiation reaction module based on PIC code framework Osiris 4.0. The success of reproducing Ref. [73]'s main results of studying the polarized seeded cascade marks the code's reliability in dealing with complicated multi-stage QED processes. We have used this to demonstrate a two-pulse-pair production scheme for experimentally measuring the effect of the gamma-ray polarization state on the NBW pair creation and find the optimized condition for maximizing the yield of pair production when we rotate the laser polarization direction. This was achieved through our numerical model and parameterized through a set of normalized differential equations. The simulation result predicts a difference in yield of over 50% by simply changing the polarization directions of two linearly polarized laser pulses, which should be an easily measurable signature in a real experiment. We also broadly discuss the criteria for the laser and electron beam parameters under practical units to design an actual experiment, which is achievable in the near future. Notice that the model we present in this work (see in Section B) has the limitation that it requires the lepton beam to be initially unpolarized and using a field with a fixed direction, like a linearly polarized laser [145]. As a result, our simplified model applies to the situations studied in this work. In a general field configuration, the lepton spin and photon polarization components combining all three orthogonal directions ($\boldsymbol{\varepsilon}$, $\boldsymbol{\beta}$, $\boldsymbol{\kappa}$) must be considered and is currently being implemented in the Osiris 4.0 framework (see in Section 3.2.1).

CHAPTER 5

Gamma Flash Measurement by Polarization

5.1 Introduction

New multi-PW power lasers are on the verge of creating an entirely new state in the laboratory dominated by the interplay of strong-field quantum electrodynamics (QED) processes and ultra-relativistic plasma effects [157, 158, 101, 49, 159]. These 'QED-plasmas' are found in extreme astrophysical environments, such as pulsar magnetospheres [160, 161], but have yet to be realised in the laboratory. In this chapter[1], we will describe a possible way to observe this behaviour by observing the bright flashes of hard photons, which are a hallmark of QED plasmas, using polarimetry. The two dominant processes in laser-generated QED-plasmas are hard photon emission as electrons (and positrons) in the plasma are accelerated by the strong laser and plasma electromagnetic fields (nonlinear inverse Compton scattering - NLCS). The burst of hard photons is therefore one of the observables of strong-field QED effects in a plasma. The brilliant NLCS 'x-ray flash'[2][157, 162] is predicted to be one of the most prominent signatures that the QED-plasma regime has been reached and thus a first unambiguous observation of this is a high priority [163, 164, 165, 166]. Several groups have reported an observation of the NLCS x-ray flash but the background was very high

[1]This chapter summarizes: Q. Qian, C.P. Ridgers, S.V. Bulanov, T. Grismayer, P. Hadjisolomo, D. Seipt, M. Vranic, A.G.R. Thomas, "Bright polarised x-ray flashes from dense plasmas" (submitted). Co-authored with C.P. Ridgers, I performed all simulations and analyses presented in this paper.

[2]Note that the hard photons are often referred to as gamma-rays for photon energies $> 1\,\mathrm{MeV}$. We will refer to all hard photons as X-rays for simplicity. This is because we consider hard photons with 1-100 keV energies as well as those above 1 MeV.

[167, 168]. The main source of background x-ray emission in the >keV energy range is from bremsstrahlung emission as electrons in the laser-produced plasma scatter from the ions. The bremsstrahlung occurs over a much longer timescale than the NLCS (tens of ps compared to 100 fs), and so it is difficult to model using PIC. Recent simulations using a hybrid-PIC model have simulated the bremsstrahlung for the required 100 ps [169] and shown that the background is much higher than expected from previous, shorter timescale PIC simulations [170]. Hybrid-PIC has recently been used to show that NLCS may be observed clearly above bremsstrahlung only at intensities $> 10^{22}\,\mathrm{Wcm}^{-2}$ [171], and within a certain range of target thickness [172]. Observing the x-ray flash at lower intensities more commonly available in experiments ($\sim 10^{21}\,\mathrm{Wcm}^{-2}$) is therefore a challenge.

In this work, we will show that the NLCS flash gives rise to highly polarized x-rays (50-70%) in the energy range 1-10 keV. And for the moderate laser intensity region we studied here ($I \sim 10^{21}\,\mathrm{Wcm}^{-2}$), at higher photon energies (> MeV), the polarization becomes almost complete. This demonstrates that X-ray polarimetry is an ideal tool to observe the X-ray flash and so the onset of the QED-plasma regime. The study of X-ray polarization and its measurement has gained importance recently in various fields, including atomic physics [173], astrophysics [174], and laser-plasma interactions [175], with measurement ranges from a few keV to GeV. It is worth mentioning that the bremsstrahlung process could also generate polarized X-rays. However, the polarized light from bremsstrahlung is mainly in the side direction perpendicular to the plane of the laser beam and the target normal, unlike the signal from NLCS, which is basically along or opposite to the laser propagation direction [176]. One can easily rule out polarized X-rays from the bremsstrahlung effect by taking several measurements around the targets.

5.2 Model for Hard Photon Polarization

We would like to predict the expected degree of polarization of the hard photons emitted in a given laser-plasma interaction. Here we will build a simple model to do this. We will consider only the simplest case of a laser interacting with a slab target. This is a case often realized experimentally. We will assume a fully-ionized aluminum target, with electron density $n_e = 450 n_c$. $n_c = 1.75 \times 10^{21}\,\mathrm{cm}^{-3}$ is the critical density for 800 nm light. The plasma skin depth for this solid target is $\delta_p = \frac{\omega_{pe}}{c} = \sqrt{\frac{n_c}{n_e}}\lambda$, here λ is the laser wavelength. In our model, as the laser pulse intensity is under the relativistic region, the relativistic skin depth is a more relevant scale length. It can be approximated as: $\delta_p^r \approx a_0\sqrt{\frac{n_c}{n_e}}\lambda$. We assume that the number of electrons that interact with the laser is $N_e = n_e \pi w_0^2 \delta_p^r$. The laser is linearly polarized, with wavelength $\lambda = 800\,\mathrm{nm}$, and temporal duration $\tau_0 = 20\,\mathrm{fs}$. For simplicity of calculation, we further assume that the intensity within the laser spot size w_0 is uniform. The spot size in the model is $\sqrt{2}$ smaller than the spot size used in the PIC simulation, which has a transverse Gaussian profile, ensuring that the power at focus remains the same.

We can estimate the quantum parameter χ_e reached by electrons in the plasma using the following formula [177]

$$\chi_e = 0.1\sqrt{\frac{I}{10^{21}\,\mathrm{Wcm}^{-2}}}\frac{E}{500\,\mathrm{MeV}}. \tag{5.1}$$

The laser intensity I is related to a_0 by $I \sim a_0^2 \times 10^{18}\mathrm{Wcm}^{-2}/(\lambda\ [\mu\mathrm{m}])^2$. If we assume that the electron energy $E = a_0 m_e c^2$ then χ_e depends only on a_0.

We solve the evolution of the energy of the electrons during collision, starting from the equation for the radiative energy loss [177]:

$$\frac{d\gamma}{dt} = -\frac{2\alpha_f c}{3\lambda_c}\chi_e^2(t) g(\chi_e)\ , \tag{5.2}$$

where $G(\chi_e)$ is the gaunt factor for quantum radiation correction, $g(\chi_e) \approx [1 + 4.8(1 + \chi_e)\ln(1 + 1.7\chi_e) + 2.44\chi_e^2]^{-2/3}$. The electrons will generate polarized x-rays with spectrum

$S(\varepsilon_\gamma, \boldsymbol{\xi})$, where ε_γ is the energy and $\boldsymbol{\xi}$ is the polarization state. Because the electrons that participate in the NLC process here are mainly unpolarized. The x-ray photons can only be linearly polarized, so we replace the Stokes vector $\boldsymbol{\xi}$ with the linearly polarized degree ξ, which $\xi \in \{-1, +1\}$, $\xi = +1$, the photon fully polarized along the laser polarization direction, $\hat{\boldsymbol{o}}_1$, and when $\xi = -1$, the photon fully polarized along direction $\hat{\boldsymbol{o}}_2$, which is perpendicular to laser polarization direction $\hat{\boldsymbol{o}}_1$ and laser propogation $\hat{\boldsymbol{k}}$. How the polarization bases are defined is discussed in Section 2.10.2 in detail. The radiation spectrum can be obtained by integrating the polarization-resolved NLCS spectrum generated at every time step over the total interaction time τ_0,

$$S(\varepsilon_\gamma, \xi_k) = C_0 \int_0^{\tau_0} dt F_{\mathrm{NLC}}(\chi_e(t), \varepsilon_\gamma, \xi). \tag{5.3}$$

The explicit form of the polarization resolved NLCS spectrum $F_{\mathrm{NLC}}(\chi_e, \varepsilon_\gamma, \xi)$ is given in equations A.15 and A.25. The number of photons radiated with energy above ε_{th}: $N_\gamma(\varepsilon_{th})$ can be calculated simply by integrating the photon spectrum above the energy threshold ε_{th} and then multiplying by the estimated number of electrons in the interaction N_e, i.e.

$$N_\gamma(\varepsilon_{th}, \xi) = N_e \times \int_{\varepsilon_{th}}^{\infty} d\varepsilon_\gamma \; S(\varepsilon_\gamma, \xi). \tag{5.4}$$

The expected degree of linear polarization can be calculated as:

$$\langle \xi_3 \rangle(\varepsilon_\gamma) = \frac{S(\varepsilon_\gamma, +1) - S(\varepsilon_\gamma, -1)}{S(\varepsilon_\gamma, +1) + S(\varepsilon_\gamma, -1)}. \tag{5.5}$$

Also, the expected degree of linear polarization above the energy threshold ε_{th} is:

$$\langle \xi_3 \rangle(\varepsilon_{th}) = \frac{N(\varepsilon_{th}, +1) - N(\varepsilon_{th}, -1)}{N(\varepsilon_{th}, +1) + N(\varepsilon_{th}, -1)}. \tag{5.6}$$

5.3 Comparison of Hard Photon Polarization Model to PIC Simulations

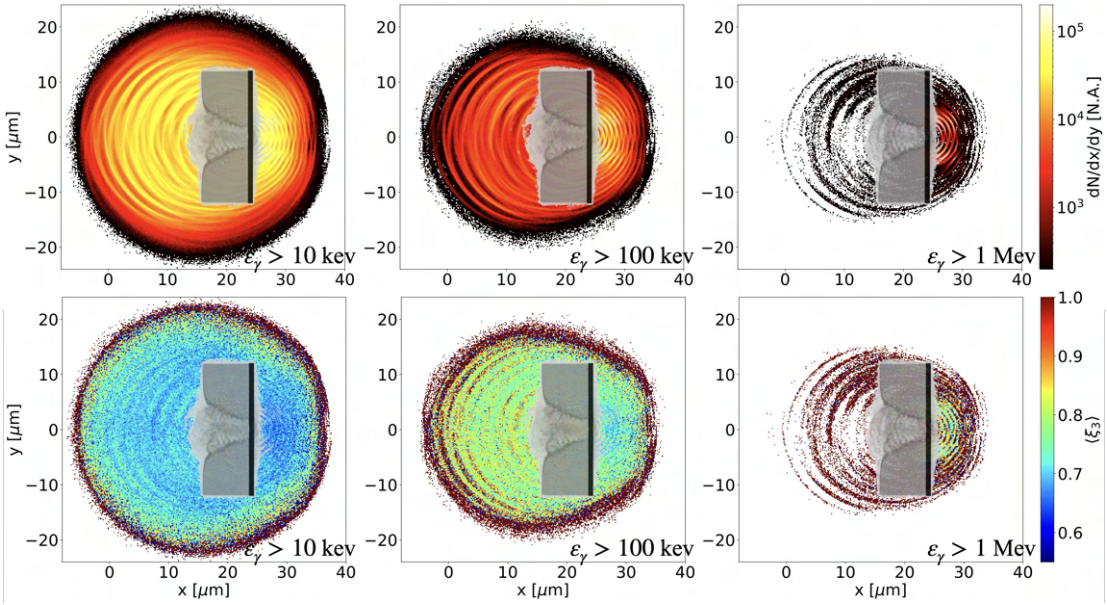

Figure 5.1: Top row: Photon density distribution in x-y simulation plane for the population with energy above (a) 10 keV, (b) 100 keV, (c) 1MeV after the laser fully reflected from the target. Bottom row: Photon linear polarization distribution in the x-y simulation plane for the population with energy above (d) 10 keV, (e) 100 keV, (f) 1MeV after the laser fully reflected from the target. $\langle\xi_3\rangle$ measures the photon averaged linear polarization degree, which, when the photon is fully polarized along the laser polarization direction, is $\langle\xi_3\rangle = 1$. The gray scale plot shows the target electron density distribution.

For comparison to the model in Sec. 5.2, we conduct 2-D spin and polarization-resolved PIC simulations for the laser pulse impinging upon a $0.8\,\mu$m thick Al foil $n_p = 450n_c$ with $8\,\mu$m thick $n_p = 5n_c$ pre-plasma in front of the foil. The laser has $a_0 = 15,\ 20,\ 25,\ 30,\ 40$, wavelength $\lambda = 0.8\,\mu$m, spot size $w_0 = 4\,\mu$m and duration $\tau_0 = 20\,$fs. The laser is linearly polarized along the y-direction in the simulation plane and initially travels in the positive x-direction in the simulation. We choose a larger laser spot size compared to the simple model because, in the simulation, the laser has a transverse Gaussian profile, whereas in the model, we simply assume the intensity within the spot size is uniform. First, we show OSIRIS simulation results for a laser with $a_0 = 25$ interacting with the target. Figure 5.1 shows both

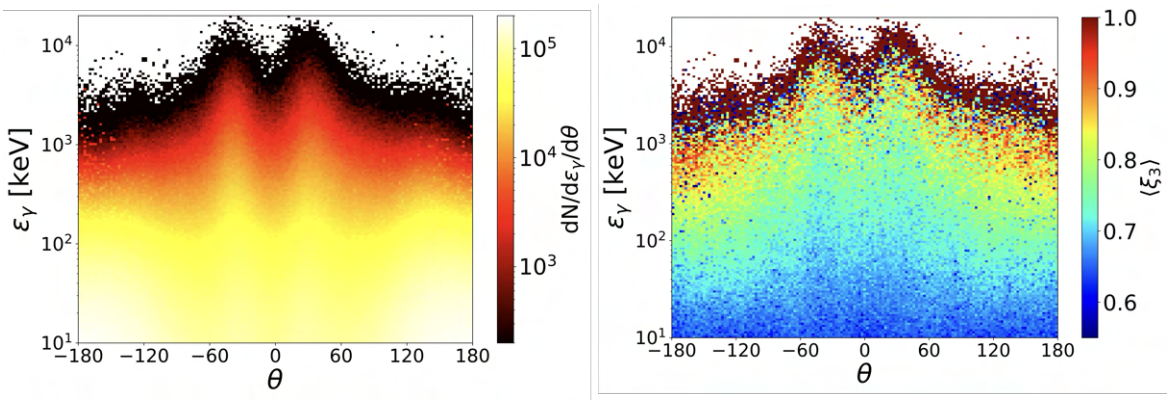

Figure 5.2: Angle-resolved (a) Photon density distribution $\frac{d^2N}{d\theta dE}$, (b) Photon linear polarization $\langle\xi_3\rangle$ distribution. This angular density/polarization map corresponds to the same simulation shown in Fig. 5.1.

the x-ray photon density and their average degree of linear polarization ($\langle\xi_3\rangle$), in the x-y simulation plane (which is also the emission plane), for the population with energy above 10, 100 keV, and 1 MeV. We also plot the target electron density distribution as a reference on top of the photon distribution. Figure 5.2 shows the angular-energy distribution of the photon density and the degree of linear polarization in the emission plane. Both figures show that X-ray photons with energy between 10 and 100 keV have a relatively uniform spatial and angular distribution in the emission plane and are more likely to travel in the negative x direction. Higher energy ($> 100\,\text{keV}$) x-ray photons are more likely to travel in the positive x direction. We can also see that the linear polarization degree increases with the photon energy.

Figures 5.3 and 5.4 show the prediction of the photon yield and the degree of photon polarization above a certain energy threshold based on the simplified model described in section 5.2. We plot the photon yield and the degree of polarization from the simulations in figures 5.3, 5.4 and 5.5. For different a_0 these are also listed in the tables 5.1, 5.2 and 5.3.

Although the simulations and the simplified model are based on similar physical principles, their setups differ considerably, resulting in quantitative differences in both photon yield and polarization degree. Nevertheless, both approaches display consistent qualitative trends within the explored intensity range ($a_0 = 10$–50): the linear polarization of emitted x-rays

decreases with increasing laser a_0 and increases with photon energy. Notably, for photons with energies above 10,keV, the polarization degree remains above 65% and can exceed 80% at higher energies. These results provide valuable insights for future experimental design.

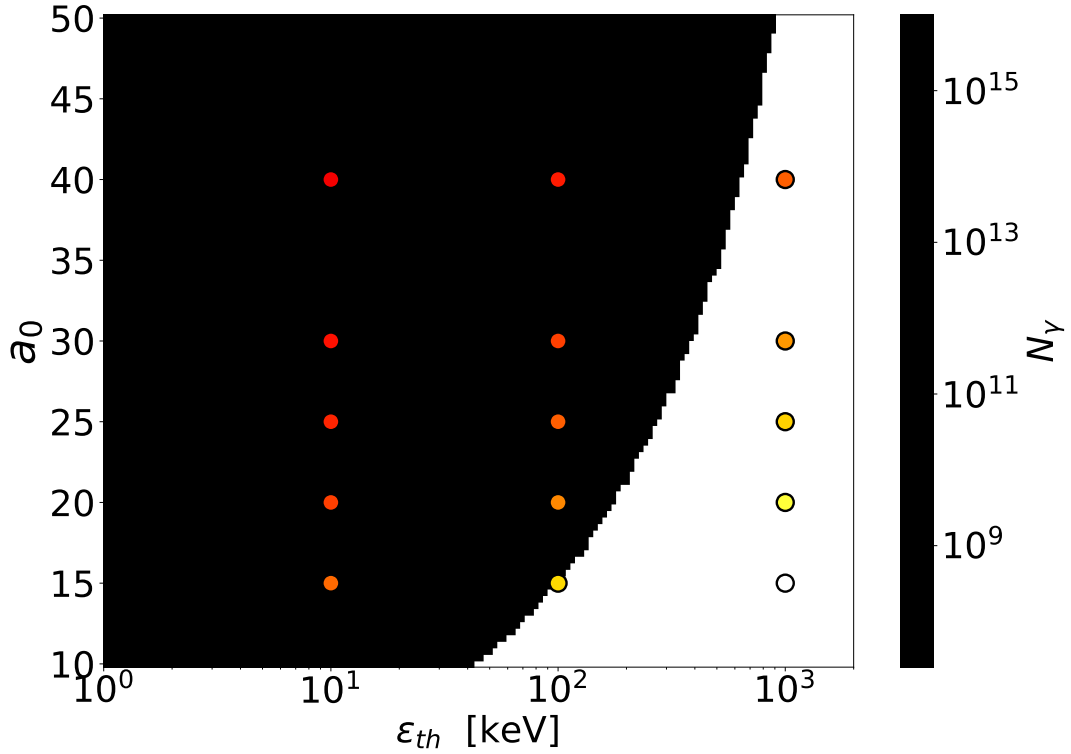

Figure 5.3: NLCS x-ray photon number above energy ε_{th} in a laser solid target interaction with different laser intensity a_0

Energy ε_{th}	$a_0 = 15$	$a_0 = 20$	$a_0 = 25$	$a_0 = 30$	$a_0 = 40$
$> 10\,\mathrm{keV}$	$N_\gamma = 3.19 \times 10^{11}$	1.1×10^{12}	2.5×10^{12}	4.6×10^{12}	9.7×10^{12}
$> 100\,\mathrm{keV}$	$N_\gamma = 1.2 \times 10^{10}$	1.25×10^{11}	4.4×10^{11}	1.16×10^{11}	3.35×10^{11}
$> 1\,\mathrm{MeV}$	$N_\gamma = 7 \times 10^{6}$	1.2×10^{9}	1.5×10^{10}	8.2×10^{10}	4.36×10^{11}

Table 5.1: Simulation results shown in Fig. 5.3 to compare with the analytic prediction of NLCS x-ray photon number above energy ε_{th} in a laser solid target interaction with different laser intensity a_0.

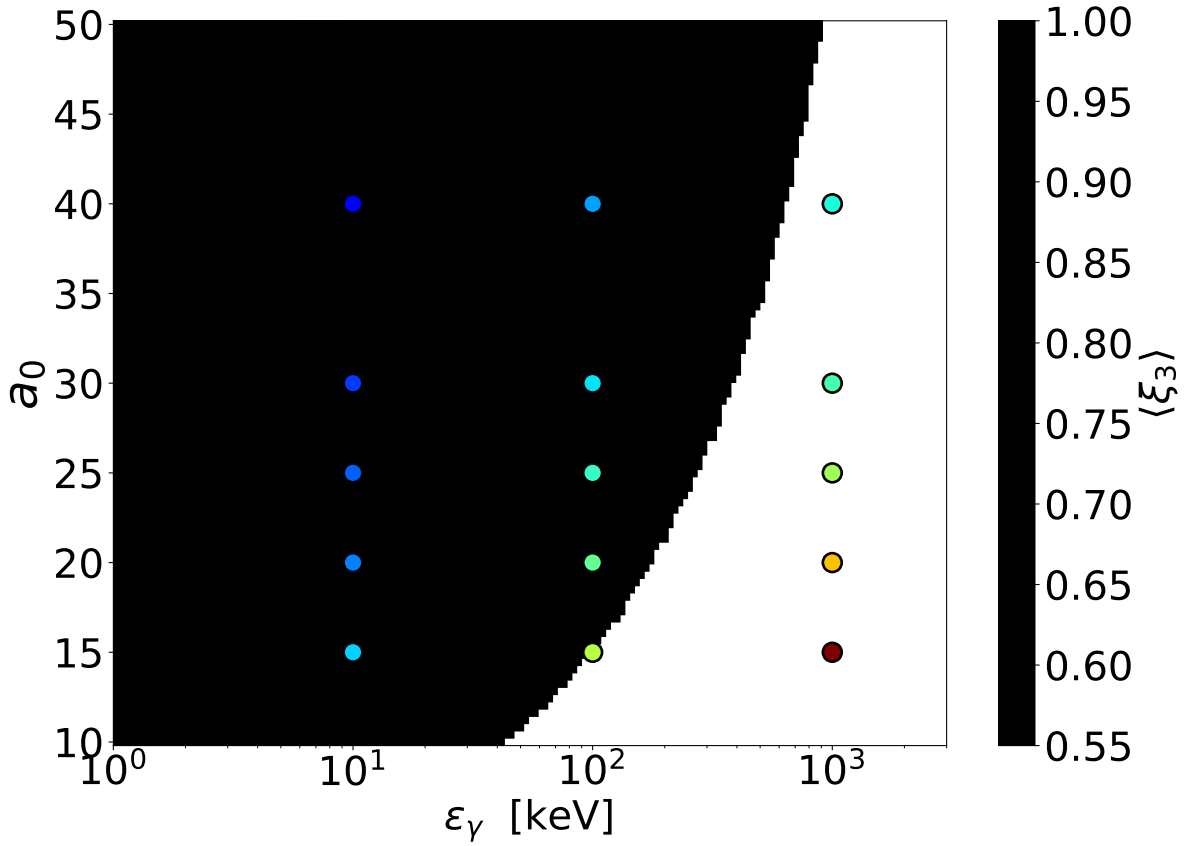

Figure 5.4: NLCS x-ray photon polarization in a laser solid target interaction as a function of a_0 and the energy of the emitted photon

Energy ε_γ	$a_0 = 15$	$a_0 = 20$	$a_0 = 25$	$a_0 = 30$	$a_0 = 40$
= 10 keV	$\langle \xi_3 \rangle = 70\%$	67.6%	64.9%	63.1%	60.5%
= 100 keV	$\langle \xi_3 \rangle = 81\%$	76.8%	73.7%	70.8%	67.8%
= 1 MeV	$\langle \xi_3 \rangle = 100\%$	87.1%	79.6%	74.5%	72.3%

Table 5.2: Simulation results shown in Fig. 5.4 to compare with the analytic prediction of NLCS x-ray photon polarization in a laser solid target interaction as a function of a_0 and the energy of the emitted photon

Energy ε_{th}	$a_0 = 15$	$a_0 = 20$	$a_0 = 25$	$a_0 = 30$	$a_0 = 40$
> 10 keV	$\langle \xi_3 \rangle = 74\%$	73.1%	69.5%	67.8%	66%
,> 100 keV	$\langle \xi_3 \rangle = 81.9\%$	79.7%	75.6%	73%	71%
> 1 MeV	$\langle \xi_3 \rangle = 99\%$	89.5%	79%	77%	74.6%

Table 5.3: Simulation results shown in Fig. 5.5 to compare with the analytic prediction of NLCS x-ray photon polarization for photons above energy ε_{th} in a laser solid target interaction with different laser intensity a_0

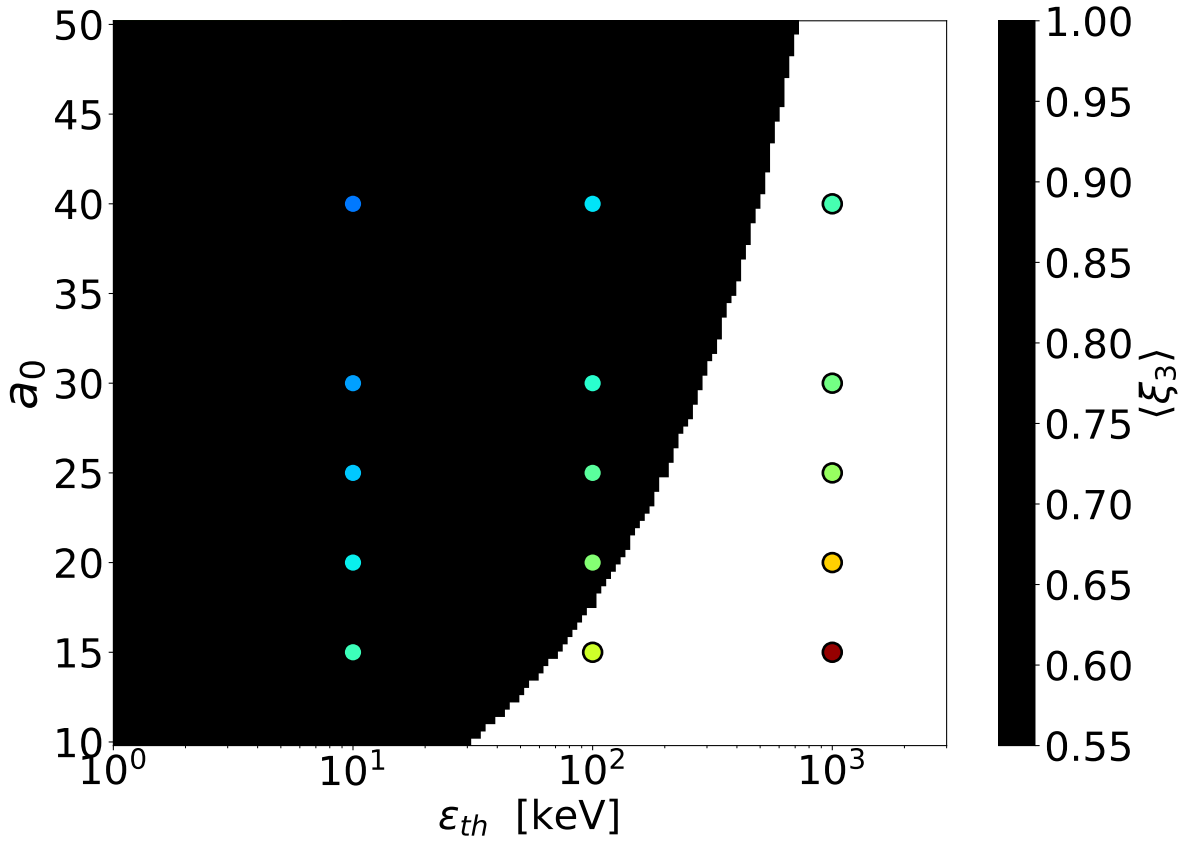

Figure 5.5: NLCS x-ray photon polarization for photon above energy ε_{th} in a laser solid target interaction with different laser intensity a_0

5.4 Conclusions

By employing a newly developed emission module in the OSIRIS PIC code, we demonstrate that keV photons generated via nonlinear Compton scattering (NLCS) in $>$ 1 PW laser-plasma interactions are highly polarized, with degrees of polarization exceeding 80%. This stands in clear contrast to x-rays produced by other mechanisms, such as bremsstrahlung, which typically exhibit much lower polarization. As a result, x-ray polarimetry offers a promising diagnostic for distinguishing NLCS x-ray flashes from background sources.

CHAPTER 6

Spin and Polarization-Resolved QED Cascades

6.1 Introduction

The rapid advancement of high-power laser technology over the past several decades has significantly propelled research across numerous fields of physics. With multi-10 PW laser systems expected to become operational in the coming years, laser-plasma interactions are poised to enter a new regime where quantum electrodynamic (QED) effects can profoundly alter the collective behavior of plasmas. This regime, often referred to as "QED plasma" in the literature, is typically found only in some of the most extreme astrophysical environments. One of the most famous phenomena predicted in the QED plasma region is the QED cascades[1]. Hot, dense electron-positron pairs and gamma-ray photons can be generated during the cascade, converting energy into the creation of real particles. The secret behind this prolific particle generation is the chain reaction of two fundamental SFQED processes: the nonlinear Compton process (NLC), in which the high-energy lepton inside the strong field gives its energy to generate high-energy gamma rays, and the nonlinear Breit-Wheeler process, in which high-energy gamma rays inside the strong field decay into electron-positron pairs. The quantum parameters χ_e is used to characterize the QED processes, which are

[1]This chapter summarizes: Q. Qian, D. Seipt, M. Vranic, T. E. Grismayer, T. G. Blackburn, C.P. Ridgers, A. G. R. Thomas, "Polarized electron-positron pair plasma generation in QED cascades" (in preparation). I completed all simulations and analysis, with theoretical work conducted jointly with A. G. R. Thomas.

likely to occur when $\chi_e > 1$. In reality, this condition can be most easily achieved through the collision of a high-energy lepton beam with a laser beam or through the collision of two intense laser beams onto a seeding target. The first setup, in some literature called a shower-type cascade, only requires one high-intensity laser beam; the pair production is constrained by the energy of the electron beam. The second setup is called an avalanche-type cascade, which requires two high-intensity laser beams. Inside the standing wave structure formed by two lasers crossing each other, the field is strong enough to accelerate particles to high energy and cause further pair production until the field is depleted. In this way, the pair production process can be more efficient.

The QED cascade has been well studied using the unpolarized SFQED model. Interesting phenomena, such as the prolific generation of electron-positron pairs and strong absorption of a laser field, have been observed in the simulations [178, 179, 141]. However, there are still relatively few spin-polarized QED cascade calculations that appear in the literature. The existing one is calculated under an idealized setup, like in a rotating electric field [73], or by studying the QED cascade using two linearly polarized lasers [156]. The QED cascade is a multistage process with chaotic particle motion during the interaction. It will be interesting to have a full PIC simulation to see whether spin and polarization effects can be observable in this complicated interaction system.

In this work, we present our recent results on longitudinally polarized electron-positron beam generation through both shower-type and avalanche-type cascades. The avalanche-type cascade formed by two high-intensity CP lasers enables us to generate a spin-polarized electron-positron pair plasma with an averaged degree of longitudinal polarization $\langle S_{lon} \rangle = \langle \boldsymbol{s} \cdot \hat{\boldsymbol{v}} \rangle > 20\%$, where $\hat{\boldsymbol{v}}$ is the direction of electron/positron velocity, and a maximum degree of longitudinal polarization of more than 30%. The shower-type cascade from a single CP laser colliding with an unpolarized electron beam can generate a polarized electron-positron beam with an averaged degree of longitudinal polarization $\langle S_{lon} \rangle > 40\%$, and the high-energy part of the positron beam, which accounts for $> 8\%$ of the initial electron beam population, gains

over 70% longitudinal polarization. We scan parameters such as target density and laser intensity for the avalanche-type cascade, as well as laser intensity and beam energy for the shower-type cascade, to investigate the impact of these parameters on the polarization effect in the QED cascade process. We also try to provide an intuitive physical model to explain the polarization mechanism. The proposed laser parameters are moderate compared to the QED cascades study in the literature. Our work presents a novel approach to generating a longitudinally polarized electron-positron plasma through the QED cascade and a method for generating a highly polarized longitudinal positron beam using a simple all-optical setup.

6.2 Spin Polarized Avalanche Cascade by Two CP Lasers

We begin our study by investigating spin- and polarization-resolved QED avalanche cascades. The setup of the simulation is shown in Fig. 6.1. Our two-dimensional simulations use two circularly polarized lasers ($a_0 = 600$, $\lambda_0 = 1$ μm, $\tau = 20$ fs, and spot size $w_0 = 4$ μm) colliding on a 1 μm-thick, $6, \mu$m-thick target with a density of 5×10^{23} cm^{-3}. The lasers are co-rotating, symmetrically positioned, and phase-matched relative to the target to form an overlapping standing wave that alternates between regions dominated by electric and magnetic fields.

Key simulation results are presented in Fig. 6.2: panels (a) and (b) show the spatial distribution of longitudinal polarization for electrons and positrons, respectively, while panels (c) and (d) display their density profiles after the cascade and during the full laser overlap. Our findings reveal that both electrons and positrons achieve an average longitudinal polarization above 20%, peaking at 30%. After the cascade, the expanding electron-positron pairs form an approximately spherical distribution, with the highest degree of polarization concentrated near the laser propagation axis. The total charge of the polarized pairs can exceed $\sim$1 nC, and the generated pair plasma is dense enough to exhibit collective effects.

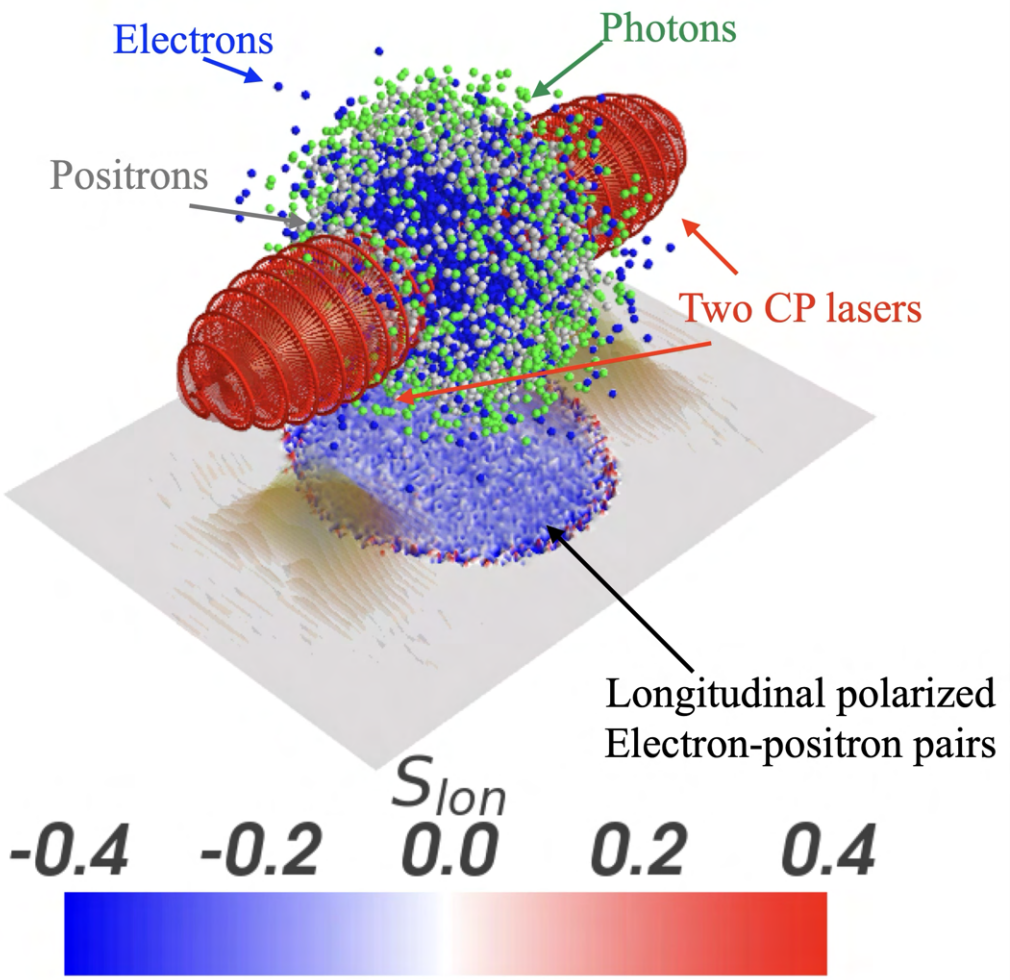

Figure 6.1: Spin polarized QED cascades

A key observation is that the direction of longitudinal polarization can be reversed simply by switching the laser helicity, as shown in Fig. 6.3. Despite this reversal, the spin and density distributions remain otherwise unchanged. The angular momentum distribution for positrons (see Fig. 6.4) shows the strongest polarization for particles near the axis, peaking

at emission angles of approximately $\pm 10°$. Notably, reversing the laser helicity only changes the sign of the longitudinal polarization, demonstrating a direct correlation between the helicity of the driving laser fields and that of the produced electron-positron pairs.

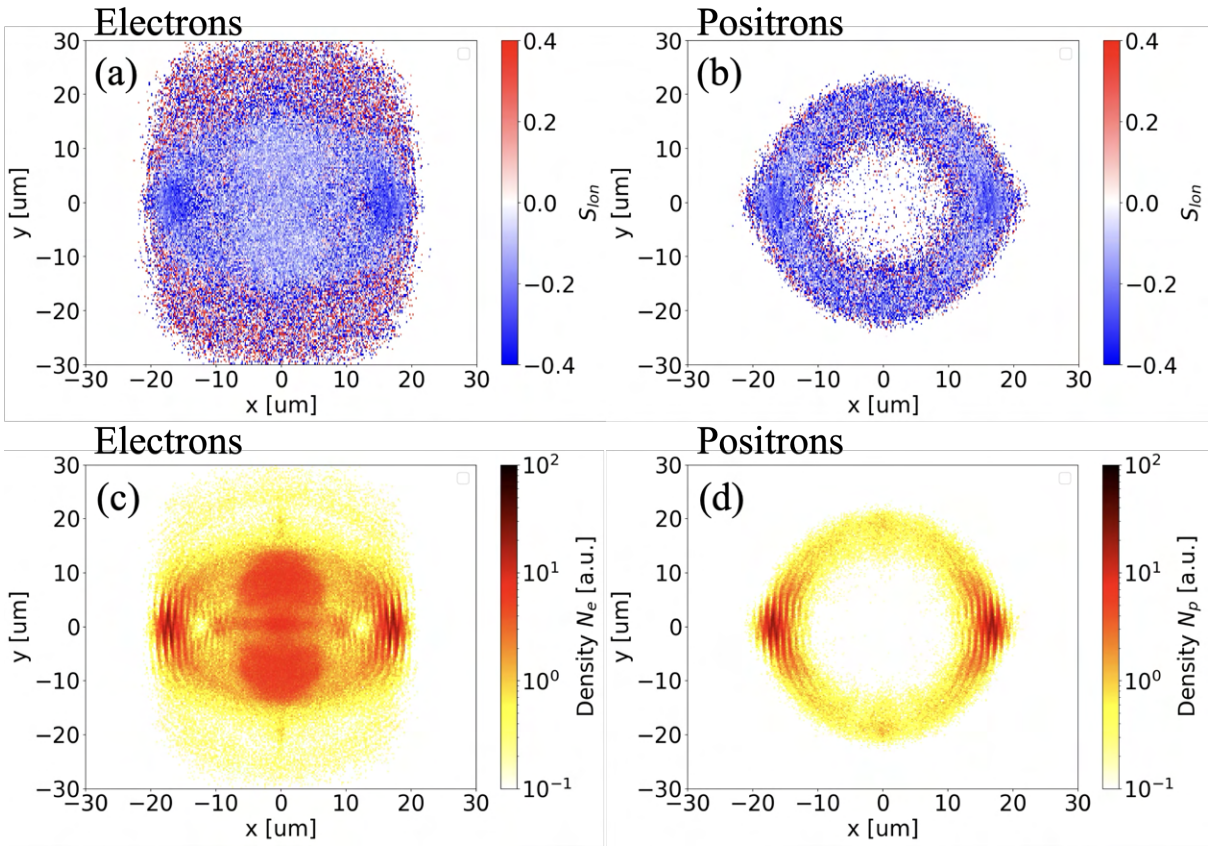

Figure 6.2: QED cascade simulation result of (a) spatial distribution of longitudinal spin for electrons and (b) positrons; (c) spatial distribution of density for electrons and (d) positrons.

To further analyze the cascades, we systematically varied several parameters: laser intensity (a_0 from 450 to 800), target density (from 2×10^{23} to 2×10^{24} cm^{-3}), laser duration (10 to 80 fs) and summarized in Fig. 6.5. We observe that positron polarization decreases at higher target densities, where increased pair multiplicity leads to significant shielding of the laser field. Otherwise, positron polarization shows relatively weak dependence on these input parameters. In contrast, electron polarization increases with multiplicity, suggesting that the polarized electron population originates primarily from generated pairs rather than the initial target electrons.

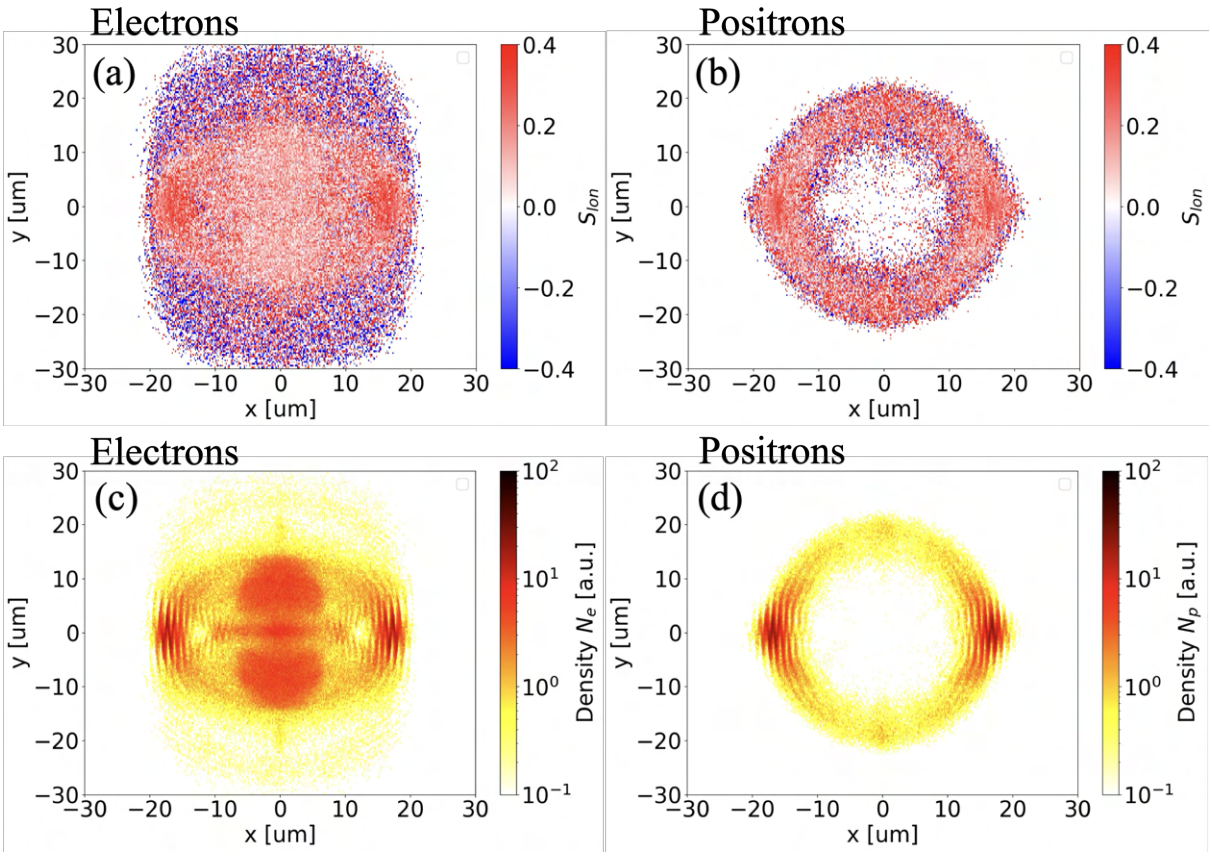

Figure 6.3: QED cascade simulation result of (a) spatial distribution of longitudinal spin for electrons and (b) positrons; (c) spatial distribution of density for electrons and (d) positrons when changing the helicity of both CP lasers

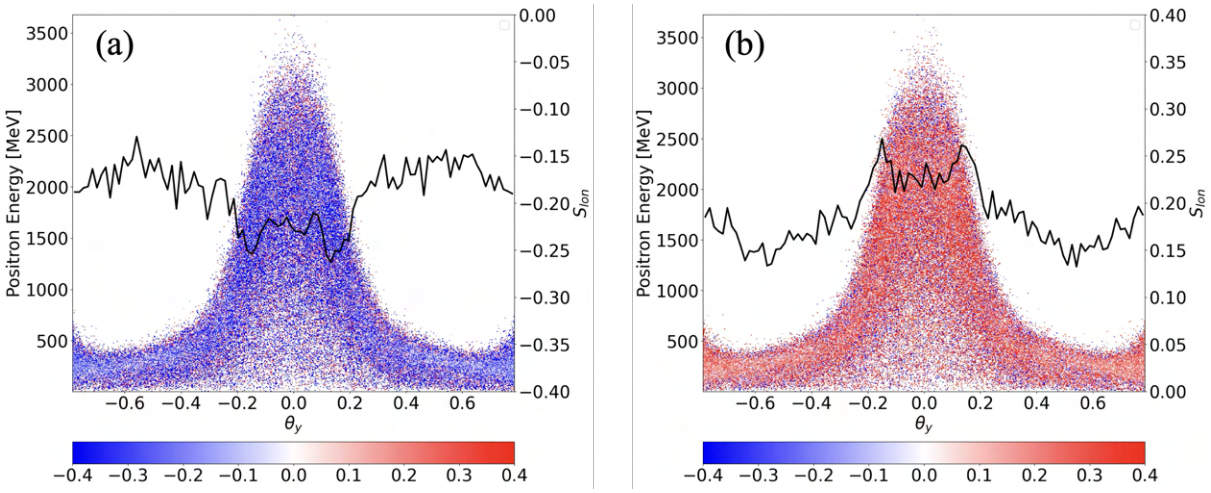

Figure 6.4: The positron longitudinal spin distribution in angular and energy phase space (a) both CP lasers polarization right-handed (b) both CP lasers polarization left-handed

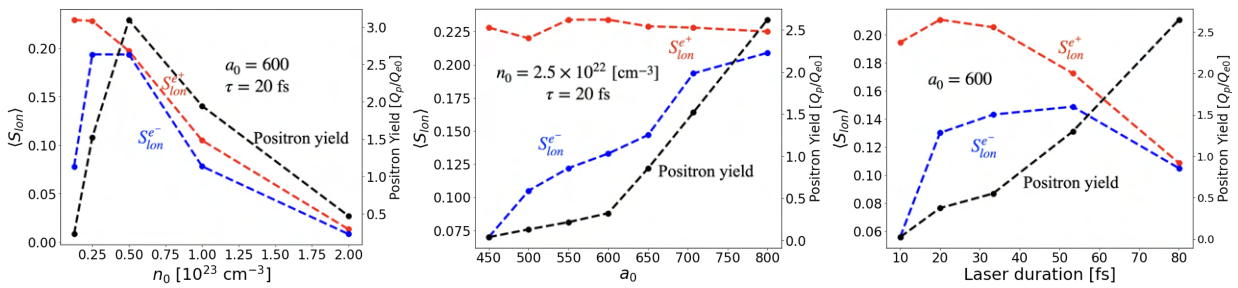

Figure 6.5: Parameter scan to demonstrate the relationship between longitudinal spin and yield, with respect to target density n_0, laser intensity a_0, and laser duration τ

Given the complex nature of the cascade dynamics, we sought to identify which polarization-related effects most significantly impact spin polarization. Fig. 6.6 compares the longitudinal spin polarization S_{lon} for the full spin- and polarization-resolved model (left-most), with variants in which either radiation-induced spin change or spin polarization at pair creation is omitted, or the anomalous magnetic moment is set to zero. Our results indicate that, for positrons, radiation-induced spin change and spin polarization from pair creation contribute almost equally to the observed polarization. For electrons, radiation-induced spin effects dominate, since most simulated electrons originate from the target rather than pair production. For both electrons and positrons, the presence of a nonzero anomalous magnetic moment is crucial; when $a_e = 0$, the resulting longitudinal polarization is nearly eliminated.

Since our target is initially unpolarized and the photons generated during the cascade exhibit only weak circular polarization, longitudinal polarization cannot arise directly from radiation-induced spin change or from spin- and polarization-resolved pair production alone. Our analysis (see Fig. 6.6) reveals that one of the dominant contributors to longitudinal polarization is the anomalous magnetic moment. It is reasonable to conjecture that polarization dynamics begin with either radiation-induced spin change or spin polarization at pair creation, which tends to align particle spins transversely to their motion but is correlated with the local field. Subsequently, spin precession in the field generated by the circularly polarized (CP) lasers leads to the emergence of stable longitudinal polarization.

To partially verify this mechanism, we tracked the trajectories and spin evolution of

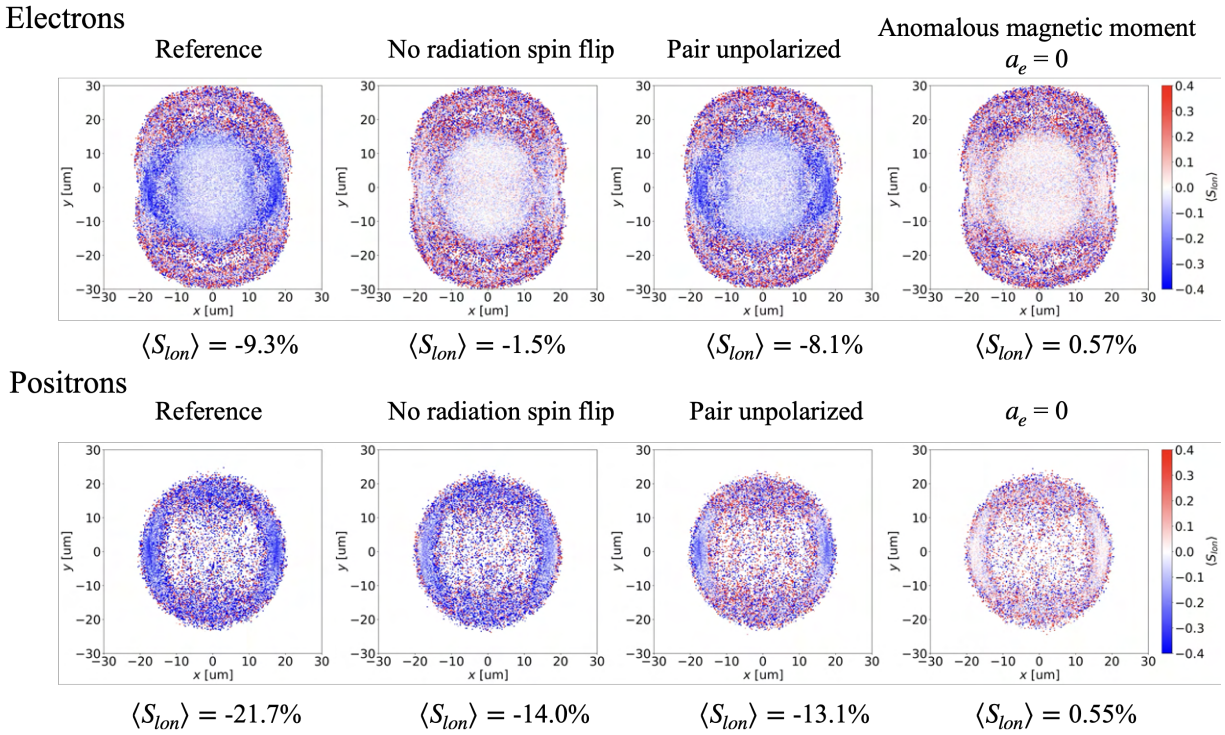

Figure 6.6: The spatial distribution of longitudinal spin S_{lon}, without radiation-induced spin change, for pair production with a particle born unpolarized, and with the anomalous magnetic moment equal to zero

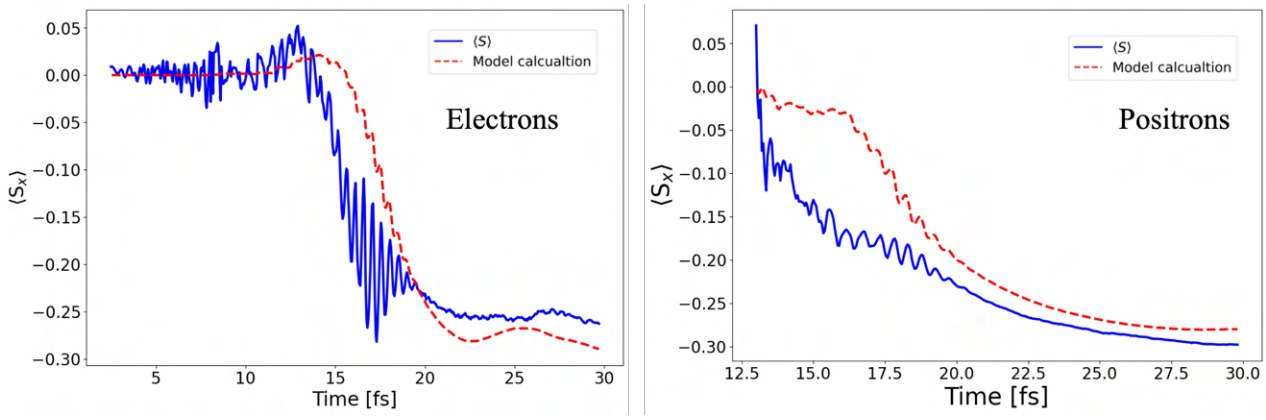

Figure 6.7: Evolution of the longitudinal spin compared with the result calculated using equation 6.1

2,000 particles positioned near the laser propagation axis. The time evolution of the spin component along the x-direction (blue curve in Fig. 6.7) is compared with the predicted longitudinal spin (red dashed curve), which is calculated using the tracked transverse spin

and the fields encountered by the particles, according to Eq.6.1. This equation is derived by projecting the B-K-S equation Eq. (6.2) onto the longitudinal direction; the classical precession term is detailed in Jackson's textbook on classical electrodynamics[83]. The close agreement between the two curves strongly supports our hypothesis regarding the underlying mechanism of longitudinal polarization.

$$\begin{aligned}\frac{dS_{\parallel}}{dt} =& -\frac{e}{m}S_{\perp}\cdot\left[\left(\frac{g}{2}-1\right)\beta\times B+\left(\frac{g\beta}{2}-\frac{1}{\beta}\right)E\right]\\ &-\frac{\alpha m}{\sqrt{3}\pi\gamma}S_{\parallel}\int_0^{\infty}\frac{u^2du}{(1+u)^3}\mathrm{IntK}_{1/3}\end{aligned} \tag{6.1}$$

These equations show that if the anomalous magnetic moment is zero then the longitudinal component of the spin will be effectively non-evolving, consistent with the simulation result in Fig. 6.6.

6.3 Spin Polarized Shower-Type Cascade by Collision Between a CP Laser and an Unpolarized Beam

Given the complexity of avalanche-type cascades' dynamics, we also consider a simpler scenario—a shower-type cascade—which is illustrated in Fig. 6.8. In this setup, a circularly polarized laser collides head-on with a high-energy, initially unpolarized electron beam. We perform two-dimensional simulations of particle spin dynamics under these conditions, using a laser with $a_0 = 700$, $\lambda_0 = 1$ μm, $\tau = 26.7$ fs, and a spot size of $w_0 = 8$ μm, propagating from left to right. The incident electron beam, traveling from right to left, is monoenergetic with initial $\gamma = 1000$, which is about 511 MeV, and features a Gaussian density profile with width $r_0 = 1$ μm, length $l_0 = 2$ μm, and density $n_e = 1.0 \times 10^{18}$ cm^{-3}—parameters typical for laser wakefield-accelerated beams.

The post-collision spatial distributions of electrons and positrons are presented in Fig. 6.9:

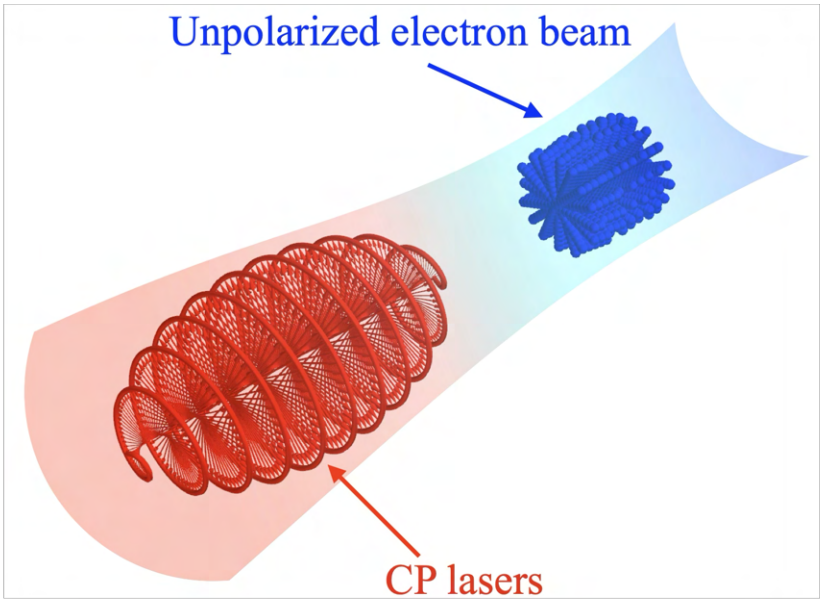

Figure 6.8: Spin polarized QED cascade

panels (a) and (b) show the longitudinal polarization, while panels (c) and (d) display the corresponding density profiles. The results indicate that both electrons and positrons are primarily deflected by the laser field and subsequently co-propagate with it. Notably, the positrons attain a high average longitudinal polarization, $\langle S^p_{\text{lon}} \rangle > 38\%$, with peak values exceeding 70% under optimal laser parameters.

For electrons, the polarization distributions exhibit two distinct components. The leading edge of the electron beam (rightmost region) is formed from the original electron beam and tends to have lower polarization. In contrast, regions where electrons and positrons overlap display higher polarization, similar to that of the positrons—these electrons are predominantly created via pair production during the collision. For the parameters used here, the positron yield reaches $Q_p = 0.7 Q_{e0}$.

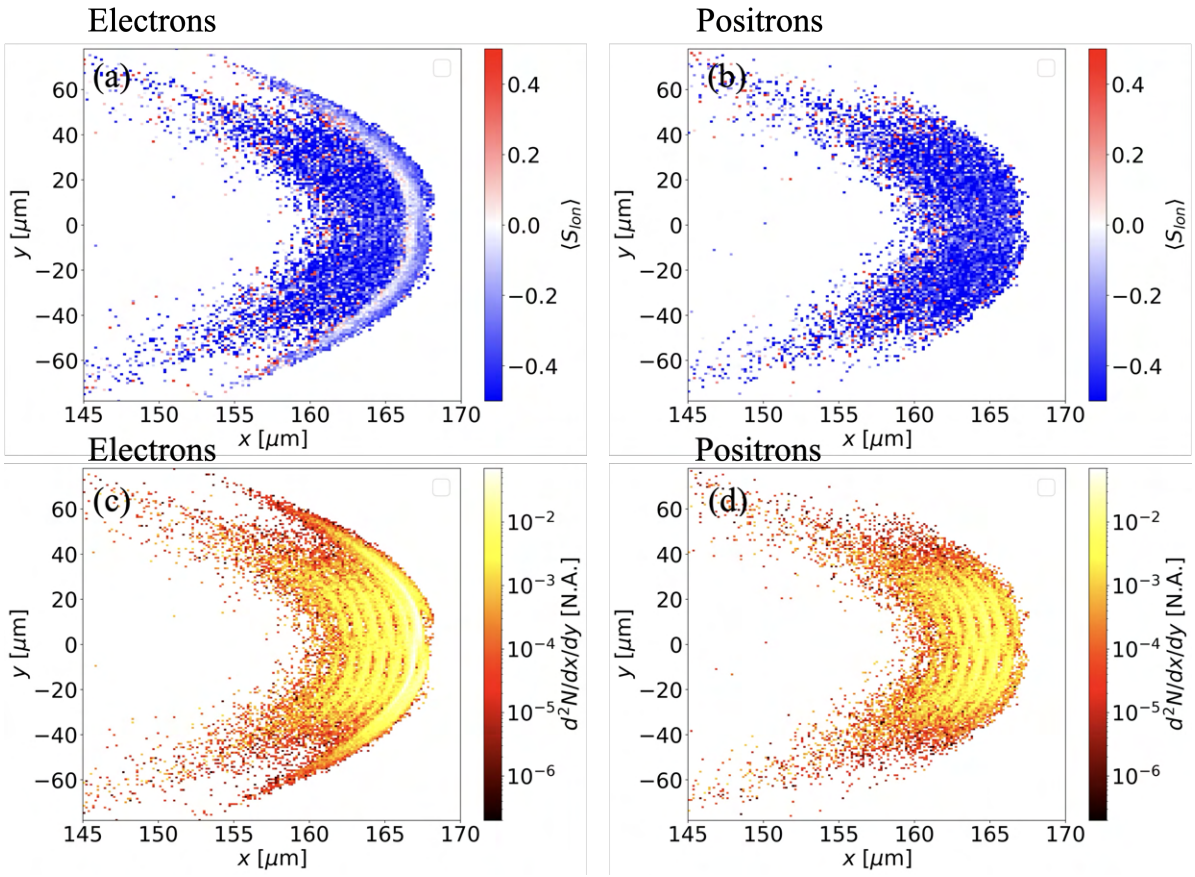

Figure 6.9: QED cascade simulation result of (a) spatial distribution of longitudinal spin for electrons and (b) positrons; (c) spatial distribution of density for electrons and (d) positrons.

Similar to what is observed in avalanche cascade scenarios, the direction of the longitudinal polarization can be reversed simply by switching the relative rotation direction of the two lasers, while the spin and density distributions remain otherwise unchanged, as demonstrated in Fig. 6.10.

We then performed a series of parameter scans to examine how the average longitudinal polarization for electrons and positrons, as well as the positron yield, evolves under different experimental conditions. Keeping the laser duration fixed at $\tau = 26.7$ fs and the initial beam energy at $\gamma = 1000$, we varied the laser intensity a_0 from 400 to 2000. As shown in the left plot of Fig. 6.11, the longitudinal polarization of the positron beam increases with laser intensity, saturating for $a_0 > 1250$. Next, maintaining the laser duration at $\tau = 26.7$ fs and the intensity at $a_0 = 700$, we varied the initial beam energy from $\gamma = 250$ to 2000. We

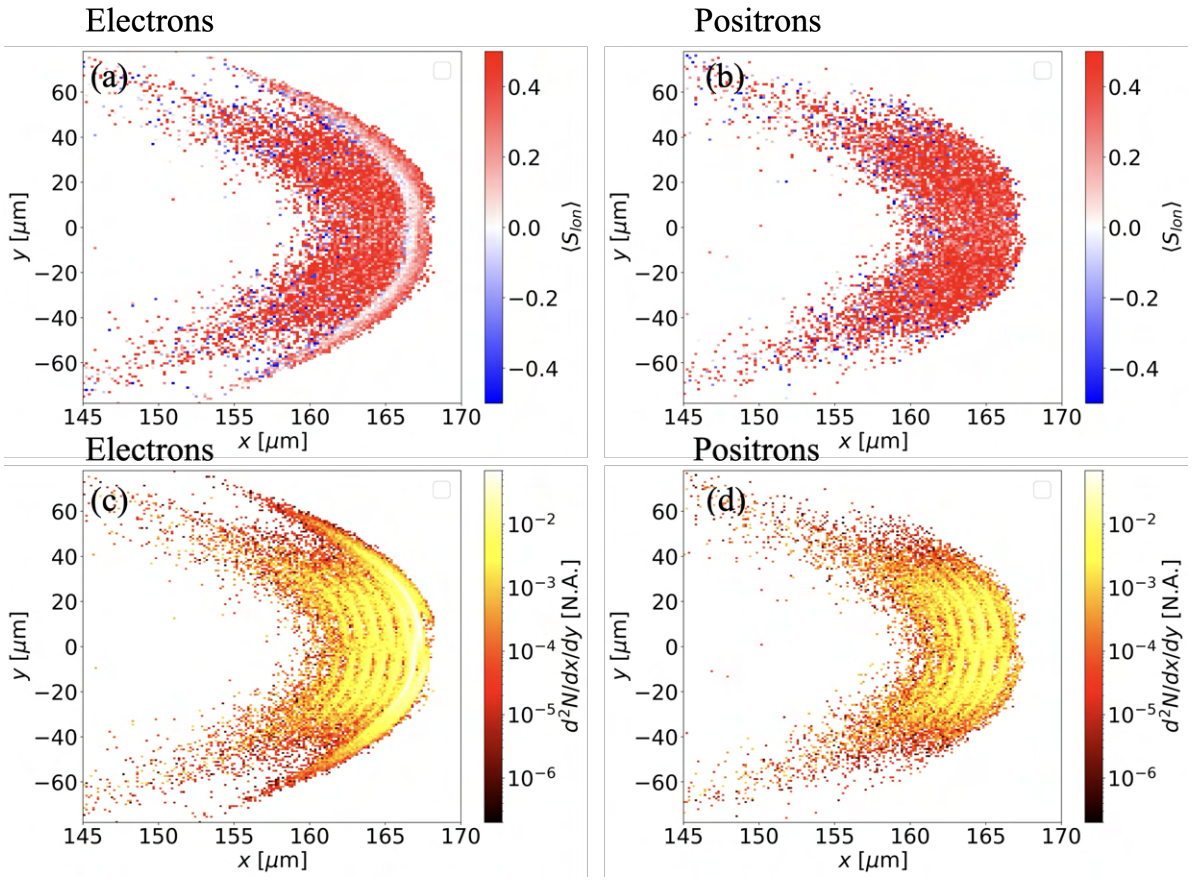

Figure 6.10: QED cascade simulation result of (a) spatial distribution of longitudinal spin for electrons and (b) positrons; (c) spatial distribution of density for electrons and (d) positrons.

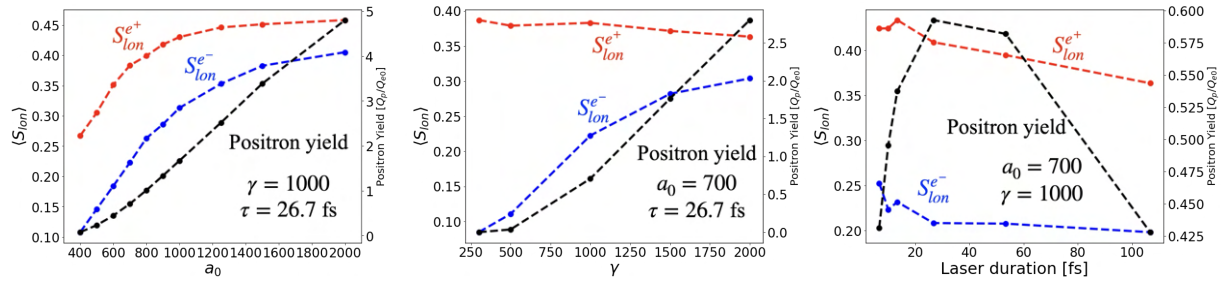

Figure 6.11: Parameter scan to demonstrate the relationship between longitudinal spin and yield, with respect to laser intensity a_0, initial beam energy γ, and laser duration τ

observed that the positron longitudinal polarization decreases only slightly with increasing beam energy, indicating a weak dependence on this parameter. Similarly, when scanning the laser duration from $\tau = 13.3$ fs to 106.7 fs, while keeping $a_0 = 700$, we found the positron polarization to be largely insensitive to changes in pulse duration.

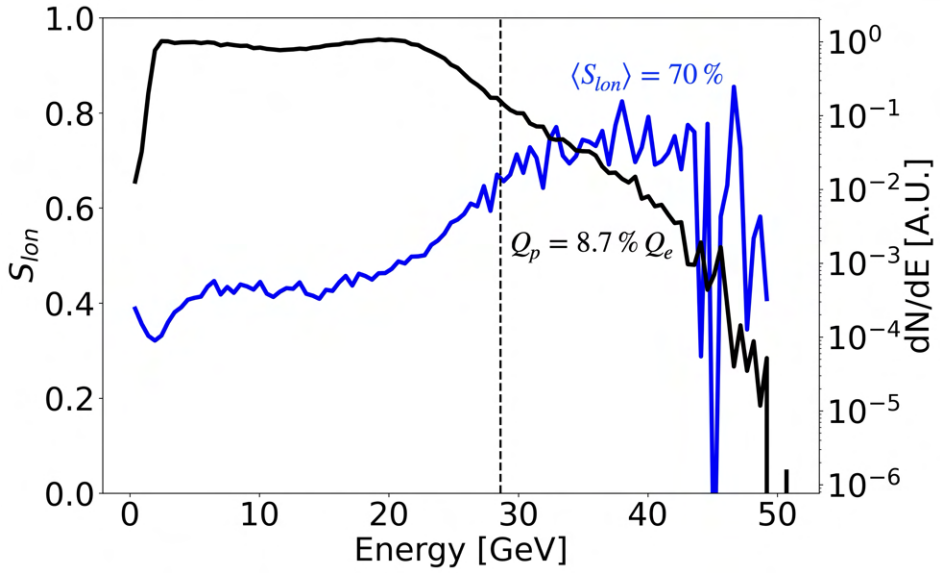

Figure 6.12: The spin and positron density with respect to energy for a beam with an initial energy of 511 MeV ($\gamma = 1000$) collides with a CP laser with $a_0 = 1500$. The averaged longitudinal spin is 45% and the spin for the high-energy part of the beam is 70%, with a population of 8.7% of the initial electron beam.

From these parameter scans, we identified optimal conditions for generating highly longitudinally polarized positron beams: high laser intensity and relatively low initial beam energy. For instance, under $a_0 = 1500$, $\gamma = 1000$, and $\tau = 26.7$ fs, the average longitudinal polarization of the positron beam reaches 45%. Fig. 6.12 shows the spin and positron density with respect to energy, and we can see that the high-energy portion of the positron beam achieves even greater polarization, exceeding 70%, and comprises 8.7% of the initial electron beam charge. Such beams could be of significant interest for future particle physics experiments requiring highly polarized positron sources.

To further probe the polarization mechanism, we investigated which physical effects most influence spin polarization. Figure 6.13 presents the longitudinal spin $S_{\rm lon}$ for several cases: the fully spin- and polarization-resolved model, simulations without radiation-induced spin change, pair production with initially unpolarized particles, and tests with the anomalous magnetic moment set to zero. Our analysis shows that, for positrons, spin polarization at pair creation plays a more significant role than radiation-induced spin change, while for electrons,

these two effects contribute nearly equally. This contrasts with the avalanche-type cascade case, and we discuss possible reasons for this difference later in the text. In both electron and positron beams, the anomalous magnetic moment is crucial: when $\alpha = 0$, almost no longitudinal polarization is observed.

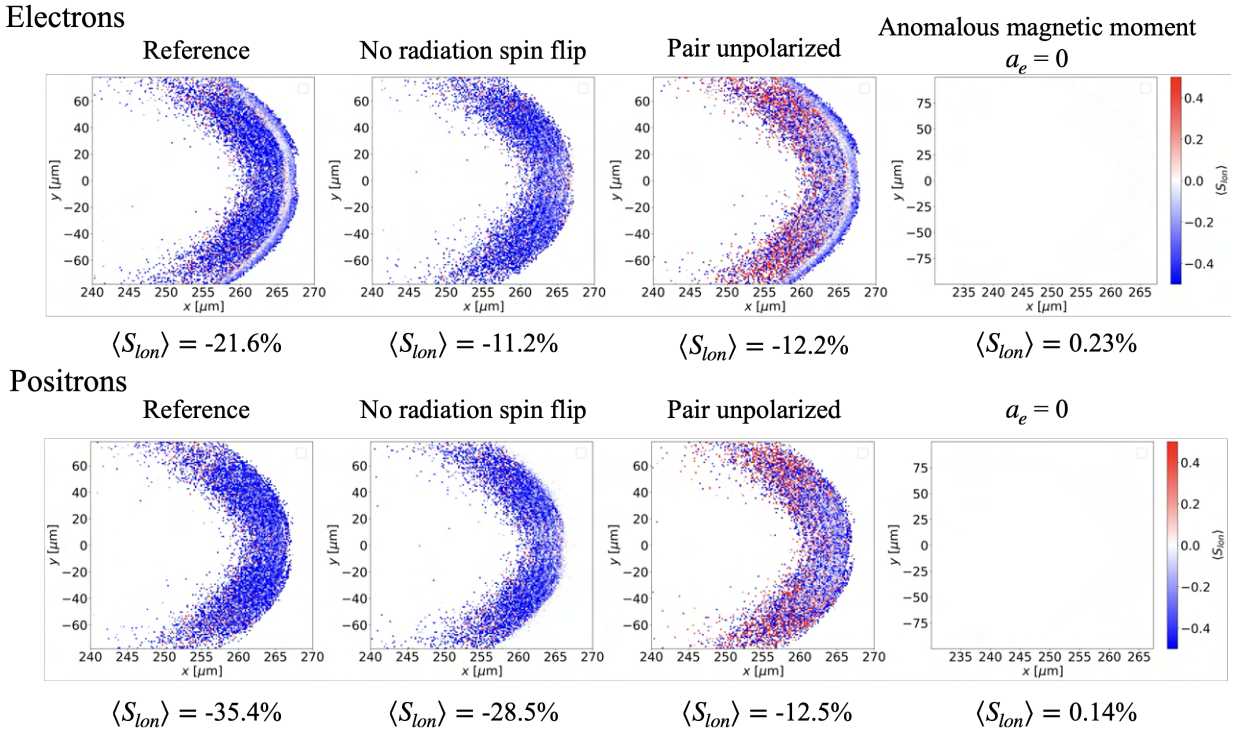

Figure 6.13: The spatial distribution of longitudinal spin S_{lon}, without radiation-induced spin change, for pair production with a particle born unpolarized, and with the anomalous magnetic moment equal to zero

We also performed detailed particle tracking for 2,000 particles within the beam. The evolution of the spin projection along the laser propagation direction (x) is shown as the blue curve in Fig. 6.14. The red dashed curve, calculated using Eq. 6.1 with tracked transverse spin and the instantaneous fields experienced by the particles, closely matches the direct simulation results, further supporting our understanding of the polarization process.

Despite the very different setups, the polarization dynamics of the shower-type cascade bear strong similarities to those of the avalanche-type cascade. First, in both cases, the particle beams ultimately co-propagate with the CP laser and undergo laser-driven accelera-

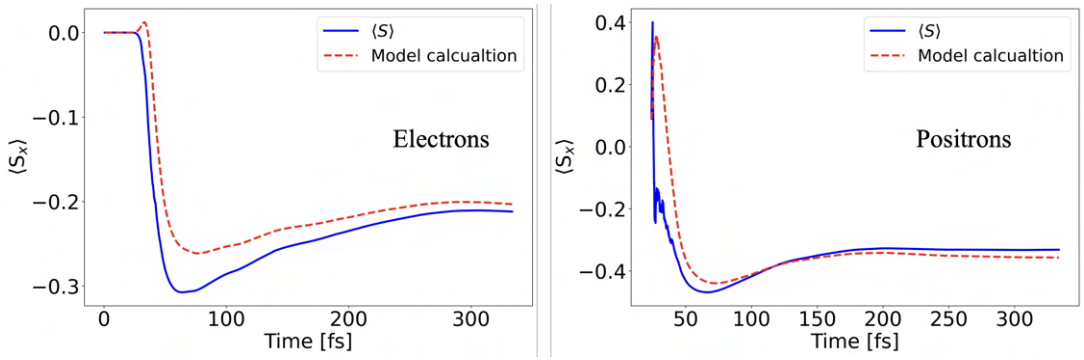

Figure 6.14: Evolution of the longitudinal spin compared with the result calculated using equation 6.1

tion after the cascade. Second, parameter scans demonstrate that the degree of longitudinal polarization is weakly dependent on variables such as laser intensity, initial beam energy, and laser duration. Third, reversing the laser's helicity reverses the direction of longitudinal polarization while leaving the spin and density distributions unchanged—a behavior consistent across both scenarios (see Fig. 6.10). Fourth, the longitudinal spin evolution in both setups can be accurately predicted using the same theoretical model, suggesting that quantum spin effects initially polarize the beam transversely, followed by spin precession into the longitudinal direction. We therefore propose that the fundamental mechanism for generating longitudinal polarization is largely similar for both shower- and avalanche-type cascades. Accordingly, a comprehensive understanding of polarization in the shower-type cascade will likely shed light on the origin of polarization in avalanche-type cascades as well.

6.4 Study the Origin of Longitudinal Spin Polarization

We investigate the origin of longitudinal spin by examining its evolution in more detail. To facilitate this analysis, we smooth the spin evolution curve using an averaged radiation-induced spin change model together with the classical spin precession, which can be written as:

$$\frac{d\boldsymbol{S}}{dt} = \left(\frac{d\boldsymbol{S}}{dt}\right)_T - P\left[\psi_1(\chi)\boldsymbol{S} + \psi_2(\chi)(\boldsymbol{S}\cdot\hat{\boldsymbol{k}})\hat{\boldsymbol{k}} + \psi_3(\chi)\hat{\boldsymbol{\beta}}\right] \tag{6.2}$$

Here, $P = \frac{\alpha_f m_e c^2}{\sqrt{3}\gamma\hbar\omega_L}$, $\psi_1(\chi) = \int_0^\infty u''duK_{2/3}(u')$, $\psi_2(\chi) = \int_0^\infty u''du\int_{u'}^\infty dxK_{1/3}(x) - \psi_1(\chi)$, $\psi_3(\chi) = \int_0^\infty u''duK_{1/3}(u)$, and $u'' = u^2/(1+u)^3$. $\left(\frac{d\boldsymbol{S}}{dt}\right)_T$ is the T-BMT equation.

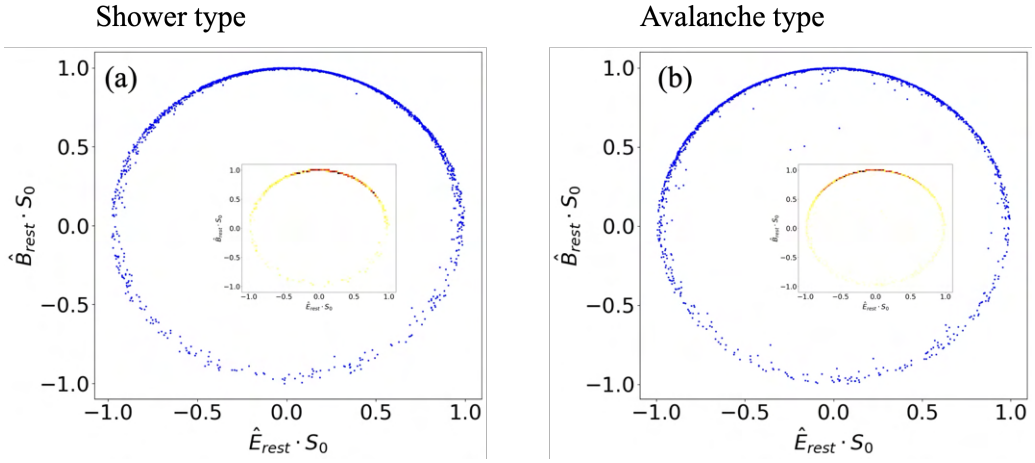

Figure 6.15: The initial spin direction with respect to the rest frame E and B field direction for (a) shower-type cascade, (b) avalanche-type cascade.

While the spin dynamics now follow a deterministic equation, quantum radiation reaction, and pair production continue to be evaluated using the same Monte Carlo (MC) routines as before. This modification has only a minor effect on the characteristics of shower and avalanche-type spin-polarized cascades, with the resulting yield, momentum, and longitudinal spin distributions remaining nearly unchanged. In this averaged model, particle spin lengths may take on any value between 0 and 1.

Particle tracking shows that, at birth, particles' spin directions generally align with the magnetic field in the rest frame for both shower and avalanche cascades (see Fig. 6.15). The spin evolution of 500 tracked positrons for both cascade types is presented in Fig. 6.16. In both shower- and avalanche-type cascades, the longitudinal spin exhibits oscillatory behavior between 0 and $-\langle|S|\rangle$, where $\langle|S|\rangle$ is the average spin length. Notably, in the avalanche case, the average longitudinal polarization $\langle S_{lon}\rangle$ is approximately half the average spin length $\langle|S|\rangle/2$. We also observe that the average spin length in avalanche cascades is much shorter

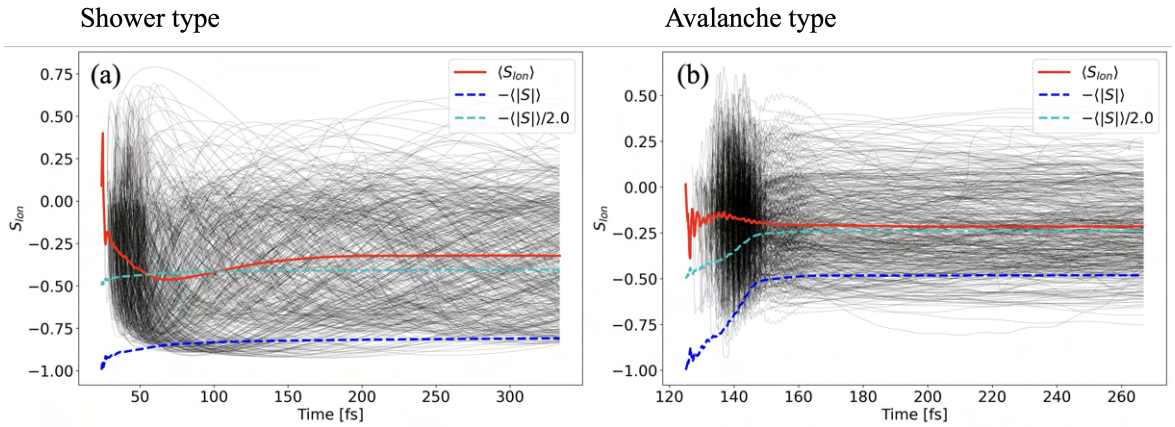

Figure 6.16: The evolution of longitudinal polarization for 500 particles in the simulation and the average longitudinal polarization for (a) shower-type cascade, (b) avalanche-type cascade. The blue curve shows the change in the spin length.

than in shower cascades.

This distinction can be attributed to the quantum parameter χ_e experienced by the particles in these processes. Fig. 6.17 shows the χ_e evolution for 500 positrons in both cascade types. In shower cascades, particles experience high χ_e for only short intervals—specifically during rapid acceleration or deflection by the laser pulse. By contrast, avalanche cascades feature prolonged periods where χ_e remains high, corresponding to the duration in which the standing wave structure is present. Inside a rotating field, the spin length of a particle decreases when the radiation-induced spin decay rate exceeds the gain rate. Therefore, particles exposed to high χ_e for longer durations exhibit shorter spin lengths. This explains qualitatively why average spin lengths are lower in avalanche cascades than in showers.

Furthermore, the correlation between spin length and exposure to high χ_e can be substantiated by examining the relationship between particle creation time and final spin length in the two types of cascades. Figure 6.18 shows the final spin length as a function of positron birth time for (a) shower cascades and (b) avalanche cascades. In shower cascades, there is little to no correlation, as high χ_e conditions arise from instantaneous acceleration or deceleration, largely independent of the particle's birth time. In contrast, for avalanche cascades, positrons born earlier are subjected to longer periods of high χ_e, leading to a strong

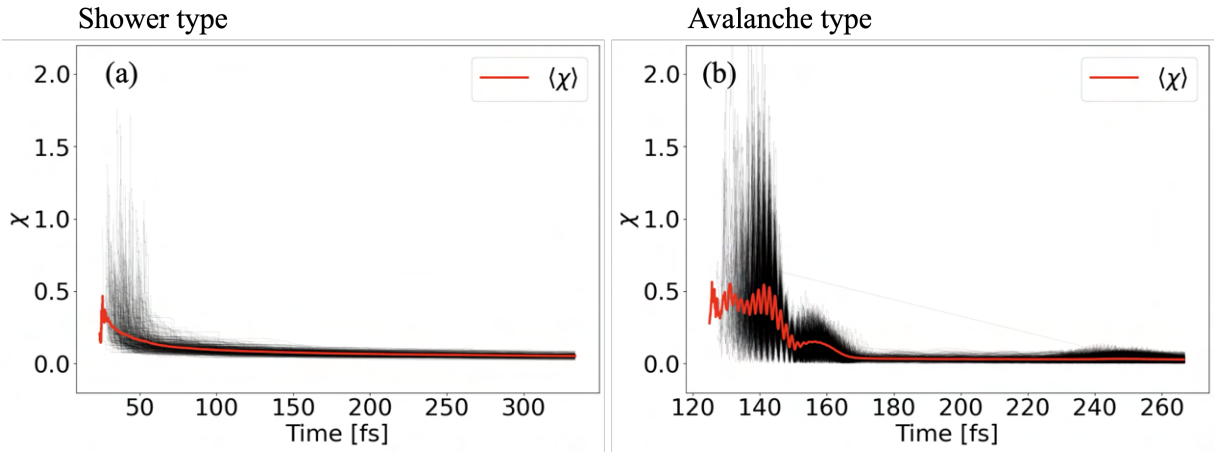

Figure 6.17: The evolution of χ_e for 500 particles tracked in the simulation and the averaged $\langle\chi\rangle$ (a) shower-type cascade, (b) avalanche-type cascade.

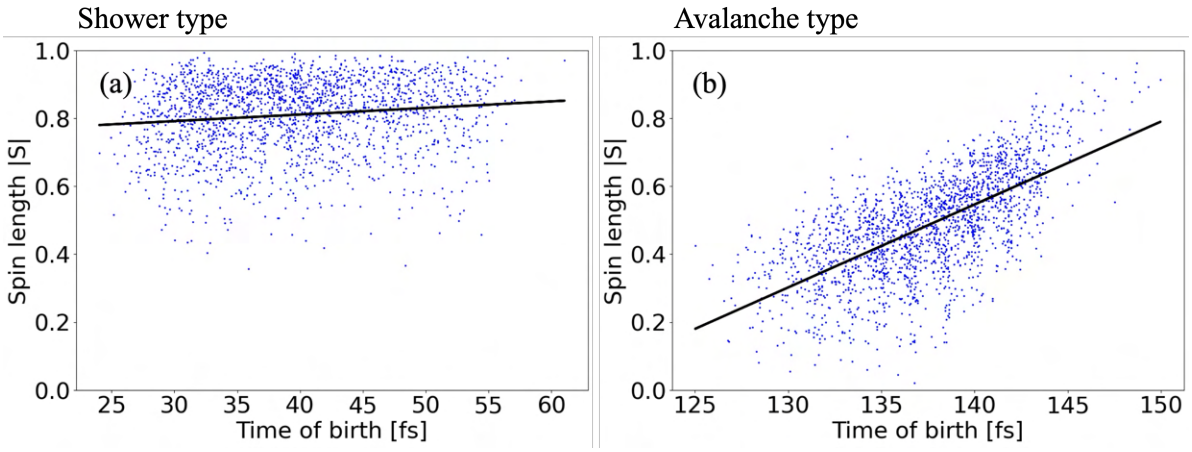

Figure 6.18: The correlation between the length of the spin and the time when the particles are born in the simulation, for (a) shower-type cascade, (b) avalanche-type cascade. The earlier the particles are born, the longer they interact with the field.

correlation between earlier birth times and reduced final spin lengths.

In shower cascades, neither the spin length, its initial orientation, nor its subsequent evolution as particles co-propagate with the laser is strongly influenced by the pulse duration. Our tracking analysis thus explains why the measured longitudinal spin remains largely insensitive to laser pulse length. Additionally, this result suggests that, for shower-type cascades, a lower initial electron beam energy produces lower-energy positrons that encounter reduced quantum parameters (χ_e) at birth. Consequently, decreasing the initial electron

beam energy leads to a slightly higher final longitudinal spin.

To further elucidate spin evolution, we consider an even more simplified case using our particle tracking code. Here, a single particle is placed in an infinite plane wave laser, with its spin initially aligned with the magnetic field and motion opposite to the laser. The code incorporates standard EM field pushers and modified classical radiation reaction. Spin evolution follows equation 6.2.

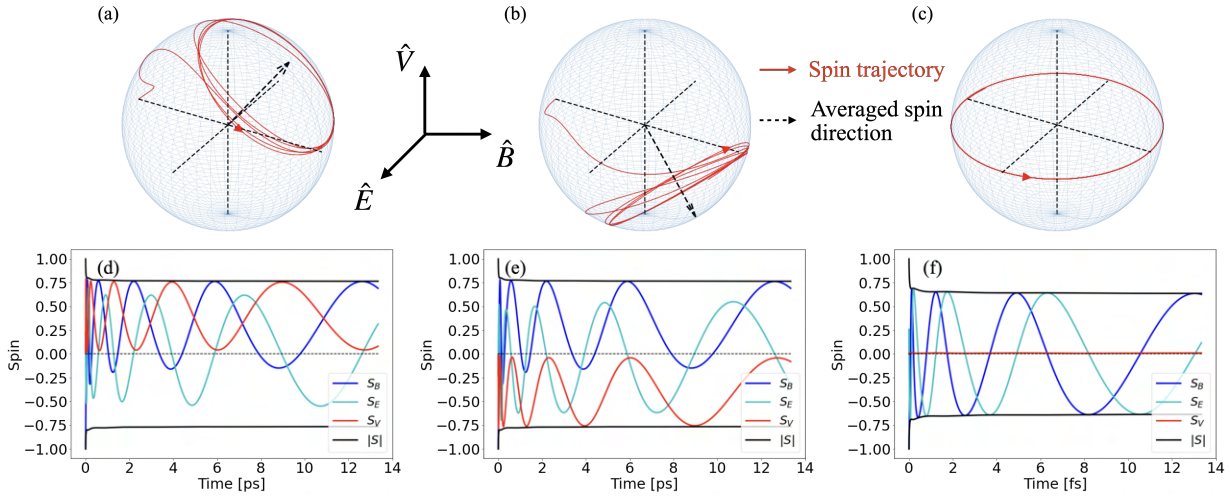

Figure 6.19: The spin trajectory from the particle tracking code for an electron born initially inside an infinite plane wave laser field with intensity $a_0 = 700$ and counterpropagating with the laser with spin pointing in the magnetic field direction. It then deflected and travels together with the laser. (a), (b), (c): the red curve shows the spin trajectory in $(\hat{\boldsymbol{v}}, \hat{\boldsymbol{B}}, \hat{\boldsymbol{E}})$ coordinate, which for highly relativistic particle are nearly mutually orthogonal with each other, the black dashed arrow shows the time averaged spin direction when spin trajectory forms a stable circle under the $(\hat{\boldsymbol{v}}, \hat{\boldsymbol{B}}, \hat{\boldsymbol{E}})$ bases. (d), (e), (f): The evolution of the length of the spin $|\boldsymbol{S}|$ (black) and spin component in $\hat{\boldsymbol{B}}$ (blue), $\hat{\boldsymbol{E}}$ (cyan), and $\hat{\boldsymbol{v}}$ (red), direction. (a), (d), (b), (e) are calculated with real anomalous magnetic moment value $\alpha(\chi)$, which depends on χ_e, while (c), (f) are calculated with anomalous magnetic moment $a_e = 0$. (a), (d) and (b), (e) are calculated with different laser helicities.

Figure 6.20 shows the spin evolution of a particle with initial energy $\gamma = 200$ interacting with a laser of intensity $a_0 = 700$, represented in the $(\hat{\boldsymbol{B}}, \hat{\boldsymbol{E}}, \hat{\boldsymbol{v}})$ coordinate system. In this basis, $\hat{\boldsymbol{v}}$ is the direction of the particle's velocity, while $\hat{\boldsymbol{B}}$ and $\hat{\boldsymbol{E}}$ correspond to the directions of the magnetic and electric fields experienced by the particle, respectively. As the particle

is deflected and travels with the laser, its velocity remains predominantly along the laser propagation direction, deviating by only a_0/γ. As a result, the $(\hat{\boldsymbol{B}}, \hat{\boldsymbol{E}}, \hat{\boldsymbol{v}})$ axes remain nearly orthogonal. We choose this coordinate system because, in this basis, the spin precession axis remains fixed in time, making it an ideal frame to analyze the spin dynamics.

In panels (a) and (c), the anomalous magnetic moment parameter α is set to zero; in panels (b) and (d), it is assigned a χ_e- dependent value, $\alpha(\chi_e)$. Even in this simplified scenario, the longitudinal spin evolves similarly to that in a shower cascade, oscillating between 0 and $|\boldsymbol{S}|$. When $\alpha = 0$, the longitudinal component remains negligible. Reversing the laser's rotation direction inverts the oscillation, causing the longitudinal spin to range between zero and $-|\boldsymbol{S}|$.

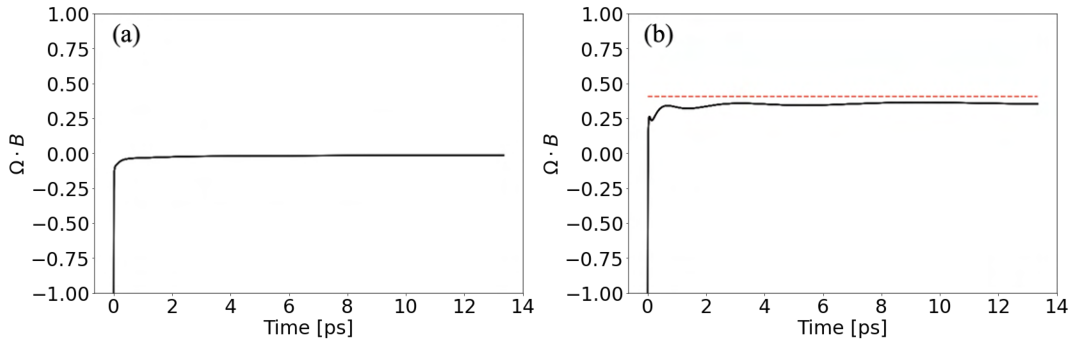

Figure 6.20: The spin rotation axis along B field direction for (a) when anamalous magnetic moment $\alpha = 0$, (b) with real anamalous magnetic moment value $\alpha(\chi_e)$, which depends on χ_e.

The distinct behavior resulting from different α values can be visualized by examining the spin precession axis components (see Fig. 6.20). When $\alpha = 0$, the axis has only small components along the magnetic field, while for $\alpha = \alpha(\chi_e)$, this component is significant. Since radiation and pair production initially polarize the particle spin perpendicular to velocity, the precession axis must deviate from the velocity direction to enable precession toward it.

To predict the average degree of longitudinal polarization, it is essential to determine the direction of the "non-evolving" spin axis—i.e., the axis along which spin projections remain constant. In what follows, we derive the form of this axis for particles co-propagating with

an infinite plane circularly polarized laser wave.

$$\frac{d\boldsymbol{s}}{dt} = \boldsymbol{\Omega} \times \boldsymbol{s} + \boldsymbol{R} \approx \boldsymbol{\Omega} \times \boldsymbol{s} \tag{6.3}$$

Which $\mathbf{R}$ is the radiation-induced spin change term, and under the scenario when the beam copropagates together with the laser, is negligible. We change the variable from t to laser phase $\phi = \omega_0(z/c - t)$. The time derivative of laser phase, under the ultra-relativistic limit, and assumes that the beam longitudinal momentum is much greater than the transverse component.

$$\frac{d\phi}{dt} = \omega_0(\beta_\parallel - 1) = \omega_0(\sqrt{1 - \beta_\perp^2} - 1) \approx -\frac{\omega_0}{2}\beta_\perp^2 \tag{6.4}$$

Which $\beta_\parallel$ is the velocity component along the laser propagation direction $\hat{\boldsymbol{k}}$, $\beta_\perp$ is the velocity component perpendicular to the laser propagation direction. We can then rewrite the equation as:

$$\frac{d\boldsymbol{s}}{dt} = -\frac{\omega_0}{2}\beta_\perp^2 \frac{d\boldsymbol{s}}{d\phi} = \boldsymbol{\Omega} \times \boldsymbol{s} \tag{6.5}$$

As a result, we have

$$\frac{d\boldsymbol{s}}{d\phi} = -\frac{2\boldsymbol{\Omega}}{\beta_\perp^2 \omega_0} \times \boldsymbol{s} = \boldsymbol{\Omega}_\phi \times \boldsymbol{s}\ , \tag{6.6}$$

where $\boldsymbol{\Omega}_\phi = -\frac{2\boldsymbol{\Omega}}{\beta_\perp^2 \omega_0}$. We may project this equation onto the unit vector spin $\hat{\boldsymbol{q}}$:

$$\hat{\boldsymbol{q}} \cdot \frac{d\boldsymbol{s}}{d\phi} = \frac{ds_q}{d\phi} - \boldsymbol{s} \cdot \frac{d\hat{\boldsymbol{q}}}{d\phi} \tag{6.7}$$

Assuming that $\frac{d\hat{\boldsymbol{q}}}{d\phi} = \hat{\boldsymbol{k}} \times \hat{\boldsymbol{q}}$, i.e., that the axis undergoes a rotation such that it returns to its original orientation every time ϕ changes by 2π, we obtain:

$$\frac{ds_q}{d\phi} = (\Omega_\phi \times \boldsymbol{s}) \cdot \hat{\boldsymbol{q}} + \boldsymbol{s} \cdot \hat{\boldsymbol{k}} \times \hat{\boldsymbol{q}} = \boldsymbol{s} \cdot \left((\boldsymbol{\Omega}_\phi + \hat{\boldsymbol{k}}) \times \hat{\boldsymbol{q}}\right) \tag{6.8}$$

This equation vanishes when $\hat{\boldsymbol{q}}$ is parallel to $\boldsymbol{\Omega}_\phi + \hat{\boldsymbol{k}}$, indicating that this direction defines the non-evolving spin axis. Let $\boldsymbol{\Omega}_\phi = \Omega_\phi \hat{\boldsymbol{\Omega}}$, where $\hat{\boldsymbol{\Omega}}$ is a unit vector along the spin precession

axis. The explicit expression for $\hat{\boldsymbol{q}}$ is then:

$$\hat{\boldsymbol{q}} = \frac{\Omega_\phi \hat{\boldsymbol{\Omega}} + \hat{\boldsymbol{k}}}{|\Omega_\phi \hat{\boldsymbol{\Omega}} + \hat{\boldsymbol{k}}|} \tag{6.9}$$

We look a little more in detail at the expression of $\boldsymbol{\Omega_\phi}$:

$$\boldsymbol{\Omega_\phi} = -\frac{e}{m_e c}\frac{2\boldsymbol{\Omega}}{\beta_\perp^2 \omega_0} = -\frac{e}{m_e c \omega_0}\frac{2}{\beta_\perp^2}\left[\alpha\frac{\gamma}{\gamma+1}(\boldsymbol{\beta}\cdot\boldsymbol{B})\boldsymbol{\beta} + \left(\alpha+\frac{1}{\gamma}\right)\boldsymbol{B} - \left(\alpha+\frac{1}{\gamma+1}\right)\boldsymbol{\beta}\times\boldsymbol{E}\right] \tag{6.10}$$

Under the ultra relativistic limit, and assuming the EM field is a plane wave, we have $\boldsymbol{B} = \hat{\boldsymbol{k}} \times \boldsymbol{E}$. For particle motion inside CP laser, we further assume that the perpendicular velocity component is in the magnetic field direction $\hat{\boldsymbol{B}}$:

$$\begin{aligned}
\boldsymbol{\Omega_\phi} &\approx -\frac{e}{m_e c\omega_0}\frac{2}{\boldsymbol{\beta}_\perp^2}\left[\left(\alpha+\frac{1}{\gamma}\right)\left((1-\beta_\parallel)B\hat{\boldsymbol{B}} - \beta_\perp B\hat{\boldsymbol{k}}\right) - \alpha\beta_\perp B(\beta_\parallel\hat{\boldsymbol{k}} + \beta_\perp\hat{\boldsymbol{B}})\right] \\
&\approx -\frac{e}{m_e c\omega_0}\frac{2}{\boldsymbol{\beta}_\perp^2}\left[\left(\alpha+\frac{1}{\gamma}\right)\beta_\perp B\left(\frac{1}{2}\beta_\perp\hat{\boldsymbol{B}} - \hat{\boldsymbol{k}}\right) - \alpha\beta_\perp B\left(\beta_\perp\hat{\boldsymbol{B}} + \left(1-\frac{1}{2}\beta_\perp^2\right)\hat{\boldsymbol{k}}\right)\right]
\end{aligned} \tag{6.11}$$

By ignoring the higher-order term, and letting $\frac{eB}{m_e c} = \omega_0 a_0$, and letting $\beta_\perp = a_0/\gamma$, we finally have:

$$\boldsymbol{\Omega_\phi} \approx -\left[\frac{1}{2}\left(\alpha a_0 + \frac{a_0}{\gamma}\right)\frac{a_0^2}{\gamma^2}\hat{\boldsymbol{B}} - \frac{a_0^2}{\gamma^2}\hat{\boldsymbol{k}}\right]\frac{2\gamma^2}{a_0^2} = \left(\alpha a_0 + \frac{a_0}{\gamma}\right)\hat{\boldsymbol{B}} - 2\hat{\boldsymbol{k}} \tag{6.12}$$

As a result, the expression of $\hat{\boldsymbol{q}}$ can be written as:

$$\hat{\boldsymbol{q}} \approx \frac{\left(\alpha a_0 + \frac{a_0}{\gamma}\right)\hat{\boldsymbol{B}} - \hat{\boldsymbol{k}}}{\sqrt{\left(\alpha a_0 + \frac{a_0}{\gamma}\right)^2 + 1}} \tag{6.13}$$

In the limit that $\gamma \gg \frac{1}{\alpha}$, the expression can be further simplified as:

$$\hat{\boldsymbol{q}} \approx \frac{\alpha a_0 \hat{\boldsymbol{B}} - \hat{\boldsymbol{k}}}{\sqrt{1+\alpha^2 a_0^2}}\,, \tag{6.14}$$

which is a function only for α and a_0. Finally, we test our model using numerical simulations. The results are shown in Fig. 6.21 (a), (b), and (c). These figures demonstrate that the spin non-precession axis (indicated by the black arrow) closely aligns with the time-averaged spin direction (shown by the black dashed arrow).

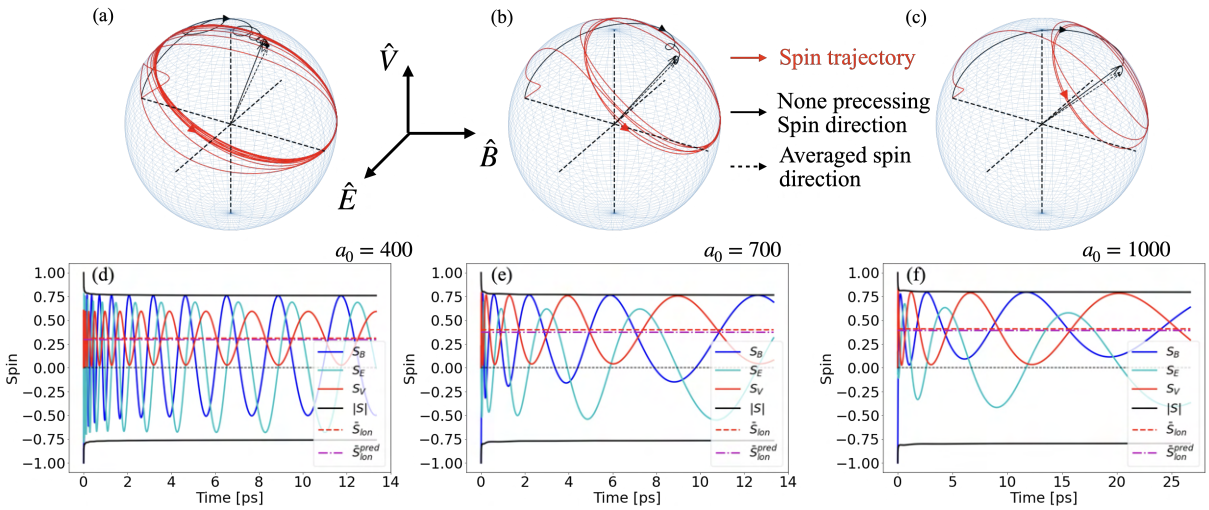

Figure 6.21: (a), (b), (c): Prediction of nonprecession spin direction, calculated using Eq. (6.13) compared with the averaged spin direction under $(\hat{\boldsymbol{v}}, \hat{\boldsymbol{B}}, \hat{\boldsymbol{E}})$ basis. The averaged spin direction are calculated by taking the time average of the spin direction when the spin trajectory forms a stable circle under the $(\hat{\boldsymbol{v}}, \hat{\boldsymbol{B}}, \hat{\boldsymbol{E}})$ basis. (d), (e), (f): The predicted averaged longitudinal spin (purple dashed), calculated using Eq. (6.15) compared with the time-averaged longitudinal spin result (red dashed) from the particle tracking code. The averaged spin direction and the time-averaged longitudinal spin value are calculated by taking the time-average of the spin direction when the spin trajectory forms a stable circle under the $(\hat{\boldsymbol{v}}, \hat{\boldsymbol{B}}, \hat{\boldsymbol{E}})$ basis. We show the comparison for a variety of laser intensity a_0: (a), (d) are calculated with $a_0 = 400$; (b), (e) $a_0 = 700$;(c), (f) $a_0 = 1000$.

For spins initialized along the magnetic field direction, the expected longitudinal spin is given by

$$\bar{S}_{\text{lon}} = |S| \frac{\alpha a_0}{\sqrt{1+\alpha^2 a_0^2}} \frac{1}{\sqrt{1+\alpha^2 a_0^2}} = \frac{\alpha a_0}{1+\alpha^2 a_0^2} |S|. \tag{6.15}$$

In Fig. 6.21 (e), (f), and (g), we compare this analytic prediction with the averaged longitudinal spin obtained from our simulations and find strong agreement between the two.

From the equation, we observe that the averaged longitudinal spin initially increases with the laser parameter a_0, reaching a maximum at $a_0 = 1/\alpha$, and then gradually decreases as a_0 increases further. This trend qualitatively agrees with the intensity dependence of the shower cascade scaling observed in Figure 6.11. By analytically determining the maximum of the expression, we find that the predicted maximum averaged longitudinal spin degree is 50%.

6.5 Conclusion

We investigate spin and polarization effects in two primary QED cascade regimes: shower-type cascades, arising from collisions between high-energy electron beams and laser pulses, and avalanche-type cascades, initiated by counter-propagating intense lasers that form a standing wave. While earlier studies mostly addressed unpolarized cascades, our work demonstrates the robust generation of longitudinally polarized plasmas in both scenarios.

Specifically, avalanche-type cascades driven by counter-propagating circularly polarized (CP) lasers produce electron-positron pair plasmas with average longitudinal polarization exceeding 20% and peak values over 30%. For shower-type cascades—where a CP laser interacts with an unpolarized electron beam—the resulting positron populations reach average longitudinal polarizations above 40%. Under optimal conditions, the highest-energy positrons (constituting more than 8% of the initial beam) can attain polarization levels above 70%.

Despite the complexity of QED cascade dynamics, we conduct a comprehensive parameter scan for both configurations. We find that the positron polarization degree is only weakly dependent on parameters such as laser intensity (a_0), target density (n_0), initial beam energy (γ_0), and pulse duration (τ), highlighting the robustness of the polarization effect. To identify the dominant spin dynamics, we systematically isolate and disable various quantum and classical processes in our simulations. This analysis reveals that the observed longitudinal po-

larization results from a multistage spin-evolution process, involving both quantum-induced spin flips (which preferentially align the spin along the local field direction) and classical spin precession (which rotates the spin toward the longitudinal direction).

To further clarify these mechanisms, we develop an intuitive physical model for the shower-type cascade, providing detailed insights into the polarization process. For the more complex avalanche scenario, a complete understanding of the field and particle interactions remains an open area for further investigation.

From an application perspective, our results introduce a practical, all-optical approach for generating highly polarized positron beams via QED cascades. This advance not only holds significant promise for future particle physics experiments but also deepens our understanding of particle dynamics in extreme astrophysical settings.

CHAPTER 7

Other SFQED Laser-Plasma Studies

The author has also contributed theoretical work to other studies exploring strong-field quantum electrodynamics (SFQED) phenomena within high-intensity laser-plasma interactions[1].

7.1 On Strong Magnetic Field Measurement

We investigated the suitability of using GeV laser wakefield-accelerated electron beams to measure strong, $B > 0.1$ MT, magnetic fields. This method is explored as an alternative to proton deflectometry, which cannot be used for quantitative measurement using conventional analysis techniques at these extreme field strengths. Quantum radiation reaction on the probe provides an additional measurement of the strength and length of fields, extending the standard deflectometry measurement that can only measure the path-integrated fields. A paper on this topic was published in Russell et al. [180]. The author ran simulations and developed the theory for the electron beam dynamics.

As the high energy electrons of the probe beam are deflected by the strong fields in the object plane they will radiate. By emitting photons, the electron beam gives up energy

[1]This chapter summarizes: (1) B. K. Russell, P. T. Campbell, Q. Qian, J. A. Cardarelli, S. S. Bulanov, S. V. Bulanov, G. M. Grittani, D. Seipt, L. Willingale, A. G. R. Thomas, "Ultrafast relativistic electron probing of extreme magnetic. The study's central concept was proposed by B. K. Russell and P. T. Campbell. I collaborated with B. K. Russell to develop the theoretical framework for ultrafast relativistic electron probing of extreme magnetic fields. (2) Q. Qian, D. Seipt, Y. Ma, A. G. R. Thomas, "Quantum radiation effect in high-energy wakefield stages" (in preparation). I carried out all simulations and analyses in this work. The theory was formulated in collaboration with A. G. R. Thomas, while simulation guidance was provided by D. Seipt and Y. Ma.

thereby shifting the mean energy of the beam and causing the energy spread of the beam to increase. These effects are given by the equations [136],

$$\left(\frac{d\langle \mathbf{p}\rangle}{dt}\right)_{mod\ cl} = -\frac{\langle gP_{cl}\hat{\mathbf{p}}\rangle}{c}, \tag{7.1}$$

$$\left(\frac{d\sigma^2}{dt}\right)_{st} \approx \frac{\alpha_f c b^2}{\lambda\!\!\!^{-}_c}\left(\frac{55b}{24\sqrt{3}}\langle\gamma\rangle^4 - \frac{8}{3}\sigma^2\langle\gamma\rangle\right) \tag{7.2}$$

where Eqn. (7.1) gives the change in average value of the momentum and Eqn. (7.2) gives the change in the variance of a beam with $\sigma^2 = \langle\gamma^2\rangle - \langle\gamma\rangle^2$. Eqn. (7.2) is only valid assuming the beam energy distribution is always Gaussian, the energy spread is small $\sigma \ll \langle\gamma\rangle$ and $\eta \ll 1$. P_{cl} is the power classically emitted to synchrotron radiation given by,

$$P_{cl} = \frac{2\alpha_f}{3\lambda\!\!\!^{-}_c} m_e c^3 \eta^2, \tag{7.3}$$

where α_f is the fine structure constant, $\lambda\!\!\!^{-}_c$ is the reduced Compton wavelength, and η is the quantum efficiency parameter defined as the ratio of the field strength in the rest frame of the electron beam to the Schwinger field $E_s = 1.32 \times 10^{18}$ Vm^{-1}. For a highly relativistic beam where $\gamma \gg 1$, $\eta \equiv \gamma b = \gamma|\mathbf{E}_\perp + \mathbf{v}\times\mathbf{B}|/E_s$. The Gaunt factor $g(\eta)$ acts as a quantum correction to the classical emission spectrum for η approaching unity and has been fit to $g(\eta) \approx [1 + 4.8(1+\eta)\ln(1+1.7\eta) + 2.44\eta^2]^{-2/3}$.

Consider an electron beam with a Gaussian energy spread propagating through a constant magnetic field that is perpendicular to the propagation direction. We can solve analytically for the decay in the average value of the Lorentz factor γ using Eqn. (7.1),

$$\langle\gamma\rangle \approx \left(\frac{1}{\langle\gamma_0\rangle} + \kappa t\right)^{-1}, \tag{7.4}$$

$$\kappa = \frac{2\alpha_f c^3 B_\perp^2}{3\lambda\!\!\!^{-}_c E_s^2}, \tag{7.5}$$

where $\langle\gamma_0\rangle$ is the average initial Lorentz factor. Additionally we have taken $\langle p\rangle \approx m_e c\langle\gamma\rangle$.

Here we have assumed $\eta \ll 1$ so $g \approx 1$, and additionally $\sigma \ll \langle\gamma\rangle$. This can be rearranged to solve for the perpendicular magnetic field,

$$B_\perp = \sqrt{\frac{3\lambda_c E_s^2}{2\alpha_f c^2 l_B}\left(\frac{1}{\langle\gamma\rangle} - \frac{1}{\langle\gamma_0\rangle}\right)}, \tag{7.6}$$

where $l_B = ct$ is the length of the magnetic field assuming highly relativistic electrons. Eqn. (7.4) can be substituted into Eqn. (7.2) to give,

$$\sigma = \langle\gamma\rangle^2\sqrt{\frac{\sigma_0^2}{\langle\gamma_0\rangle^4} + At}, \tag{7.7}$$

where $A = (\alpha_f c^4 B_\perp^3 55)/(24E_s^3\sqrt{3}\lambda_c)$. We can note an interesting result here. If the initial and final mean γ and energy spread can be measured, then Eqn. (7.4) will give $B_\perp^2 l_B$ while Eqn. (7.7) will give $B_\perp^3 l_B$. Additionally, if the deflection of the beam is measured, the solution will give $B_\perp l_B$, therefore, if at least two of the three measurements can be made then $B_\perp$ and l_B can be found uniquely.

If η is not $\ll 1$, then $g \neq 1$ and cannot be removed from the integrals solved to get Eqns. (7.4) and (7.7). An analytical solution can be found by Taylor expanding g, however it is not simple to manipulate the solutions to obtain $B_\perp$. If necessary, the best option may be to numerically solve Eqn. (7.1) and the version of Eqn. (7.2) without the $\eta \ll 1$ approximation (Eqn. (3.4) reported by Ridgers *et al.* [136]).

The range of validity of the approximations used to derive these analytical expressions can be found by comparing them to simulated results. Fig. 7.1 shows a comparison of the analytical model (Eqn. (7.4)) to simulated results. The simulations were performed using the particle-in-cell (PIC) code [151, 150]. In the code, a Monte Carlo algorithm is coupled to the classical PIC loop to enable the simulation of multi-photon Compton scattering and multi-photon Breit-Wheeler pair creation under the local constant field approximation (LCFA). The simulations start with a collimated, 1 GeV mono-energetic electron beam. The beam is then propagated through a 2D region of constant magnetic field directed perpendicular

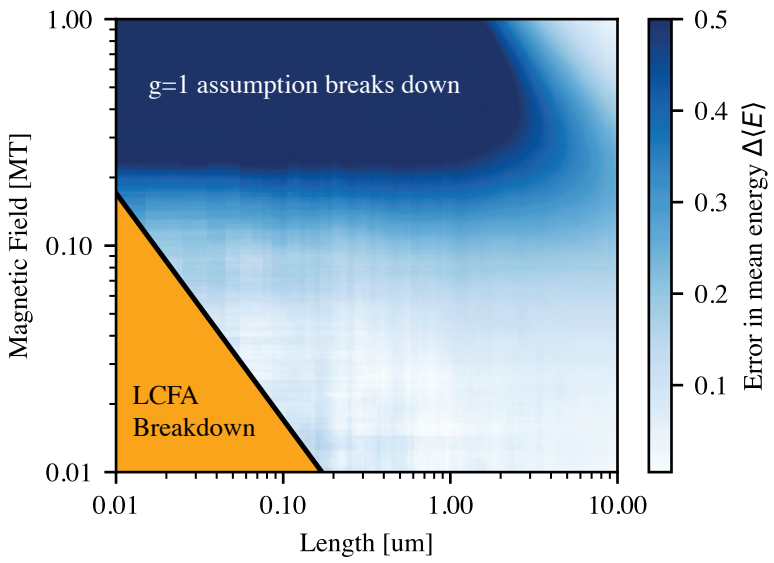

Figure 7.1: Relative difference of the mean energy prediction between the PIC simulations and the simplified analytic model. The orange region marks the parameter space where the LCFA breaks down. The dark blue region shows where the simplified analytic model breaks down.

to the electron motion. Simulations were performed for a range of magnetic field strengths varying from 0.01 to 1 MT, and the length of the constant field region from 0.01 to 10 μm. This parameter space is motivated by the range of values we might expect based on simulations of laser-solid interactions [180]. The results from the PIC simulation are taken to be the reference or "ground truth" value. Fig. 7.1 shows the relative difference of the mean energy loss between the PIC simulation results and the analytic model ($|\langle E\rangle_{PIC} - \langle E\rangle_{analytic}|/\langle E\rangle_{PIC}$) using Eqn. (7.4).

For the parameter range shown here, the analytic model well predicts the mean energy loss when the magnetic field strength is below 0.05 MT. The prediction assumes that $\eta \ll 1$, therefore it cannot give an accurate prediction at large field strengths. The nonlinearity η ranges from 0.0044 to 0.44 for the simulated values. Similar results are found for the analytical expression for the energy spread (Eqn. (7.7)). Additionally, note that the LCFA used for the simulations will be invalid when the magnetic fields are weak and short because the photon formation length, $l_{formation} = m_e c/eB$, will exceed the length of the fields. This

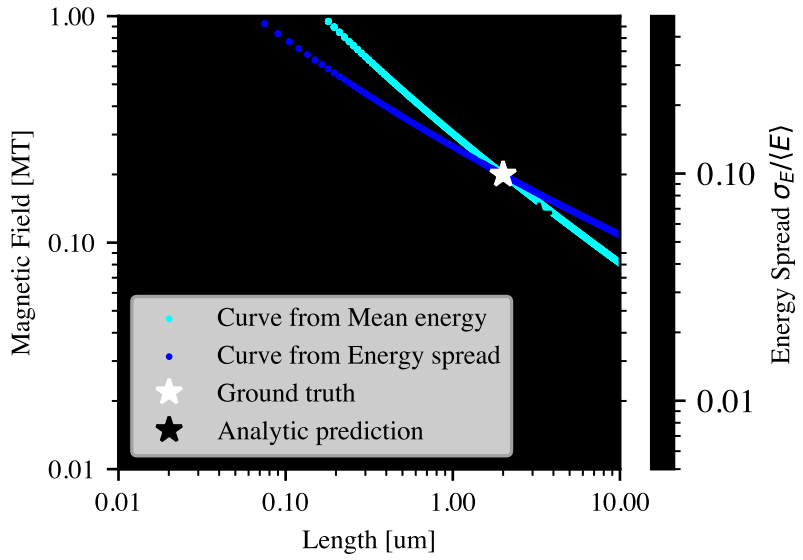

Figure 7.2: Illustration of how we can use the mean energy and energy spread measurement of the electron beam before and after it passes through a constant magnetic field region to obtain the strength and the length of the field. The cyan curve and the blue curve represent all the potential magnetic field strength and length combinations for a particular mean energy and the energy spread. The crossing point of the two curves coincides with the ground truth from the PIC simulation, represented by a white star. The black star is the prediction using the analytic Eqns. (7.6) and (7.7).

region has been blocked out in Fig. 7.1. A similar comparison was performed for the numerical integration of Eqns. (7.1) and (7.2). A better agreement with the PIC simulations in mean energy and energy spread was found from these equations. However, when the magnetic field strength exceeds 0.5 MT ($\eta > 0.22$), the numerical integration cannot precisely predict the energy spread. This is because Eqn. (7.2) assumes the shape of the energy distribution to be approximately Gaussian. However, when quantum radiation reaction is significant, the energy distribution deviates from the Gaussian distribution.

Given the exact measurement of the initial and final energy and energy spread of the electron beam, Eqns. (7.6) and (7.7) correspond to two lines of solutions for possible $B_\perp$ and l_B. These lines only cross at a single point giving a unique solution for these parameters. In Fig. 7.2, Eqns. (7.1) and (7.2) were solved numerically to find the mean energy and energy spread after passing through a range of field strengths and lengths of field. The colormap

shows the energy spread σ_E normalized to the average energy of the beam $\langle E \rangle$. The beam is initially 1 GeV and monoenergetic. The cyan line is a line of constant final mean energy, and the blue line is a line of constant energy spread. The values for final mean energy and energy spread were chosen such that they would result in a crossing point at 0.2 MT, 2 μm. An OSIRIS simulation was run to confirm that a 0.2 MT, 2 μm constant magnetic field would result in the expected mean energy and energy spread, and is plotted as a white star. The calculated strength and length of the field from Eqns. (7.6) and (7.7) are plotted as a black star, which underestimates the strength, and overestimates the length of the field. This is due to the assumption of small η being invalid for the simulated parameters. Although the analytical equations do not precisely predict the crossing point, they allow for an order-of-magnitude estimation of the strength and length of fields. For an experiment, similar analysis could be performed, where all solutions that would result in the measured final mean energy and energy spread given a measured initial energy and energy spread could be solved for numerically. However, experimental measurements have errors. Error in the measurement of energy spread and mean energy will result in the lines in Fig. 7.2 having finite widths. These widths will result in a crescent-shaped region of overlap, i.e. error in the strength and length of the field. The aspect ratio ($\Delta B_\perp / \Delta l_B$) of this region of overlap will depend non-linearly on the position of overlap of the lines. This effect is demonstrated in Fig. 7.3, in which a 10% measurement error in mean energy loss and spread is assumed. Taking the measured mean energy loss to be 51 MeV ($\Delta\langle\gamma\rangle = 100$), the red, blue, and purple regions show the possible values of B-field strength and length if the energy spread is 10%, 8%, or 6% respectively. If the lines cross at large B and small l_B, then there will be a much larger error in B than l_B. If they cross at small B and large l_B, there will be a much larger error in l_B than B.

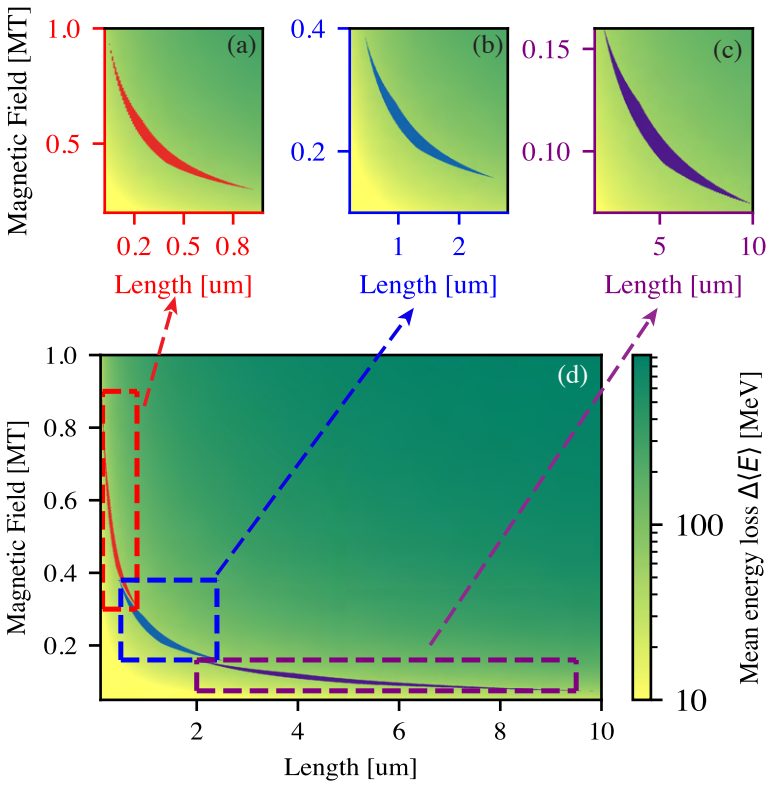

Figure 7.3: Demonstration of the non-linear dependence of the aspect ratio of the overlapping region with the position of the region. Here, we assume a 10% measurement error in mean energy loss and spread. For an energy loss of 51 MeV, the plot shows what the possible values of B-field strength and length are if the energy spread is 10%, 8%, or 6%, corresponding to the (a) red, (b) blue, and (c) purple areas in plot (d).

7.2 SFQED in a Plasma Wakefield

The chirped-pulse amplified technique pioneered by Mourou and his colleagues significantly shortened the pulse duration and intensified the laser's peak, fostering ideal conditions for using it as a driver for a laser wakefield accelerator (LWFA). The laser wakefield [10] is generated by interacting a high intensity ($a_0 \geq 1$) short pulse laser with underdense plasma. The laser's ponderomotive force pushes the electrons away, leaving a bubble containing strong longitudinal and transverse focusing fields ($\sim$ 100 GV/m). That field can provide a strong acceleration force, accelerating electrons to GeV energy in just a few centimeters.

One objective in developing laser wakefield acceleration technology is to establish a compact TeV-level or even 10 TeV-level [181] beam collider facility. It is widely acknowledged that electrons are unlikely to accelerate to TeV with a circular collider because of the effect of radiation reaction. Although LWFA has an acceleration gradient much higher than that of traditional accelerators, the radiation reaction is an important consideration. The strong transverse-focusing fields in a plasma wakefield will lead to betatron oscillations. The wiggling electrons emit radiation that can decelerate the electrons and modify the energy spectrum of the beam. The wiggler parameter K is commonly used to quantify whether the radiation is in the undulator regime or the wiggler regime. A simple expression to estimate the wiggler parameter for the electron beam inside the wakefield is $K = \gamma k_\beta r_\beta$. Here γ is the relativistic parameter, k_β is the betatron oscillation wave number, and r_β is the oscillation amplitude. For a 100 GeV electron beam inside the wakefield, the parameter K is on the order of several hundred, well in the wiggler regime. The radiation is incoherent and has a synchrotron-like spectrum. The power radiated by an electron in the wakefield is then $P_u \propto \gamma^2 k_\beta^2 K^2$. By examining this scaling law, we can get some insight into how the beam will behave during the radiation event. Considering a Gaussian beam located on the axis of the wakefield, electrons in the beam having different oscillation amplitudes will have different wiggler parameters K and lose different amounts of energy during radiation. This orbit effect could induce an increase in beam energy spread, which we call the classical radiation

spread effect. On the other hand, radiation could also decrease the spread of beam energy because electrons with higher energy will radiate more energy compared to electrons with lower energy [182], which we call radiation cooling.

The radiation effect becomes stronger as the beam energy gradually increases during the acceleration process. It will be important to keep the radiation force smaller than the acceleration. As beam energy reaches above 100 GeV, the radiation reaction behavior can deviate from the classical approximation. In this case, the quantum radiation effect will appear and cause "stochastic heating," which can be an intrinsic beam energy spread mechanism for high-energy accelerators. In the absence of dephasingless acceleration schemes [183, 184], due to dephasing and laser depletion, multiple LWFA stages are required to build a TeV-class beam collider. The coupling efficiency between acceleration stages depends highly on the beam emittance and energy spread [185]. As a result, understanding how quantum radiation reaction influences the evolution of beam energy and energy spread is important for constructing an LWFA-based TeV-class beam collider. Studying how radiation effects influence beam emittance is another important aspect. We find that in the radiation-dominated region, where the radiation reaction force is comparable to the wakefield's acceleration force, the beam's emittance can significantly decrease, forming a ring-shaped pattern in phase space. We provide an analytic explanation for the emergence of this pattern. Moreover, preservation of the spin polarization of the beam is crucial [186], and therefore it is also necessary to evaluate the influence of quantum radiation-induced spin-flips in the acceleration process.

7.2.1 QED Effect for Beam Transportation Inside Wakefield

We begin by estimating the quantum parameter χ_e for a TeV (or even 10 TeV) electron beam inside a typical LWFA. For simplicity, we assume that the wakefield operates in the "bubble" or "blowout" regime [187]; More complex schemes such as acceleration in hollow channels [188] where the focusing forces are weaker would clearly lead to a reduction in the effects

described here. In this regime, the averaged focusing field inside the wakefield experienced by the beam E_{focus} can be written as:

$$E_{focus} = |\boldsymbol{E}_\perp + \boldsymbol{v} \times \boldsymbol{B}| \simeq \frac{e n_p}{2\epsilon_0} \sigma_r \tag{7.8}$$

Here, n_p is the plasma density, σ_r is the transverse size of the beam, and for a gaussian beam, it is the RMS spread of the transverse distribution. We assume that the beam transverse phase space follows the matching condition inside the wakefield. The beam size σ_r, transverse energy spread σ_{u_r} and the normalized emittance ε_n has the following relationship:

$$\sigma_r = \sqrt{\frac{\varepsilon_n}{\gamma k_\beta}}, \quad \sigma_{u_r} = \sqrt{\varepsilon_n \gamma k_\beta} \tag{7.9}$$

Here, γ is the Lorentz factor of the beam; we assume $\gamma \gg 1$, $k_\beta = k_p/\sqrt{2\gamma}$ is the betatron oscillation wavenumber. The quantum parameter may be approximated as $\chi_e \approx \gamma \frac{E_{focus}}{E_s}$, where $E_s = m_e^2 c^3 / e\hbar$ is the critical or Schwinger field. Inserting the expression for the focusing field explicitly, we obtain

$$\chi_e \approx \lambda\!\!\!^{-}_c (\gamma/2)^{3/4} (\omega_p/c)^{3/2} \sqrt{\varepsilon_n} \tag{7.10}$$

We can rewrite χ_e as a function of beam energy $\mathcal{E}_{beam}$ in units of TeV, plasma density n_p in units of 10^{18} cm^{-3}, and normalized emittance ε_n in units of mm mrad as

$$\chi_e \approx 10^{-3} \times \left(\mathcal{E}_{beam}\ [\text{TeV}]\right)^{3/4} \times \left(n_p\ [10^{18}\ \text{cm}^{-3}]\right)^{3/4} \times \sqrt{\varepsilon_n\ [\text{mm mrad}]}\ . \tag{7.11}$$

Based on Eq. 7.11, we first estimate the quantum parameter χ_e experienced by a TeV electron beam inside a plasma wakefield accelerator with various beam emittances and background plasma densities.

The scalings are demonstrated in Fig. 7.4, in which the heatmap represents the magnitude

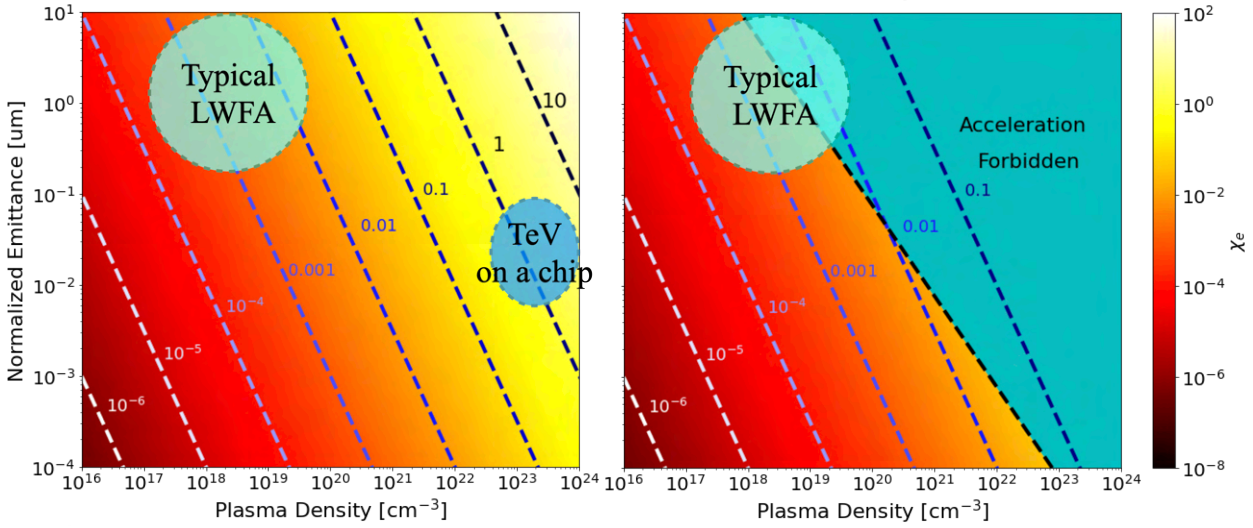

Figure 7.4: (left) Quantum parameter χ_e heat map for a matched gaussian beam as a function of beam emittance, accelerated to 1 TeV using plasma accelerator stages with different plasma densities. (right) Including radiation friction restricts acceleration.

of χ_e and the blue dashed line marks some particular values of χ_e. We mark two regions in the top plots. The light blue circle represents the parameter space where typical LWFA operates. For a TeV electron beam inside this region, the quantum parameter χ_e is on the order of 10^{-4} to 10^{-2}. The dark blue circle is the parameter space proposed by Tajima et al., in which they propose a high-gradient solid-density LWFA, also known as "TeV on a chip" [189]. The quantum parameter χ_e for a TeV beam inside this region will be much higher, of order 0.1 to 1. In the right plot, we include the influence of radiation reaction, marking the region where the radiation force will be greater than the acceleration force as "forbidden". Note that the acceleration force is estimated using standard scalings [190] for the 3D bubble regime:

$$F_{acc} = \frac{1}{2}\sqrt{a_0} m_e c \omega_p \tag{7.12}$$

The radiation reaction force under the assumptions that the emission is collinear and $\chi_e \ll 1$ can be expressed in terms of χ_e as [136]

$$F_{rad} = \frac{2\alpha_f}{3\lambda\!\!\!^{-}_c} m_e c^2 \chi_e^2 \,. \tag{7.13}$$

Inserting the expression 7.10 for χ_e, we obtain

$$F_{rad} \approx \frac{\alpha\hbar c}{3\sqrt{2}}\gamma^{3/2}\left(\frac{\omega_p}{c}\right)^3 \varepsilon_n. \tag{7.14}$$

By equating equations 7.12 and 7.14, we can obtain the condition of the acceleration forbidden region due to radiation reaction as a function of plasma density n_p *and* normalized emittance ε_n:

$$\varepsilon_n = \frac{3}{\sqrt{2}\alpha}\frac{c}{\lambda_c\omega_p}\frac{\sqrt{a_0}}{\gamma^{3/2}} \tag{7.15}$$

We use equation 7.15 to plot the black dashed line on the right hand side plot in Fig. 7.4, which marks the boundary of the acceleration forbidden region. Assume the normalized emittance doesn't change during the acceleration. The LWFA work under the parameters of this region cannot accelerate the beam to TeV energy due to strong radiation reaction force. We can find that for an electron beam with 1 mm mad emittance, one can not build a TeV electron accelerator using LWFA with plasma density above 2×10^{19} cm^{-3}. The high radiation friction force might be a fundamental problem in building high-density TeV class plasma-based accelerators unless the beam emittance can be cooled down during beam propagation. We will show in the later session that the radiation reaction force can actually significantly reduce the beam emittance for high-density plasma-based accelerators, which can loosen this acceleration forbidden condition.

7.2.2 Radiation Induced Energy Spread

Then, we will explore the radiation effect on the beam energy spread. We use the particle-in-cell code Osiris [151, 150] to simulate an externally injected witness beam inside the wakefield. QED effects are taken into account in the simulation by a Monte Carlo algorithm [191] that generates photons sampling from the quantum radiation spectrum. The simulation parameters chosen here are typical for a laser wakefield acceleration stage; the laser wavelength $\lambda = 0.8\ um$ with normalized laser intensity $a_0 = 6.2$. The laser pulse is injected into a pre-

ionized plasma channel with a parabolic density profile and center density $n_0 = 10^{18}$ cm^{-3}. The high-energy electron beam with an initial mean energy of 100, 150, 200 GeV and 1% energy spread is loaded at the tail of the wakefield bubble. The beam transverse spatial and momentum distribution are all Gaussian, with a spread of σ_r and σ_{u_r}. The spatial and momentum spread follows the matching condition inside the wakefield, as shown previously in equation 7.9. To illustrate the effect of the radiation-induced energy spread in acceptable simulation time, we make the beam's emittance relatively large, and the averaged radiation back-reaction force equals the acceleration force from the wakefield. Fig. 7.5 shows the evolution of energy spread for simulations of 100, 150, 200 GeV electron beams inside the wakefield. We run the same beam parameters using the quantum and classical radiation modules and compare the results with the analytic models. We develop a simple analytic model for the beam energy spread evolution and try to match it with the simulation result:

We first calculate the influence of the electron inside the beam having different betatron orbits. The radiation reaction force inside the wakefield scales with $F_{rad} \propto r_\beta^2$, where r_β is the betatron amplitude. For example, on-axis particles will not radiate, whereas off-axis particles radiate strongly. This orbit effect-induced energy spread can be estimated as:

$$\frac{d}{dt}\left(\frac{\sigma_\gamma}{\gamma}\right)^2_{orbit} = \frac{d}{dt}\left(\frac{F_{rad}(\varepsilon_n)t}{\gamma}\right)^2 \tag{7.16}$$

Here, the acceleration force and the radiation reaction are balanced, so the beam energy remains unchanged. We can get:

$$\frac{d}{dt}\left(\frac{\sigma_\gamma}{\gamma}\right)^2_{orbit} = \frac{2}{9}\left(\frac{\alpha_f c}{\lambda\!\!\!^{-}_c \gamma}\right)^2 \chi_e^4 g_1^2(\chi_e) t \tag{7.17}$$

From [136], we can obtain the expression for quantum stochastic radiation-induced energy

spread:

$$\frac{d}{dt}\left(\frac{\sigma_\gamma}{\gamma}\right)^2_{stoch} = \frac{d}{dt}\left(\frac{\int(\hbar\omega)^2 F(\omega) f(p) d\omega}{\gamma}\right)^2 = \frac{55\alpha_f c}{24\sqrt{3}\lambda\!\!\!^{-}_c \gamma}\chi_e^3 g_2(\chi_e) \tag{7.18}$$

Finally, we also have radiation cooling due to electrons with higher energy parts of the beam radiating more energy than those with low energy parts, so that the energy spread can be reduced:

$$\frac{d}{dt}\left(\frac{\sigma_\gamma}{\gamma}\right)^2_{radcool} = \frac{d}{dt}\left(\frac{2\Delta\gamma F_{rad} t}{\gamma^2}\right) = -\frac{8\alpha_f c}{3\lambda\!\!\!^{-}_c \gamma}\chi_e^2\left(\frac{\sigma_\gamma}{\gamma}\right)^2 g_1(\chi_e) \tag{7.19}$$

Because the orbit effect-induced energy spread and quantum stochastic effect-induced energy spread are separate effects, their coupling is a second-order process, and we therefore ignore it in our model.

$$\begin{aligned}\frac{d}{dt}\left(\frac{\sigma_\gamma}{\gamma}\right)^2_{total} &\approx \frac{d}{dt}\left(\frac{\sigma_\gamma}{\gamma}\right)^2_{orbit} + \frac{d}{dt}\left(\frac{\sigma_\gamma}{\gamma}\right)^2_{stoch} + \frac{d}{dt}\left(\frac{\sigma_\gamma}{\gamma}\right)^2_{radcool} \\ &\approx C_{orbit} g_2 \chi_e^3 + C_{stoch} g_1^2 \chi_e^4 t - C_{radcool} g_1 \chi_e^2 \left(\frac{\sigma_\gamma}{\gamma}\right)^2\end{aligned} \tag{7.20}$$

We can see from Fig. 7.5 that the model using equation 7.17, 7.18, 7.19, 7.20 agrees well with both quantum and classical simulation. Running a full simulation for a 1 TeV beam acceleration will be very expensive, so we try to predict the energy spread for a TeV beam with different emittances and accelerate it by wakefield with various plasma densities using our simplified analytic model.

Fig. 7.6 (a) plots the relative energy spread of a 1 GeV beam with 1 % energy spread accelerated to 1 TeV for different background plasma densities and beam normalized emittances predicted by Eq. (7.20). Fig. 7.6 (b) plots the relative energy spread induced only by the quantum spreading effect. We assume the plasma density for all the acceleration stages is the same, and the beam emittance is conserved for simplicity. The heatmap shows

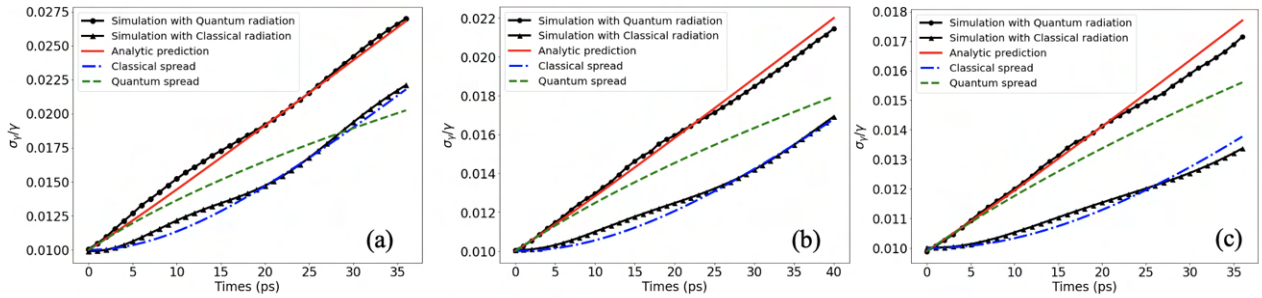

Figure 7.5: Simulation results of the beam energy spread evolution for initial beam energy (a) 50 GeV, (b) 100 GeV, (c) 200 GeV using classical radiation and quantum radiation model. The results are compared with the model that estimates only classical orbit effect-induced energy spread (blue dashed curve), only quantum stochastic effect-induced energy spread (green dashed curve), and the summation of the two contributions together (red curve).

the relative energy spread calculated using our radiation-induced energy spread model. We derive useful scaling laws for the relative energy spread in terms of different background plasma densities and beam emittances. They are valid when the quantum parameter χ is much smaller than 1. We begin with an estimate of the time required to accelerate the beam to 1 TeV, assuming the radiation reaction is small:

$$t_0 = 1\ [\text{TeV}]/F_{acc} = 69.4[\text{ns}] \times a_0^{-0.5} \times (n_0[10^{18}\text{cm}^{-3}])^{-0.5} \tag{7.21}$$

The classical orbit effect induced energy spread for a beam accelerated to 1 TeV can be estimated as:

$$\frac{\sigma_{class}}{\gamma} = 8.47\% \times a_0^{-0.5} \times (n_0[10^{18}\text{cm}^{-3}]) \times (\epsilon_0[\text{mm mrad}]) \tag{7.22}$$

$$\frac{\sigma_{qed}}{\gamma} = 0.84\% \times a_0^{-0.25} \times (n_0[10^{18}\text{cm}^{-3}])^{0.875} \times (\epsilon_0[\text{mm mrad}])^{0.75} \tag{7.23}$$

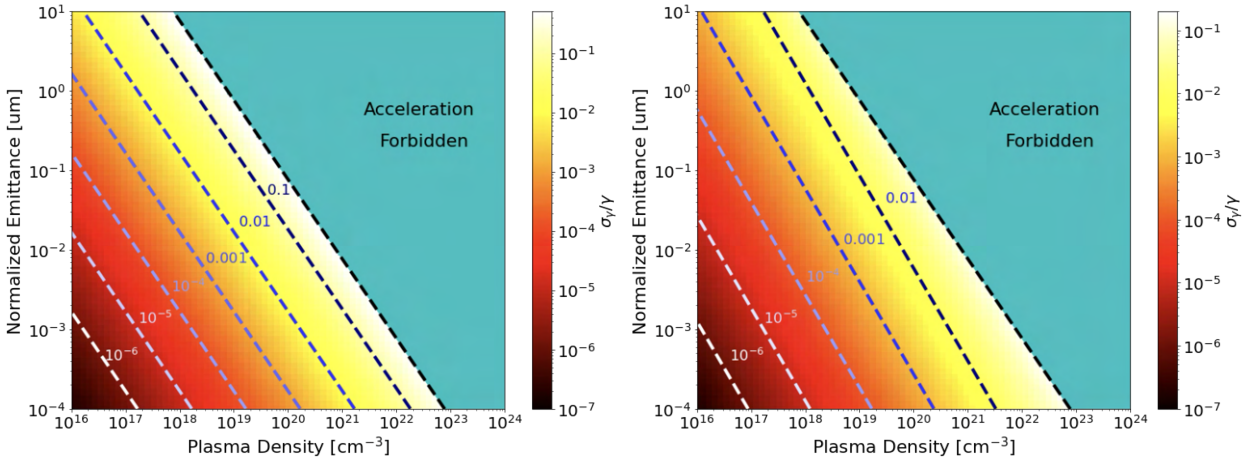

Figure 7.6: (a) Energy spread σ_γ/γ heat map for a Gaussian beam with different emittance accelerated to 1 TeV using LWFA stages with different plasma densities. (b) Heat map for purely quantum radiation effect induced energy spread.

We should also take into account the radiation-cooling effect:

$$\begin{aligned}\frac{\sigma_{rad}}{\gamma} &\approx \frac{\sqrt{\sigma_{class}^2 + \sigma_{qed}^2 - \sigma_{cool}^2}}{\gamma} \\ &\approx \frac{\sigma_{class}}{\gamma}(1 - 0.165 \times a_0^{-0.5} \times n_0[10^{18}\mathrm{cm}^{-3}] \times \epsilon_0[\mathrm{mm\ mrad}])\end{aligned} \tag{7.24}$$

The blue dashed lines on the plots are the contour of some typical energy spread calculated using our energy spread scaling law shown in Eq. 7.23 and 7.24. We can find that the energy spread from the classical radiation effect is about ten times larger than the quantum radiation effect. Also, we could see that if we choose to use laser-plasma accelerators with low plasma density and small emittance, the radiation-induced energy spread is greatly reduced. We should mention that keeping a small energy spread is significant for preserving beam emittance due to the chromatic self-emittance growth effect, as discussed in [185]. It is noted that the energy spread should be smaller than 10^{-3}, which is preferred for the laser-wakefield-based TeV-class accelerator. As a result, from Fig. 7.6, we could find that it will be ideal to build an LWFA-based TeV collider with plasma density around 10^{17} cm^{-3}.

7.2.3 Radation-induced emittance cooling

We study radiation-induced emittance cooling through a simplified Osiris 2D simulation. We start with a 10 GeV beam with 1% energy spread, normalized emittance equal to 1 μm propagating inside an infinitely long ion channel with a constant acceleration field. The focusing force and acceleration field are set by Eq. (7.8) and (7.12), which are the same as the wakefield in the bubble region with densities equal 10^{18}, 10^{20}, 10^{22} cm^{-3}. Fig. 7.7 shows the evolution of normalized emittance for plasma density equals 10^{18} (black curve), 10^{20} (blue curve), and 10^{22} cm^{-3} (red curve). We can see that the normalized emittance will significantly cool down for high plasma density ion channels. The normalized emittance can be reduced to a few nm for a density equal 10^{22} cm^{-3}. The top three plots in Fig. 7.8 shows what the beam transverse phase space looks like at the end of three simulations. We can also see that the transverse phase space of the beam can be significantly modified for high-density channels. The original Gaussian distribution becomes a ring shape. The bottom three plots in Fig. 7.8 compare the evolution of energy spread calculated with our model with the simulation result. We can see that for high-density situations, the beam energy spread (black curve) is much smaller than the full energy spread model prediction (blue dashed curve), and brings it closer to the prediction where only the quantum radiation-induced stochastic broadening effect is taken into account (green dashed curve). The formation of this ring-shaped distribution can suppress the radiation-induced energy spread due to the orbit effect.

7.2.4 Asymptotic Limit for Beam Transverse Distribution Inside Wakefield

We develop a simple analytic explanation for the ring-shaped distribution formation process. The model describes the motion of particles inside a linear focusing force with constant acceleration and radiation back-reaction. We show that under reasonable approximation,

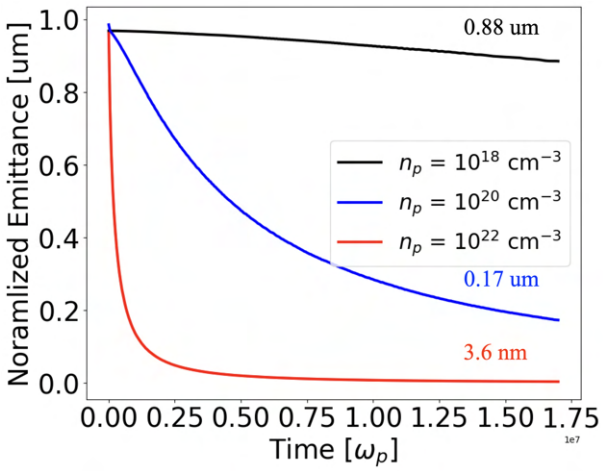

Figure 7.7: Radiation-induced emittance cooling for a beam propagating inside a channel field with constant acceleration. The field is the same as the wakefield in the bubble region for plasma density n_p equal 10^{18} cm^{-3}, 10^{20} cm^{-3} and 10^{22} cm^{-3}. The beam normalized starts at $1\mu m$. The emittance cooling becomes substantial for a high-density wakefield.

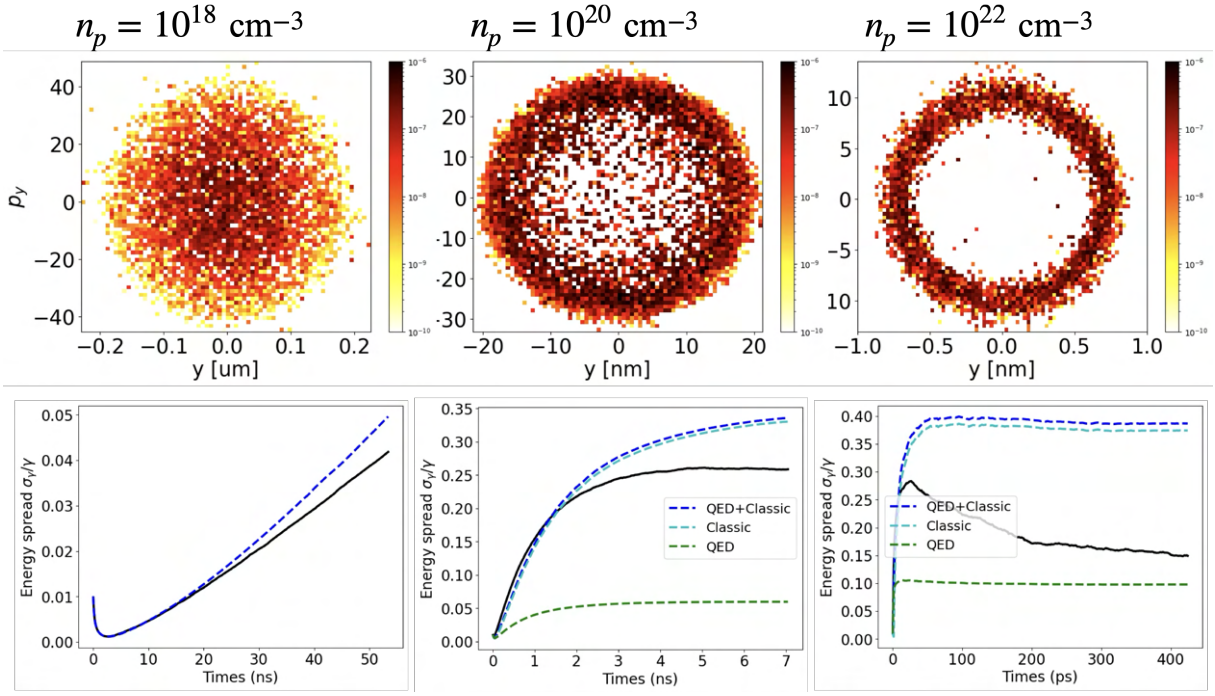

Figure 7.8: The phase space distribution at the end of the simulation for plasma density n_p equal 10^{18} cm^{-3}, 10^{20} cm^{-3} and 10^{22} cm^{-3}. The beam starts with a 2D Gaussian distribution in transverse phase space, and in a high-density scenario where radiation reaction is significant, the transverse phase space distribution evolves into a ring-shaped distribution. This ring-shaped distribution can suppress the radiation-induced energy spread from the orbit effect.

particles starting with different locations in transverse phase space will asymptotically fall onto a narrow ring. We begin with the equation of motion, in terms of proper time τ:

$$\frac{d\gamma}{d\tau} = \gamma\kappa \tag{7.25}$$

$$\frac{dp_r}{d\tau} = -\gamma\alpha r - \gamma^2\beta r^2 p_r \tag{7.26}$$

Here, κ is the parameter for representing the acceleration force strength, α represents the focusing force strength, and β represents the radiation force strength. We assume that the particle's longitudinal momentum is much bigger than the transverse component p_r. We also assume that the radiation reaction force is smaller than the acceleration and focusing forces. We can get the solution for γ:

$$\gamma = \gamma_0 e^{\kappa\tau} \tag{7.27}$$

We assume the envelope variation is slow compared to the betatron oscillations; using WKB approximation, the radial orbit is:

$$r = A(\tau)\sin(\Psi) \tag{7.28}$$

Which $\Psi = \int \sqrt{\gamma\alpha}d\tau$, the transverse momentum is then

$$p_r = \frac{dr}{d\tau} \approx \sqrt{\alpha\gamma}A\cos(\Psi) \tag{7.29}$$

Let

$$J = \frac{p_r^2}{2\sqrt{\alpha\gamma}} + \frac{r^2\sqrt{\alpha\gamma}}{2} \approx \sqrt{\alpha\gamma}\frac{A^2}{2} \tag{7.30}$$

We time p_r on both the sides of Eq. 7.26:

$$\frac{d}{d\tau}\left(\frac{p_r^2}{2}\right)+\alpha\gamma\frac{d}{d\tau}\left(\frac{r^2}{2}\right)=-\beta\gamma^2r^2p_r^2 \tag{7.31}$$

Assume the energy change is slow, ignore $\frac{d\gamma}{d\tau}$ term, we can combine terms on the left-hand side and get:

$$\frac{dJ}{d\tau}=-\frac{\beta\gamma^{3/2}}{\sqrt{\alpha}}r^2p_r^2 \tag{7.32}$$

On the right-hand side $r^2p_r^2 \approx \alpha\gamma A^4\sin^2\Psi\cos^2\Psi$, cycle average can get $\langle r^2p_r^2\rangle = \alpha\gamma A^4/8 = J^2/2$. Plug in the equation:

$$\frac{dJ}{d\tau}=-\frac{\beta\gamma^{3/2}}{2\sqrt{\alpha}}J^2 \tag{7.33}$$

We can obtain the solution of J:

$$J=\frac{J_0}{1+\frac{\beta}{2\sqrt{\alpha}}J_0\int\gamma^{3/2}d\tau} \tag{7.34}$$

Here $J_0 = p_{r0}^2/2\sqrt{\alpha\gamma_0}+r_0^2\sqrt{\alpha\gamma_0}/2$. We can then get the solution for transverse orbit and momentum:

$$r=\sqrt{\frac{2J}{\sqrt{\gamma\alpha}}}\sin\Psi,\quad p_r=\sqrt{2J\sqrt{\gamma\alpha}}\cos\Psi \tag{7.35}$$

We apply Eq. 7.27 to solve $\int\gamma^{3/2}d\tau$ on the right-hand side of the Eq. 7.34 for linear acceleartion.

$$\int\gamma^{3/2}d\tau=\frac{2\gamma_0^{3/2}}{3\kappa}\left(e^{3/2\kappa\tau}-1\right) \tag{7.36}$$

The asymptotic limit of momentum is as $\tau\to\infty$

$$|r|_{\tau\to\infty}=\frac{1}{\gamma}\sqrt{\frac{6\kappa}{\beta}},\quad |p_r|_{\tau\to\infty}=\sqrt{\frac{6\alpha\kappa}{\gamma\beta}} \tag{7.37}$$

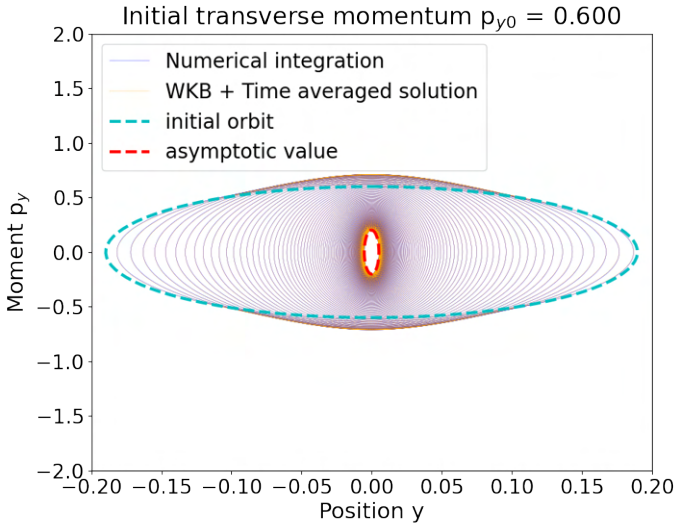

Figure 7.9: Asymptotic limit of transverse phase space distribution for a beam inside the channel field with constant acceleration in radiation dominanted region.

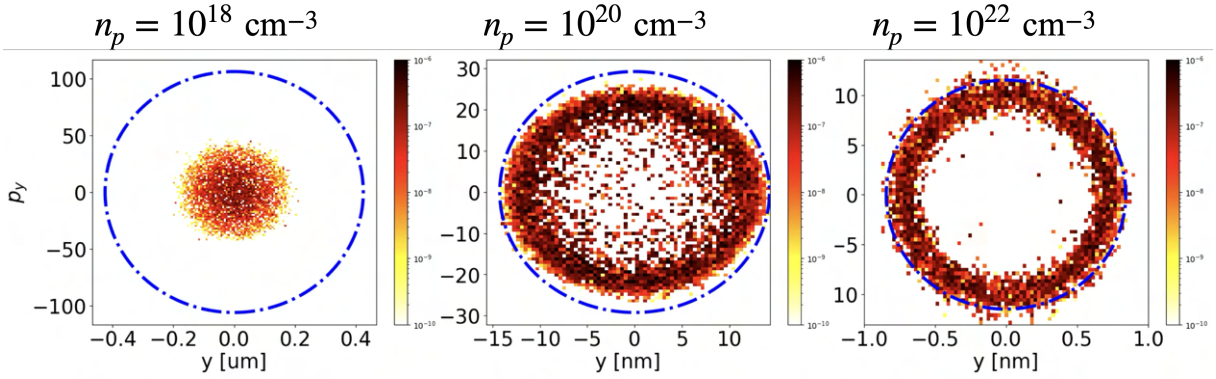

Figure 7.10: Transverse phase space result compared with the asymptotic orbits predicted by our model

This is independent of the initial condition of the particle transverse phase space J_0. We demonstrate this in Fig. 7.9, which shows that particles starting with different positions in the transverse phase space will fall into the same asymptotic orbit. As a result, any kind of initial distribution will fall into a ring shape distribution in the radiation-dominant region. We confirm this by comparing the asymptotic orbit in predicted Eq. (7.37) with the ion channel acceleration simulation result, shown in Fig. 7.10. We do see that in the radiation-dominant region, where beam emittance shrinks significantly, its transverse phase space falls into a ring shape distribution whose radius can be well predicted by our model.

7.2.5 QED Effect on Spin Transportation

Finally, we use our recently developed spin and polarization-resolved QED module in PIC code OSIRIS to explore the radiation effect on spin transportation inside the wakefield. This algorithm includes classical spin dynamics using the Thomas-Bargmann-Michel-Telegdi (T-BMT) equations and a Monte-Carlo sampling algorithm to calculate the radiative spin transitions. For high-energy lepton colliders, collisions between spin-polarized electron and positron beams are preferred to study possible new physics beyond the standard model [192, 193]. Recent studies relevant to high-power laser facilities have shown that the spin and polarization-resolved QED code is useful to explore condition lepton beam spin distributions [54, 4, 142], polarized gamma-ray generation, and multi-staged QED processes like helicity-transfer, and to be presented in plasma instabilities [75].

J. Vieira et al. have explored the influence of classical spin precession on polarized particle transportation, and they conclude that the classical spin precession-induced depolarization can be controlled for the beam inside the wakefield. Here, with our more comprehensive model, which includes radiation-induced spin change, we revisit this problem and give a more realistic estimation of the polarized beam transportation inside the wakefield. The simulations were again conducted under a simplified scenario with a 10 GeV beam initially polarized along beam propagation direction $\boldsymbol{x}$ with 1% energy spread, normalized emittance equal to 1 um propagating inside an infinitely long ion channel with a constant acceleration field. The focusing force and acceleration field are the same as the plasma field with density equals 10^{18}, 10^{20}, 10^{22} cm^{-3}. The evolution of averaged spin polarization for the whole beam is shown in Fig. 7.11. Generally, the radiative effect does not influence the polarized beam transportation inside the laser wakefield for lower density.

7.2.6 Beam Inside an Ion Channel

In this section, we provide our complete derivation of our energy spread model, following the derivation from [182]. We begin with the differential equation of a single particle:

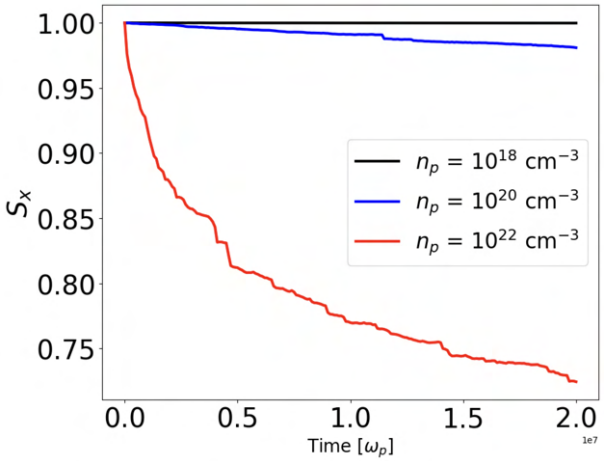

Figure 7.11: QED effect for spin transportation inside wakefield

$$\frac{d\gamma}{dt} = -\frac{1}{2}\tau_R c^2 K^4 \left(x_0^2 + \frac{u_{x0}^2}{\gamma_0 K^2}\right)\gamma^2 \tag{7.38}$$

We can obtain the energy evolution equation of a single particle:

$$\gamma = \gamma_0 \left[1 + \frac{1}{2}\tau_R c^2 K^4 \left(\gamma_0 x_0^2 + \frac{u_{x0}^2}{K^2}\right) t\right]^{-1} \tag{7.39}$$

To obtain the equation for beam dynamics, we can rewrite each quantity in terms of a centroid and a deviation, i.e., $\gamma_0 = \langle\gamma_0\rangle + \delta\gamma_0$, $x_0 = \langle x_0\rangle + \delta x_0$, $u_{x0} = \delta u_{x0}$. Here, we assume the beam is on the center of the wakefield bubble, $\langle x_0\rangle = 0$. We also assume the deviation follows the Gaussian distribution. As a result, $\langle\delta x_0^2\rangle = \sigma_{x0}^2$, $\langle\delta u_{x0}^2\rangle = \sigma_{u_{x0}}^2$, $\langle\delta\gamma_0^2\rangle = \sigma_{\gamma_0}^2$. We can first derive the evolution of the averaged energy of the beam:

$$\begin{aligned}
\langle\gamma\rangle &= \left\langle \gamma_0 \left[1 + A\left(\gamma_0 x_0^2 + \frac{u_{x0}^2}{K^2}\right) t\right]^{-1} \right\rangle \\
&\approx \left\langle (\langle\gamma_0\rangle + \delta\gamma_0)\left[1 - A\left((\langle\gamma_0\rangle + \delta\gamma_0)\delta x_0^2 + \frac{\delta u_{x0}^2}{K^2}\right) t\right] \right\rangle \\
&= \langle\gamma_0\rangle \left[1 - A\left(\langle\gamma_0\rangle\sigma_{x0}^2 + \frac{\sigma_{\gamma_0}^2}{\langle\gamma_0\rangle}\sigma_{x0}^2 + \frac{\sigma_{u_{x0}}^2}{K^2}\right) t\right] \\
&\approx \langle\gamma_0\rangle \left[1 - A\left(\langle\gamma_0\rangle\sigma_{x0}^2 + \frac{\sigma_{u_{x0}}^2}{K^2}\right) t\right]
\end{aligned} \tag{7.40}$$

Here, we ignore the higher order term $\sim \sigma_{\gamma_0}^2\sigma_{x0}^2$. Let $A = \frac{1}{2}\tau_R c^2 K^4$ to simplified the expression. To calculate the energy spread σ_γ^2, we first calculate $\langle\gamma^2\rangle$.

$$\begin{aligned}
\langle\gamma^2\rangle &= \left\langle \gamma_0^2 \left[1 + A\left(\gamma_0 x_0^2 + \frac{u_{x0}^2}{K^2}\right)t\right]^{-2} \right\rangle \\
&\approx \left\langle (\langle\gamma_0\rangle + \delta\gamma_0)^2 \left[1 - A\left((\langle\gamma_0\rangle + \delta\gamma_0)\delta x_0^2 + \frac{\delta u_{x0}^2}{K^2}\right)t\right]^2 \right\rangle \\
&\approx \langle\gamma_0\rangle^2 + \sigma_{\gamma_0}^2 \\
&- 2At\left(\langle\gamma_0\rangle^3\sigma_{x0}^2 + 3\langle\gamma_0\rangle\sigma_{x0}^2\sigma_{\gamma_0}^2 + \langle\gamma_0\rangle^2\frac{\sigma_{u_{x0}}^2}{K^2} + \sigma_{\gamma_0}^2\frac{\sigma_{u_{x0}}^2}{K^2}\right) \\
&+ A^2t^2\left(3{\gamma_0}^4\sigma_{x_0}^4 + 3{\gamma_0}^2\frac{\sigma_{u_{x0}}^4}{K^4} + 2{\gamma_0}^2\sigma_{x_0}^2\frac{\sigma_{u_{x0}}^2}{K^2}\right)
\end{aligned} \tag{7.41}$$

Notice if the quantities follow the Gaussian distribution, e.g., for spatial deviation δx_0, we have the relationship $\langle\delta x_0^4\rangle = 3\sigma_{x0}^4$. We also ignore higher-order terms. The evolution of the energy spread, assuming the initial energy is small, can be expressed as:

$$\begin{aligned}
\sigma_\gamma^2 =& \langle\gamma^2\rangle - \langle\gamma\rangle^2 \\
\approx& \sigma_{\gamma_0}^2 - 4At\left(\langle\gamma_0\rangle\sigma_{x0}^2\sigma_{\gamma_0}^2 + \sigma_{\gamma_0}^2\frac{\sigma_{u_{x0}}^2}{K^2}\right) \\
&+ 2A^2t^2\left({\gamma_0}^4\sigma_{x_0}^4 + {\gamma_0}^2\frac{\sigma_{u_{x0}}^4}{K^4}\right)
\end{aligned} \tag{7.42}$$

We can also obtain the differential equation of energy spread change:

$$\frac{d\sigma_\gamma^2}{dt} = 2\left\langle\gamma\frac{d\gamma}{dt}\right\rangle - 2\langle\gamma\rangle\frac{d\langle\gamma\rangle}{dt} \tag{7.43}$$

7.2.7 Boltzmann Radiation Reaction

To include quantum radiation-induced energy spread, we need to describe the evolution of the witness beam distribution function in terms of a Boltzmann-like equation first,

$$\frac{\partial f}{\partial t} + \vec{v} \cdot \frac{\partial f}{\partial \vec{x}} + q(\vec{E} + \vec{v} \times \vec{B}) \cdot \frac{\partial f}{\partial \vec{p}} = \left. \frac{\delta f}{\delta t} \right|_{emission} \tag{7.44}$$

where the right hand side corresponds to the change in the distribution function in a short period of time owing to the effect of multiple point-like radiation emission events. We assume that pair production and higher order processes are negligible for the conditions of interest. Two different models may be used for the right hand side operator. First a modified classical operator using a simplified ultra-relativistic form of the Landau and Lifshitz prescription, including a factor to include the suppression of the radiated power due to quantum emission,

$$\left. \frac{\delta f}{\delta t} \right|^{C}_{emission} = \frac{1}{p^2} \frac{\partial}{\partial p} \left(p^2 \frac{P_{rad}}{c} f \right) \tag{7.45}$$

where

$$P_{rad} = \frac{2\alpha_f c \chi_e^2}{3\lambda\!\!\!^{-}_c}$$

And secondly a fully stochastic treatment of the emission using the quantum synchrotron emission differential cross-section.

$$\begin{aligned} \left. \frac{\delta f}{\delta t} \right|^{Q}_{emission} &= -\lambda_\gamma(\chi_e) f \\ &+ \frac{b}{2m_e c} \int_p^\infty dp' \lambda_\gamma(\chi'_e) \rho_{\chi_\gamma}(\chi'_e, \chi_\gamma) \frac{p'^2}{p^2} f(\mathbf{p}') \end{aligned} \tag{7.46}$$

Here, electron quantum efficiency parameter $\chi_e = \gamma b$. For $\gamma \gg 1$, $b = |\mathbf{E}_\perp + \mathbf{v} \times \mathbf{B}|/E_s$. $\chi_\gamma = (h\nu b)/(2m_e c^2)$ is the quantum efficiency parameter for an emitted photon with energy $h\nu b$. λ_γ is the photon emission rate, which under quasi-static weak-field approximations is:

$$\lambda_\gamma(\chi_e) = \frac{\sqrt{3}\alpha_f c}{\lambda_c}\frac{\chi_e}{\gamma}h(\chi_e) \qquad h(\chi_e) = \int_0^{\chi_e/2} d\chi_\gamma \frac{F(\chi_e,\chi_\gamma)}{\chi_\gamma} \tag{7.47}$$

$F(\chi_e, \chi_\gamma)$ is the quantum synchroton function givne in Sokolov & Ternov, for $\chi_\gamma < \chi_e/2$,

$$F(\chi_e,\chi_\gamma) = \frac{3\chi_\gamma^2}{\chi_e^2} y K_{2/3}(y) + \left(1 - \frac{2\chi_\gamma}{\chi_e}\right) y \int_y^\infty dt K_{5/3}(t) \tag{7.48}$$

which $y = 4\chi_\gamma/[3\chi_e(\chi_e - 2\chi_\gamma)]$ and K_n are modified Bessel functions of the second kind.For $\chi_\gamma \leq \chi_e/2$, $F(\chi_e, \chi_\gamma) = 0$. The probability that a photon is emitted with a given χ_γ (by an electron with energy χ_e) is $\rho(\chi_e, \chi_\gamma)d\chi_\gamma = [1/h(\chi_e)][F(\chi_e, \chi_\gamma)/\chi_\gamma]d\chi_\gamma$

Notice that the focusing field inside the wakefield depends almost linearly on the transverse displacement of the electrons. We try to calculate the evolution of the mean momentum $\langle \mathbf{p} \rangle$ first.

$$\begin{aligned} n_e \left(\frac{\mathrm{d}\langle \mathbf{p}\rangle}{\mathrm{d}t}\right)_{st} &= -\int_0^\infty \mathrm{d}r \mathrm{d}^3\mathbf{p}\mathbf{p}\lambda_\gamma(\chi_e) f \\ &+ \int_0^\infty \mathrm{d}r \mathrm{d}^3\mathbf{p}\mathbf{p}\frac{b}{2m_e c}\int_p^\infty \mathrm{d}p' \lambda_\gamma(\chi_e')\rho_{\chi_\gamma}(\chi_e', \chi_\gamma)\frac{p'^2}{p^2} f \end{aligned} \tag{7.49}$$

We can get

$$\begin{aligned} n_e \left(\frac{\mathrm{d}\langle \mathbf{p}\rangle}{\mathrm{d}t}\right)_{st} &= -\int \mathrm{d}r \int \mathrm{d}^3\vec{p}\vec{p}\lambda_\gamma(\chi_e) f \\ &+ \int \mathrm{d}r \int \mathrm{d}^3\vec{p}\vec{p}\lambda_\gamma(\chi_e) f(\vec{p}) \left(p - \frac{(h\nu)_{\mathrm{av}}}{c}\right) \end{aligned} \tag{7.50}$$

Canceling the identical term and using $gP_{cl} = \lambda_\gamma(h\nu)_{av}$ yields

$$n_e \left(\frac{\mathrm{d}\langle \mathbf{p}\rangle}{\mathrm{d}t}\right)_{st} = -\frac{\langle gP_{cl}\hat{\mathbf{p}}\rangle}{c} \tag{7.51}$$

We can also obtain the equation for the evolution of σ^2 by using the same procedure.

Since $\sigma^2 = \langle\gamma^2\rangle - \langle\gamma\rangle^2$. We first need to get an equation for the $(\mathrm{d}\langle\gamma^2\rangle/\mathrm{d}t)_{st}$ and $(\mathrm{d}\langle\gamma\rangle^2/\mathrm{d}t)_{st}$

$$\begin{aligned} n_e\left(\frac{\mathrm{d}\langle\gamma^2\rangle}{\mathrm{d}t}\right)_{st} &= -\int \mathrm{d}r \int \mathrm{d}^3\mathbf{p}\gamma^2\lambda_\gamma(\chi_e)f \\ &+ \int \mathrm{d}r \int \mathrm{d}^3\mathbf{p}\gamma^2\frac{b}{2m_ec}\int_p^\infty \mathrm{d}p'\lambda_\gamma(\chi_e')\rho_{\chi_\gamma}(\chi_e',\chi_\gamma)\frac{p'^2}{p^2}f(\vec{p}') \end{aligned} \tag{7.52}$$

This gives:

$$\begin{aligned} n_e\left(\frac{\mathrm{d}\langle\gamma^2\rangle}{\mathrm{d}t}\right)_{st} &= -\int \mathrm{d}r \int \mathrm{d}^3\vec{p}\gamma^2\lambda_\gamma(\chi_e)f \\ &+ \int \mathrm{d}r \int \mathrm{d}^3\vec{p}\lambda_\gamma(\chi_e)f(\vec{p})\left(\gamma^2 - 2\gamma\frac{(h\nu)_{\mathrm{av}}}{m_ec^2} + \frac{[(h\nu)^2]_{\mathrm{av}}}{m_e^2c^4}\right) \end{aligned} \tag{7.53}$$

We identify $S = \lambda[(h\nu)^2]_{\mathrm{av}}$ and get

$$\left(\frac{\mathrm{d}\langle\gamma^2\rangle}{\mathrm{d}t}\right)_{st} = -2\frac{\langle\gamma g P_{cl}\rangle}{m_ec^2} + \frac{\langle S\rangle}{m_e^2c^4}. \tag{7.54}$$

Finally to get equation for $(\mathrm{d}\sigma^2/\mathrm{d}t)_{st}$ we identify $\sigma^2 = \langle\gamma^2\rangle - \langle\gamma\rangle^2$. Therefore,

$$\begin{aligned} \left(\frac{\mathrm{d}\sigma^2}{\mathrm{d}t}\right)_{st} &= \left(\frac{\mathrm{d}\langle\gamma^2\rangle}{\mathrm{d}t}\right) - \left(\frac{\mathrm{d}\langle\gamma\rangle^2}{\mathrm{d}t}\right) \\ &= 2\left\langle\gamma\frac{\mathrm{d}\gamma}{\mathrm{d}t}\right\rangle - 2\langle\gamma\rangle\left(\frac{\mathrm{d}\langle\gamma\rangle}{\mathrm{d}t}\right). \end{aligned} \tag{7.55}$$

Here, the angle brackets operation represents averaging over gamma and transverse displacement distribution. Because the focusing field depends almost linearly on the transverse displacement of the electrons, we could rewrite P_{cl} as $P_{cl} = A(\gamma_0 x_0^2 + \frac{u_{x_0}^2}{K^2})$, where A is a constant. Also, notice that γ is time-dependent, which under first-order approximation is $\gamma \approx \gamma_0 - P_{cl}t$. We could rewrite the equations of energy spread as follows:

$$\left(\frac{\mathrm{d}\langle\sigma^2\rangle}{\mathrm{d}t}\right)_{st} = 2\frac{\left\langle(\gamma_0 - gA(\gamma_0 x_0^2 + \frac{u_{x_0}^2}{K^2})t)(gA(\gamma_0 x_0^2 + \frac{u_{x_0}^2}{K^2}))\right\rangle}{m_e c^2} + \frac{\langle S\rangle}{m_e^2 c^4} - \left\langle\gamma_0 - A(\gamma_0 x_0^2 + \frac{u_{x_0}^2}{K^2})t\right\rangle \frac{\left\langle gA(\gamma_0 x_0^2 + \frac{u_{x_0}^2}{K^2})\right\rangle}{m_e c^2} \tag{7.56}$$

To obtain an explicit form of the change of energy spread with respect to beam parameter, we could first write the quantities in terms of the combination of centroid and deviation, i.e. $\gamma_0 = \langle\gamma\rangle_0 + \delta\gamma_0$, $x_0 = \delta x_0$, $u_{x0} = \delta u_{x0}$ for an on-axis beam. We assume the beam transverse spatial, momentum distribution, and energy distribution are Gaussian, so that $\langle\delta\gamma_0^2\rangle = \sigma_{\gamma_0}^2$, $\langle\delta {x_0}^2\rangle = \sigma_{x_0}^2$, $\langle\delta u_{x0}^2\rangle = \sigma_{u_{x0}}^2$, $\langle\delta x_0^4\rangle = 3\sigma_{x_0}^4$, $\langle\delta u_{x0}^4\rangle = 3\sigma_{u_{x0}}^4$. Since the quantum parameter in this work is typically on the order of 0.001, the Gaunt factor g can be considered as 1. After some algebra and dropping higher order terms, we obtain:

$$\left(\frac{\mathrm{d}\langle\sigma^2\rangle}{\mathrm{d}t}\right)_{st} \approx -2A\sigma_{\gamma 0}^2\sigma_{x0}^2 + 2A^2 t(\gamma^2\sigma_{x0}^4 + \frac{\sigma_{u_{x0}}^4}{K^4}) + \frac{\langle S\rangle}{m_e^2 c^4} \tag{7.57}$$

7.3 Conclusion

In this section, we conclude our work on the application of quantum radiation reaction on extreme magnetic field measurement and for the future TeV-class LWFA. In our first work, we demonstrate that the signature of strong field QED effects can be leveraged to measure the extreme field strengths generated in future high-intensity laser-plasma interactions, which traditional field field measurement techniques like proton deflectometry fail to work. We propose utilizing the quantum radiation reaction signal from a GeV-class electron beam interacting with intense fields as an additional method to measure both the strength and spatial extent of these fields. By accurately measuring the initial and final mean energy and energy spread, we can differentiate between the field strength and the field length.

In our second work, we try to resolve an interesting question about whether χ can become

significant for TeV-class beams traversing a plasma channel field in future LWFA-staged accelerators. We derive a scaling law that links χ to the electron beam energy, normalized emittance ε_n, and plasma density n_e, which determines the ion channel's field strength. Although our predictions show that these values are relatively modest, the cumulative quantum effects over a meter-long plasma channel can still significantly impact the beam.

We examine radiation's effects on the beam's energy spread and emittance, as both are crucial for beam quality. An analytical model is developed to describe the evolution of energy spread for a beam inside an ion channel under a constant acceleration force from the plasma structure. These predictions are compared with OSIRIS PIC simulations, confirming the model's validity. Using this model, we predict the radiation-induced energy spread for varying beam emittances and plasma densities when accelerating a 1 GeV beam to 1 TeV. Our findings indicate that, for beams with a transverse Gaussian profile, energy spread due to the orbit effect surpasses that caused by quantum stochastic effects. The orbit effect-induced energy spread can be mitigated by employing a ring-shaped beam. Meanwhile, the quantum stochastic effect is inherent to the radiation process and can be controlled by reducing plasma density.

Additionally, we assess how radiation effects influence beam emittance. In the radiation-dominated region, where the radiation reaction force is comparable to the wakefield's acceleration force, the beam's emittance is strongly modified by the radiation effect and significantly decreases. A featured ring-shaped pattern is formed in phase space, and we provide an analytic explanation for the emergence of this pattern. Finally, we explore how radiation affects the transport of polarized beams in the wakefield, noting that polarization degradation occurs primarily at high plasma densities. This comprehensive study of radiation's impact on high-energy beams inside the wakefield offers valuable insights into designing future staged LWFA and high-density LWFA accelerators.

CHAPTER 8

Conclusion

In this thesis, we introduce a polarized strong-field QED kinetic framework for simulating relativistic laser-plasma interactions, with a focus on the often-overlooked aspects of spin and polarization in leptons and photons. We present three key studies that underscore their significance in this field. First, we investigate the impact of photon polarization on the Breit-Wheeler pair production process using an all-optical setup. We then demonstrate how photon polarization can serve as an indicator of strong-field quantum electrodynamics (QED) processes. Lastly, we examine the effects of spin and polarization in QED cascades, concentrating on the generation of polarized electron-positron pair plasma. Additionally, we present the creation of longitudinally polarized electron/positron beams, which hold promise for particle physics research. Beyond our exploration of spin and polarization effects, we also investigate the application of polarization-averaged models to study QED effects in forthcoming laser-plasma interactions. This includes utilizing QED effects to probe the super-intense magnetic fields generated by petawatt-class laser pulses in plasma and evaluating the potential influence of QED effects on future TeV-class staged laser wakefield accelerators. This section concludes by summarizing the findings from previous chapters and discussing possible future directions for spin and polarization-resolved QED research.

8.1 Parametric Study of the Polarization Dependence of NBW Process Using Two Laser Pulses

In Chapter 4, we propose an all-optical experimental setup designed to demonstrate the influence of photon polarization on the nonlinear Breit-Wheeler (NBW) pair production process. This setup involves two linearly polarized laser pulses that sequentially interact with an electron beam. The first laser pulse generates a linearly polarized photon beam with a polarization direction matching that of the laser. This polarized photon beam can then collide with the second laser pulse, decaying into electron-positron pairs via the NBW process. By rotating the polarization direction of either laser pulse, one can control the photon polarization direction, providing a versatile platform to study the effects of polarization on the NBW process.

We have implemented spin and polarization dependencies into the QED module of the PIC code OSIRIS. Simulation results demonstrate that when the polarization direction of the second laser pulse is rotated from parallel to perpendicular relative to the first laser pulse, while keeping other conditions constant, the difference in positron yield reaches a maximum. This yield variation ranges from 23% to 70%, depending on the laser parameters. To interpret these findings, we developed an analytic model that effectively predicts the simulation outcomes. In this model, we identified dominant parameters for the process:

- $\chi_1 = 2\frac{\hbar\omega_0}{m_e c^2} a_{01}\gamma_0$ a quantum parameter calculated using the initial energy γ of the electron beam and the normalized intensity a_{01} of the first laser pulse.

- $\chi_2 = 2\frac{\hbar\omega_0}{m_e c^2} a_{02}\gamma_0$, a quantum parameter for the second laser pulse.

We use this model to optimize experimental parameters. There is a trade-off between maximizing positron production and enhancing yield differences by altering laser polarization directions. This trade-off arises because photon polarization from the nonlinear Compton scattering (NLCS) process increases as χ_1 decreases, while the polarization response in the

NBW process varies with χ_2

For designing a practical experiment, it is essential to establish laser and electron beam parameters in applicable units. We predict the requirements for the duration and intensity of the laser pulses. Critically, the first pulse must be less intense to prevent electron-positron pair generation during the initial collision, and long enough to enable efficient energy transfer from the electron beam to the polarized photon beam. Conversely, the second pulse must be significantly more intense for the pair formation when interacting with the polarized photons of the first collision, yet short enough to avoid depletion of high-energy photons through the NBW process. The laser conditions proposed in this work are achievable at recently developed 10-petawatt-class laser facilities, such as those at ELI and SULF. We use a beam energy of approximately 1-2 GeV, which is also typical for laser wakefield acceleration (LWFA) beams. However, this experiment involves the collision of an LWFA electron beam with two laser pulses, making precise alignment of the three beams challenging. Achieving this will likely require high laser pointing stability.

8.2 Gamma Flash Measurement by Polarisation

A key characteristic of QED plasmas is the observation of bright flashes of hard photons produced through the NLC process. However, photons generated from bremsstrahlung processes are also significant and difficult to distinguish when analyzing the total photon count or energy spectrum alone. We propose utilizing photon polarization as a distinct signature to identify the NLC process. Photons generated via NLC are predominantly polarized, with a polarization degree of at least 50%, whereas photons from bremsstrahlung are essentially unpolarized.

To explore this concept, we developed a simplified model to predict the degree of polarization and the number of photons generated at various laser intensities. This model was compared with results from a 2D PIC simulation. Although the simulation results differ

somewhat from the model predictions due to differences in their setups, both indicate a similar trend. Specifically, the model overly simplifies the target profile and does not account for processes like direct laser acceleration, leading to an underestimation of electron energy. Within the range of laser intensities studied, with normalized vector potential a_0 between $10 \sim 50$, we found that linear polarization decreases as a_0 increases and grows with photon energy. For photon energies exceeding 10 keV, the degree of polarization is above 65% and can exceed 80% at higher photon energies. These findings are valuable for designing future experiments that employ X-ray polarimetry to distinguish NLCS X-ray flashes from other background sources.

8.3 Spin Polarized QED Cascades

Recent advances in high-power laser technology have opened new frontiers in physics, enabling access to laser intensities where quantum electrodynamic (QED) effects profoundly influence plasma behavior—creating what is known as "QED plasma." In this regime, which resembles some of the most extreme astrophysical environments, QED cascades give rise to prolific production of electron-positron pairs and gamma-ray photons. These cascades can be initiated by either colliding high-energy lepton beams with intense lasers (shower-type) or by intersecting multiple powerful laser beams (avalanche-type). Although QED cascades have been widely studied with unpolarized models, research into spin-polarized cascades remains limited and primarily involves simplified conditions. The complex, nonlinear dynamics involved call for comprehensive studies—especially with full particle-in-cell (PIC) simulations—to uncover possible spin and polarization effects.

In Chapter 6, we present our investigation of spin and polarization dynamics in both shower-type and avalanche-type QED cascades. Our results show a robust tendency for longitudinal plasma polarization in both scenarios. Notably, avalanche-type cascades driven by counter-propagating circularly polarized (CP) lasers yield electron-positron plasmas with

average longitudinal polarization surpassing 20

We conduct extensive parameter scans for both configurations and find that the degree of positron polarization is only weakly dependent on key parameters such as laser intensity (a_0), target density (n_0), initial beam energy (γ_0), and pulse duration (τ), highlighting the robustness of the observed polarization. By systematically turning on and off various quantum and classical spin processes in our simulations, we identify a multistage polarization mechanism: quantum effects tend to align spin along the field direction, while classical precession drives spin toward the longitudinal direction.

To elucidate these results, we develop a simple physical model for shower-type cascades that offers detailed insight into the polarization mechanism. For avalanche-type cascades, further research is needed to fully unravel the more complex interplay of intense fields and particle motion.

From an applications standpoint, our findings introduce a practical, all-optical method for generating highly polarized positron beams via QED cascades. This advance holds significant promise for future particle physics experiments and deepens our understanding of matter under extreme astrophysical conditions.

8.4 Ultrafast Relativistic Electron Probing of Extreme Magnetic Fields

The signature of strong field QED effects can be leveraged to measure the extreme field strengths generated in future high-intensity laser-plasma interactions. A 10 PW class laser, when tightly focused, can achieve normalized laser intensities of $a_0 > 500$. It's predicted that such interactions can generate magnetic fields with strengths exceeding 0.1 MT. Traditional field measurement techniques, such as proton deflectometry, are unsuitable for quantitative analysis at these elevated field strengths because the deflection angles become excessively large, causing the proton trajectories to intersect.

In this study, we propose utilizing the quantum radiation reaction signal from a GeV-class electron beam interacting with intense fields as an additional method to measure both the strength and spatial extent of these fields. We directed a 1 GeV electron beam onto a region of intense magnetic fields with strengths ranging from 0.01 MT to 1 MT and a thickness of several micrometers, generated by an ultraintense laser ($I > 10^{23}$ W/cm^2) interacting with a solid target. The changes in the mean energy and energy spread induced by quantum radiation effects scale differently depending on the field strength and its length. Consequently, by accurately measuring the initial and final mean energy and energy spread, we can differentiate between the field strength and the field length.

We also address the impact of measurement uncertainties on this field-probing method. A significant source of measurement error can arise from beam divergence. To ensure accurate field measurements, it is essential to use a beam with minimal divergence; the beam's size should be smaller than the spatial variation of the target fields. This requirement dictates that the target must be positioned a few millimeters to a centimeter from the gas target exit, depending on the beam's divergence angle.

8.5 Radiation Effect for Future Tev-Classed Plasma-Based Accelerators

The quantum parameter χ is known to increase with the relativistic factor γ of the electron. This raises an important question about whether χ can become significant for TeV-class beams traversing a plasma channel field in future LWFA-staged accelerators. To address this, we derive a scaling law that links χ to the electron beam energy, normalized emittance ε_n, and plasma density n_e, which determines the ion channel's field strength. Our analysis predicts that for TeV beams with practical beam emittances and plasma densities, χ values range from 10^{-4} to 10^{-2}. Although these values are relatively modest, the cumulative quantum effects over a meter-long plasma channel can still significantly impact the beam.

We examine radiation's effects on the beam's energy spread and emittance, as both are crucial for beam quality. An analytical model is developed to describe the evolution of energy spread for a beam inside an ion channel under a constant acceleration force from the plasma structure. These predictions are compared with OSIRIS PIC simulations, confirming the model's validity. Using this model, we predict the radiation-induced energy spread for varying beam emittances and plasma densities when accelerating a 1 GeV beam to 1 TeV. Our findings indicate that, for beams with a transverse Gaussian profile, energy spread due to the orbit effect surpasses that caused by quantum stochastic effects. The orbit effect-induced energy spread can be mitigated by employing a ring-shaped beam. Meanwhile, the quantum stochastic effect is inherent to the radiation process and can be controlled by reducing plasma density.

Additionally, we assess how radiation effects influence beam emittance. In the radiation-dominated region, where the radiation reaction force is comparable to the wakefield's acceleration force, the beam's emittance can significantly decrease, forming a ring-shaped pattern in phase space. An analytic explanation is provided for the emergence of this pattern. Finally, we explore how radiation affects the transport of polarized beams in the wakefield, noting that polarization degradation occurs primarily at high plasma densities. This comprehensive study of radiation's impact on high-energy beams inside the wakefield offers valuable insights into designing future staged LWFA and high-density LWFA accelerators.

8.6 Perspective

The simulations we have proposed pave the way for future experimental designs that will explore spin- and polarization-resolved QED effects. As petawatt-class high-intensity lasers begin to operate, the experimental conditions for some of these setups are now attainable. Lepton spin and gamma-ray polarimetry have been developed with various configurations to detect different energy ranges. For instance, scattering polarimetry is used to detect

polarization signals in the energy range of tens of keV to MeV, while pair production polarimetry is suited for photon energies from several MeV to over GeV. For electron/positron spin measurements, Mott polarimetry is applicable at MeV-scale energies, Møller polarimetry functions from MeV to GeV scales, and Compton polarimetry is effective for lepton energies above the GeV scale. These techniques have been employed in particle colliders and studies of extreme astrophysical phenomena but have rarely been applied to high-intensity laser-plasma interactions and laboratory astrophysics scenarios.

The polarimetry apparatus must be at least several meters long, necessitating special experimental designs. This effort is certainly worthwhile, as GeV-class polarized leptons generated in laser-plasma interactions are beneficial for particle physics and offer a more compact and cost-effective alternative to traditional accelerators. Polarized gamma-ray photons can indicate the formation of QED plasma and demonstrate fundamental polarization-dependent strong-field QED physics. To observe the effect of polarization on QED cascades, the power of current high-intensity lasers would need to double, aiming to be a goal for future generations of high-power laser facilities. It will be exciting to witness polarized electron-positron plasma generated in the laboratory, as this phenomenon naturally occurs only in some extreme astrophysical events. The high repetition rate of petawatt-class lasers will also be crucial for applying polarized beams from laser-plasma interactions in particle physics research, as it allows for more data points in experiments, thereby enhancing statistical reliability.

Our spin and polarization resolved QED code is also aimed at shedding light on the dynamics of extreme astrophysical objects in the distant universe. Gamma-ray photons, as the most abundant messengers we detect from the high-energy universe, provide invaluable insights into particle acceleration and the conversion of energy from relativistic jets into non-thermal radiation. However, deciphering the processes behind gamma-ray production is challenging due to the existence of multiple plausible emission scenarios, often indistinguishable from one another. The polarization state of photons contains critical information that can reveal the field configurations during their generation. Thus, measuring the polar-

ization signal provides a new dimension to the study of these extreme astrophysical objects. There has been substantial progress in developing Gamma-ray Burst (GRB) polarimeters and polarization-sensitive Compton telescopes. POLAR-2, a second-generation dedicated GRB polarimeter, is currently under development for a planned launch in 2024. Additionally, NASA has selected the COSI, a second-generation polarization-sensitive Compton Telescope, slated for launch in 2025.

Our spin and polarization resolved QED module, built onto the PIC code, allows for self-consistent simulation of processes that can occur under extreme astrophysical conditions. Looking ahead, we plan to explore the dynamics of relativistic plasmas under extreme fields, such as relativistic magnetic reconnection, shocks, and current filamentation. These processes are related to gamma-ray bursts from neutron star mergers, black hole formation, and even extreme lab astrophysics experiments involving high-intensity lasers interacting with targets. The polarization signals in these extreme plasma processes can be unique: for instance, studies have shown that polarization features can uncover mechanisms responsible for turbulence transitions in relativistic collisionless shocks. We aim to delve into the unique information carried by photon polarization, and potentially by lepton spin as well, driven by our curiosity to understand some of the most energetic and luminous phenomena occurring billions of light years away.

Lastly, our algorithm still has significant room for improvement. Currently, our Monte Carlo-based approach involves comparing a random number with the event rate, but its accuracy is heavily dependent on the time step. The optical depth method, however, can maintain accuracy without being constrained by time step size. Implementing this method in the future could enhance our algorithm's efficiency. The large number of particles generated from extremely strong field QED events, such as QED cascades, consumes substantial memory. The memory requirements and run speed increase exponentially with both laser duration and intensity, which significantly limits the parameter space we can explore for extreme QED processes. A potential solution is the particle merging algorithm. By com-

bining particles that are close in both location and momentum phase space into a single particle, we can significantly reduce memory usage, particularly as large numbers of particles are generated by NLCS and NBW processes. This technique has already been applied to an unpolarized strong field QED model in OSIRIS. However, a detailed study is needed to determine if we can apply particle merging similarly while considering spin and polarization states.

Moreover, future extensions of our algorithm could include additional physical models. For instance, incorporating vacuum birefringence effects for photons would be valuable for studying changes in photon polarization as they travel through strong magnetic fields in extreme astrophysical environments or for upcoming vacuum birefringence experiments at XFEL facilities. Including spin and polarization-resolved linear Compton scattering (LCS) and linear Breit-Wheeler (LBW) processes is also crucial. These processes occur more frequently in extreme astrophysical environments compared to NLC and NBW. For example, polarized synchrotron soft photons can undergo LCS with cold relativistic electrons in an outflow, producing hard gamma-ray photons—a process known as synchrotron self-Compton. These high-energy photons can then collide to generate electron-positron pairs through the LBW process. Including LCS and LBW would enable a more comprehensive simulation of the physics occurring in extreme astrophysical objects.

APPENDIX A

Spin and Polarization Resolved-QED Cross Section

According to equation 7 in [124], the probability of the NLCS or NBW process can be expressed as:

$$\begin{aligned}\mathbb{P} =&\langle\mathbb{P}\rangle + \mathbf{n}_\gamma \cdot \mathbf{P}_\gamma + \mathbf{n}_1 \cdot \mathbf{P}_1 + \mathbf{n}_0 \cdot \mathbf{P}_0 + \mathbf{n}_\gamma \cdot \mathbf{P}_{\gamma 1} \cdot \mathbf{n}_1 + \mathbf{n}_\gamma \cdot \mathbf{P}_{\gamma 0} \cdot \mathbf{n}_0 \\ &+ \mathbf{n}_1 \cdot \mathbf{P}_{10} \cdot \mathbf{n}_0 + \mathbf{P}_{\gamma 10,ijk}\mathbf{n}_{\gamma i}\mathbf{n}_{1j}\mathbf{n}_{0k},\end{aligned} \tag{A.1}$$

which $\mathbf{n}_0$ and $\mathbf{n}_1$ are the Lepton's initial and final Stokes vector. $\mathbf{n}_\gamma$ is the stokes vector for the photon:

$$\mathbf{n}_\gamma = \boldsymbol{z} = \xi_1 \boldsymbol{\epsilon}_{EB} + \xi_2 \boldsymbol{\epsilon}_2 + \xi_3 \boldsymbol{\epsilon}_E. \tag{A.2}$$

A.1 NLCS Process

Under LCFA approximation, the photon emission rate by an electron can be written as:

$$\{\langle\mathbb{P}^{\mathrm{C}}\rangle, \mathbf{P}_0^{\mathrm{C}}, \cdots\} = \frac{\alpha}{4}\int \frac{d\sigma}{b_0}\{\langle\hat{\mathbb{R}}^{\mathrm{C}}\rangle, \mathbf{R}_0^{\mathrm{C}}, \cdots\}, \tag{A.3}$$

Here, $b_0 = kp$ is the dimensionless longitudinal momentum of the original particle that entered the laser. According to Torgrimsson [124] equation 43-50, we obtain the polarization-

resolved emission spectrum:

$$\langle\hat{\mathbb{R}}^{\mathrm{C}}\rangle = -\mathrm{Ai}_1(z) - \kappa\frac{\mathrm{Ai}'(z)}{z}, \tag{A.4}$$

$$\hat{\mathbf{R}}_0^{\mathrm{C}} = \lambda\frac{\mathrm{Ai}(z)}{\sqrt{z}}\hat{\boldsymbol{\beta}}, \tag{A.5}$$

$$\hat{\mathbf{R}}_1^{\mathrm{C}} = u\frac{\mathrm{Ai}(z)}{\sqrt{z}}\hat{\boldsymbol{\beta}}, \tag{A.6}$$

$$\hat{\mathbf{R}}_\gamma^{\mathrm{C}} = -\frac{\mathrm{Ai}'(z)}{z}\hat{\boldsymbol{\varepsilon}}\cdot\mathbf{S}\cdot\hat{\boldsymbol{\varepsilon}}, \tag{A.7}$$

$$\hat{\mathbf{R}}_{01}^{\mathrm{C}} = -\mathrm{Ai}_1(z)(\mathbf{1}_\perp + [\kappa-1]\mathbf{1}_\parallel) - \frac{\mathrm{Ai}'(z)}{z}(2\mathbf{1}_\perp + \kappa\mathbf{1}_\parallel), \tag{A.8}$$

$$\hat{\mathbf{R}}_{\gamma 0}^{\mathrm{C}} = -u\frac{\mathrm{Ai}(z)}{\sqrt{z}}\mathbf{S}\cdot\hat{\boldsymbol{\beta}} - \lambda\left(\mathrm{Ai}_1(z) + \left[1+\frac{1}{1-\lambda}\right]\frac{\mathrm{Ai}'(z)}{z}\right)\boldsymbol{\epsilon}_2\hat{\mathbf{k}}, \tag{A.9}$$

$$\hat{\mathbf{R}}_{\gamma 1}^{\mathrm{C}} = -\lambda\frac{\mathrm{Ai}(z)}{\sqrt{z}}\mathbf{S}\cdot\hat{\boldsymbol{\beta}} - u\left(\mathrm{Ai}_1(z) + (2-\lambda)\frac{\mathrm{Ai}'(z)}{z}\right)\boldsymbol{\epsilon}_2\hat{\mathbf{k}}, \tag{A.10}$$

$$\begin{aligned}\hat{\mathbf{R}}_{\gamma 01}^{\mathrm{C}} = &-\frac{\lambda u}{2}\mathrm{Ai}_1(z)\mathbf{S} - \frac{\mathrm{Ai}'(z)}{z}\hat{\varepsilon}\cdot\mathbf{S}\cdot\hat{\varepsilon}\left(\frac{\kappa}{2}\mathbf{1}_\perp + \mathbf{1}_\parallel\right)\\ &-\frac{\tilde{\kappa}}{2}\frac{\mathrm{Ai}'(z)}{z}\hat{\boldsymbol{\beta}}\cdot\mathbf{S}\cdot\hat{\varepsilon}\; i\boldsymbol{\sigma}_2^{(3)} + \frac{\mathrm{Ai}(z)}{\sqrt{z}}\boldsymbol{\epsilon}_2\left(u\hat{\mathbf{k}}\hat{\boldsymbol{\beta}} - \lambda\hat{\boldsymbol{\beta}}\hat{\mathbf{k}}\right).\end{aligned} \tag{A.11}$$

Here, λ is the momentum ratio between the radiated photon and the initial energy of the electron, $u = \lambda/(1-\lambda)$ is the momentum ratio between the radiated photon and the final energy of the electron. $\kappa = 1/(1-\lambda)+(1-\lambda)$, $\tilde{\kappa} = 1/(1-\lambda)-(1-\lambda)$. $\mathbf{S} = \boldsymbol{\epsilon}_1\boldsymbol{\sigma}_1^{(3)} + \boldsymbol{\epsilon}_3\boldsymbol{\sigma}_3^{(3)} = \boldsymbol{\epsilon}_E(\hat{\boldsymbol{\varepsilon}}\hat{\boldsymbol{\varepsilon}} - \hat{\boldsymbol{\beta}}\hat{\boldsymbol{\beta}}) + \boldsymbol{\epsilon}_{EB}\hat{\boldsymbol{\varepsilon}}\hat{\boldsymbol{\beta}} + \hat{\boldsymbol{\beta}}\hat{\boldsymbol{\varepsilon}}$, $z = (u/\chi)^{2/3}$, χ is the quantum parameter. $\hat{\boldsymbol{\varepsilon}}$ and $\hat{\boldsymbol{\beta}}$ are unit

vectors (anti)parallel to the local electric and magnetic fields.

We can rearrange the polarization-resolved NLC spectrum so that the expected spin and polarization state after one NLC event can be easily observed:

$$F = F_0 + \mathbf{n}_\gamma \cdot \mathbf{F} = F_0 + \xi_1 F_1 + \xi_2 F_2 + \xi_3 F_3, \tag{A.12}$$

which $\mathbf{F} = \boldsymbol{\epsilon}_{EB} F_1 + \boldsymbol{\epsilon}_2 F_2 + \boldsymbol{\epsilon}_E F_3$. We start by solving the lepton spin term F_0. Note here, $\mathbf{s}_i = \mathbf{n}_0$, $\mathbf{s}_f = \mathbf{n}_1$.

$$\begin{aligned} F_0 &= \langle \hat{\mathbb{R}}^{\mathrm{C}} \rangle + \mathbf{s}_i \cdot \hat{\mathbf{R}}_0^{\mathrm{C}} + \mathbf{s}_f \cdot \hat{\mathbf{R}}_1^{\mathrm{C}} + \mathbf{s}_f \cdot \hat{\mathbf{R}}_{01}^{\mathrm{C}} \cdot \mathbf{s}_i \\ &= -\mathrm{Ai}_1(z) - \kappa \frac{\mathrm{Ai}'(z)}{z} + \lambda \frac{\mathrm{Ai}(z)}{\sqrt{z}} (\mathbf{s}_i \cdot \hat{\boldsymbol{\beta}}) + u \frac{\mathrm{Ai}(z)}{\sqrt{z}} (\mathbf{s}_f \cdot \hat{\boldsymbol{\beta}}) \\ &+ \mathbf{s}_f \cdot \left[-\mathrm{Ai}_1(z)(\mathbf{1} + (\kappa - 2)\mathbf{1}_\parallel) - \frac{\mathrm{Ai}'(z)}{z}(2\mathbf{1} + (\kappa - 2)\mathbf{1}_\parallel) \right] \cdot \mathbf{s}_i. \end{aligned} \tag{A.13}$$

We use $\mathbf{1}_\perp = \mathbf{1} - \mathbf{1}_\parallel$ to replace $\mathbf{1}_\perp$. We can also express this spectrum in terms of the modified Bessel function: $\mathrm{Ai}_1(z) = \frac{1}{\pi\sqrt{3}} \mathrm{IntK}_{1/3}(u')$, $\mathrm{Ai}'(z)/z = -\frac{1}{\pi\sqrt{3}} \mathrm{K}_{2/3}(u')$, $\mathrm{Ai}(z)/\sqrt{z} = -\frac{1}{\pi\sqrt{3}} \mathrm{K}_{1/3}(u')$, which we have $u' = 2u/3\chi = \frac{2}{3} z^{3/2}$. We then get, ignoring the common constant factor:

$$\begin{aligned} F_0 = &- \mathrm{IntK}_{1/3}(u') + \kappa \mathrm{K}_{2/3}(u') + \lambda (\mathbf{s}_i \cdot \hat{\boldsymbol{\beta}}) \mathrm{K}_{1/3}(u') \\ &+ u (\mathbf{s}_f \cdot \hat{\boldsymbol{\beta}}) \mathrm{K}_{1/3}(u') + \left(-\mathrm{IntK}_{1/3}(u') + 2\mathrm{K}_{2/3}(u') \right) (\mathbf{s}_f \cdot \mathbf{s}_i) \\ &+ \lambda u \left(-\mathrm{IntK}_{1/3}(u') + \mathrm{K}_{2/3}(u') \right) (\mathbf{s}_f \cdot \hat{\mathbf{k}})(\mathbf{s}_i \cdot \hat{\mathbf{k}}). \end{aligned} \tag{A.14}$$

Rearrange the terms related to the final spin state, and we get:

$$
\begin{aligned}
F_0 = &- \mathrm{Int}\mathrm{K}_{1/3}(u') + \kappa \mathrm{K}_{2/3}(u') + \lambda(\mathbf{s}_i \cdot \hat{\boldsymbol{\beta}})\mathrm{K}_{1/3}(u') \\
&+ \mathbf{s}_f \cdot \Big(u\mathrm{K}_{1/3}(u')\hat{\boldsymbol{\beta}} + \left(-\mathrm{Int}\mathrm{K}_{1/3}(u') + 2\mathrm{K}_{2/3}(u')\right)\mathbf{s}_i \\
&+ \lambda u \left(-\mathrm{Int}\mathrm{K}_{1/3}(u') + \mathrm{K}_{2/3}(u')\right)(\mathbf{s}_i \cdot \hat{\mathbf{k}})\hat{\mathbf{k}} \Big).
\end{aligned}
\tag{A.15}
$$

Notice that the spin-resolved radiation rate can be written as:

$$
F_0 = w + \mathbf{s}_f \cdot \mathbf{g}. \tag{A.16}
$$

$$
w = -\mathrm{Int}\mathrm{K}_{1/3}(u') + \kappa \mathrm{K}_{2/3}(u') + \lambda(\mathbf{s}_i \cdot \hat{\boldsymbol{\beta}})\mathrm{K}_{1/3}(u'), \tag{A.17}
$$

$$
\begin{aligned}
\mathbf{g} = &u\mathrm{K}_{1/3}(u')\hat{\boldsymbol{\beta}} + \left(-\mathrm{Int}\mathrm{K}_{1/3}(u') + 2\mathrm{K}_{2/3}(u')\right)\mathbf{s}_i \\
&+ \lambda u \left(-\mathrm{Int}\mathrm{K}_{1/3}(u') + \mathrm{K}_{2/3}(u')\right)(\mathbf{s}_i \cdot \hat{\mathbf{k}})\hat{\mathbf{k}}
\end{aligned}
\tag{A.18}
$$

Which w is the unpolarised, spin-averaged NLCS rate. We can also obtain the expected spin polarisation vector:

$$
\langle \boldsymbol{s} \rangle = \frac{\mathbf{g}}{w}. \tag{A.19}
$$

Then, we calculate terms related to photon polarization. We do this by separate terms along $\boldsymbol{\epsilon}_{EB}$, $\boldsymbol{\epsilon}_2$, and $\boldsymbol{\epsilon}_B$, as F_1, F_2 and F_3. Notice that here, $\mathbf{S} = \boldsymbol{\epsilon}_E \cdot (\hat{\boldsymbol{\varepsilon}}\hat{\boldsymbol{\varepsilon}} - \hat{\boldsymbol{\beta}}\hat{\boldsymbol{\beta}}) + \boldsymbol{\epsilon}_{EB} \cdot (\hat{\boldsymbol{\varepsilon}}\hat{\boldsymbol{\beta}} + \hat{\boldsymbol{\beta}}\hat{\boldsymbol{\varepsilon}})$.

We start with the spectrum related to the diagonal polarization component F_1:

$$\begin{aligned}
F_1 &= \boldsymbol{\epsilon}_{EB} \cdot \left(\hat{\mathbf{R}}^{\mathrm{C}}_{\gamma} + \hat{\mathbf{R}}^{\mathrm{C}}_{\gamma 0} \cdot \mathbf{s}_i + \hat{\mathbf{R}}^{\mathrm{C}}_{\gamma 1} \cdot \mathbf{s}_f + \mathbf{s}_f \cdot \hat{\mathbf{R}}^{\mathrm{C}}_{\gamma 01} \cdot \mathbf{s}_i \right) \\
&= -\frac{\mathrm{Ai}(z)}{\sqrt{z}} \left(u(\mathbf{s}_i \cdot \hat{\boldsymbol{\varepsilon}}) + \lambda(\mathbf{s}_f \cdot \hat{\boldsymbol{\varepsilon}}) \right) \\
&- \frac{\lambda u}{2} \mathrm{Ai}_1(z) \left((\mathbf{s}_f \cdot \hat{\boldsymbol{\varepsilon}})(\mathbf{s}_i \cdot \hat{\boldsymbol{\beta}}) + (\mathbf{s}_f \cdot \hat{\boldsymbol{\beta}})(\mathbf{s}_i \cdot \hat{\boldsymbol{\varepsilon}}) \right) \\
&- \frac{\tilde{\kappa}}{2} \frac{\mathrm{Ai}'(z)}{z} \varepsilon_{abc} (\mathbf{s}_f)_a (\mathbf{s}_i)_b \hat{\mathbf{k}}_c \\
&= -\frac{\mathrm{Ai}(z)}{\sqrt{z}} \left(u(\mathbf{s}_i \cdot \hat{\boldsymbol{\varepsilon}}) + \lambda(\mathbf{s}_f \cdot \hat{\boldsymbol{\varepsilon}}) \right) \\
&- \frac{\lambda u}{2} \mathrm{Ai}_1(z) \left((\mathbf{s}_f \cdot \hat{\boldsymbol{\varepsilon}})(\mathbf{s}_i \cdot \hat{\boldsymbol{\beta}}) + (\mathbf{s}_f \cdot \hat{\boldsymbol{\beta}})(\mathbf{s}_i \cdot \hat{\boldsymbol{\varepsilon}}) \right) \\
&- \frac{\tilde{\kappa}}{2} \frac{\mathrm{Ai}'(z)}{z} (\mathbf{s}_f \times \mathbf{s}_i) \cdot \hat{\mathbf{k}}.
\end{aligned} \tag{A.20}$$

By replacing the Airy function with the modified Bessel function, ignoring the common constant factor. We get the following:

$$\begin{aligned}
F_1 &= -\mathrm{K}_{1/3}(u') \left(u(\mathbf{s}_i \cdot \hat{\boldsymbol{\varepsilon}}) + \lambda(\mathbf{s}_f \cdot \hat{\boldsymbol{\varepsilon}}) \right) \\
&- \frac{\lambda u}{2} \mathrm{Int}\mathrm{K}_{1/3}(u') \left((\mathbf{s}_f \cdot \hat{\boldsymbol{\varepsilon}})(\mathbf{s}_i \cdot \hat{\boldsymbol{\beta}}) + (\mathbf{s}_f \cdot \hat{\boldsymbol{\beta}})(\mathbf{s}_i \cdot \hat{\boldsymbol{\varepsilon}}) \right) \\
&+ \frac{\tilde{\kappa}}{2} \mathrm{K}_{2/3}(u') (\mathbf{s}_f \times \mathbf{s}_i) \cdot \hat{\mathbf{k}}.
\end{aligned} \tag{A.21}$$

We then look at the term related to circular polarized F_2

$$
\begin{aligned}
F_2 = & \boldsymbol{\epsilon}_2 \cdot \left(\hat{\mathbf{R}}^{\mathrm{C}}_{\gamma} + \hat{\mathbf{R}}^{\mathrm{C}}_{\gamma 0} \cdot \mathbf{s}_i + \hat{\mathbf{R}}^{\mathrm{C}}_{\gamma 1} \cdot \mathbf{s}_f + \mathbf{s}_f \cdot \hat{\mathbf{R}}^{\mathrm{C}}_{\gamma 01} \cdot \mathbf{s}_i \right) \\
= & -\lambda \left(\mathrm{Ai}_1(z) + \left[1 + \frac{1}{1-\lambda} \right] \frac{\mathrm{Ai}'(z)}{z} \right) (\mathbf{s}_i \cdot \hat{\mathbf{k}}) \\
& - u \left(\mathrm{Ai}_1(z) + (2-\lambda) \frac{\mathrm{Ai}'(z)}{z} \right) (\mathbf{s}_f \cdot \hat{\mathbf{k}}) \\
& + \frac{\mathrm{Ai}(z)}{\sqrt{z}} \left(u (\mathbf{s}_f \cdot \hat{\mathbf{k}})(\mathbf{s}_i \cdot \hat{\boldsymbol{\beta}}) - \lambda (\mathbf{s}_f \cdot \hat{\boldsymbol{\beta}})(\mathbf{s}_i \cdot \hat{\mathbf{k}}) \right) \\
= & -\lambda \left(\mathrm{Ai}_1(z) + \left[1 + \frac{1}{1-\lambda} \right] \frac{\mathrm{Ai}'(z)}{z} \right) (\mathbf{s}_i \cdot \hat{\mathbf{k}}) \\
& - u \left(\mathrm{Ai}_1(z) + (2-\lambda) \frac{\mathrm{Ai}'(z)}{z} \right) (\mathbf{s}_f \cdot \hat{\mathbf{k}}) \\
& + \frac{\mathrm{Ai}(z)}{\sqrt{z}} \left(\frac{u}{2} + \frac{\lambda}{2} \right) \left((\mathbf{s}_f \cdot \hat{\mathbf{k}})(\mathbf{s}_i \cdot \hat{\boldsymbol{\beta}}) - (\mathbf{s}_f \cdot \hat{\boldsymbol{\beta}})(\mathbf{s}_i \cdot \hat{\mathbf{k}}) \right) \\
& + \frac{\mathrm{Ai}(z)}{\sqrt{z}} \left(\frac{u}{2} - \frac{\lambda}{2} \right) \left((\mathbf{s}_f \cdot \hat{\mathbf{k}})(\mathbf{s}_i \cdot \hat{\boldsymbol{\beta}}) + (\mathbf{s}_f \cdot \hat{\boldsymbol{\beta}})(\mathbf{s}_i \cdot \hat{\mathbf{k}}) \right).
\end{aligned}
\tag{A.22}
$$

Using the vector identity $(\mathbf{A} \times \boldsymbol{\beta}) \cdot (\mathbf{C} \times \mathbf{D}) = (\mathbf{A} \cdot \mathbf{C})(\boldsymbol{\beta} \cdot \mathbf{D}) - (\mathbf{A} \cdot \mathbf{D})(\boldsymbol{\beta} \cdot \mathbf{C})$, also, $\hat{\mathbf{k}} \times \hat{\boldsymbol{\beta}} = \hat{\boldsymbol{\varepsilon}}$, replacing the Airy function with the modified Bessel function, we get:

$$
\begin{aligned}
F_2 = & \frac{\tilde{\kappa}}{2} \mathrm{K}_{1/3}(u') \left((\mathbf{s}_f \times \mathbf{s}_i) \cdot \hat{\boldsymbol{\varepsilon}} \right) \\
& - \left(\lambda \mathrm{Int}\mathrm{K}_{1/3}(u') - \tilde{\kappa} \mathrm{K}_{2/3}(u') \right) (\mathbf{s}_i \cdot \hat{\mathbf{k}}) \\
& - \left(u \mathrm{Int}\mathrm{K}_{1/3}(u') - \tilde{\kappa} \mathrm{K}_{2/3}(u') \right) (\mathbf{s}_f \cdot \hat{\mathbf{k}}) \\
& + \frac{\lambda u}{2} \mathrm{K}_{1/3}(u') \left((\mathbf{s}_f \cdot \hat{\mathbf{k}})(\mathbf{s}_i \cdot \hat{\boldsymbol{\beta}}) + (\mathbf{s}_f \cdot \hat{\boldsymbol{\beta}})(\mathbf{s}_i \cdot \hat{\mathbf{k}}) \right).
\end{aligned}
\tag{A.23}
$$

Finally, we look at the term related to linear polarized F_3

$$
\begin{aligned}
F_3 &= \boldsymbol{\epsilon}_E \cdot \left(\hat{\mathbf{R}}^{\mathrm{C}}_{\gamma} + \hat{\mathbf{R}}^{\mathrm{C}}_{\gamma 0} \cdot \mathbf{s}_i + \hat{\mathbf{R}}^{\mathrm{C}}_{\gamma 1} \cdot \mathbf{s}_f + \mathbf{s}_f \cdot \hat{\mathbf{R}}^{\mathrm{C}}_{\gamma 01} \cdot \mathbf{s}_i \right) \\
&= -\frac{\mathrm{Ai}'(z)}{z} + \frac{\mathrm{Ai}(z)}{\sqrt{z}} \left(\frac{q_1}{s_1} (\mathbf{s}_i \cdot \hat{\boldsymbol{\beta}}) + \frac{q_1}{s_0} (\mathbf{s}_f \cdot \hat{\boldsymbol{\beta}}) \right) \\
&- \frac{q_1^2}{2 s_0 s_1} \mathrm{Ai}_1(z) \left((\mathbf{s}_f \cdot \hat{\boldsymbol{\varepsilon}})(\mathbf{s}_i \cdot \hat{\boldsymbol{\varepsilon}}) - (\mathbf{s}_f \cdot \hat{\boldsymbol{\beta}})(\mathbf{s}_i \cdot \hat{\boldsymbol{\beta}}) \right) \\
&- \frac{\kappa}{2} \frac{\mathrm{Ai}'(z)}{z} (\mathbf{s}_f \cdot \mathbf{s}_i) - \left(1 - \frac{\kappa}{2} \right) \frac{\mathrm{Ai}'(z)}{z} (\mathbf{s}_f \cdot \hat{\mathbf{k}})(\mathbf{s}_i \cdot \hat{\mathbf{k}}).
\end{aligned}
\tag{A.24}
$$

Replace the Airy function with the modified Bessel function, we get:

$$
\begin{aligned}
F_3 &= \mathrm{K}_{2/3}(u') + \left(u(\mathbf{s}_i \cdot \hat{\boldsymbol{\beta}}) + \lambda(\mathbf{s}_f \cdot \hat{\boldsymbol{\beta}}) \right) \mathrm{K}_{1/3}(u') \\
&- \frac{\lambda u}{2} \mathrm{IntK}_{1/3}(u') \left((\mathbf{s}_f \cdot \hat{\boldsymbol{\varepsilon}})(\mathbf{s}_i \cdot \hat{\boldsymbol{\varepsilon}}) - (\mathbf{s}_f \cdot \hat{\boldsymbol{\beta}})(\mathbf{s}_i \cdot \hat{\boldsymbol{\beta}}) \right) \\
&+ \frac{\kappa}{2} \mathrm{K}_{2/3}(u') (\mathbf{s}_f \cdot \mathbf{s}_i) - \frac{\lambda u}{2} \mathrm{K}_{2/3}(u') (\mathbf{s}_f \cdot \hat{\mathbf{k}})(\mathbf{s}_i \cdot \hat{\mathbf{k}}).
\end{aligned}
\tag{A.25}
$$

We can find that if we replace $\hat{\boldsymbol{\varepsilon}}$ as $-\mathbf{s}$, $\hat{\boldsymbol{\beta}}$ as $-\boldsymbol{\beta} = -\hat{\mathbf{v}} \times \mathbf{s}$, and $\hat{\mathbf{k}}$ as $\hat{\mathbf{v}}$, equation A.15, A.21, A.23, A.25 will be the same as the equation (13) and (14) in Chen PRD 2022. Notice that in Chen's equations, $F_0 = dW_{11} + dW_{22}$, $F_1 = dW_{12} + dW_{21}$, $F_2 = i(dW_{12} - dW_{21})$, $F_3 = dW_{11} - dW_{22}$.

One important special case is the spectrum radiated by an unpolarized electron/positron beam. We obtain this by taking $\mathbf{s}_i = 0$ and $\mathbf{s}_f = 0$ in Eq. (A.12):

$$
F^{unpol} = -\mathrm{IntK}_{1/3}(u') + \kappa \mathrm{K}_{2/3}(u') + \xi_3 \mathrm{K}_{2/3}(u')
\tag{A.26}
$$

The radiated photon polarization state under this scenario can only have ξ_3 component, which is the linear polarization, with the expected degree of linear polarization:

$$\langle \xi_3^{unpol} \rangle = \frac{\mathrm{K}_{2/3}(u')}{-\mathrm{Int}\mathrm{K}_{1/3}(u') + \kappa \mathrm{K}_{2/3}(u')} \tag{A.27}$$

In addition to the photon emission contribution at $O(\alpha)$, we also need the $O(\alpha)$ contribution from the one-loop electron self-energy. More precisely, these contributions are coming from the interference of the one-loop self-energy at $O(\alpha)$ with the "free" propagation of the electron. The expression is given by:

$$R_0^L = \int d\lambda \alpha \left[\mathrm{Ai}_1(z) + 2g \frac{\mathrm{Ai}'(z)}{z} \right] \tag{A.28}$$

$$\boldsymbol{R}_i^L = \boldsymbol{R}_f^L = \alpha \int d\lambda \alpha \frac{\mathrm{Ai}(z)}{\sqrt{z}} \hat{B} \tag{A.29}$$

$$R_{if}^L = R_0^L + \alpha \int d\lambda \alpha \frac{\mathrm{Gi}(z)}{\sqrt{z}} (\hat{K}\hat{E} - \hat{\varepsilon}\hat{K}) \tag{A.30}$$

where Gi is the Scorer function.Airy and Scorer functions are the real and imaginary parts of the integral:

$$\mathrm{Ai}(z) + i\mathrm{Gi}(z) = \frac{1}{\pi} \int_0^\infty dt e^{i\left(zt + \frac{t^3}{3}\right)} \tag{A.31}$$

The Muller matrix M^L for the loop is constructed analogously to:

$$M^L = \begin{pmatrix} R_0^L & \boldsymbol{R}_f^L \\ \boldsymbol{R}_i^L & R_{if}^L \end{pmatrix} \tag{A.32}$$

A.2 NBW Pair Production Process

The nonlinear Breit-Wheeler pair production rate can be written as:

$$\{\langle\mathbb{P}^{\rm BW}\rangle, \mathbf{P}_0^{\rm BW}, \cdots\} = \frac{\alpha}{4}\int \frac{d\sigma}{b_0}\{\langle\hat{\mathbb{R}}^{\rm BW}\rangle, \mathbf{R}_0^{\rm BW}, \cdots\}, \tag{A.33}$$

According to Torgrimsson [124] equation 43-50, this gives the polarization-resolved emission spectrum:

$$\langle\hat{\mathbb{R}}^{\rm BW}\rangle = {\rm Ai}_1(z) - \kappa\frac{{\rm Ai}'(z)}{z}, \tag{A.34}$$

$$\hat{\mathbf{R}}_2^{\rm BW} = \frac{1}{1-\tilde{\lambda}}\frac{{\rm Ai}(\tilde{z})}{\sqrt{\tilde{z}}}\hat{\boldsymbol{\beta}}, \tag{A.35}$$

$$\hat{\mathbf{R}}_3^{\rm BW} = \frac{1}{\tilde{\lambda}}\frac{{\rm Ai}(\tilde{z})}{\sqrt{\tilde{z}}}\hat{\boldsymbol{\beta}}, \tag{A.36}$$

$$\hat{\mathbf{R}}_\gamma^{\rm BW} = \frac{{\rm Ai}'(\tilde{z})}{\tilde{z}}\hat{\boldsymbol{\varepsilon}}\cdot\mathbf{S}\cdot\hat{\boldsymbol{\varepsilon}}, \tag{A.37}$$

$$\hat{\mathbf{R}}_{23}^{\rm BW} = -{\rm Ai}_1(\tilde{z})(\mathbf{1}_\perp + [\kappa+1]\mathbf{1}_\parallel) - \frac{{\rm Ai}'(\tilde{z})}{\tilde{z}}(2\mathbf{1}_\perp + \kappa\mathbf{1}_\parallel), \tag{A.38}$$

$$\hat{\mathbf{R}}_{\gamma 2}^{\rm BW} = \frac{1}{\tilde{\lambda}}\frac{{\rm Ai}(\tilde{z})}{\sqrt{\tilde{z}}}\mathbf{S}\cdot\hat{\boldsymbol{\beta}} + \frac{1}{1-\tilde{\lambda}}\left({\rm Ai}_1(\tilde{z}) + \left[1 - \frac{1-\tilde{\lambda}}{\tilde{\lambda}}\right]\frac{{\rm Ai}'(\tilde{z})}{\tilde{z}}\right)\boldsymbol{\epsilon}_2\hat{\mathbf{k}}, \tag{A.39}$$

$$\hat{\mathbf{R}}_{\gamma 3}^{\rm BW} = \frac{1}{1-\tilde{\lambda}}\frac{{\rm Ai}(\tilde{z})}{\sqrt{\tilde{z}}}\mathbf{S}\cdot\hat{\boldsymbol{\beta}} - \frac{1}{\tilde{\lambda}}\left({\rm Ai}_1(\tilde{z}) + \left[1 - \frac{\tilde{\lambda}}{1-\tilde{\lambda}}\right]\frac{{\rm Ai}'(\tilde{z})}{\tilde{z}}\right)\boldsymbol{\epsilon}_2\hat{\mathbf{k}}, \tag{A.40}$$

$$\begin{aligned}\hat{\mathbf{R}}_{\gamma 23}^{\rm BW} = {}& \frac{\tilde{u}}{2}{\rm Ai}_1(\tilde{z})\mathbf{S} + \frac{{\rm Ai}'(\tilde{z})}{z}\hat{\boldsymbol{\varepsilon}}\cdot\mathbf{S}\cdot\hat{\boldsymbol{\varepsilon}}\left(\frac{\rho}{2}\mathbf{1}_\perp + \mathbf{1}_\parallel\right) \\ & + \frac{\tilde{\rho}}{2}\frac{{\rm Ai}'(\tilde{z})}{\tilde{z}}\hat{\boldsymbol{\beta}}\cdot\mathbf{S}\cdot\hat{\boldsymbol{\varepsilon}}\; i\boldsymbol{\sigma}_2^{(3)} + \frac{{\rm Ai}(\tilde{z})}{\sqrt{\tilde{z}}}\boldsymbol{\epsilon}_2\left(\frac{\hat{\mathbf{k}}\hat{\boldsymbol{\beta}}}{\tilde{\lambda}} - \frac{\hat{\boldsymbol{\beta}}\hat{\mathbf{k}}}{1-\tilde{\lambda}}\right).\end{aligned} \tag{A.41}$$

Here, $\tilde{\lambda}$ are the momentum ratios between the positron and the initial photon. $\rho =$

$(1-\tilde{\lambda})/\tilde{\lambda}+\tilde{\lambda}/(1-\tilde{\lambda})$, $\tilde{\rho}=(1-\tilde{\lambda})/\tilde{\lambda}-\tilde{\lambda}/(1-\tilde{\lambda})$, and $\tilde{z}=(\tilde{u}/\chi)^{2/3}$, with $\tilde{u}=1/\tilde{\lambda}+1/(1-\tilde{\lambda})$.

Following the way the as how we rearrange the NLC spectrum, we can also rewrite the polarization-resolved NBW spectrum as:

$$G = G_0 + \mathbf{n}_\gamma \cdot \mathbf{G} = G_0 + \xi_1 G_1 + \xi_2 G_2 + \xi_3 G_3, \tag{A.42}$$

which $\mathbf{G} = \boldsymbol{\epsilon}_{EB} G_1 + \boldsymbol{\epsilon}_2 G_2 + \boldsymbol{\epsilon}_E G_3$. We start by solving the Lepton spin term G_0. Note here, $\mathbf{s}_e = \mathbf{n}_2$, $\mathbf{s}_p = -\mathbf{n}_3$.

$$\begin{aligned} G_0 &= \langle \hat{\mathbb{R}}^{\mathrm{BW}} \rangle + \mathbf{s}_e \cdot \hat{\mathbf{R}}_2^{\mathrm{BW}} - \mathbf{s}_p \cdot \hat{\mathbf{R}}_3^{\mathrm{BW}} - \mathbf{s}_p \cdot \hat{\mathbf{R}}_{23}^{\mathrm{BW}} \cdot \mathbf{s}_e \\ &= \mathrm{Ai}_1(\tilde{z}) - \rho \frac{\mathrm{Ai}'(\tilde{z})}{\tilde{z}} + \frac{1}{1-\tilde{\lambda}} \frac{\mathrm{Ai}(\tilde{z})}{\sqrt{\tilde{z}}} (\mathbf{s}_e \cdot \hat{\boldsymbol{\beta}}) - \frac{1}{\tilde{\lambda}} \frac{\mathrm{Ai}(\tilde{z})}{\sqrt{\tilde{z}}} (\mathbf{s}_p \cdot \hat{\boldsymbol{\beta}}) \\ &+ \mathbf{s}_p \cdot \left[\mathrm{Ai}_1(\tilde{z})(\mathbf{1} + \kappa \mathbf{1}_\parallel) + \frac{\mathrm{Ai}'(\tilde{z})}{\tilde{z}} (2\mathbf{1} + (\rho - 2)\mathbf{1}_\parallel) \right] \cdot \mathbf{s}_e. \end{aligned} \tag{A.43}$$

Similar as the NLCS spectrum, we can also replace the Airy function with the modified Bessel function: $\mathrm{Ai}_1(\tilde{z}) = \frac{1}{\pi\sqrt{3}} \mathrm{IntK}_{1/3}(\tilde{u}')$, $\mathrm{Ai}'(\tilde{z})/\tilde{z} = -\frac{1}{\pi\sqrt{3}} \mathrm{K}_{2/3}(\tilde{u}')$, $\mathrm{Ai}(\tilde{z})/\sqrt{\tilde{z}} = -\frac{1}{\pi\sqrt{3}} \mathrm{K}_{1/3}(\tilde{u}')$, which $\tilde{u}' = \frac{2}{3\chi_\gamma}\tilde{u} = \frac{2}{3}\tilde{z}^{3/2}$. We then get, ignoring the common constant factor:

$$\begin{aligned} G_0 &= \mathrm{IntK}_{1/3}(\tilde{u}') + \rho \mathrm{K}_{2/3}(\tilde{u}') + \frac{1}{1-\tilde{\lambda}} (\mathbf{s}_e \cdot \hat{\boldsymbol{\beta}}) \mathrm{K}_{1/3}(\tilde{u}') \\ &- \frac{1}{\tilde{\lambda}} (\mathbf{s}_p \cdot \hat{\boldsymbol{\beta}}) \mathrm{K}_{1/3}(\tilde{u}') + \left(\mathrm{IntK}_{1/3}(\tilde{u}') - 2\mathrm{K}_{2/3}(\tilde{u}') \right) (\mathbf{s}_p \cdot \mathbf{s}_e) \\ &+ \left(\rho \mathrm{IntK}_{1/3}(\tilde{u}') - (\rho - 2)\mathrm{K}_{2/3}(\tilde{u}') \right) (\mathbf{s}_p \cdot \hat{\mathbf{k}})(\mathbf{s}_e \cdot \hat{\mathbf{k}}). \end{aligned} \tag{A.44}$$

Then, we calculate terms related to photon polarization. We do this by separate terms along $\boldsymbol{\epsilon}_{EB}$, $\boldsymbol{\epsilon}_2$, and $\boldsymbol{\epsilon}_B$, as G_1, G_2 and G_3. We start with the spectrum related to diagonal polarization component G_1:

$$
\begin{aligned}
G_1 &= \boldsymbol{\epsilon}_{EB} \cdot \left(\hat{\mathbf{R}}_{\gamma}^{\mathrm{BW}} + \hat{\mathbf{R}}_{\gamma 2}^{\mathrm{BW}} \cdot \mathbf{s}_e - \hat{\mathbf{R}}_{\gamma 3}^{\mathrm{BW}} \cdot \mathbf{s}_p - \mathbf{s}_p \cdot \hat{\mathbf{R}}_{\gamma 23}^{\mathrm{BW}} \cdot \mathbf{s}_e \right) \\
&= \frac{\mathrm{Ai}(\tilde{z})}{\sqrt{\tilde{z}}} \left(\frac{1}{\tilde{\lambda}} (\mathbf{s}_e \cdot \hat{\boldsymbol{\varepsilon}}) - \frac{1}{1-\tilde{\lambda}} (\mathbf{s}_p \cdot \hat{\boldsymbol{\varepsilon}}) \right) \\
&- \tilde{u} \mathrm{Ai}_1(\tilde{z}) \left((\mathbf{s}_p \cdot \hat{\boldsymbol{\varepsilon}})(\mathbf{s}_e \cdot \hat{\boldsymbol{\beta}}) + (\mathbf{s}_p \cdot \hat{\boldsymbol{\beta}})(\mathbf{s}_e \cdot \hat{\boldsymbol{\varepsilon}}) \right) \\
&- \frac{\tilde{\rho}}{2} \frac{\mathrm{Ai}'(\tilde{z})}{\tilde{z}} \varepsilon_{abc} (\mathbf{s}_p)_a (\mathbf{s}_e)_b \hat{\mathbf{k}}_c \\
&= \frac{\mathrm{Ai}(\tilde{z})}{\sqrt{\tilde{z}}} \left(\frac{1}{\tilde{\lambda}} (\mathbf{s}_e \cdot \hat{\boldsymbol{\varepsilon}}) - \frac{1}{1-\tilde{\lambda}} (\mathbf{s}_p \cdot \hat{\boldsymbol{\varepsilon}}) \right) \\
&- \tilde{u} \mathrm{Ai}_1(\tilde{z}) \left((\mathbf{s}_p \cdot \hat{\boldsymbol{\varepsilon}})(\mathbf{s}_e \cdot \hat{\boldsymbol{\beta}}) + (\mathbf{s}_p \cdot \hat{\boldsymbol{\beta}})(\mathbf{s}_e \cdot \hat{\boldsymbol{\varepsilon}}) \right) \\
&- \frac{\tilde{\rho}}{2} \frac{\mathrm{Ai}'(\tilde{z})}{\tilde{z}} (\mathbf{s}_p \times \mathbf{s}_e) \cdot \hat{\mathbf{k}}.
\end{aligned}
\tag{A.45}
$$

Apply the notation used in the other group and replace the Airy function with the modified Bessel function, ignoring the common constant factor. We get:

$$
\begin{aligned}
G_1 &= \mathrm{K}_{1/3}(\tilde{u}') \left(\frac{1}{\tilde{\lambda}} (\mathbf{s}_e \cdot \hat{\boldsymbol{\varepsilon}}) - \frac{1}{1-\tilde{\lambda}} (\mathbf{s}_p \cdot \hat{\boldsymbol{\varepsilon}}) \right) \\
&- \frac{\tilde{u}}{2} \mathrm{IntK}_{1/3}(\tilde{u}') \left((\mathbf{s}_p \cdot \hat{\boldsymbol{\varepsilon}})(\mathbf{s}_e \cdot \hat{\boldsymbol{\beta}}) + (\mathbf{s}_p \cdot \hat{\boldsymbol{\beta}})(\mathbf{s}_e \cdot \hat{\boldsymbol{\varepsilon}}) \right) \\
&+ \frac{\tilde{\rho}}{2} \mathrm{K}_{2/3}(\tilde{u}') (\mathbf{s}_p \times \mathbf{s}_e) \cdot \hat{\mathbf{k}}.
\end{aligned}
\tag{A.46}
$$

We then look at the term related to circular polarized G_2

$$
\begin{aligned}
G_2 &= \boldsymbol{\epsilon}_2 \cdot \left(\hat{\mathbf{R}}_{\gamma}^{\mathrm{BW}} + \hat{\mathbf{R}}_{\gamma 2}^{\mathrm{BW}} \cdot \mathbf{s}_e - \hat{\mathbf{R}}_{\gamma 3}^{\mathrm{BW}} \cdot \mathbf{s}_p - \mathbf{s}_p \cdot \hat{\mathbf{R}}_{\gamma 23}^{\mathrm{BW}} \cdot \mathbf{s}_e \right) \\
&= \frac{1}{1-\tilde{\lambda}} \left(\mathrm{Ai}_1(\tilde{z}) + \left[1 - \frac{1-\tilde{\lambda}}{\tilde{\lambda}} \right] \frac{\mathrm{Ai}'(\tilde{z})}{\tilde{z}} \right) (\mathbf{s}_e \cdot \hat{\mathbf{k}}) \\
&\quad + \frac{1}{\tilde{\lambda}} \left(\mathrm{Ai}_1(\tilde{z}) + \left[1 - \frac{\tilde{\lambda}}{1-\tilde{\lambda}} \right] \frac{\mathrm{Ai}'(\tilde{z})}{\tilde{z}} \right) (\mathbf{s}_p \cdot \hat{\mathbf{k}}) \\
&\quad - \frac{\mathrm{Ai}(\tilde{z})}{\sqrt{\tilde{z}}} \left(\frac{1}{\tilde{\lambda}} (\mathbf{s}_p \cdot \hat{\mathbf{k}})(\mathbf{s}_e \cdot \hat{\boldsymbol{\beta}}) - \frac{1}{1-\tilde{\lambda}} (\mathbf{s}_p \cdot \hat{\boldsymbol{\beta}})(\mathbf{s}_e \cdot \hat{\mathbf{k}}) \right) \\
&= \frac{1}{1-\tilde{\lambda}} \left(\mathrm{Ai}_1(\tilde{z}) + \left[1 - \frac{1-\tilde{\lambda}}{\tilde{\lambda}} \right] \frac{\mathrm{Ai}'(\tilde{z})}{\tilde{z}} \right) (\mathbf{s}_e \cdot \hat{\mathbf{k}}) \\
&\quad + \frac{1}{\tilde{\lambda}} \left(\mathrm{Ai}_1(\tilde{z}) + \left[1 - \frac{\tilde{\lambda}}{1-\tilde{\lambda}} \right] \frac{\mathrm{Ai}'(\tilde{z})}{\tilde{z}} \right) (\mathbf{s}_p \cdot \hat{\mathbf{k}}) \\
&\quad - \frac{\mathrm{Ai}(\tilde{z})}{\sqrt{\tilde{z}}} \left(\frac{1}{2\tilde{\lambda}} + \frac{1}{2(1-\tilde{\lambda})} \right) \left((\mathbf{s}_p \cdot \hat{\mathbf{k}})(\mathbf{s}_e \cdot \hat{\boldsymbol{\beta}}) - (\mathbf{s}_p \cdot \hat{\boldsymbol{\beta}})(\mathbf{s}_e \cdot \hat{\mathbf{k}}) \right) \\
&\quad - \frac{\mathrm{Ai}(\tilde{z})}{\sqrt{\tilde{z}}} \left(\frac{1}{2\tilde{\lambda}} - \frac{1}{2(1-\tilde{\lambda})} \right) \left((\mathbf{s}_p \cdot \hat{\mathbf{k}})(\mathbf{s}_e \cdot \hat{\boldsymbol{\beta}}) + (\mathbf{s}_p \cdot \hat{\boldsymbol{\beta}})(\mathbf{s}_e \cdot \hat{\mathbf{k}}) \right).
\end{aligned}
\tag{A.47}
$$

Using the vector identity $(\mathbf{A} \times \boldsymbol{\beta}) \cdot (\mathbf{C} \times \mathbf{D}) = (\mathbf{A} \cdot \mathbf{C})(\boldsymbol{\beta} \cdot \mathbf{D}) - (\mathbf{A} \cdot \mathbf{D})(\boldsymbol{\beta} \cdot \mathbf{C})$, also, $\hat{\mathbf{k}} \times \hat{\boldsymbol{\beta}} = \hat{\boldsymbol{\varepsilon}}$ (laser propagates in $-\hat{\mathbf{k}}$ direction), replacing the Airy function with the modified Bessel function, we get:

$$
\begin{aligned}
G_2 = &- \frac{\tilde{u}}{2} \mathrm{K}_{1/3}(\tilde{u}') \left((\mathbf{s}_p \times \mathbf{s}_e) \cdot \hat{\boldsymbol{\varepsilon}} \right) \\
&+ \left(\frac{1}{1-\tilde{\lambda}} \mathrm{IntK}_{1/3}(\tilde{u}') + \tilde{\rho} \mathrm{K}_{2/3}(\tilde{u}') \right) (\mathbf{s}_e \cdot \hat{\mathbf{k}}) \\
&+ \left(\frac{1}{\tilde{\lambda}} \mathrm{IntK}_{1/3}(\tilde{u}') - \tilde{\rho} \mathrm{K}_{2/3}(\tilde{u}') \right) (\mathbf{s}_p \cdot \hat{\mathbf{k}}) \\
&- \frac{\tilde{\rho}}{2} \mathrm{K}_{1/3}(\tilde{u}') \left((\mathbf{s}_p \cdot \hat{\mathbf{k}})(\mathbf{s}_e \cdot \hat{\boldsymbol{\beta}}) + (\mathbf{s}_p \cdot \hat{\boldsymbol{\beta}})(\mathbf{s}_e \cdot \hat{\mathbf{k}}) \right).
\end{aligned}
\tag{A.48}
$$

Finally, we look at the term related to linear polarized G_3

$$
\begin{aligned}
G_3 &= \boldsymbol{\epsilon}_E \cdot \left(\hat{\mathbf{R}}^{\mathrm{C}}_{\gamma} + \hat{\mathbf{R}}^{\mathrm{C}}_{\gamma 2} \cdot \mathbf{s}_e - \hat{\mathbf{R}}^{\mathrm{C}}_{\gamma 3} \cdot \mathbf{s}_p - \mathbf{s}_p \cdot \hat{\mathbf{R}}^{\mathrm{C}}_{\gamma 23} \cdot \mathbf{s}_e \right) \\
&= \frac{\mathrm{Ai}'(\tilde{z})}{\tilde{z}} + \frac{\mathrm{Ai}(\tilde{z})}{\sqrt{\tilde{z}}} \left(-\frac{1}{\tilde{\lambda}} (\mathbf{s}_e \cdot \hat{\boldsymbol{\beta}}) + \frac{1}{1-\tilde{\lambda}} (\mathbf{s}_p \cdot \hat{\boldsymbol{\beta}}) \right) \\
&- \frac{\tilde{u}}{2} \mathrm{Ai}_1(\tilde{z}) \left((\mathbf{s}_p \cdot \hat{\boldsymbol{\varepsilon}})(\mathbf{s}_e \cdot \hat{\boldsymbol{\varepsilon}}) - (\mathbf{s}_p \cdot \hat{\boldsymbol{\beta}})(\mathbf{s}_e \cdot \hat{\boldsymbol{\beta}}) \right) \\
&- \frac{\rho}{2} \frac{\mathrm{Ai}'(\tilde{z})}{\tilde{z}} (\mathbf{s}_p \cdot \mathbf{s}_e) - \left(1 - \frac{\rho}{2} \right) \frac{\mathrm{Ai}'(\tilde{z})}{\tilde{z}} (\mathbf{s}_p \cdot \hat{\mathbf{k}})(\mathbf{s}_e \cdot \hat{\mathbf{k}}).
\end{aligned}
\tag{A.49}
$$

Replace the Airy function with the modified Bessel function, and we get:

$$
\begin{aligned}
G_3 = &- \mathrm{K}_{2/3}(\tilde{u}') + \left(-\frac{1}{\tilde{\lambda}} (\mathbf{s}_e \cdot \hat{\boldsymbol{\beta}}) + \frac{1}{1-\tilde{\lambda}} (\mathbf{s}_p \cdot \hat{\boldsymbol{\beta}}) \right) \mathrm{K}_{1/3}(\tilde{u}') \\
&- \frac{\tilde{u}}{2} \mathrm{IntK}_{1/3}(\tilde{u}') \left((\mathbf{s}_p \cdot \hat{\boldsymbol{\varepsilon}})(\mathbf{s}_e \cdot \hat{\boldsymbol{\varepsilon}}) - (\mathbf{s}_p \cdot \hat{\boldsymbol{\beta}})(\mathbf{s}_e \cdot \hat{\boldsymbol{\beta}}) \right) \\
&+ \frac{\rho}{2} \mathrm{K}_{2/3}(\tilde{u}') (\mathbf{s}_p \cdot \mathbf{s}_e) - \left(1 - \frac{\rho}{2} \right) \mathrm{K}_{2/3}(\tilde{u}') (\mathbf{s}_p \cdot \hat{\mathbf{k}})(\mathbf{s}_e \cdot \hat{\mathbf{k}}).
\end{aligned}
\tag{A.50}
$$

We can find that if we replace $\hat{\boldsymbol{\varepsilon}}$ as $-\mathbf{s}$, $\hat{\boldsymbol{\beta}}$ as $-\boldsymbol{\beta} = -\hat{\mathbf{v}} \times \mathbf{s}$, and $\hat{\mathbf{k}}$ as $\hat{\mathbf{v}}$, equation A.44, A.46, A.48, A.50 will be the same as the equation (23) in Chen [145].

The expected spin direction for the generated electron can be obtained by averaging over the spin state for the positron in Eq. (A.42):

$$
\begin{aligned}
G = &\ \mathrm{IntK}_{1/3}(\tilde{u}') + \rho \mathrm{K}_{2/3}(\tilde{u}') - \xi_3 \mathrm{K}_{2/3}(\tilde{u}') \\
&+ \mathbf{s}_e \cdot \left[\left(\frac{1}{1-\tilde{\lambda}} - \xi_3 \frac{1}{\tilde{\lambda}} \right) \mathrm{K}_{1/3}(\tilde{u}') \hat{\boldsymbol{\beta}} + \xi_1 \frac{1}{\tilde{\lambda}} \mathrm{K}_{1/3}(\tilde{u}') \hat{\boldsymbol{\varepsilon}} \right. \\
&\left. + \xi_2 \left(\frac{1}{1-\tilde{\lambda}} \mathrm{IntK}_{1/3}(\tilde{u}') + \tilde{\rho} \mathrm{K}_{2/3}(\tilde{u}') \right) \hat{\boldsymbol{k}} \right]
\end{aligned}
\tag{A.51}
$$

We can rewrite the spectrum as:

$$
G = w_0 + \boldsymbol{j}_e \tag{A.52}
$$

which:

$$w_0 = \mathrm{Int}\mathrm{K}_{1/3}(\tilde{u}') + \rho\mathrm{K}_{2/3}(\tilde{u}') - \xi_3\mathrm{K}_{2/3}(\tilde{u}') \tag{A.53}$$

$$\begin{aligned}\boldsymbol{j}_e = &\left(\frac{1}{1-\tilde{\lambda}} - \xi_3\frac{1}{\tilde{\lambda}}\right)\mathrm{K}_{1/3}(\tilde{u}')\hat{\boldsymbol{\beta}} + \xi_1\frac{1}{\tilde{\lambda}}\mathrm{K}_{1/3}(\tilde{u}')\hat{\boldsymbol{\varepsilon}} \\ &+ \xi_2\left(\frac{1}{1-\tilde{\lambda}}\mathrm{Int}\mathrm{K}_{1/3}(\tilde{u}') + \tilde{\rho}\mathrm{K}_{2/3}(\tilde{u}')\right)\hat{\boldsymbol{k}}\end{aligned} \tag{A.54}$$

The expected spin vector for the generated electron is then:

$$\langle \mathbf{s}_e \rangle = \frac{\boldsymbol{j}_e}{w_0} \tag{A.55}$$

Similarly, we can obtain the expected spin vector for the generated positron.

$$G = w_0 + \boldsymbol{j}_p \tag{A.56}$$

which:

$$w_0 = \mathrm{Int}\mathrm{K}_{1/3}(\tilde{u}') + \rho\mathrm{K}_{2/3}(\tilde{u}') - \xi_3\mathrm{K}_{2/3}(\tilde{u}') \tag{A.57}$$

$$\begin{aligned}\boldsymbol{j}_p = &\left(-\frac{1}{\tilde{\lambda}} + \xi_3\frac{1}{1-\tilde{\lambda}}\right)\mathrm{K}_{1/3}(\tilde{u}')\hat{\boldsymbol{\beta}} - \xi_1\frac{1}{1-\tilde{\lambda}}\mathrm{K}_{1/3}(\tilde{u}')\hat{\boldsymbol{\varepsilon}} \\ &+ \xi_2\left(\frac{1}{\tilde{\lambda}}\mathrm{Int}\mathrm{K}_{1/3}(\tilde{u}') - \tilde{\rho}\mathrm{K}_{2/3}(\tilde{u}')\right)\hat{\boldsymbol{k}}\end{aligned} \tag{A.58}$$

The expected spin vector for the generated electron is then:

$$\langle \mathbf{s}_p \rangle = \frac{\boldsymbol{j}_p}{w_0} \tag{A.59}$$

One important special case here is the dependence of the NBW spectrum on photon polarization only, ignoring the dependence on the generated electron and positron spins. We obtain this by setting $\mathbf{s}_e = 0$ and $\mathbf{s}_p = 0$:

$$G^{unpol} = \mathrm{Int}\mathrm{K}_{1/3}(\tilde{u}') + \rho\mathrm{K}_{2/3}(\tilde{u}') - \xi_3\mathrm{K}_{2/3}(\tilde{u}') \tag{A.60}$$

And the corresponding NBW rate:

$$R^{unpol} = C_0 \int_0^1 d\tilde{\lambda}\ \frac{\alpha m_e^2 c^4}{\sqrt{3}\pi\hbar^2\omega^2} \left[\mathrm{Int}\mathrm{K}_{1/3}(\tilde{u}') + \rho\mathrm{K}_{2/3}(\tilde{u}') - \xi_3\mathrm{K}_{2/3}(\tilde{u}')\right] \tag{A.61}$$

We can see that the NBW spectrum depends only on the linear degree of polarization ξ_3. The pair production yield from the NBW process only depends on ξ_3.

APPENDIX B

Simplified Algorithm under the Reduced Basis

In our spin- and polarization-dependent QED PIC algorithm, we also provide an alternative option with a reduced-spin and polarization basis. Here, the spin basis we use is called the non-precession basis, which is along the rest frame magnetic field direction, and we only count the linear polarization for photons. Although, in general, spin precession may lead to other components of the spin vector, notably longitudinal polarization, the radiative processes only increase the spin component in the $\boldsymbol{\beta}$ direction and only cause the $\boldsymbol{\epsilon}$ and $\boldsymbol{\kappa}$ components to decay away. Hence, this simplified model is still applicable for situations such as an unpolarized lepton beam interacting with a constant EM field or with a plane electromagnetic field in which the magnetic field in the rest frame of the particle does not rotate in the direction (although it can oscillate in the negative and positive directions).

The flow chart for the calculation of the quantum radiation process involved in spin and polarization is shown in Fig. B.1. The code uses the classical Lorentz pusher and the T-BMT equation-based spin pusher to update the position, momentum, and spin of the particle for each time step. Then, we calculate the lepton's local non-precessing basis $\boldsymbol{\zeta}$ and project the spin vector onto the basis to obtain the lepton spin state $s = \boldsymbol{S} \cdot \boldsymbol{\zeta}$. We also calculate the quantum parameter χ_q for each lepton. The particle state information s and χ_q enable us to find the probability of the quantum radiation process. This probability is the criterion for entering the Monte Carlo-based spin and polarization-dependent quantum radiation module.

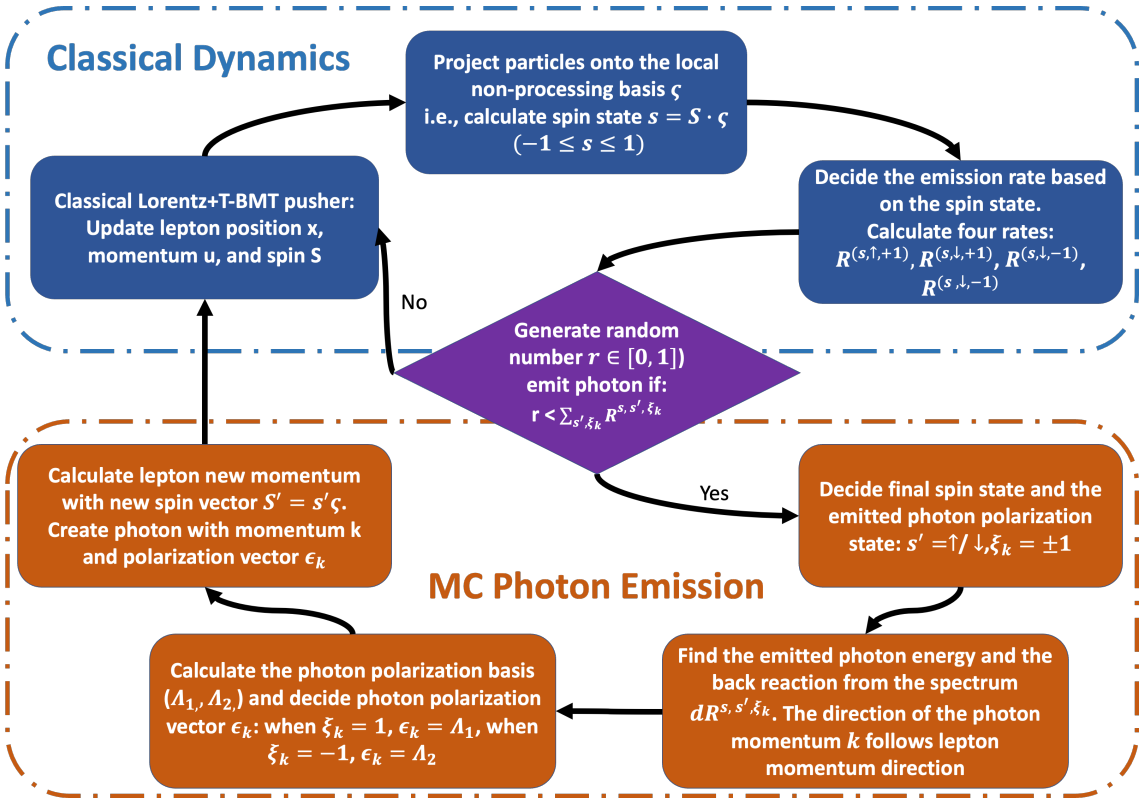

Figure B.1: Flow chart for spin-polarized NLCS algorithm with under reduced spin and polarization basis

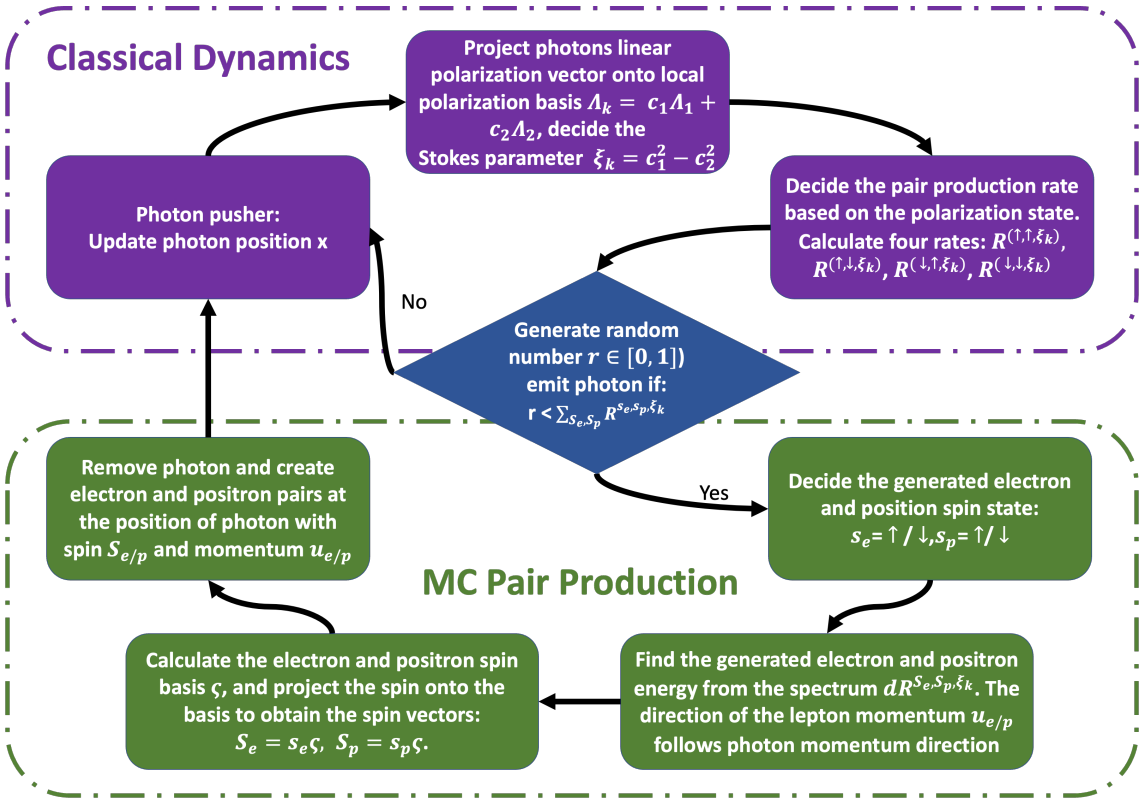

Figure B.2: Flow chart for spin-polarized NBW algorithm under reduced spin and polarization basis

In this module, we first determine the final spin state of the lepton s' and the radiated photon Stokes parameter ξ_k. Then the photon's energy is obtained based on the radiation spectrum R^{s,s',ξ_k} decided by the lepton's initial and final spin state and the Stokes parameter of the radiated photon. Due to the assumption of collinear emission, the direction of the photon momentum $\boldsymbol{k}$ follows the lepton momentum direction. We calculate the polarization basis ($\boldsymbol{\Lambda}_1$, $\boldsymbol{\Lambda}_2$) and decide the direction of photon polarization vector $\boldsymbol{\epsilon}_k$ based on ξ_k: if $\xi_k = 1$, $\boldsymbol{\epsilon}_k = \boldsymbol{\Lambda}_1$; if $\xi_k = -1$, $\boldsymbol{\epsilon}_k = \boldsymbol{\Lambda}_2$. Finally, we update the lepton momentum and the spin vector $\boldsymbol{S}'$, which $\boldsymbol{S}' = s'\boldsymbol{\zeta}$.

Fig. B.2 is the flow chart for calculating the spin and polarization-involved pair production process. We begin with the classical photon pusher, which considers the photon as a particle traveling with the speed of light without any interaction in the medium. When a quantum process occurs, we calculate the polarization basis for the photon and project the photon

polarization vector onto the basis to obtain the Stokes parameter ξ_k. The code uses the photon quantum parameter χ_q and its Stokes parameter ξ_k to calculate the probability of polarization-dependent pair production. This probability is the criterion for entering the Monte Carlo-based spin and polarization-dependent pair production module. In this module, we first decide the generated electron and positron pair spin states s_e and s_p. Then, we obtain the energy of the generated electron-positron pair based on the NBW spectrum R^{s_e,s_p,ξ_k}. The generated electron and positron pair momentum direction follows the photon momentum direction. We calculate the spin basis $\boldsymbol{\zeta}$ for the generated pair to obtain their spin vector $\boldsymbol{S}_{e/p} = s_{e/p}\boldsymbol{\zeta}$. The photon that participates in the pair production process gives all its energy to the electron-positron pair and will be eliminated from the code.

APPENDIX C

Code Verification for Initially Polarized Beam

C.1 NLCS Photon Spectrum for Different Spin-Polarized Lepton

We look at the situation when the electron is initially spin-polarized along or opposite to the rest frame magnetic field direction, i.e., $S_\beta = -1$ or $S_\beta = 1$. We test the spectrum under different quantum parameters of the electron with $\chi = 0.01$, 1, and 99 and compared the result of the code with the closed-form expression shown in Fig. C.1. The radiated photon can only be linearly polarized. The blue curve shows the photon spectrum with a diagonal polarization component $\xi_3 < 0$, and the orange curve shows the photon spectrum with a diagonal polarization component from $\xi_3 > 0$ in the simulation. We can see that both curves agree well with the closed-form expression. We can also find that the degree of linear polarization depends on the energy of the radiated photon, where the higher the photon energy, the higher its degree of linear polarization.

We look at the cases when the electron is initially spin-polarized along or opposite to the rest frame electric field direction, i.e., $S_\varepsilon = -1$ or $S_\varepsilon = 1$. We test the spectrum under different quantum parameters of the electron with $\chi = 0.01$, 1, and 99. In this case, the radiated photon has both linear and diagonal polarization components. In Fig. C.2, the blue curve shows the photon spectrum with a linear polarization component $\xi_3 < 0$, and the orange curve shows the photon spectrum with a linear polarization component $\xi_3 > 0$

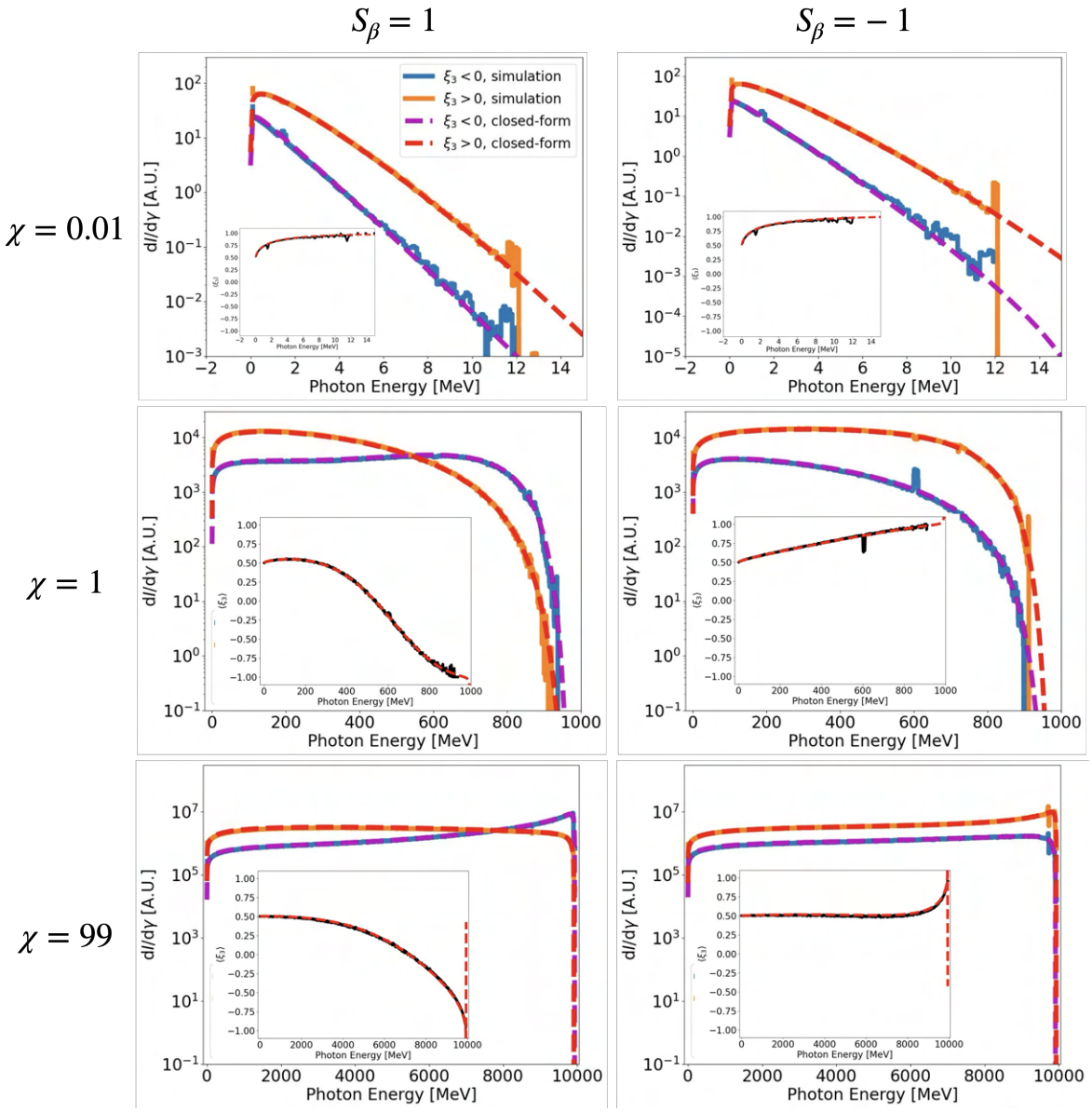

Figure C.1: Benchmark of linearly polarized (ξ_3) photon spectrum from the NLC process for a fully polarized lepton beam inside a constant magnetic field. The particle spin is either fully parallel or antiparallel to the rest frame electric field direction $\hat{\boldsymbol{\beta}}$. The classical particle dynamics, radiation back reaction, and radiation-induced spin change are all switched off for simplicity. We scan the spectrum through $\chi = 0.01$, $\chi = 1$, and $\chi = 99$.

from the simulation. In Fig. C.3, the blue curve shows the photon spectrum with a diagonal polarization component $\xi_1 < 0$, and the orange curve shows the photon spectrum with a diagonal polarization component from $\xi_1 > 0$ in the simulation. We can see that both curves agree well with the closed-form expression. We can also find that the degree of linear

and diagonal polarization depends on the energy of the radiated photon, where the higher the photon energy, the lower its degree of linear polarization, and the higher its degree of diagonal polarization.

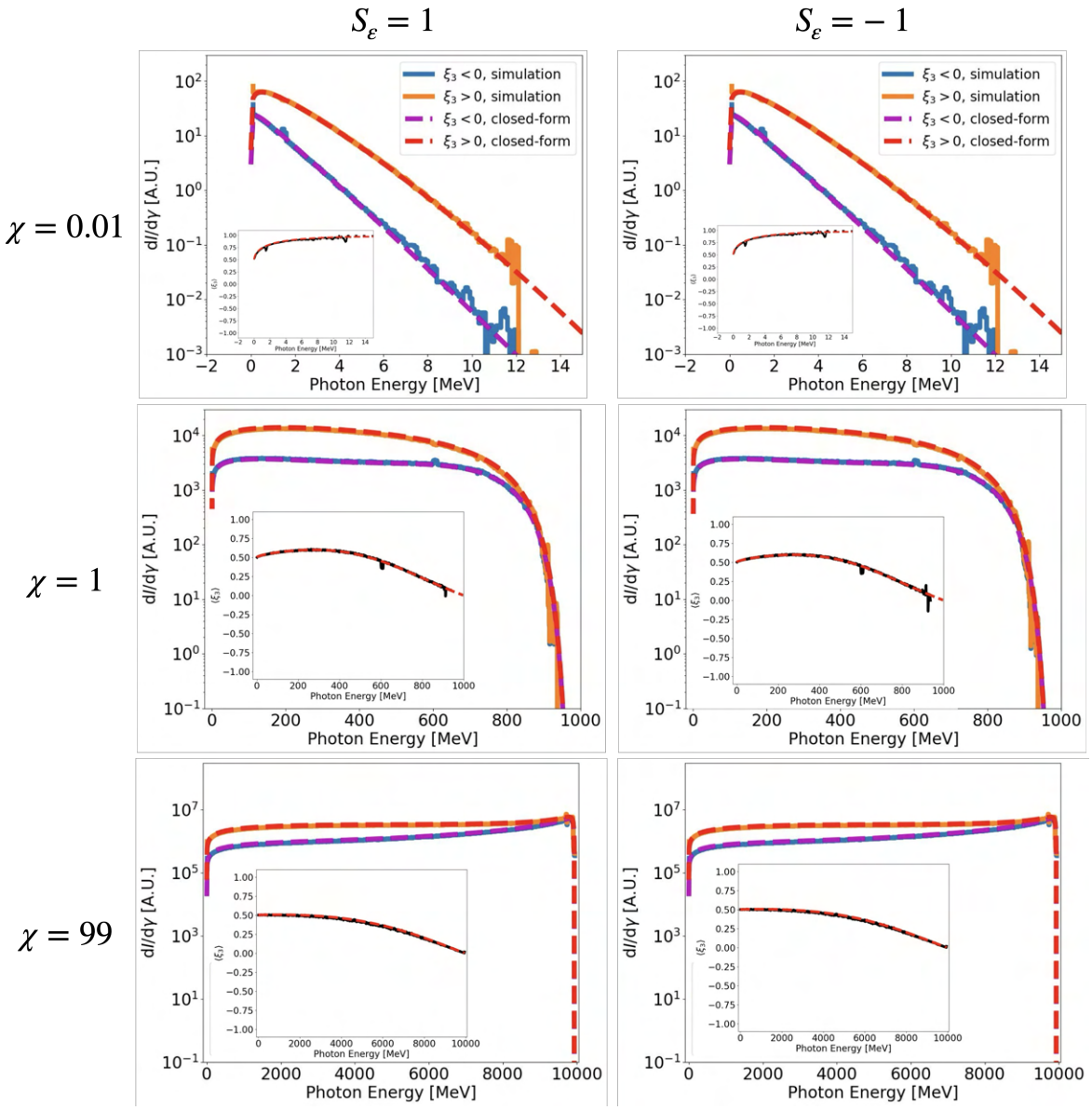

Figure C.2: Benchmark of linearly polarized (ξ_3) photon spectrum from the NLC process for a fully polarized lepton beam inside a constant magnetic field. The particle spin is either fully parallel or antiparallel to the rest frame electric field direction $\hat{\boldsymbol{\varepsilon}}$. The classical particle dynamics, radiation back reaction, and radiation induced spin change are all switched off for simplicity. We scan the spectrum through $\chi = 0.01$, $\chi = 1$, and $\chi = 99$.

We look at the cases where the electron is initially spin-polarized along or opposite to

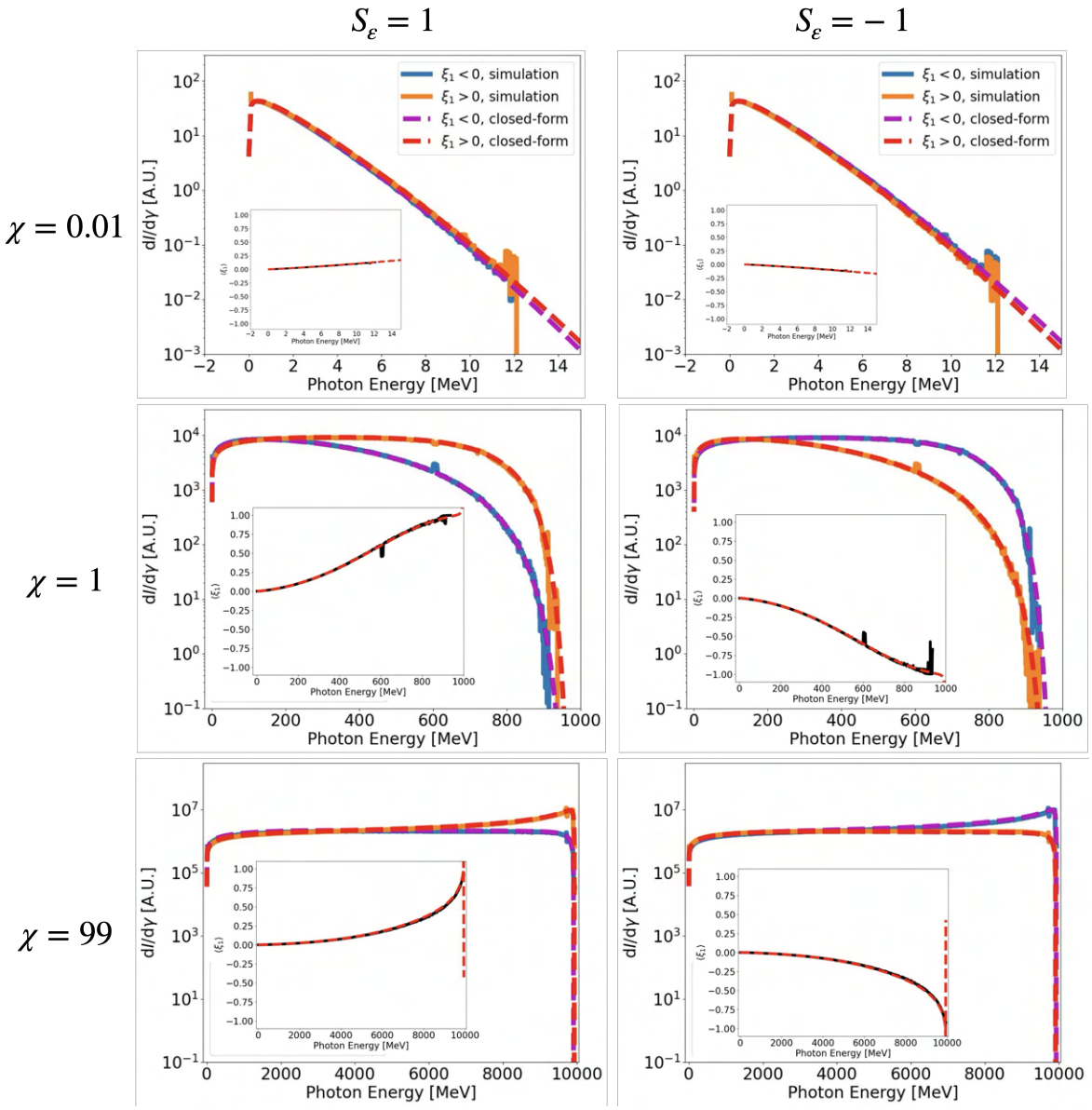

Figure C.3: Benchmark of diagonal polarized (ξ_1) photon spectrum from the NLC process for a fully polarized lepton beam inside a constant magnetic field. The particle spin is either fully parallel or antiparallel to the rest frame electric field direction $\hat{\boldsymbol{\varepsilon}}$. The classical particle dynamics, radiation back reaction, and radiation induced spin change are all switched off for simplicity. We scan the spectrum through $\chi = 0.01$, $\chi = 1$, and $\chi = 99$.

the rest frame magnetic field direction, i.e., $S_k = -1$ or $S_k = 1$. We tested the spectrum under different quantum parameters of the electron with $\chi = 0.01$, 1, and 99. In this case, the radiated photon has both linear and circular polarization components. In Fig. C.4, the blue curve shows the photon spectrum with a linear polarization component $\xi_3 < 0$, and

the orange curve shows the photon spectrum with a linear polarization component $\xi_3 > 0$ from the simulation. In Fig. C.5, the blue curve shows the photon spectrum with a circular polarization component $\xi_2 < 0$, and the orange curve shows the photon spectrum with a circular polarization component from $\xi_2 > 0$ in the simulation. We can see that both curves agree well with the closed-form expression. We can also find that the degree of linear and circular polarization depends on the energy of the radiated photon; the higher the photon energy, the lower its degree of linear polarization and the higher its degree of circular polarization.

C.2 NBW Pair Production Spectrum for Different Polarized Photon

We look at the situation of a fully linearly polarized photon beam with polarization state $\xi_3 = -1$ or $\xi_3 = 1$. We test the spectrum under different quantum parameters of the photon beam with $\chi = 1$, 10, and 99 and compared the result of the code with the closed-form expression shown in Fig. C.6. The generated positron spin can only be in the rest frame magnetic field direction. The blue curve shows the positron spectrum with spin component $S_\beta < 0$ in the rest frame magnetic field direction, and the orange curve shows the positron spectrum with spin component in the rest frame magnetic field direction $S_\beta > 0$ from the simulation. We can see that both curves agree well with the closed-form expression.

We then look at the situation of a fully diagonally polarized photon beam with polarization state $\xi_1 = -1$ or $\xi_1 = 1$. We tested the spectrum under different quantum parameters of the photon beam with $\chi = 1$, 10, and 99. The generated positron spin can be both in the rest frame magnetic field and in the rest frame electric field direction. In Fig. C.7, the blue curve shows the positron spectrum with spin component $S_\beta < 0$ in the rest frame magnetic field direction, and the orange curve shows the positron spectrum with spin component $S_\beta > 0$ in the rest frame magnetic field direction from the simulation. In Fig. C.8, the blue curve shows

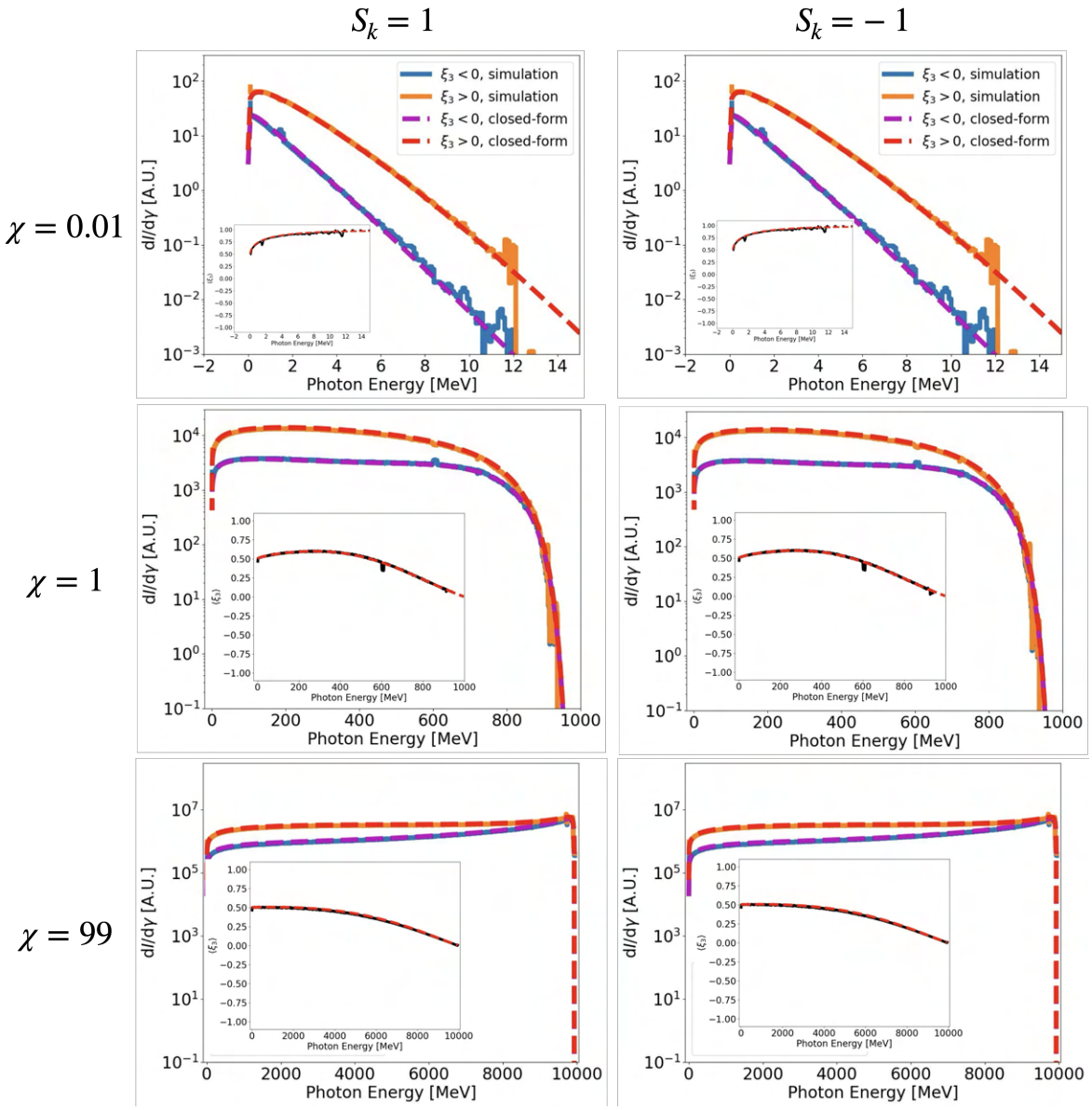

Figure C.4: Benchmark of linearly polarized (ξ_3) photon spectrum from the NLC process for a fully polarized lepton beam inside a constant magnetic field. The particle spin is either fully parallel or anti-parallel to the particle momentum direction $\hat{\boldsymbol{k}}$. The classical particle dynamics, radiation back reaction, and radiation-induced spin change are all switched off for simplicity. We scan the spectrum through $\chi = 0.01$, $\chi = 1$, and $\chi = 99$.

the positron spectrum with spin component $S_\varepsilon < 0$ in rest frame electric field direction, and the orange curve shows the positron spectrum with spin component $S_\varepsilon > 0$ in rest frame electric field direction from the simulation. We can see that both curves agree well with the closed-form expression.

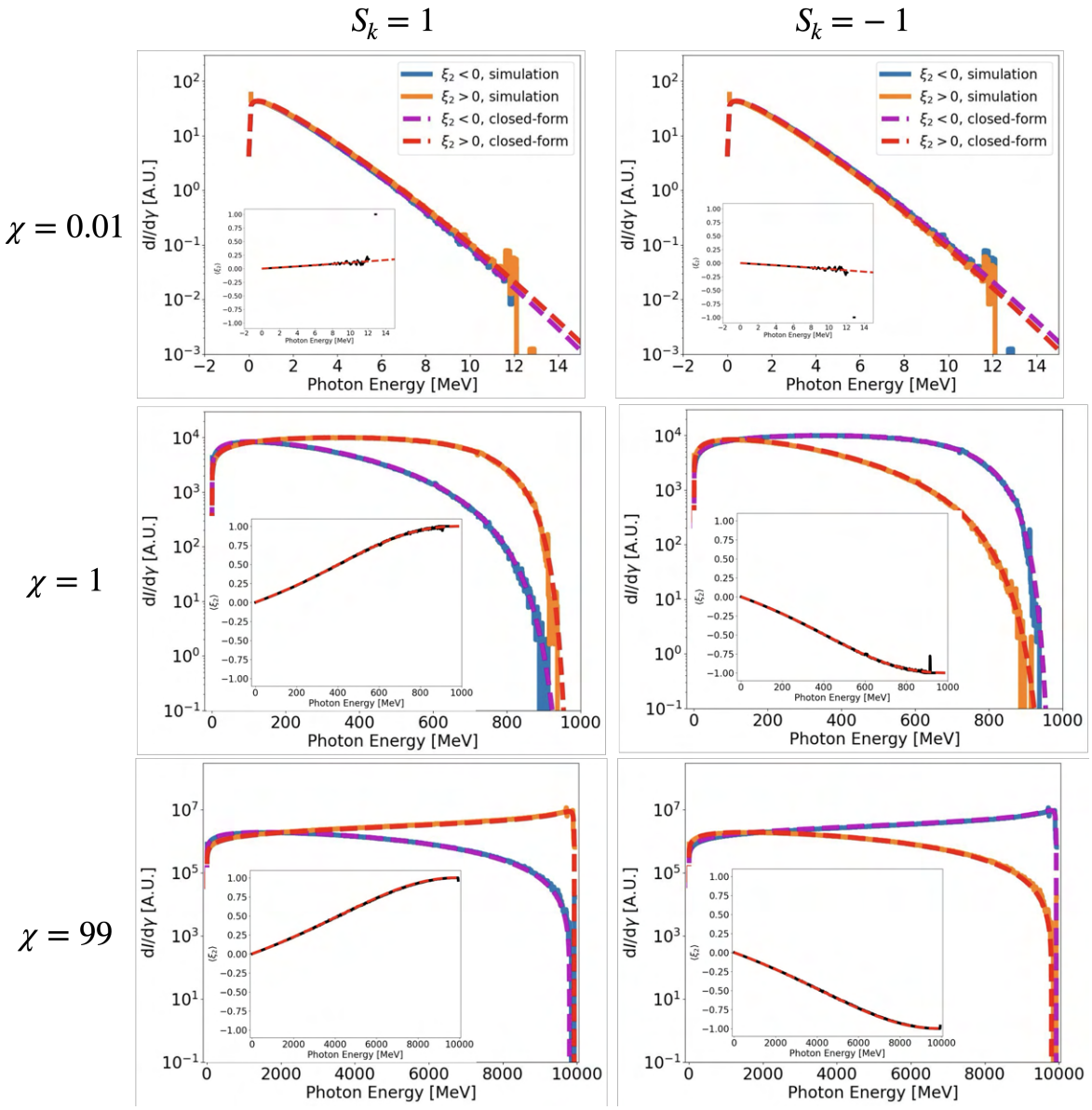

Figure C.5: Benchmark of circularly polarized (ξ_2) photon spectrum from the NLC process for a fully polarized lepton beam inside a constant magnetic field. The particle spin is either fully parallel or anti-parallel to the particle momentum direction $\hat{\boldsymbol{k}}$. The classical particle dynamics, radiation back reaction, and radiation-induced spin change are all switched off for simplicity. We scan the spectrum through $\chi = 0.01$, $\chi = 1$, and $\chi = 99$.

We then look at the situation of a fully circularly polarized photon beam with polarization state $\xi_2 = -1$ or $\xi_2 = 1$. We tested the spectrum under different quantum parameters of the photon beam with $\chi = 1$, 10, and 99. The generated positron spin can be in the rest frame magnetic field and the momentum direction. In Fig. C.9, the blue curve shows the positron

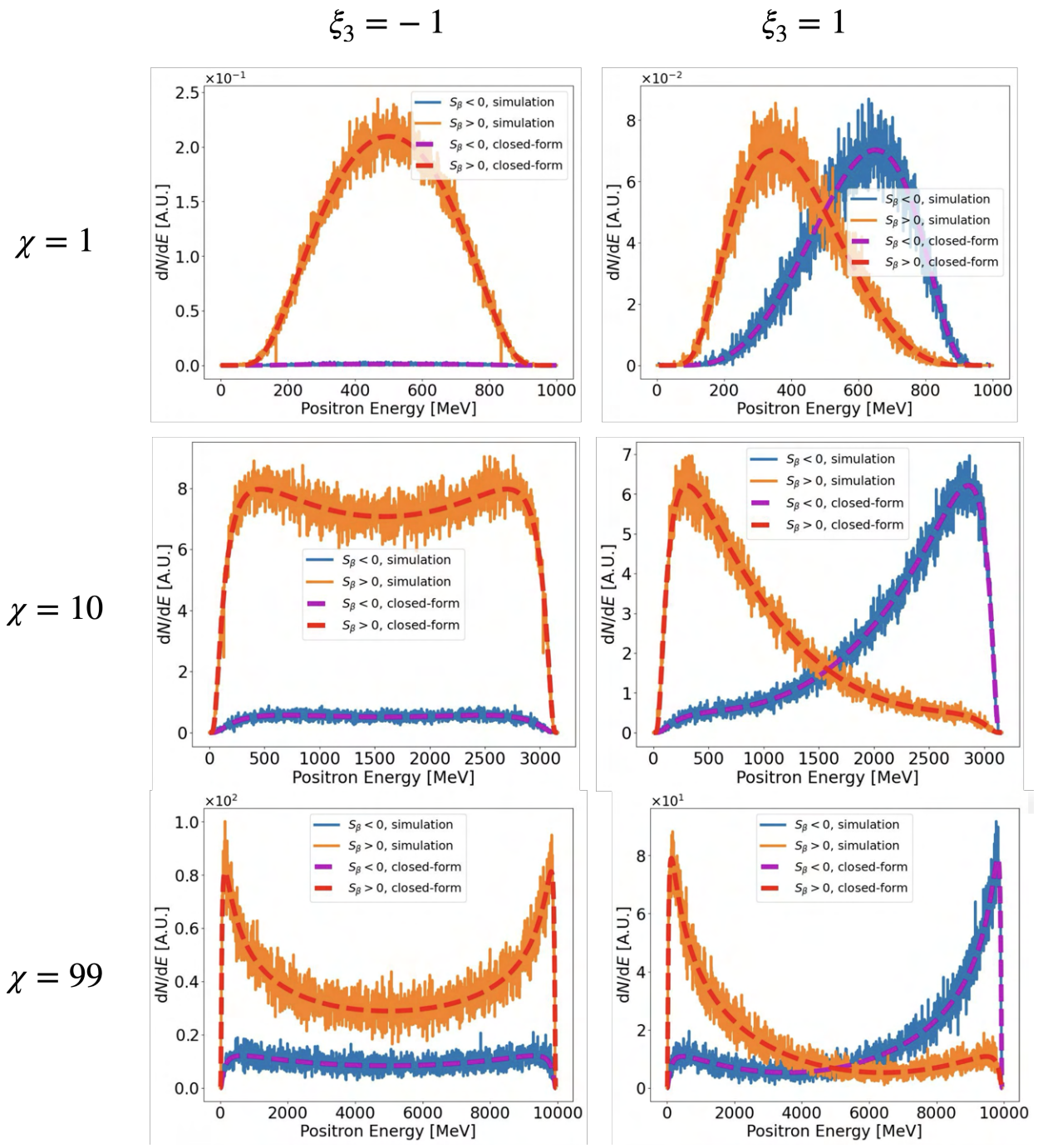

Figure C.6: Benchmark of positron spectrum for spin component S_β from the NBW process for a polarized photon beam inside a constant magnetic field. The photon polarization is either $\xi_3 = -1$ or $\xi_3 = 1$. The classical particle dynamics, radiation back reaction, and radiation-induced spin change are all switched off for simplicity. We scan the spectrum through $\chi = 1$, $\chi = 10$, and $\chi = 99$.

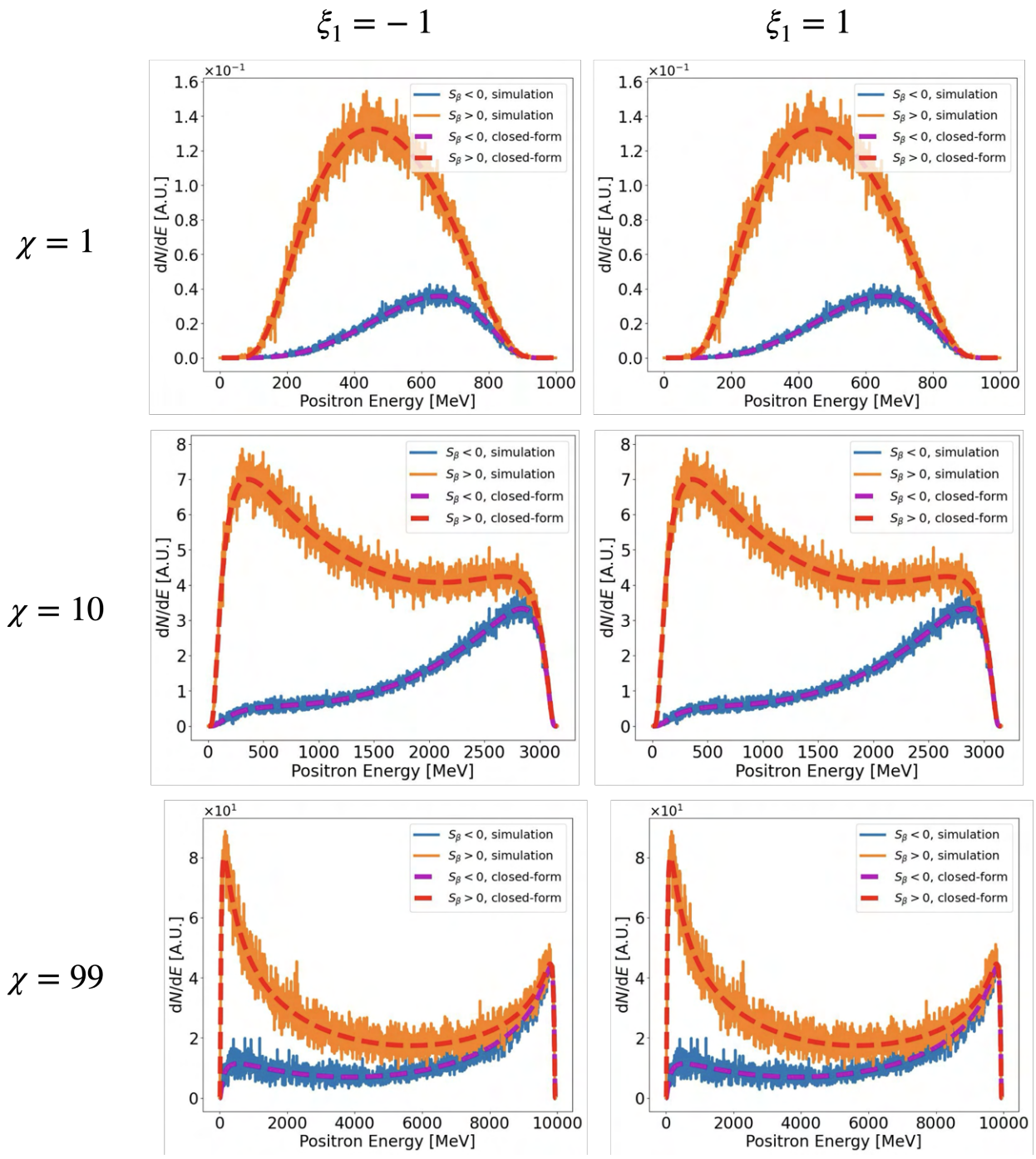

Figure C.7: Benchmark of positron spectrum for spin component S_β from the NBW process for a polarized photon beam inside a constant magnetic field. The photon polarization is either $\xi_3 = -1$ or $\xi_3 = 1$. The classical particle dynamics, radiation back reaction, and radiation-induced spin change are all switched off for simplicity. We scan the spectrum through $\chi = 1$, $\chi = 10$, and $\chi = 99$.

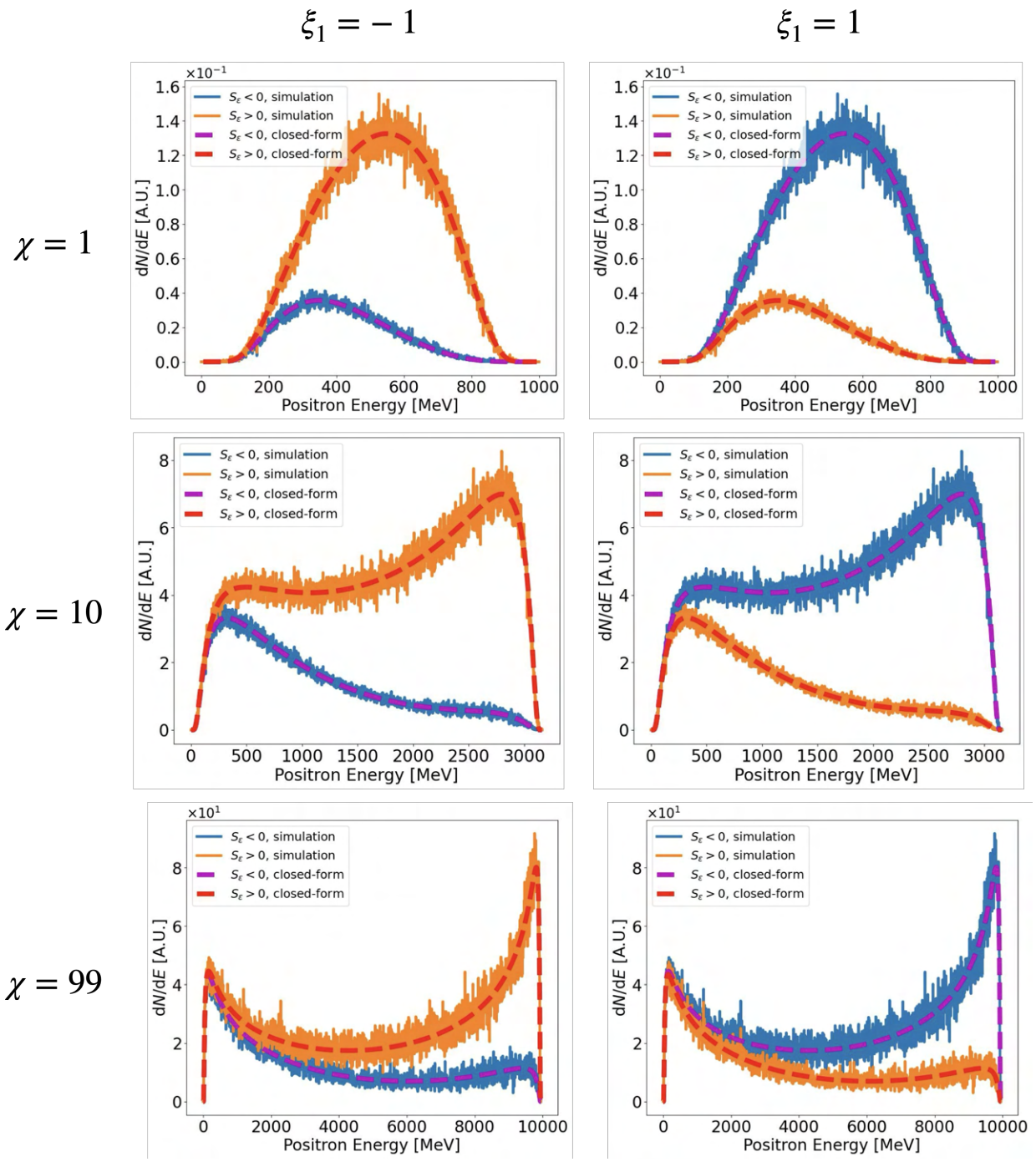

Figure C.8: Benchmark of positron spectrum for spin component S_ε from the NBW process for a polarized photon beam inside a constant magnetic field. The photon polarization is either $\xi_1 = -1$ or $\xi_1 = 1$. The classical particle dynamics, radiation back reaction, and radiation-induced spin change are all switched off for simplicity. We scan the spectrum through $\chi = 1$, $\chi = 10$, and $\chi = 99$.

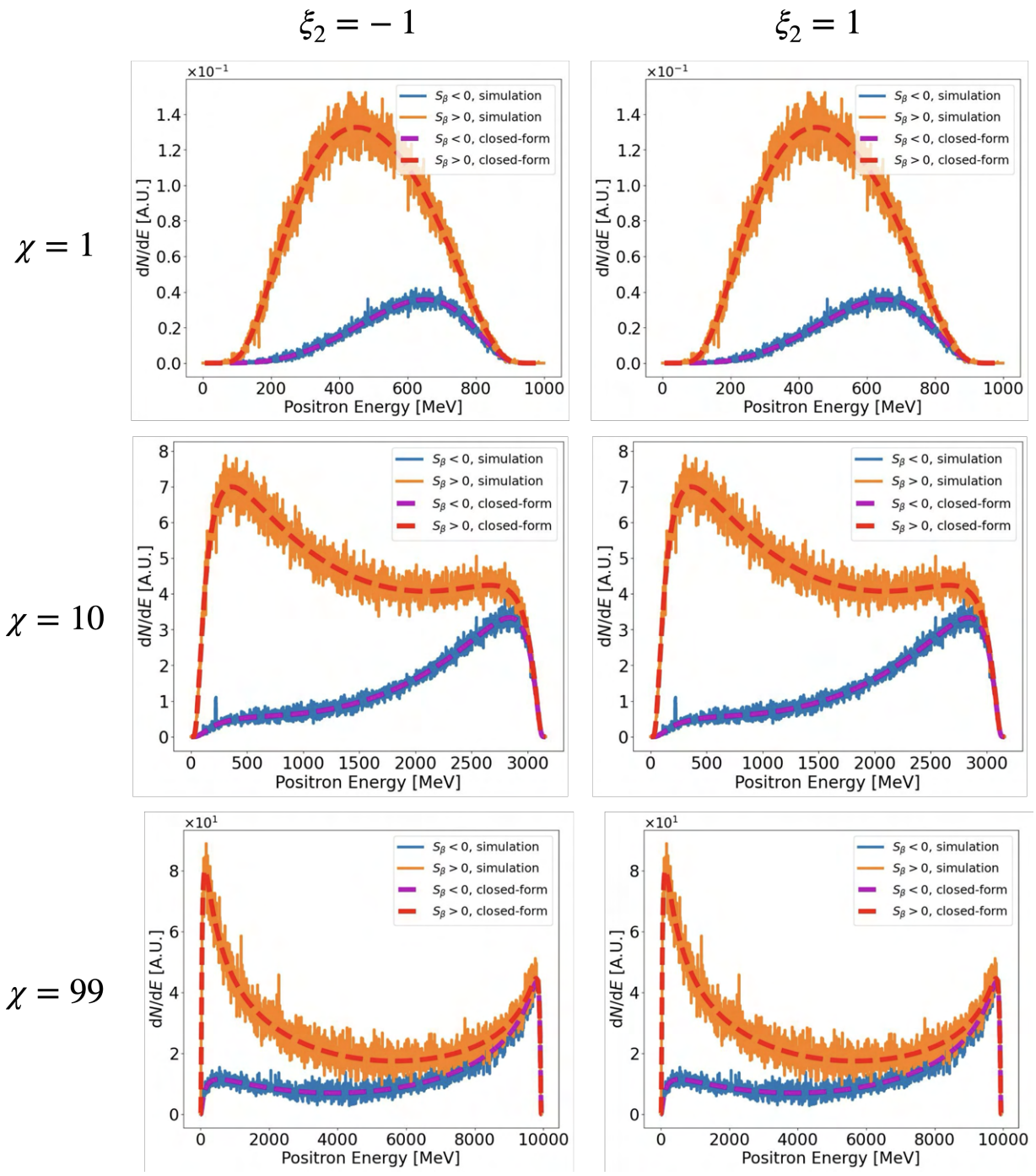

Figure C.9: Benchmark of positron spectrum for spin component S_β from the NBW process for a polarized photon beam inside a constant magnetic field. The photon polarization is either $\xi_3 = -1$ or $\xi_3 = 1$. The classical particle dynamics, radiation back reaction, and radiation induced spin change are all switched off for simplicity. We scan the spectrum through $\chi = 1$, $\chi = 10$, and $\chi = 99$.

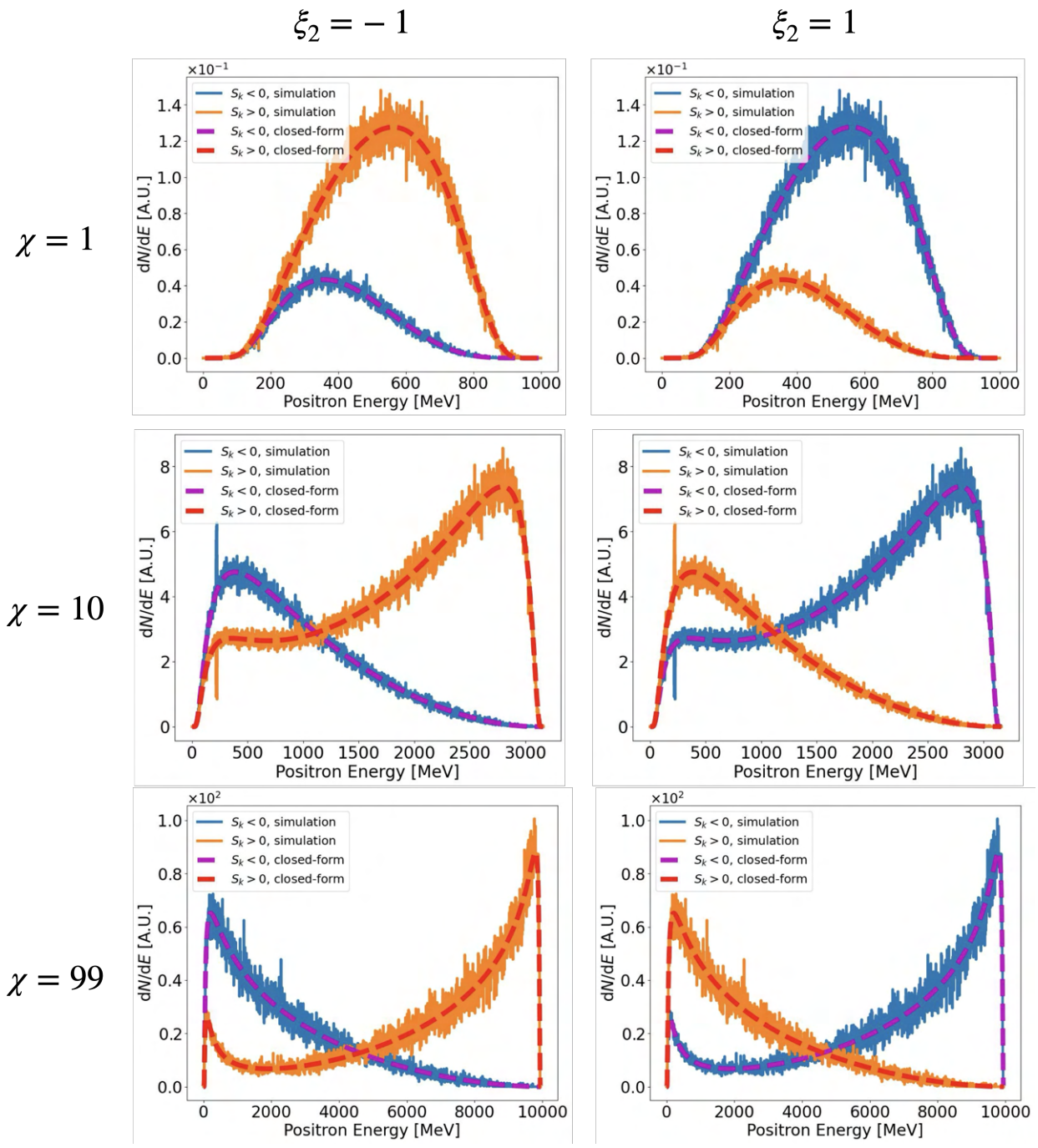

Figure C.10: Benchmark of positron spectrum for spin component S_k from the NBW process for a polarized photon beam inside a constant magnetic field. The photon polarization is either $\xi_2 = -1$ or $\xi_2 = 1$. The classical particle dynamics, radiation back reaction, and radiation induced spin change are all switched off for simplicity. We scan the spectrum through $\chi = 1$, $\chi = 10$, and $\chi = 99$.

spectrum with spin component $S_\beta < 0$ in the rest frame magnetic field direction, and the orange curve shows the positron spectrum with spin component $S_\beta > 0$ in the rest frame magnetic field direction from the simulation. In Fig. C.10, the blue curve shows the positron spectrum with spin component $S_k < 0$ in the positron momentum direction, and the orange curve shows the positron spectrum with spin component $S_k > 0$ in the positron momentum direction from the simulation. We can see that both curves agree well with the closed-form expression.

BIBLIOGRAPHY

[1] Michael Gabler, P Cerdá-Durán, JA Font, N Stergioulas, and E Müller. Modulating magnetar emission by magneto-elastic oscillations. *Astronomische Nachrichten*, 335(3):240–245, 2014.

[2] Malcolm S Longair. *High energy astrophysics*. Cambridge university press, 2011.

[3] Yue-Yue Chen, Pei-Lun He, Rashid Shaisultanov, Karen Z. Hatsagortsyan, and Christoph H. Keitel. Polarized positron beams via intense two-color laser pulses. *Phys. Rev. Lett.*, 123:174801, Oct 2019.

[4] Yan-Fei Li, Rashid Shaisultanov, Karen Z. Hatsagortsyan, Feng Wan, Christoph H. Keitel, and Jian-Xing Li. Ultrarelativistic electron-beam polarization in single-shot interaction with an ultraintense laser pulse. *Phys. Rev. Lett.*, 122:154801, Apr 2019.

[5] Kun Xue, Zhen-Ke Dou, Feng Wan, Tong-Pu Yu, Wei-Min Wang, Jie-Ru Ren, Qian Zhao, Yong-Tao Zhao, Zhong-Feng Xu, and Jian-Xing Li. Generation of highly-polarized high-energy brilliant γ-rays via laser-plasma interaction. *Matter and Radiation at Extremes*, 5(5):054402, 07 2020.

[6] Yan-Fei Li, Yue-Yue Chen, Karen Z. Hatsagortsyan, and Christoph H. Keitel. Helicity transfer in strong laser fields via the electron anomalous magnetic moment. *Phys. Rev. Lett.*, 128:174801, Apr 2022.

[7] Yan-Fei Li, Rashid Shaisultanov, Yue-Yue Chen, Feng Wan, Karen Z. Hatsagortsyan, Christoph H. Keitel, and Jian-Xing Li. Polarized ultrashort brilliant multi-gev γ rays via single-shot laser-electron interaction. *Phys. Rev. Lett.*, 124:014801, Jan 2020.

[8] Yan-Fei Li, Yue-Yue Chen, Wei-Min Wang, and Hua-Si Hu. Production of highly polarized positron beams via helicity transfer from polarized electrons in a strong laser field. *Phys. Rev. Lett.*, 125:044802, Jul 2020.

[9] Donna Strickland and Gerard Mourou. Compression of amplified chirped optical pulses. *Optics communications*, 55(6):447–449, 1985.

[10] T. Tajima and J. M. Dawson. Laser electron accelerator. *Physical Review Letters*, 43(267), 1979.

[11] Stuart PD Mangles, CD Murphy, Zulfikar Najmudin, Alexander George Roy Thomas, JL Collier, Aboobaker E Dangor, EJ Divall, PS Foster, JG Gallacher, CJ Hooker, et al.

Monoenergetic beams of relativistic electrons from intense laser–plasma interactions. *Nature*, 431(7008):535–538, 2004.

[12] Amina E Hussein, Nancy Senabulya, Yong Ma, MJV Streeter, Brendan Kettle, Stephen JD Dann, Félicie Albert, Nicolas Bourgeois, Silvia Cipiccia, Jason M Cole, et al. Laser-wakefield accelerators for high-resolution x-ray imaging of complex microstructures. *Scientific reports*, 9(1):3249, 2019.

[13] JM Cole, JC Wood, NC Lopes, K Poder, RL Abel, S Alatabi, JSJ Bryant, A Jin, S Kneip, K Mecseki, et al. Laser-wakefield accelerators as hard x-ray sources for 3d medical imaging of human bone. *Scientific reports*, 5(1):13244, 2015.

[14] Andrea Macchi, Marco Borghesi, and Matteo Passoni. Ion acceleration by superintense laser-plasma interaction. *Reviews of Modern Physics*, 85(2):751–793, 2013.

[15] Anatoly Maksimchuk, Shaoting Gu, Kirk Flippo, Donald Umstadter, and V Yu Bychenkov. Forward ion acceleration in thin films driven by a high-intensity laser. *Physical Review Letters*, 84(18):4108, 2000.

[16] Brendan Dromey, Matthew Zepf, A Gopal, K Lancaster, MS Wei, K Krushelnick, M Tatarakis, N Vakakis, S Moustaizis, R Kodama, et al. High harmonic generation in the relativistic limit. *Nature physics*, 2(7):456–459, 2006.

[17] F Dollar, P Cummings, V Chvykov, L Willingale, M Vargas, V Yanovsky, C Zulick, A Maksimchuk, AGR Thomas, and K Krushelnick. Scaling high-order harmonic generation from laser-solid interactions to ultrahigh intensity. *Physical review letters*, 110(17):175002, 2013.

[18] Y al Wang, E Granados, F Pedaci, D Alessi, B Luther, M Berrill, and JJ Rocca. Phase-coherent, injection-seeded, table-top soft-x-ray lasers at 18.9 nm and 13.9 nm. *Nature photonics*, 2(2):94–98, 2008.

[19] Adrien Depresseux, Eduardo Oliva, Julien Gautier, F Tissandier, J Nejdl, M Kozlova, G Maynard, JP Goddet, Amar Tafzi, A Lifschitz, et al. Table-top femtosecond soft x-ray laser by collisional ionization gating. *Nature Photonics*, 9(12):817–821, 2015.

[20] Jason M Cole, Daniel R Symes, Nelson C Lopes, Jonathan C Wood, Kristjan Poder, Saleh Alatabi, Stanley W Botchway, Peta S Foster, Sarah Gratton, Sara Johnson, et al. High-resolution μct of a mouse embryo using a compact laser-driven x-ray betatron source. *Proceedings of the National Academy of Sciences*, 115(25):6335–6340, 2018.

[21] M. Roth, D. Jung, K. Falk, N. Guler, O. Deppert, M. Devlin, A. Favalli, J. Fernandez, D. Gautier, M. Geissel, R. Haight, C. E. Hamilton, B. M. Hegelich, R. P. Johnson, F. Merrill, G. Schaumann, K. Schoenberg, M. Schollmeier, T. Shimada, T. Taddeucci, J. L. Tybo, F. Wagner, S. A. Wender, C. H. Wilde, and G. A. Wurden. Bright laser-driven neutron source based on the relativistic transparency of solids. *Phys. Rev. Lett.*, 110:044802, Jan 2013.

[22] V Moskvin, A Subiel, C Desrosiers, M Wiggins, M Maryanski, M Mendonca, M Boyd, A Sorensen, S Cipiccia, R Issac, et al. Su-e-t-472: Characterization of the very high energy electrons, iso-250 mev (vhee) beam generated by alpha-x laser wakefield accelerator beam line for utilization in monte carlo simulation for biomedical experiment planning. *Medical Physics*, 39(6Part17):3813–3814, 2012.

[23] D Speck, E Bliss, J Glaze, J Herris, F Holloway, J Hunt, B Johnson, D Kuizenga, R Ozarski, H Patton, et al. The shiva laser-fusion facility. *IEEE Journal of Quantum Electronics*, 17(9):1599–1619, 1981.

[24] Tong Zhou, John Ruppe, Cheng Zhu, I-Ning Hu, John Nees, and Almantas Galvanauskas. Coherent pulse stacking amplification using low-finesse gires-tournois interferometers. *Opt. Express*, 23(6):7442–7462, Mar 2015.

[25] Alexander Rainville, Mathew Whittlesey, Christopher Pasquale, Yanwen Jing, Qiang Du, and Almantas Galvanauskas. Stable and efficient coherent pulse stacking amplification of 81 pulses with four channel coherent spatial combining at 7mj/fiber. In *CLEO 2023*, page SF3H.6. Optica Publishing Group, 2023.

[26] Alexander Rainville, Mathew Whittlesey, Christopher Pasquale, Yanwen Jing, Mingshu Chen, Siyun Chen, Hanzhang Pei, John Ruppe, Tong Zhou, Qiang Du, Zhigang Zhang, Guoqing Chang, Franz X. Kärtner, and Almantas Galvanauskas. Near-complete extraction of maximum stored energy from large-core fibers using coherent pulse stacking amplification of femtosecond pulses. *Optica*, 11(11):1540–1548, Nov 2024.

[27] Matthias F Kling, Carmen S Menoni, Cameron Geddes, Almantas Galvanauskas, Felicie Albert, Leily Kiani, Michael Chini, L Robert Baker, Keith A Nelson, Linda Young, Jeffrey Moses, Sergio Carbajo, Stavros G Demos, Franklin Dollar, Douglass Schumacher, Janet Y Tsai, Alan R Fry, and Jonathan D Zuegel. Roadmap on basic research needs for laser technology. *Journal of Optics*, 27(1):013002, dec 2024.

[28] Colin N. Danson, Constantin Haefner, Jake Bromage, Thomas Butcher, Jean-Christophe F. Chanteloup, Enam A. Chowdhury, Almantas Galvanauskas, Leonida A. Gizzi, Joachim Hein, David I. Hillier, and et al. Petawatt and exawatt class lasers worldwide. *High Power Laser Science and Engineering*, 7:e54, 2019.

[29] Leily Kiani, Tong Zhou, Seung-Whan Bahk, Jake Bromage, David Bruhwiler, E. Michael Campbell, Zenghu Chang, Enam Chowdhury, Michael Downer, Qiang Du, Eric Esarey, Almantas Galvanauskas, Thomas Galvin, Constantin Häfner, Dieter Hoffmann, Chan Joshi, Manoj Kanskar, Wei Lu, Carmen Menoni, Michael Messerly, Sergey B. Mirov, Mark Palmer, Igor Pogorelsky, Mikhail Polyanskiy, Erik Power, Brendan Reagan, Jorge Rocca, Joshua Rothenberg, Bruno E. Schmidt, Emily Sistrunk, Thomas Spinka, Sergei Tochitsky, Navid Vafaei-Najafabadi, Jeroen van Tilborg, Russell Wilcox, Jonathan Zuegel, and Cameron Geddes. High average power ultrafast laser technologies for driving future advanced accelerators. *Journal of Instrumentation*, 18(08):T08006, aug 2023.

[30] VI Ritus. Quantum effects of the interaction of elementary particles with an intense electromagnetic field. *J. Sov. Laser Res.;(United States)*, 6(5):497–617, 1985.

[31] P Zhang, SS Bulanov, D Seipt, AV Arefiev, and AGR Thomas. Relativistic plasma physics in supercritical fields. *Physics of Plasmas*, 27(5):050601, 2020.

[32] Donald B Melrose. *Quantum plasmadynamics: unmagnetized plasmas*, volume 735. Springer, 2008.

[33] Donald B Melrose. *Quantum plasmadynamics: magnetized plasmas*, volume 854. Springer, 2013.

[34] Dmitri A Uzdensky and Shane Rightley. Plasma physics of extreme astrophysical environments. *Reports on Progress in Physics*, 77(3):036902, mar 2014.

[35] D. Uzdensky, M. Begelman, A. Beloborodov, R. Blandford, S. Boldyrev, B. Cerutti, F. Fiuza, D. Giannios, T. Grismayer, M. Kunz, N. Loureiro, M. Lyutikov, M. Medvedev, M. Petropoulou, A. Philippov, E. Quataert, A. Schekochihin, K. Schoeffler, L. Silva, L. Sironi, A. Spitkovsky, G. Werner, V. Zhdankin, J. Zrake, and E. Zweibel. Extreme plasma astrophysics, 2019.

[36] Peter Goldreich and William H. Julian. Pulsar Electrodynamics. *The Astrophysical Journal*, 157:869, August 1969.

[37] Fábio Cruz, Thomas Grismayer, and Luis O. Silva. Kinetic model of large-amplitude oscillations in neutron star pair cascades. *The Astrophysical Journal*, 908(2):149, feb 2021.

[38] Fábio Cruz, Thomas Grismayer, Alexander Y. Chen, Anatoly Spitkovsky, and Luis O. Silva. Coherent emission from qed cascades in pulsar polar caps. *The Astrophysical Journal Letters*, 919(1):L4, sep 2021.

[39] Remo Ruffini, Gregory Vereshchagin, and She-Sheng Xue. Electron–positron pairs in physics and astrophysics: From heavy nuclei to black holes. *Physics Reports*, 487(1):1–140, 2010.

[40] N. V. Elkina, A. M. Fedotov, I. Yu. Kostyukov, M. V. Legkov, N. B. Narozhny, E. N. Nerush, and H. Ruhl. Qed cascades induced by circularly polarized laser fields. *Phys. Rev. ST Accel. Beams*, 14:054401, May 2011.

[41] C.P. Ridgers, J.G. Kirk, R. Duclous, T.G. Blackburn, C.S. Brady, K. Bennett, T.D. Arber, and A.R. Bell. Modelling gamma-ray photon emission and pair production in high-intensity laser–matter interactions. *Journal of Computational Physics*, 260:273–285, 2014.

[42] A. Gonoskov, S. Bastrakov, E. Efimenko, A. Ilderton, M. Marklund, I. Meyerov, A. Muraviev, A. Sergeev, I. Surmin, and E. Wallin. Extended particle-in-cell schemes for physics in ultrastrong laser fields: Review and developments. *Phys. Rev. E*, 92:023305, Aug 2015.

[43] T. Grismayer, M. Vranic, J. L. Martins, R. A. Fonseca, and L. O. Silva. Laser absorption via quantum electrodynamics cascades in counter propagating laser pulses. *Physics of Plasmas*, 23(5):056706, 05 2016.

[44] K. Ta Phuoc, S. Corde, C. Thaury, V. Malka, A. Tafzi, J. P. Goddet, R. C. Shah, S. Sebban, and A. Rousse. All-optical compton gamma-ray source. *Nature Photonics*, 6:308–311, May 2012.

[45] G. Sarri, D. J. Corvan, W. Schumaker, J. M. Cole, A. Di Piazza, H. Ahmed, C. Harvey, C. H. Keitel, K. Krushelnick, S. P. D. Mangles, Z. Najmudin, D. Symes, A. G. R. Thomas, M. Yeung, Z. Zhao, and M. Zepf. Ultrahigh brilliance multi-mev γ-ray beams from nonlinear relativistic thomson scattering. *Phys. Rev. Lett.*, 113:224801, Nov 2014.

[46] K. Poder, M. Tamburini, G. Sarri, A. Di Piazza, S. Kuschel, C. D. Baird, K. Behm, S. Bohlen, J. M. Cole, D. J. Corvan, M. Duff, E. Gerstmayr, C. H. Keitel, K. Krushelnick, S. P. D. Mangles, P. McKenna, C. D. Murphy, Z. Najmudin, C. P. Ridgers, G. M. Samarin, D. R. Symes, A. G. R. Thomas, J. Warwick, and M. Zepf. Experimental signatures of the quantum nature of radiation reaction in the field of an ultraintense laser. *Phys. Rev. X*, 8:031004, Jul 2018.

[47] J. M. Cole, K. T. Behm, E. Gerstmayr, T. G. Blackburn, J. C. Wood, C. D. Baird, M. J. Duff, C. Harvey, A. Ilderton, A. S. Joglekar, K. Krushelnick, S. Kuschel, M. Marklund, P. McKenna, C. D. Murphy, K. Poder, C. P. Ridgers, G. M. Samarin, G. Sarri, D. R. Symes, A. G. R. Thomas, J. Warwick, M. Zepf, Z. Najmudin, and S. P. D. Mangles. Experimental evidence of radiation reaction in the collision of a high-intensity laser pulse with a laser-wakefield accelerated electron beam. *Phys. Rev. X*, 8:011020, Feb 2018.

[48] A. S. Pirozhkov, A. Sagisaka, K. Ogura, E. A. Vishnyakov, A. N. Shatokhin, C. D. Armstrong, T. Zh. Esirkepov, B. Gonzalez Izquierdo, T. A. Pikuz, P. Hadjisolomou, M. A. Alkhimova, C. Arran, I. P. Tsygvintsev, P. Valenta, S. A. Pikuz, W. Yan, T. M. Jeong, S. Singh, O. Finke, G. Grittani, M. Nevrkla, C. Lazzarini, A. Velyhan, T. Hayakawa, Y. Fukuda, J. K. Koga, M. Ishino, Ko. Kondo, Y. Miyasaka, A. Kon, M. Nishikino, Y. V. Nosach, D. Khikhlukha, A. O. Kolesnikov, E. N. Ragozin, V. A. Gasilov, D. Kumar, J. Nejdl, P. V. Sasorov, S. Weber, D. Margarone, Y. Kato, G. Korn, H. Kiriyama, K. Kondo, C. Ridgers, T. Kawachi, M. Kando, and S. V. Bulanov. Demonstration of the brightest nano-size gamma source, 2024.

[49] A. Gonoskov, T. G. Blackburn, M. Marklund, and S. S. Bulanov. Charged particle motion and radiation in strong electromagnetic fields. *Rev. Mod. Phys.*, 94:045001, Oct. 2022.

[50] David J Griffiths and Darrell F Schroeter. *Introduction to quantum mechanics*. Cambridge university press, 2018.

[51] Walther Gerlach and Otto Stern. Der experimentelle nachweis der richtungsquantelung im magnetfeld. *Zeitschrift für Physik*, 9:349–352, Dec 1922.

[52] Paul Dirac. *The Principles of Quantum Mechanics*. Clarendon Press, Oxford,, 1930.

[53] D. Del Sorbo, D. Seipt, T. G. Blackburn, A. G. R. Thomas, C. D. Murphy, J. G. Kirk, and C. P. Ridgers. Spin polarization of electrons by ultraintense lasers. *Phys. Rev. A*, 96:043407, Oct 2017.

[54] Daniel Seipt, Dario Del Sorbo, Christopher P. Ridgers, and Alec G. R. Thomas. Ultrafast polarization of an electron beam in an intense bichromatic laser field. *Phys. Rev. A*, 100:061402, Dec 2019.

[55] Joachim Kessler. *Polarized electrons*, volume 1. Springer Science & Business Media, 1985.

[56] U Gradmann. Surface magnetism. *Journal of magnetism and magnetic materials*, 100(1-3):481–496, 1991.

[57] K. Abe, T. Akagi, P. L. Anthony, R. Antonov, R. G. Arnold, T. Averett, H. R. Band, J. M. Bauer, H. Borel, P. E. Bosted, V. Breton, J. Button-Shafer, J. P. Chen, T. E. Chupp, J. Clendenin, C. Comptour, K. P. Coulter, G. Court, D. Crabb, M. Daoudi, D. Day, F. S. Dietrich, J. Dunne, H. Dutz, R. Erbacher, J. Fellbaum, A. Feltham, H. Fonvieille, E. Frlez, D. Garvey, R. Gearhart, J. Gomez, P. Grenier, K. A. Griffioen, S. Hoibraten, E. W. Hughes, C. Hyde-Wright, J. R. Johnson, D. Kawall, A. Klein, S. E. Kuhn, M. Kuriki, R. Lindgren, T. Liu, R. M. Lombard-Nelsen, J. Marroncle, T. Maruyama, X. K. Maruyama, J. McCarthy, W. Meyer, Z.-E. Meziani, R. Minehart, J. Mitchell, J. Morgenstern, G. G. Petratos, R. Pitthan, D. Pocanic, C. Prescott, R. Prepost, P. Raines, B. Raue, D. Reyna, A. Rijllart, Y. Roblin, L. S. Rochester, S. E. Rock, O. A. Rondon, I. Sick, L. C. Smith, T. B. Smith, M. Spengos, F. Staley, P. Steiner, S. St. Lorant, L. M. Stuart, F. Suekane, Z. M. Szalata, H. Tang, Y. Terrien, T. Usher, D. Walz, J. L. White, K. Witte, C. C. Young, B. Youngman, H. Yuta, G. Zapalac, B. Zihlmann, and D. Zimmermann. Precision measurement of the deuteron spin structure function g_1^d. *Phys. Rev. Lett.*, 75:25–28, Jul 1995.

[58] V.Yu. Alexakhin, Yu. Alexandrov, G.D. Alexeev, M. Alexeev, A. Amoroso, B. Badełek, F. Balestra, J. Ball, J. Barth, G. Baum, M. Becker, Y. Bedfer, C. Bernet, R. Bertini, M. Bettinelli, R. Birsa, J. Bisplinghoff, P. Bordalo, F. Bradamante, A. Bressan, G. Brona, E. Burtin, M.P. Bussa, V.N. Bytchkov, A. Chapiro, A. Cicuttin, M. Colantoni, A.A. Colavita, S. Costa, M.L. Crespo, N. d'Hose, S. Dalla Torre, S. Das, S.S. Dasgupta, R. De Masi, N. Dedek, D. Demchenko, O.Yu. Denisov, L. Dhara, V. Diaz, A.M. Dinkelbach, S.V. Donskov, V.A. Dorofeev, N. Doshita, V. Duic, W. Dünnweber, A. Efremov, P.D. Eversheim, W. Eyrich, M. Faessler, P. Fauland, A. Ferrero, L. Ferrero, M. Finger, M. Finger, H. Fischer, J. Franz, J.M. Friedrich, V. Frolov, R. Garfagnini, F. Gautheron, O.P. Gavrichtchouk, S. Gerassimov, R. Geyer, M. Giorgi, B. Gobbo, S. Goertz, A.M. Gorin, O.A. Grajek, A. Grasso, B. Grube, A. Guskov, F. Haas, J. Hannappel, D. von Harrach, T. Hasegawa, S. Hedicke, F.H. Heinsius, R. Hermann, C. Heß, F. Hinterberger, M. von Hodenberg, N. Horikawa, S. Horikawa, I. Horn, C. Ilgner, A.I. Ioukaev, I. Ivanchin, O. Ivanov, T. Iwata, R. Jahn, A. Janata, R. Joosten, N.I. Jouravlev, E. Kabuß, D. Kang, B. Ketzer, G.V. Khaustov, Yu.A. Khokhlov, Yu.

Kisselev, F. Klein, K. Klimaszewski, S. Koblitz, J.H. Koivuniemi, V.N. Kolosov, E.V. Komissarov, K. Kondo, K. Königsmann, I. Konorov, V.F. Konstantinov, A.S. Korentchenko, A. Korzenev, A.M. Kotzinian, N.A. Koutchinski, O. Kouznetsov, K. Kowalik, D. Kramer, N.P. Kravchuk, G.V. Krivokhizhin, Z.V. Kroumchtein, J. Kubart, R. Kuhn, V. Kukhtin, F. Kunne, K. Kurek, M.E. Ladygin, M. Lamanna, J.M. Le Goff, M. Leberig, A.A. Lednev, A. Lehmann, J. Lichtenstadt, T. Liska, I. Ludwig, A. Maggiora, M. Maggiora, A. Magnon, G.K. Mallot, C. Marchand, J. Marroncle, A. Martin, J. Marzec, L. Masek, F. Massmann, T. Matsuda, D. Matthiä, A.N. Maximov, W. Meyer, A. Mielech, Yu.V. Mikhailov, M.A. Moinester, T. Nagel, O. Nähle, J. Nassalski, S. Neliba, D.P. Neyret, V.I. Nikolaenko, K. Nikolaev, A.A. Nozdrin, V.F. Obraztsov, A.G. Olshevsky, M. Ostrick, A. Padee, P. Pagano, S. Panebianco, D. Panzieri, S. Paul, D.V. Peshekhonov, V.D. Peshekhonov, G. Piragino, S. Platchkov, J. Pochodzalla, J. Polak, V.A. Polyakov, G. Pontecorvo, A.A. Popov, J. Pretz, S. Procureur, C. Quintans, S. Ramos, G. Reicherz, E. Rondio, A.M. Rozhdestvensky, D. Ryabchikov, V.D. Samoylenko, A. Sandacz, H. Santos, M.G. Sapozhnikov, I.A. Savin, P. Schiavon, C. Schill, L. Schmitt, W. Schroeder, D. Seeharsch, M. Seimetz, D. Setter, O.Yu. Shevchenko, H.-W. Siebert, L. Silva, L. Sinha, A.N. Sissakian, M. Slunecka, G.I. Smirnov, F. Sozzi, A. Srnka, F. Stinzing, M. Stolarski, V.P. Sugonyaev, M. Sulc, R. Sulej, V.V. Tchalishev, S. Tessaro, F. Tessarotto, A. Teufel, L.G. Tkatchev, S. Trippel, G. Venugopal, M. Virius, N.V. Vlassov, R. Webb, E. Weise, Q. Weitzel, R. Windmolders, W. Wiślicki, K. Zaremba, M. Zavertyaev, E. Zemlyanichkina, J. Zhao, R. Ziegler, and A. Zvyagin. The deuteron spin-dependent structure function g1d and its first moment. *Physics Letters B*, 647(1):8–17, 2007.

[59] Haakon Olsen and L. C. Maximon. Photon and electron polarization in high-energy bremsstrahlung and pair production with screening. *Phys. Rev.*, 114:887–904, May 1959.

[60] R. Märtin, G. Weber, R. Barday, Y. Fritzsche, U. Spillmann, W. Chen, R. D. DuBois, J. Enders, M. Hegewald, S. Hess, A. Surzhykov, D. B. Thorn, S. Trotsenko, M. Wagner, D. F. A. Winters, V. A. Yerokhin, and Th. Stöhlker. Polarization transfer of bremsstrahlung arising from spin-polarized electrons. *Phys. Rev. Lett.*, 108:264801, Jun 2012.

[61] D. Abbott, P. Adderley, A. Adeyemi, P. Aguilera, M. Ali, H. Areti, M. Baylac, J. Benesch, G. Bosson, B. Cade, A. Camsonne, L. S. Cardman, J. Clark, P. Cole, S. Covert, C. Cuevas, O. Dadoun, D. Dale, H. Dong, J. Dumas, E. Fanchini, T. Forest, E. Forman, A. Freyberger, E. Froidefond, S. Golge, J. Grames, P. Guèye, J. Hansknecht, P. Harrell, J. Hoskins, C. Hyde, B. Josey, R. Kazimi, Y. Kim, D. Machie, K. Mahoney, R. Mammei, M. Marton, J. McCarter, M. McCaughan, M. McHugh, D. McNulty, K. E. Mesick, T. Michaelides, R. Michaels, B. Moffit, D. Moser, C. Muñoz Camacho, J.-F. Muraz, A. Opper, M. Poelker, J.-S. Réal, L. Richardson, S. Setiniyaz, M. Stutzman, R. Suleiman, C. Tennant, C. Tsai, D. Turner, M. Ungaro, A. Variola, E. Voutier, Y. Wang, and Y. Zhang. Production of highly polarized positrons using polarized electrons at mev energies. *Phys. Rev. Lett.*, 116:214801, May 2016.

[62] P. L. Anthony, R. G. Arnold, C. Arroyo, K. Baird, K. Bega, J. Biesiada, P. E. Bosted, M. Breuer, R. Carr, G. D. Cates, J-P. Chen, E. Chudakov, M. Cooke, F. J. Decker, P. Decowski, A. Deur, W. Emam, R. Erickson, T. Fieguth, C. Field, J. Gao, K. Gustafsson, R. S. Hicks, R. Holmes, E. W. Hughes, T. B. Humensky, G. M. Jones, L. J. Kaufman, Yu. G. Kolomensky, K. S. Kumar, D. Lhuillier, R. Lombard-Nelsen, P. Mastromarino, B. Mayer, R. D. McKeown, R. Michaels, M. Olson, K. D. Paschke, G. A. Peterson, R. Pitthan, K. Pope, D. Relyea, S. E. Rock, O. Saxton, G. Shapiro, J. Singh, P. A. Souder, Z. M. Szalata, W. A. Tobias, B. T. Tonguc, J. Turner, B. Tweedie, A. Vacheret, D. Walz, T. Weber, J. Weisend, D. Whittum, M. Woods, and I. Younus. Observation of parity nonconservation in møller scattering. *Phys. Rev. Lett.*, 92:181602, May 2004.

[63] G. MoortgatPick, T. Abe, G. Alexander, B. Ananthanarayan, A.A. Babich, V. Bharadwaj, D. Barber, and A. Bartl. Polarized positrons and electrons at the linear collider. *Physics Reports*, 460(4):131–243, 2008.

[64] Tanmoy Chattopadhyay. Hard x-ray polarimetry—an overview of the method, science drivers, and recent findings. *Journal of Astrophysics and Astronomy*, 42:106, 2021.

[65] The Event Horizon Telescope Collaboration. First m87 event horizon telescope results. viii. magnetic field structure near the event horizon. *The Astrophysical Journal Letters*, 910(1):L13, mar 2021.

[66] Niccolò Bucciantini, Riccardo Ferrazzoli, Matteo Bachetti, John Rankin, Niccolò Di Lalla, Carmelo Sgrò, Nicola Omodei, Takao Kitaguchi, Tsunefumi Mizuno, Shuichi Gunji, and et al. Simultaneous space and phase resolved x-ray polarimetry of the crab pulsar and nebula. *Nature Astronomy*, 7(5):602–610, 2023.

[67] Ioannis Liodakis, Alan P. Marscher, Iván Agudo, Andrei V. Berdyugin, Maria I. Bernardos, Giacomo Bonnoli, George A. Borman, Carolina Casadio, Victor Casanova, Elisabetta Cavazzuti, and et al. Polarized blazar x-rays imply particle acceleration in shocks. *Nature*, 611(7937):677–681, 2022.

[68] Denis Bernard, Tanmoy Chattopadhyay, Fabian Kislat, and Nicolas Produit. *Gamma-Ray Polarimetry*, pages 1–42. Springer Nature Singapore, Singapore, 2022.

[69] John Tomsick, Steven Boggs, Andreas Zoglauer, Dieter H. Hartmann, Marco Ajello, Eric Burns, Chris Fryer, Chris Karwin, Carolyn Kierans, Alex Lowell, and et al. The compton spectrometer and imager. In *Proceedings of 38th International Cosmic Ray Conference — PoS(ICRC2023)*, volume 444, page 745, 2023.

[70] Merlin Kole. POLAR-2: The First Large Scale Gamma-ray Polarimeter. In *Proceedings of 36th International Cosmic Ray Conference — PoS(ICRC2019)*, volume 358, page 572, 2019.

[71] Zheng Gong, Xiaofei Shen, Karen Z. Hatsagortsyan, and Christoph H. Keitel. Electron slingshot acceleration in relativistic preturbulent shocks explored via emitted photon polarization. *Phys. Rev. Lett.*, 131:225101, Nov 2023.

[72] D. Seipt and B. King. Spin- and polarization-dependent locally-constant-field-approximation rates for nonlinear compton and breit-wheeler processes. *Phys. Rev. A*, 102:052805, Nov 2020.

[73] D. Seipt, C. P. Ridgers, D. Del Sorbo, and A. G. R. Thomas. Polarized qed cascades. *New J. Phys.*, 23:053025, 2021.

[74] B. King, N. Elkina, and H. Ruhl. Photon polarization in electron-seeded pair-creation cascades. *Phys. Rev. A*, 87:042117, Apr 2013.

[75] Zheng Gong, Karen Z. Hatsagortsyan, and Christoph H. Keitel. Electron polarization in ultrarelativistic plasma current filamentation instabilities. *Phys. Rev. Lett.*, 130:015101, Jan 2023.

[76] Zheng Gong, Karen Z. Hatsagortsyan, and Christoph H. Keitel. Spin-polarized condensed plasmoids in radiation reaction dominated magnetic reconnection. *Phys. Rev. Lett.*, 135:045101, Jul 2025.

[77] Julian Schwinger. On gauge invariance and vacuum polarization. *Phys. Rev.*, 82:664–679, Jun 1951.

[78] THOMAS ERBER. High-energy electromagnetic conversion processes in intense magnetic fields. *Rev. Mod. Phys.*, 38:626–659, Oct 1966.

[79] AI Nikishov and VI Ritus. Quantum processes in the field of a plane electromagnetic wave and in a constant field. i. *Sov. Phys. JETP*, 19(2):529–541, 1964.

[80] A. A. Sokolov and I. M. Ternov. *Synchrotron Radiation*. Akademie-Verlag, Berlin, 1 edition, 1968.

[81] G. Bassompierre, G. Bologna, D. Boget, M. Chevallier, S. Costa, J. Dufournaud, M. Farizon, B. Farizon Mazuy, A. Feliciello, M.J. Gaillard, R. Garfagnini, R. Genre, M. Gouanère, B. Ille, R. Kirsch, P. Lautesse, M. Richard, E. Rossetto, D. Sillou, and M. Spighel. Search for light neutral objects photoproduced in a crystal strong field and decaying into e^+e^- pairs. *Physics Letters B*, 355(3):584–594, 1995.

[82] Joseph John Thomson. *Conduction of electricity through gases*. Watchmaker Publishing, 2005.

[83] John David Jackson. *Classical electrodynamics*. John Wiley & Sons, 2021.

[84] J. Larmor. Lxiii. on the theory of the magnetic influence on spectra; and on the radiation from moving ions. *The London, Edinburgh, and Dublin Philosophical Magazine and Journal of Science*, 44(271):503–512, 1897.

[85] Max Abraham. Prinzipien der dynamik des elektrons. *Annalen der Physik*, 315(1):105–179, 1902.

[86] Paul Adrien Maurice Dirac. Classical theory of radiating electrons. *Proceedings of the Royal Society of London. Series A. Mathematical and Physical Sciences*, 167(929):148–169, 1938.

[87] Igor V Sokolov, Natalia M Naumova, John A Nees, Gérard A Mourou, and Victor P Yanovsky. Dynamics of emitting electrons in strong laser fields. *Physics of Plasmas*, 16(9), 2009.

[88] Anton Ilderton and Greger Torgrimsson. Radiation reaction in strong field qed. *Physics Letters B*, 725(4):481–486, 2013.

[89] Lev Davidovič Landau, Evgenij Michajlovič Lifšic, Gerhard Heber, Hardwin Jungclaussen, Georg Dautcourt, Wolfgang Weller, Adolf Kühnel, Eberhard Jäger, and Benjamin Kozik. *Lehrbuch der theoretischen Physik*, volume 1. Akademie Verlag Berlin, 1966.

[90] L. D. Landau and E. M. Lifschits. *The Classical Theory of Fields*, volume Volume 2 of *Course of Theoretical Physics*. Pergamon Press, Oxford, 1975.

[91] R. Capdessus, E. d'Humières, and V. T. Tikhonchuk. Modeling of radiation losses in ultrahigh power laser-matter interaction. *Phys. Rev. E*, 86:036401, Sep 2012.

[92] M. Vranic, J.L. Martins, R.A. Fonseca, and L.O. Silva. Classical radiation reaction in particle-in-cell simulations. *Computer Physics Communications*, 204:141–151, 2016.

[93] Suo Tang, Naveen Kumar, and Christoph H. Keitel. Plasma high-order-harmonic generation from ultraintense laser pulses. *Phys. Rev. E*, 95:051201, May 2017.

[94] S R Mane, Yu M Shatunov, and K Yokoya. Spin-polarized charged particle beams in high-energy accelerators. *Reports on Progress in Physics*, 68(9):1997, aug 2005.

[95] Paul Ehrenfest. Bemerkung über die angenäherte gültigkeit der klassischen mechanik innerhalb der quantenmechanik. *Zeitschrift für physik*, 45(7):455–457, 1927.

[96] Steven Weinberg. *The quantum theory of fields*, volume 2. Cambridge university press, 1995.

[97] W. H. Furry. On bound states and scattering in positron theory. *Phys. Rev.*, 81:115–124, Jan 1951.

[98] A. Di Piazza, C. Müller, K. Z. Hatsagortsyan, and C. H. Keitel. Extremely high-intensity laser interactions with fundamental quantum systems. *Rev. Mod. Phys.*, 84:1177–1228, Aug 2012.

[99] THOMAS HEINZL. Strong-field qed and high-power lasers. *International Journal of Modern Physics A*, 27(15):1260010, 2012.

[100] Michael E Peskin. *An Introduction to quantum field theory*. CRC press, 2018.

[101] A. Fedotov, A. Ilderton, F. Karbstein, B. King, D. Seipt, H. Taya, and G. Torgrimsson. Advances in qed with intense background fields. *Physics Reports*, 1010:1–138, 2023. Advances in QED with intense background fields.

[102] A. I. Nikishov and V. I. Ritus. Quantum processes in the field of a plane electromagnetic wave and in a constant field. i. *Sov. Phys. JETP*, 19(2):529–541, 1964.

[103] Lowell S. Brown and T. W. B. Kibble. Interaction of intense laser beams with electrons. *Phys. Rev.*, 133:A705–A719, Feb 1964.

[104] N. B. Narozhnyi, A. I. Nikishov, and V. I. Ritus. Quantum processes in the field of a circularly polarized electromagnetic wave. *Sov. Phys. JETP*, 20:622, 1965.

[105] C. Bula, K. T. McDonald, E. J. Prebys, C. Bamber, S. Boege, T. Kotseroglou, A. C. Melissinos, D. D. Meyerhofer, W. Ragg, D. L. Burke, R. C. Field, G. Horton-Smith, A. C. Odian, J. E. Spencer, D. Walz, S. C. Berridge, W. M. Bugg, K. Shmakov, and A. W. Weidemann. Observation of nonlinear effects in compton scattering. *Phys. Rev. Lett.*, 76:3116–3119, Apr 1996.

[106] Howard R. Reiss. Absorption of Light by Light. *Journal of Mathematical Physics*, 3(1):59–67, 12 2004.

[107] D. L. Burke, R. C. Field, G. Horton-Smith, J. E. Spencer, D. Walz, S. C. Berridge, W. M. Bugg, K. Shmakov, A. W. Weidemann, C. Bula, K. T. McDonald, E. J. Prebys, C. Bamber, S. J. Boege, T. Koffas, T. Kotseroglou, A. C. Melissinos, D. D. Meyerhofer, D. A. Reis, and W. Ragg. Positron production in multiphoton light-by-light scattering. *Phys. Rev. Lett.*, 79:1626–1629, Sep 1997.

[108] AI Voroshilo, EA Padusenko, and SP Roshchupkin. One-photon annihilation of an electron-positron pair in the field of pulsed circularly polarized light wave. *Laser physics*, 20(7):1679–1685, 2010.

[109] H Mitter. Quantum electrodynamics in laser fields. In *Electromagnetic Interactions and Field Theory*, pages 397–468. Springer, 1975.

[110] V.N. Baier and V.M. Katkov. Concept of formation length in radiation theory. *Physics Reports*, 409(5):261–359, 2005.

[111] Ulrik I. Uggerhøj. The interaction of relativistic particles with strong crystalline fields. *Rev. Mod. Phys.*, 77:1131–1171, Oct 2005.

[112] T. G. Blackburn, D. Seipt, S. S. Bulanov, and M. Marklund. Radiation beaming in the quantum regime. *Phys. Rev. A*, 101:012505, Jan 2020.

[113] A. Di Piazza, M. Tamburini, S. Meuren, and C. H. Keitel. Implementing nonlinear compton scattering beyond the local-constant-field approximation. *Phys. Rev. A*, 98:012134, Jul 2018.

[114] C.P. Ridgers, J.G. Kirk, R. Duclous, T.G. Blackburn, C.S. Brady, K. Bennett, T.D. Arber, and A.R. Bell. Modelling gamma-ray photon emission and pair production in high-intensity laser–matter interactions. *Journal of Computational Physics*, 260:273–285, 2014.

[115] VN Baier and VM Katkov. Processes involved in the motion of high energy particles in a magnetic field. *Sov. Phys. JETP*, 26:854, 1968.

[116] Victor Dinu, Chris Harvey, Anton Ilderton, Mattias Marklund, and Greger Torgrimsson. Quantum radiation reaction: From interference to incoherence. *Phys. Rev. Lett.*, 116:044801, Jan 2016.

[117] A. Di Piazza, M. Tamburini, S. Meuren, and C. H. Keitel. Improved local-constant-field approximation for strong-field qed codes. *Phys. Rev. A*, 99:022125, Feb 2019.

[118] T. G. Blackburn, D. Seipt, S. S. Bulanov, and M. Marklund. Benchmarking semiclassical approaches to strong-field QED: Nonlinear Compton scattering in intense laser pulses. *Physics of Plasmas*, 25(8):083108, 08 2018.

[119] A. Ilderton, B. King, and D. Seipt. Extended locally constant field approximation for nonlinear compton scattering. *Phys. Rev. A*, 99:042121, Apr 2019.

[120] C. Bamber, S. J. Boege, T. Koffas, T. Kotseroglou, A. C. Melissinos, D. D. Meyerhofer, D. A. Reis, W. Ragg, C. Bula, K. T. McDonald, E. J. Prebys, D. L. Burke, R. C. Field, G. Horton-Smith, J. E. Spencer, D. Walz, S. C. Berridge, W. M. Bugg, K. Shmakov, and A. W. Weidemann. Studies of nonlinear qed in collisions of 46.6 gev electrons with intense laser pulses. *Phys. Rev. D*, 60:092004, Oct 1999.

[121] P. Chen, G. Horton-Smith, T. Ohgaki, A.W. Weidemann, and K. Yokoya. Cain: Conglomérat d'abel et d'interactions non-linéaires. *Nuclear Instruments and Methods in Physics Research Section A: Accelerators, Spectrometers, Detectors and Associated Equipment*, 355(1):107–110, 1995. Gamma-Gamma Colliders.

[122] Anthony Hartin. Strong field qed in lepton colliders and electron/laser interactions. *International Journal of Modern Physics A*, 33(13):1830011, 2018.

[123] T. Heinzl, B. King, and A. J. MacLeod. Locally monochromatic approximation to qed in intense laser fields. *Phys. Rev. A*, 102:063110, Dec 2020.

[124] Greger Torgrimsson. Loops and polarization in strong-field qed. *New Journal of Physics*, 23(6):065001, may 2021.

[125] T. G. Blackburn, B. King, and S. Tang. Simulations of laser-driven strong-field qed with ptarmigan: Resolving wavelength-scale interference and γ-ray polarization, 2023.

[126] A. Di Piazza, K. Z. Hatsagortsyan, and C. H. Keitel. Quantum radiation reaction effects in multiphoton compton scattering. *Phys. Rev. Lett.*, 105:220403, Nov 2010.

[127] A. Ilderton, B. King, and S. Tang. Loop spin effects in intense background fields. *Phys. Rev. D*, 102:076013, Oct 2020.

[128] B. King and S. Tang. Nonlinear compton scattering of polarized photons in plane-wave backgrounds. *Phys. Rev. A*, 102:022809, Aug 2020.

[129] S. Tang, B. King, and H. Hu. Highly polarised gamma photons from electron-laser collisions. *Physics Letters B*, 809:135701, 2020.

[130] Victor Dinu and Greger Torgrimsson. Single and double nonlinear compton scattering. *Phys. Rev. D*, 99:096018, May 2019.

[131] D. Seipt, D. Del Sorbo, C. P. Ridgers, and A. G. R. Thomas. Theory of radiative electron polarization in strong laser fields. *Phys. Rev. A*, 98:023417, Aug 2018.

[132] Victor Dinu and Greger Torgrimsson. Approximating higher-order nonlinear qed processes with first-order building blocks. *Phys. Rev. D*, 102:016018, Jul 2020.

[133] Daniel Seipt and Alec G. R. Thomas. Kinetic theory for spin-polarized relativistic plasmas. *Physics of Plasmas*, 30(9):093102, 09 2023.

[134] T. Heinzl, A. Ilderton, and B. King. Classical resummation and breakdown of strong-field qed. *Phys. Rev. Lett.*, 127:061601, Aug 2021.

[135] VI Ritus. Radiative effects and their enhancement in an intense electromagnetic field. *Sov. Phys. JETP*, 30(1181):052805–20, 1970.

[136] C. P. Ridgers, T. G. Blackburn, D. Del Sorbo, L. E. Bradley, C. Slade-Lowther, C. D. Baird, S. P. D. Mangles, P. McKenna, M. Marklund, C. D. Murphy, and et al. Signatures of quantum effects on radiation reaction in laser–electron-beam collisions. *Journal of Plasma Physics*, 83(5):715830502, 2017.

[137] N. V. Elkina, A. M. Fedotov, I. Yu. Kostyukov, M. V. Legkov, N. B. Narozhny, E. N. Nerush, and H. Ruhl. Qed cascades induced by circularly polarized laser fields. *Phys. Rev. ST Accel. Beams*, 14:054401, May 2011.

[138] Ren-Tong Guo, Yu Wang, Rashid Shaisultanov, Feng Wan, Zhong-Feng Xu, Yue-Yue Chen, Karen Z. Hatsagortsyan, and Jian-Xing Li. Stochasticity in radiative polarization of ultrarelativistic electrons in an ultrastrong laser pulse. *Phys. Rev. Res.*, 2:033483, Sep 2020.

[139] Yuhui Tang, Zheng Gong, Jinqing Yu, Yinren Shou, and Xueqing Yan. Radiative polarization dynamics of relativistic electrons in an intense electromagnetic field. *Phys. Rev. A*, 103:042807, Apr 2021.

[140] A. Gonoskov, S. Bastrakov, E. Efimenko, A. Ilderton, M. Marklund, I. Meyerov, A. Muraviev, A. Sergeev, I. Surmin, and E. Wallin. Extended particle-in-cell schemes for physics in ultrastrong laser fields: Review and developments. *Phys. Rev. E*, 92:023305, Aug 2015.

[141] T. Grismayer, M. Vranic, J. L. Martins, R. A. Fonseca, and L. O. Silva. Seeded qed cascades in counterpropagating laser pulses. *Phys. Rev. E*, 95:023210, Feb 2017.

[142] D. Del Sorbo, D. Seipt, A. G. R. Thomas, and C. P. Ridgers. Electron spin polarization in realistic trajectories around the magnetic node of two counter-propagating, circularly polarized, ultra-intense lasers. *Plasma Phys. Control. Fusion*, 60:064003, 2018.

[143] D. Del Sorbo, D. Seipt, T. G. Blackburn, A. G. R. Thomas, C. D. Murphy, J. G. Kirk, and C. P. Ridgers. Spin polarization of electrons by ultraintense lasers. *Phys. Rev. A*, 96:043407, Oct 2017.

[144] VN Baier, VM Katkov, and VM Strakhovenko. Kinetics of radiative polarization. *Sov. Phys. JETP*, 31(5):908, 1970.

[145] Yue-Yue Chen, Karen Z. Hatsagortsyan, Christoph H. Keitel, and Rashid Shaisultanov. Electron spin- and photon polarization-resolved probabilities of strong-field qed processes. *Phys. Rev. D*, 105:116013, Jun 2022.

[146] M. Vranic, T. Grismayer, J.L. Martins, R.A. Fonseca, and L.O. Silva. Particle merging algorithm for pic codes. *Computer Physics Communications*, 191:65–73, 2015.

[147] T. G. Blackburn, B. King, and S. Tang. Simulations of laser-driven strong-field qed with ptarmigan: Resolving wavelength-scale interference and γ-ray polarization. *Physics of Plasmas*, 30(9):093903, 09 2023.

[148] A. R. Bell and John G. Kirk. Possibility of prolific pair production with high-power lasers. *Phys. Rev. Lett.*, 101:200403, Nov 2008.

[149] Félicie Albert, M E Couprie, Alexander Debus, Mike C Downer, Jérôme Faure, Alessandro Flacco, Leonida A Gizzi, Thomas Grismayer, Axel Huebl, Chan Joshi, M Labat, Wim P Leemans, Andreas R Maier, Stuart P D Mangles, Paul Mason, François Mathieu, Patric Muggli, Mamiko Nishiuchi, Jens Osterhoff, P P Rajeev, Ulrich Schramm, Jörg Schreiber, Alec G R Thomas, Jean-Luc Vay, Marija Vranic, and Karl Zeil. 2020 roadmap on plasma accelerators. *New Journal of Physics*, 23(3):031101, mar 2021.

[150] R. A. Fonseca, L. O. Silva, F. S. Tsung, V. K. Decyk, W. Lu, C. Ren, W. B. Mori, S. Deng, S. Lee, T. Katsouleas, and J. C. Adam. Osiris: A three-dimensional, fully relativistic particle in cell code for modeling plasma based accelerators. In Peter M. A. Sloot, Alfons G. Hoekstra, C. J. Kenneth Tan, and Jack J. Dongarra, editors, *Computational Science — ICCS 2002*, pages 342–351, Berlin, Heidelberg, 2002. Springer Berlin Heidelberg.

[151] R A Fonseca, S F Martins, L O Silva, J W Tonge, F S Tsung, and W B Mori. One-to-one direct modeling of experiments and astrophysical scenarios: pushing the envelope on kinetic plasma simulations. *Plasma Physics and Controlled Fusion*, 50(12):124034, nov 2008.

[152] Qian Qian, Daniel Seipt, Marija Vranic, Thomas E. Grismayer, Thomas G. Blackburn, Christopher P. Ridgers, and Alexander G. R. Thomas. Parametric study of the polarization dependence of nonlinear Breit–Wheeler pair creation process using two laser pulses. *Physics of Plasmas*, 30(10):103107, 10 2023.

[153] B. King and N. Elkina. Vacuum birefringence in high-energy laser-electron collisions. *Phys. Rev. A*, 94:062102, Dec 2016.

[154] Yoshihide Nakamiya and Kensuke Homma. Probing vacuum birefringence under a high-intensity laser field with gamma-ray polarimetry at the gev scale. *Phys. Rev. D*, 96:053002, Sep 2017.

[155] Feng Wan, Yu Wang, Ren-Tong Guo, Yue-Yue Chen, Rashid Shaisultanov, Zhong-Feng Xu, Karen Z. Hatsagortsyan, Christoph H. Keitel, and Jian-Xing Li. High-energy γ-photon polarization in nonlinear breit-wheeler pair production and γ polarimetry. *Phys. Rev. Res.*, 2:032049, Aug 2020.

[156] Huai-Hang Song, Wei-Min Wang, Yan-Fei Li, Bing-Jun Li, Yu-Tong Li, Zheng-Ming Sheng, Li-Ming Chen, and Jie Zhang. Spin and polarization effects on the nonlinear breit–wheeler pair production in laser-plasma interaction. *New Journal of Physics*, 23(7):075005, jul 2021.

[157] C. P. Ridgers, C. S. Brady, R. Duclous, J. G. Kirk, K. Bennett, T. D. Arber, A. P. L. Robinson, and A. R. Bell. Dense electron-positron plasmas and ultraintense γ rays from laser-irradiated solids. *Phys. Rev. Lett.*, 108:165006, Apr 2012.

[158] C. P. Ridgers, C. S. Brady, R. Duclous, J. G. Kirk, K. Bennett, T. D. Arber, and A. R. Bell. Dense electron-positron plasmas and bursts of gamma-rays from laser-generated quantum electrodynamic plasmasa). *Physics of Plasmas*, 20(5):056701, 04 2013.

[159] P. Hadjisolomou, T. M. Jeong, D. Kolenaty, A. J. Macleod, V. Olšovcová, R. Versaci, C. P. Ridgers, and S. V. Bulanov. Gamma-flash generation in multi-petawatt laser–matter interactions. *Phys. Plasmas*, 30(9):093103, Sep. 2023.

[160] A. N. Timokhin. Time-dependent pair cascades in magnetospheres of neutron stars – i. dynamics of the polar cap cascade with no particle supply from the neutron star surface. *Monthly Notices of the Royal Astronomical Society*, 408(4):2092–2114, 10 2010.

[161] Fábio Cruz, Thomas Grismayer, Alexander Y. Chen, Anatoly Spitkovsky, and Luis O. Silva. Coherent emission from qed cascades in pulsar polar caps. *The Astrophysical Journal Letters*, 919(1):L4, sep 2021.

[162] Tatsufumi Nakamura, James K. Koga, Timur Zh. Esirkepov, Masaki Kando, Georg Korn, and Sergei V. Bulanov. High-power γ-ray flash generation in ultraintense laser-plasma interactions. *Phys. Rev. Lett.*, 108:195001, May 2012.

[163] Turcu I. C. E., Negoita F., Jaroszynski D. A, McKenna P., Balascuta S., Ursescu D., Dancus I., Cernaianu M. O., Tararu M. V., Ghenuche P., Stutman D., Boianu A.,

Risca M., Zepf M., Sarri G., Dromey B., and Harvey C. High field physics and qed experiments at eli-np. *Romanian Reports in Physics*, 68:S145–1231, 2016.

[164] M. Altarelli, R. Assmann, F. Burkart, B. Heinemann, T. Heinzl, T. Koffas, A. R. Maier, D. Reis, A. Ringwald, and M. Wing. Summary of strong-field qed workshop, 2019.

[165] D. Doria, M.O. Cernaianu, P. Ghenuche, D. Stutman, K.A. Tanaka, C. Ticos, and C.A. Ur. Overview of eli-np status and laser commissioning experiments with 1 pw and 10 pw class-lasers. *Journal of Instrumentation*, 15(09):C09053, sep 2020.

[166] A. Di Piazza, L. Willingale, and J. D. Zuegel. Multi-petawatt physics prioritization (mp3) workshop report, 2022.

[167] Yinren Shou, Pengjie Wang, Seong Geun Lee, Yong Joo Rhee, Hwang Woon Lee, Jin Woo Yoon, Jae Hee Sung, Seong Ku Lee, Zhuo Pan, Defeng Kong, Zhusong Mei, Jianbo Liu, Shirui Xu, Zhigang Deng, Weimin Zhou, Toshiki Tajima, Il Woo Choi, Xueqing Yan, Chang Hee Nam, and Wenjun Ma. Brilliant femtosecond-laser-driven hard x-ray flashes from carbon nanotube plasma. *Nature Photonics*, 17(2):137–142, Feb 2023.

[168] A. S. Pirozhkov, A. Sagisaka, K. Ogura, E. A. Vishnyakov, A. N. Shatokhin, C. D. Armstrong, T. Zh. Esirkepov, B. Gonzalez Izquierdo, T. A. Pikuz, P. Hadjisolomou, M. A. Alkhimova, C. Arran, I. P. Tsygvintsev, P. Valenta, S. A. Pikuz, W. Yan, T. M. Jeong, S. Singh, O. Finke, G. Grittani, M. Nevrkla, C. Lazzarini, A. Velyhan, T. Hayakawa, Y. Fukuda, J. K. Koga, M. Ishino, Ko. Kondo, Y. Miyasaka, A. Kon, M. Nishikino, Y. V. Nosach, D. Khikhlukha, A. O. Kolesnikov, E. N. Ragozin, V. A. Gasilov, D. Kumar, J. Nejdl, P. V. Sasorov, S. Weber, D. Margarone, Y. Kato, G. Korn, H. Kiriyama, K. Kondo, C. Ridgers, T. Kawachi, M. Kando, and S. V. Bulanov. Demonstration of the brightest nano-size gamma source, 2024.

[169] S. Morris, A. Robinson, and C. Ridgers. Highly efficient conversion of laser energy to hard x-rays in high-intensity laser–solid simulations. *Physics of Plasmas*, 28(10):103304, 10 2021.

[170] Jiří Vyskočil, Ondřej Klimo, and Stefan Weber. Simulations of bremsstrahlung emission in ultra-intense laser interactions with foil targets. *Plasma Physics and Controlled Fusion*, 60(5):054013, mar 2018.

[171] Christina Ingleby, Christopher Arran Stuart Morris, Christopher Ridgers, and Kate Lancaster. A comparison of the intensity scaling for nonlinear compton scattering and bremsstrahlung x-ray emission. Article submitted to: High Power Laser Science and Engineering, March 25, 2025.

[172] B. Martinez, E. d'Humières, and L. Gremillet. Synchrotron radiation from ultrahigh-intensity laser-plasma interactions and competition with bremsstrahlung in thin foil targets. *Phys. Rev. Res.*, 2:043341, Dec 2020.

[173] S. Go, Y. Tsuzuki, H. Yoneda, Y. Ichikawa, T. Ikeda, N. Imai, K. Imamura, M. Niikura, D. Nishimura, R. Mizuno, S. Takeda, H. Ueno, S. Watanabe, T. Y. Saito, S. Shimoura, S. Sugawara, A. Takamine, and T. Takahashi. Demonstration of nuclear gamma-ray polarimetry based on a multi-layer cdte compton camera. *Scientific Reports*, 14(1):2573, 2024.

[174] Cosmin Ilie. Gamma-ray polarimetry: A new window for the nonthermal universe. *Publications of the Astronomical Society of the Pacific*, 131(1005):111001, sep 2019.

[175] Michael Schnell, Alexander Sävert, Ingo Uschmann, Maria Reuter, Maria Nicolai, Tino Kämpfer, Björn Landgraf, Oliver Jäckel, Oliver Jansen, Alexander Pukhov, Malte Christoph Kaluza, and Christian Spielmann. Optical control of hard x-ray polarization by electron injection in a laser wakefield accelerator. *Nature Communications*, 4(1):2421, 2013.

[176] J. L. Shohet, D. B. van Hulsteyn, S. J. Gitomer, J. F. Kephart, and R. P. Godwin. Polarization of x rays from laser-produced plasmas. *Phys. Rev. Lett.*, 38:1024–1027, May 1977.

[177] C. P. Ridgers, T. G. Blackburn, D. Del Sorbo, L. E. Bradley, C. Slade-Lowther, C. D. Baird, S. P. D. Mangles, P. McKenna, M. Marklund, C. D. Murphy, and et al. Signatures of quantum effects on radiation reaction in laser–electron-beam collisions. *Journal of Plasma Physics*, 83(5):715830502, 2017.

[178] J G Kirk, A R Bell, and I Arka. Pair production in counter-propagating laser beams. *Plasma Physics and Controlled Fusion*, 51(8):085008, jul 2009.

[179] T. Grismayer, M. Vranic, J. L. Martins, R. A. Fonseca, and L. O. Silva. Laser absorption via quantum electrodynamics cascades in counter propagating laser pulses. *Physics of Plasmas*, 23(5):056706, 05 2016.

[180] Brandon K. Russell, Marija Vranic, Paul T. Campbell, Alexander G. R. Thomas, Kevin M. Schoeffler, Dmitri A. Uzdensky, and Louise Willingale. Magnetic field generation in laser-solid interactions at strong-field qed relevant intensities, 2023.

[181] Particle Physics Project Prioritization Panel (P5). Executive summary of 2023 particle physics project prioritization panel (p5), 2023. Accessed: 2024-06-10.

[182] P. Michel, C. B. Schroeder, B. A. Shadwick, E. Esarey, and W. P. Leemans. Radiative damping and electron beam dynamics in plasma-based accelerators. *Phys. Rev. E*, 74:026501, Aug 2006.

[183] Alexander Debus, Richard Pausch, Axel Huebl, Klaus Steiniger, René Widera, Thomas E. Cowan, Ulrich Schramm, and Michael Bussmann. Circumventing the dephasing and depletion limits of laser-wakefield acceleration. *Phys. Rev. X*, 9:031044, Sep 2019.

[184] J. P. Palastro, J. L. Shaw, P. Franke, D. Ramsey, T. T. Simpson, and D. H. Froula. Dephasingless laser wakefield acceleration. *Phys. Rev. Lett.*, 124:134802, Mar 2020.

[185] Alec G. R. Thomas and Daniel Seipt. Modeling chromatic emittance growth in staged plasma wakefield acceleration to 1 tev using nonlinear transfer matrices. *Phys. Rev. Accel. Beams*, 24:104602, Oct 2021.

[186] J. Vieira, C.-K. Huang, W. B. Mori, and L. O. Silva. Polarized beam conditioning in plasma based acceleration. *Phys. Rev. ST Accel. Beams*, 14:071303, Jul 2011.

[187] W. Lu, C. Huang, M. Zhou, W. B. Mori, and T. Katsouleas. Nonlinear theory for relativistic plasma wakefields in the blowout regime. *Phys. Rev. Lett.*, 96:165002, Apr 2006.

[188] Spencer Gessner, Erik Adli, James M. Allen, Weiming An, Christine I. Clarke, Chris E. Clayton, Sebastien Corde, J. P. Delahaye, Joel Frederico, Selina Z. Green, Carsten Hast, Mark J. Hogan, Chan Joshi, Carl A. Lindstrøm, Nate Lipkowitz, Michael Litos, Wei Lu, Kenneth A. Marsh, Warren B. Mori, Brendan O'Shea, Navid Vafaei-Najafabadi, Dieter Walz, Vitaly Yakimenko, and Gerald Yocky. Demonstration of a positron beam-driven hollow channel plasma wakefield accelerator. *Nature Communications*, 7(1):11785, 2016.

[189] Swapan Chattopadhyay, Gérard Mourou, Vladimir D Shiltsev, and Toshiki Tajima. *Beam Acceleration in Crystals and Nanostructures*. WORLD SCIENTIFIC, 2020.

[190] W. Lu, M. Tzoufras, C. Joshi, F. S. Tsung, W. B. Mori, J. Vieira, R. A. Fonseca, and L. O. Silva. *Phys. Rev. ST Accel. Beams*, 10(6):061301, 2007.

[191] Marija Vranic, Thomas Grismayer, Ricardo A Fonseca, and Luis O Silva. Quantum radiation reaction in head-on laser-electron beam interaction. *New Journal of Physics*, 18(7):073035, jul 2016.

[192] B. Barish and J. E. Brau. The international linear collider. *International Journal of Modern Physics A*, 28(27):1330039, 2013.

[193] G. MoortgatPick, T. Abe, G. Alexander, B. Ananthanarayan, A.A. Babich, V. Bharadwaj, D. Barber, A. Bartl, A. Brachmann, S. Chen, J. Clarke, J.E. Clendenin, J. Dainton, K. Desch, and M. Diehl. Polarized positrons and electrons at the linear collider. *Physics Reports*, 460(4):131–243, 2008.